

FAST NEUTRON PHYSICS

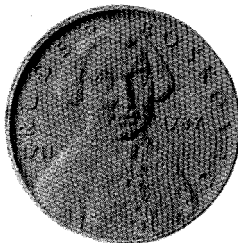
Proceedings of the International Conference
on Fast Neutron Physics,
Dubrovnik, Yugoslavia, May 26—31, 1986

Editors

Đ. Miljanić

B. Antolković

G. Paić



1986

Ruder Bošković Institute, Zagreb, Yugoslavia

O R G A N I Z A T I O N

This conference was organized in the Interuniversity Centre for Post-graduate Studies in Dubrovnik in conjunction with the 3rd Research coordination meeting of the Coordinated Research Programme on Measurement and analysis of the 14 MeV neutron nuclear data needed for fission and fusion reactor technology of the International Atomic Energy Agency. It was sponsored by the Selfmanaging Community of Interest for Science of S.R. Croatia, the Rudjer Bošković Institute and the International Atomic Energy Agency.

Conference Organizers

B. Antolković	D. Miljanić
M.K. Mehta	G. Paić

International Advisory Committee

R.S. Caswell	A. Marcinkowski
J. Csikai	P. Obložinský
F. Cvelbar	S.M. Qaim
S.M. Grimes	J.J. Schmidt
S.K. Gupta	D. Seeliger
R.C. Haight	D.L. Smith
S. Joly	A. Takahashi
H. Klein	H. Vonach

Conference secretary

Z. Kuzmić

PREFACE

The fast neutron physics represents a very important link in the international scientific collaboration between laboratories in developed and developing countries. It is almost the only nuclear physics available to poorer countries. It seemed therefore opportune to organize an international conference reviewing a number of key problems in neutron physics on the occasion of the third and final Research Coordination Meeting of the participants in the IAEA Coordinated Research Programme on Measurement and Analysis of 14 MeV Neutron Nuclear Data needed for Fission and Fusion Reactor Technology. The conference programme has included 11 invited talks and 40 contributed papers on the following topics: models for neutron reactions, data for biomedical applications, few body studies, techniques and neutron sources and fast neutron reactions. Sixty participants from 24 countries attended the conference.

It is our pleasure to acknowledge the help of all our collaborators, the advisory committee, the invited speakers and participants in creating the atmosphere necessary for the success of a scientific meeting.

Zagreb, 15 July 1986

The Editors

Note: The contributions have been published as received from the authors with no alteration.

TABLE OF CONTENTS

PREFACE	iv
Chapter I	
THEORETICAL MODELS FOR FAST NEUTRON REACTIONS	1
Recent developments in the application of the statistical multistep compound and direct theories to neutron and light ion induced reactions	
R. Bonetti	2
Model calculations of fast neutron nonelastic cross sections	
A. Marcinkowski	17
Isotopic effects in neutron induced reactions and preequilibrium particle emission	
R. Čaplar	37
Models for radiative neutron capture in the nuclear giant resonance region	
M. Potokar	52
Investigation of spin effects in exciton model codes	
H. Gruppelaar, J.M. Akkermans, Shi Xiangjun	67
Nuclear model analysis of the (n,p) reaction cross section isotope effect for the titanium isotopes	
M. Avriganu, M. Ivaşcu, V. Avriganu	71
Preequilibrium γ -rays with angular-momentum coupling	
P. Obložinský	74
Coupled channel analysis of neutron scattering from ^{12}C between 9 and 15 MeV	
L.F. Hansen, A.S. Meigooni	78

Fast polarized neutron scattering on ^{40}Ca , ^{40}Ar , ^{89}Y and ^{169}Tm for coupled-channel optical model analysis	
J.W. Hammer, W. Grum, K.-W. Hoffmann, H. Postner G. Schleußner, G. Schreder, P.A. Owono	81
Microscopic and conventional optical model analysis of 22 MeV neutron elastic scattering from Mg to Bi	
N. Olsson, B. Trostell, E. Ramström, B. Holmqvist, F.S. Dietrich	84
Phenomenology of angular distributions of fast neutron induced particle emission cross sections	
D. Hermsdorf, H. Kalka, D. Seeliger, U. Steininger	87
Chapter II	
NUCLEAR DATA FOR BIOMEDICAL APPLICATIONS	91
Dosimetry of fast neutrons with energies below 20 MeV	
G. Dietze	92
Partial kerma factors for elastic and inelastic neutron scattering from tissue-abundant elements	
R.W. Finlay, M.S. Islam	106
Refinement of neutron energy deposition and microdosimetry calculations	
R.S. Caswell, J.J. Coyne, H.M. Gerstenberg, R.B. Schwartz	122
Kerma factor of carbon for neutrons of energies between 14 and 20 MeV	
H.H. Barschall, P.M. DeLuca, R.C. Haight	135
Cross sections for fast neutron induced reactions on carbon	
B. Antolković, G. Dietze, H. Klein	137
Fast neutron interaction data from measurements with low pressure proportional counters	
H.G. Menzel, H. Schuhmacher	140

Chapter III

FEW BODY SYSTEMS

143

Scattering theory and numerical results for
few-nucleon systems

W. Glöckle

144

Recent measurements of the neutron-proton capture
cross section

P. Leleux

160

A kinematically complete n-d breakup experiment
at $E_n = 13$ MeV

K. Geißdörfer, R. Lin, A. Strate, J. Böttcher,
J. Cub, E. Finckh, G. Fuchs, B. Kratz,
S. Schindler, M. Seiter, W. Tornow

174

Evidence for a simultaneous breakup component in
nucleon scattering on carbon

B. Antolković

177

Quadrupole spectrometer measurements of (n, charged
particle) cross sections of Be, N, and O at $E = 14$ MeV

R.C. Haight

180

Interaction of neutrons with ^9Be at 14.6 MeV -
The four body breakup $2n+2\alpha$

D. Ferenc, B. Antolković, G. Paić, M. Zadro,
S. Blagus

183

^4H and (n, α) reactions on ^6Li and ^7Li

D. Miljanić, S. Blagus, M. Zadro, D. Rendić

186

Chapter IV

EXPERIMENTAL TECHNIQUES AND NEUTRON SOURCES

187

D-T neutron sources

H.H. Barschall

188

Progress in fast neutron detection techniques

H. Klein	203
A new neutron ToF facility at OKTAVIAN	
A. Takahashi, H. Sugimoto, E. Ichimura	219
The Stuttgart "SCORPION" facility for scattering experiments with fast polarized neutrons in the energy range of 7 to 8 MeV	
J.W. Hammer, G. Bulski, W. Grum, K.-W. Hoffmann, G. Keilbach, G. Schleußner, G. Schreder	224
A spectrometer for double-differential neutron-emission cross section measurements	
E. Dekempeneer, H. Liskien, L. Mewissen, F. Poortmans	227
First results at the A.P.T. - Fast neutron facility of the L.N.L.	
R. Cherubini, G. Galeazzi, F. Jimenez, C. Manduchi, G. Moschini, R. Nino, R. Policroniades, M.T. Russo Manduchi, G.F. Segato, B.M. Stievano, A. Varela	231
A deuterium/tritium gas target for the production of fast neutrons with the d-d and d-t reactions and the associated particle technique	
C. Cernigoi, R. Cherubini, G. Moschini, C. Tuniz	234
Energy and angular distributions of neutrons from the $^2\text{H}(\text{d},\text{n})^3\text{He}$ and $^3\text{H}(\text{d},\text{n})^4\text{He}$ reactions	
J. Csikai, Zs. Lantos, Cs.M. Buczko	237
The fast neutron spectrum measurement with scintillation detector	
D. Nikolić, M. Milošević, M. Pešić	240
Unfolding of scintillation spectra using approximately known response functions	
M. Zadro, M. Bogovac	243

A new application of Am-Be neutron source -
Production of 5-10 MeV gamma rays for calibration

Ye Zongyuan, Li Jingwen, Yue Gang, Shi Detang 247

Fast neutron spectrum determination with threshold
detectors at the RB reactor

M. Šokčić-Kostić, M. Pešić, D. Antić 250

Fast neutron fields at the RB nuclear reactor

M. Pešić, P. Strugar, H. Marković, D. Stefanović 253

Chapter V

FAST NEUTRON REACTIONS

257

Measurements from 5 to 10 MeV of double differential
(n, α) cross sections of Ni and Cu

E. Wattecamps, F. Arnotte 258

Fast neutron cross sections on zirconium isotopes

A. Marcinkowski, K. Stankiewicz, U. Garuska 262

Recent developments in the study of (n, α) reactions
on heavy nuclei

L. Głowacka, M. Jaskóła, J. Turkiewicz, J. Dalmás,
A. Chiadli, E. Gadioli, E. Gadioli Erba, L. Zemło 266

Anomalous behaviour of the ratio of (n, α) and (n,p)
cross sections on aluminium measured around 14.7 MeV

M. Ibn Majah, A. Ait Haddou, M. Viennot, G. Paic 269

(n,t) reaction on ^9Be at 14.6 MeV

M. Zadro, S. Blagus, D. Miljanić, D. Rendić 271

Study of $^{56}\text{Fe}(n,n'\gamma)$ reaction at 14.1 MeV

A.A. Lychagin, S.P. Simakov, O.A. Salnikov,
B.W. Dewkin, A.B. Paschenko, T. Sztaricskai, G. Petö 272

${}^7\text{Li}(n,n'){}^7\text{Li}^*$ (478) neutron angular distribution
derived from Doppler-broadened γ -energy distributions

H. Liskien, Shanglian Bao

275

Inelastic neutron scattering cross sections on
actinide nuclei (Th,U)

E. Sheldon, L.E. Beghian, J.J. Egan, G.C. Goswami,
G.H.R. Kegel, A. Mittler

279

Neutron emission from lead bombarded with 14 MeV
neutrons

T. Elfruth, D. Hermsdorf, H. Kalka, J. Pöthig,
D. Seeliger, K. Seidel, S. Unholzer

282

Neutron emission cross sections of Pb and Cu at
14.6 MeV neutron energy

K. Gul, M. Anwar, S.M. Saleem, M. Ahmad

285

Discrete γ -ray production cross sections in ${}^{52}\text{Cr}(n,x\gamma)$
at 14.6 MeV

S. Hlaváč, P. Obložinský

288

Cross section of ${}^{209}\text{Bi}(\gamma,n)$ reaction induced by Fe
thermal neutron capture γ -rays

Ye Gang, Ye Zongyuan, Li Jingwen, Shi Detang,
Huang Shengnian

292

Neutron activation cross sections of some isotopes
of molybdenum at 14.6 MeV

M. Rahman, N.I. Molla, S. Khatun, A.K.M. Fazlul Hoque,
Rahezuddin Miah and Ayesha Akhtar Khan

295

Excitation function of ${}^{93}\text{Nb}(n,{}^3\text{He}){}^{91}\text{Y}$ reaction near
its threshold: Comparison of ${}^3\text{He}$ - and ${}^3\text{H}$ -emission
probabilities

S.M. Qaim, R. Wölfle, H. Liskien

298

Yields and average cross sections of recoil charged
particles induced reactions on ${}^{11}\text{B}$, ${}^{12}\text{C}$, ${}^{13}\text{C}$, ${}^{14}\text{N}$,
 ${}^{16}\text{O}$ and ${}^{18}\text{O}$

A. Ait Haddou, M. Berrada, G. Paić

299

Activation cross-sections of some (n,p), (n,n'p) and (n, α) reactions induced by 14.8 MeV neutrons on Cr and Ti isotopes

Hoang Dac Luc, Phan Nhu Ngoc, Nguyen Van Do,
Ly Ba Bach

300

Effect of deuterium ion beam composition on the 14 MeV neutron yield from Ti-T targets

S.Y. Hurani, B.M. Wanis, H.T. Mustafa,
S.A. Nikiforov

301

Neutron flux and energy variations for a large beam diameter and a thick rotating target in close proximity

B.M. Bahal, I. Juan, S. Hurani, A.R. Mohabbis

305

LIST OF PARTICIPANTS

309

Chapter I

THEORETICAL MODELS FOR FAST NEUTRON REACTIONS

RECENT DEVELOPMENTS IN THE APPLICATION OF THE STATISTICAL MULTISTEP
COMPOUND AND DIRECT THEORIES TO NEUTRON AND PROTON INDUCED REACTIONS

R. Bonetti

Istituto di Fisica Generale Applicata dell'Università di Milano
Milano, Italy

The current status of the application of the statistical multistep compound and direct theories to reactions induced by neutron and protons at energies between 14 and 45 MeV is reviewed. Particular emphasis is given to recent calculations as the multiparticle emission within the multistep compound theory and the interplay between the multistep compound and direct processes as a function of the energy.

1. INTRODUCTION

Neutron and, more generally, nucleon beams offer an unique tool to understand nuclear reaction mechanisms and to try to get information on the structure of the nuclei involved. In comparison with the now more in fashion heavy ion reactions, the relative simplicity of nucleon induced reactions allows one to probe nuclear properties from a more fundamental point of view. Moreover, in testing new reaction mechanisms, it is quite natural that one should address himself first to the large amount of experimental data available of neutron and proton induced reactions, before attacking more involved cases as complex particles or heavy ion induced reactions.

This was indeed the path our group in Milano has followed in the last few years in applying the statistical theories of multistep compound (SMC) and direct (SMD) reactions to the experimental data. This paper will be devoted to reviewing the results obtained with SMC

and SMD in understanding the continuum spectra of (nucleon, nucleon) reactions. Emphasis will be given to recent developments as the calculation of multiparticle emission and the interplay between SMC and SMD emissions as a function of incident and outgoing energies.

II. GENERAL FEATURES AND APPLICATION OF THE SMC THEORY

The domain of applicability of the SMC and SMD theories ⁽¹⁾ to experimental data can be understood by looking at this (very famous!) typical spectrum shown below.

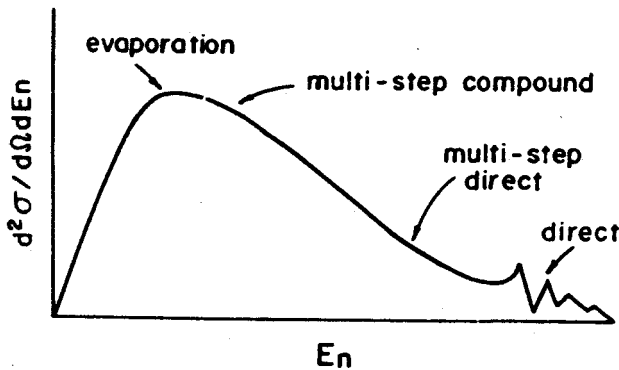


Fig. 1. Schematic spectrum of the neutrons emitted in a (p,n) reaction

At the high energy end, individual levels of the residual nucleus are found. The related angular distribution is generally forward peaked this indicating a fast, direct-like process. As the particle energy decreases, the spectrum becomes continuum, and the angular distribution loses its forward peaking becoming progressively symmetric to 90° and eventually isotropic. In this energy region the interaction time is long, and we are facing the so-called evaporation region.

The region in between, the so-called precompound region, is the one to which the SMC and SMD theories address themselves, with the multistep direct prevailing near the high energy end and the multistep compound near the low energy one. The relative importance of the two mechanisms can be only assessed by explicit calculations.

However, we should expect the entrance channel to play a very important role: this can be understood by recalling the general characteristics of the two mechanisms. The SMC describes the long lasting, quasi equilibrium compound-like processes, and requires that bound states be formed at each stage of the multistep compound chain. On the other hand, the SMD is concerned with the fast, direct like processes, and requires that at least one particle be unbound at each stage. Therefore the SMC process is expected to be important at relatively low incident energy, a situation in which bound states are most probably formed.

Our calculations found that this happens generally at energies not above 14-18 MeV. Above such values, the reaction preferentially populates unbound states and then SMD prevails. Since the bulk of neutron induced reactions with which we are mainly concerned now is at about 14 MeV, we expect this process to be particularly important in our discussion. The SMC cross section is

$$\frac{d\sigma}{dU} = \frac{\pi}{k^2} \sum_{n=1}^{\infty} \sum_{\nu=n-1}^{\infty} \frac{\langle \xi_{\nu\nu}(\nu) \Gamma_n^{\nu\nu}(\nu) \rangle}{\Gamma_n} \left[\prod_{k=1}^{n-1} \frac{\Gamma_k^d}{\Gamma_k} \right] \frac{2\pi \Gamma_1}{D_1} \quad (1)$$

where Γ_n is the total width of the states in the n^{th} stage,
 $\Gamma_n = \Gamma_n^d + \Gamma_n^b$ and $\langle \xi(\nu) \Gamma(\nu) \rangle$ is the width for the states at energy between U and $U + dU$ to escape in the continuum.

The term $2\pi \Gamma_1/D_1$ is the strength function for the formation of the first doorway state. Expression (1) contains also the evaporation contribution, the so-called r-term, this avoiding any ad-hoc addition as one has to do with the semiclassical exciton models. It could be useful to see that the r-term expression reduces easily to the traditional Hauser Feshbach one. Indeed

$$\sigma_{L, \nu}^{(r)} = \frac{\pi}{k^2} \frac{\Gamma_n^b}{\Gamma_n} \prod_{k=1}^{n-1} \frac{\Gamma_k^d}{\Gamma_k} \frac{2\pi \Gamma_1}{D_1} \quad (2)$$

substituting Γ with the corresponding Γ through relation

$$T = 2\pi \Gamma / D$$

one has

$$\text{and considering that } \Gamma_a = \Gamma_a^* = \sum_c \Gamma_a^{(c)}$$

$$G_f^{(a)} = \frac{\pi}{k^2} \frac{T_f T_i}{\sum_c T_c} \quad (3)$$

where

$$T_i = \frac{2\pi \Gamma_a}{D_a} \prod_{k=1}^{i-1} \frac{\Gamma_k^+}{\Gamma_k^-} \quad (4)$$

This expression shows that one expects the Bohr independence hypothesis to be valid only when the depletion factor is unity, therefore only when the emission probability from SMC states is negligible.

A crucial point in evaluating the cross section (1) is the calculation of both Γ^+ and Γ^- . The first choice one has to do is which kind of description of the nuclear excitation process should be adopted.

A quite natural choice for nucleon induced reactions is the p-h excitation. Therefore the complexity of the stages of the SMC chain will be defined in terms of number of excitons. Further, one has to adopt a given microscopic description of the nuclear matrix elements entering into the definition of Γ^+ and $\Gamma^{+(1)}$. The most simple assumptions are the following:

- i) the radial wave functions associated with interacting particles are l-independent and constant within the nuclear volume;
- ii) the two-body interaction is of the zero range form

$$V(\vec{r}_1, \vec{r}_2) = V_0 \frac{4}{3} \pi r_0^3 \delta(\vec{r}_1 - \vec{r}_2) \quad (5)$$

- iii) the state density is that given by Ericson and includes the angular momentum dependence

$$\rho_{r,h}(E, J) = \frac{g(E)}{P(h) (-1)^l} \left(\frac{2J+1}{\pi^{1/2} N^{3/2} \Theta^3} e^{-\frac{(J+1/2)^2}{N \Theta^2}} \right) \quad (6)$$

With these assumptions the radial overlap integrals, to the square of which Γ^+ and Γ^- are proportional, are given by quite simple analytic expressions⁽¹⁾. The first calculation, using the above assumptions have been done on (p,n), (n,p), (³He,p) reactions at 13-14 MeV⁽²⁾.

However, it was soon clear that:

- a) The strength of the residual interaction needed to fit the data was too small (0.7 MeV instead of 25 MeV, as given by DWBA analysis).
- b) The incident energy dependence of the SMC cross section was wrong,

i.e. too much cross section was predicted with increasing energy. The reason of all these problems lies in the approximations described above. We have therefore released them one by one, in successive steps. First we took into account the fact that SMC involves only bound levels. Therefore we explicitly introduced this condition into the level density which were recalculated ⁽³⁾ still using the equidistant-spacing single-particle model but cutting all the energy integrations pertaining to the excited particles at the binding energy value. The effect of this modification is shown in Fig. 2.

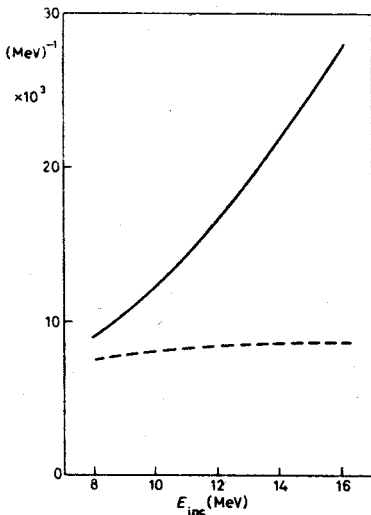


Fig. 2.

The 5-excitons (4p-1h) level density as resulting from the correction described (dotted line), compared with the result of the Ericson expression (full line), vs. the incident ^3He energy. The reaction was $^{27}\text{Al}(^3\text{He}, p)$.

In such a way the correct incident energy dependence of the SMC cross section was obtained, due to the fact that the ratio of the number of bound levels to the totality of levels decreased with energy, thus correctly describing the decreasing importance of compound-like processes with energy. On the other hand, the V_0 problem was solved by using realistic wave functions and a finite range density dependent two-body interaction ⁽⁴⁾. Harmonic oscillator wave functions were thus used to describe bound states, while for the continuum ones distorted waves generated in an optical model potential were taken. This allowed to reproduce both SMC cross section and total widths (measured by means of a fluctuation analysis ⁽⁵⁾) with a V_0 value which was close to

the DWBA one. Some examples of this fits are shown in Fig. 3.

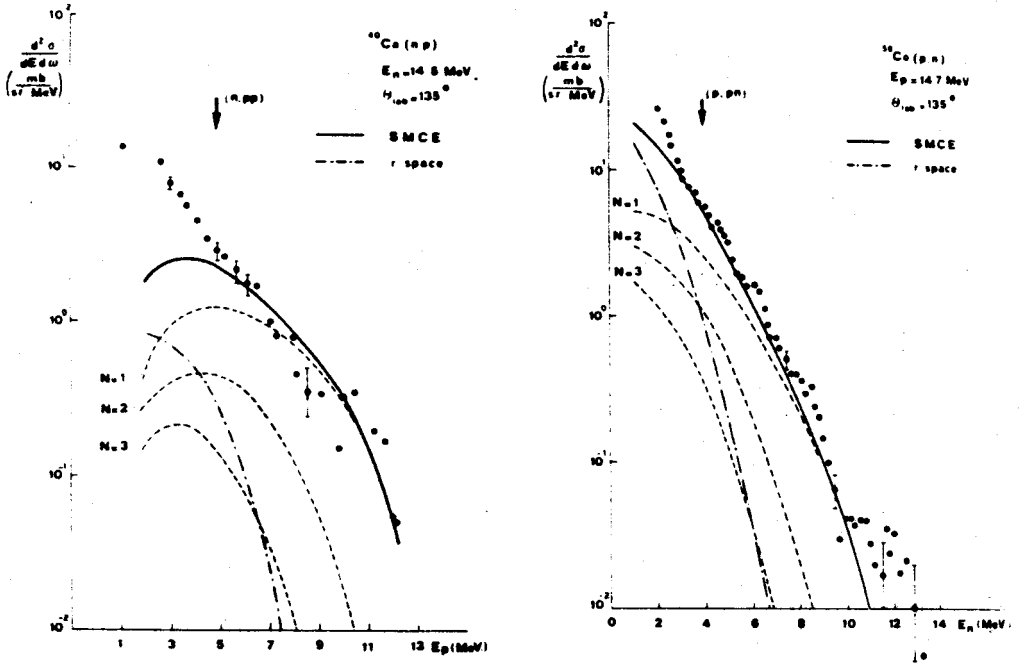


Fig. 3- Experimental and calculated spectra. The arrows indicate the thresholds of some multiple reactions.

III. CALCULATION OF THE MULTIPARTICLE EMISSION WITH THE SMC FORMALISM

In applying the SMC to a group of (n,n') reactions at 14 MeV it was clear that, while good fits were obtained at the high energy end, some strength was missing at low energy. Indeed, since measurements were made without explicit identification of the residual nucleus, the data were contaminated by such processes as $(n,2n)$ and (n,pn) . The cross section of these reactions were calculated by an extension of the SMC formalism, assuming that after emission of the first particle, the system is practically equilibrated. Therefore, the second particle emission will take place only from the residual equilibrium r -stage. This is justified by calculation of the level density as a function of the nuclear complexity (number of excitons). According to the saturation condition⁽¹⁾ set in the SMC theory, the r -stage should contain those configurations whose level density ρ_n does not exhibit the dramatic increase with n characteristic of the preequilibrium phase. This condition is quantitatively expressed as

$$\rho_{n-1} \leq k \rho_n, \quad k \approx 10$$

In the case of the $^{59}\text{Co}(n,n')$ reaction at 14 MeV, the above condition leads as a conclusion that the first three steps should belong to the preequilibrium phase, while the terms with $n > 7$ should be all included in the evaporation r -term. However, after the first particle has been emitted and has carried away at least 8 MeV, the excitation energy left is so low that equilibrium is reached with a very small number of excitons. This implies that any two particle preequilibrium emission is negligible at this energy. The formulae used were a generalization of the SMC cross section (eq. 1), where the r -stage branching ratio describing the two particle emission probability is given by

$$\frac{\Gamma_n^I}{\sum_i \Gamma_n^I} \frac{\langle \Gamma_{n-1}^{II}(\nu) \rho_s(\nu) \rangle}{\sum_i \Gamma_n^{II}} \quad (7)$$

where the first particle escape widths Γ_n^I are obtained integrating the $\langle \Gamma(\nu) \rho(\nu) \rangle$ functions over the energy intervals available by energy

conservation. For simplicity, the sum over the particle channels i is limited to neutron and protons.

The result of the two-particle contributions ⁽⁶⁾ is shown in Figs. 4 and 5 (dotted lines).

Their importance in reproducing the low energy part of the spectrum, where two particle emission is energetically possible, is evident.

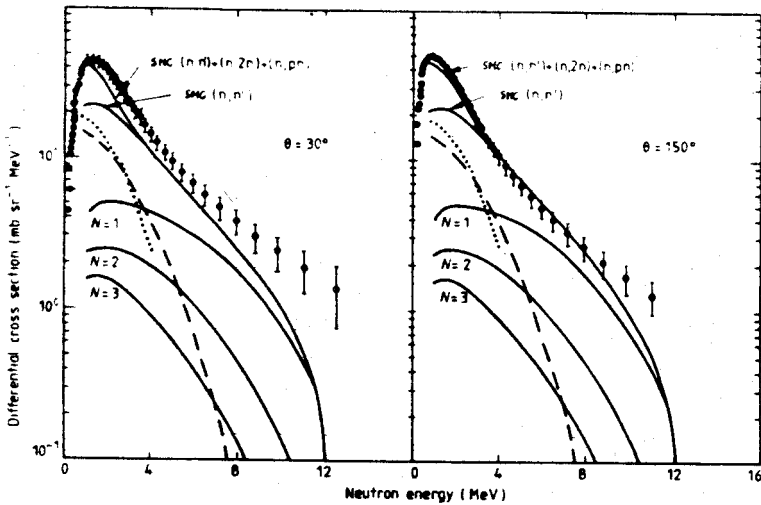
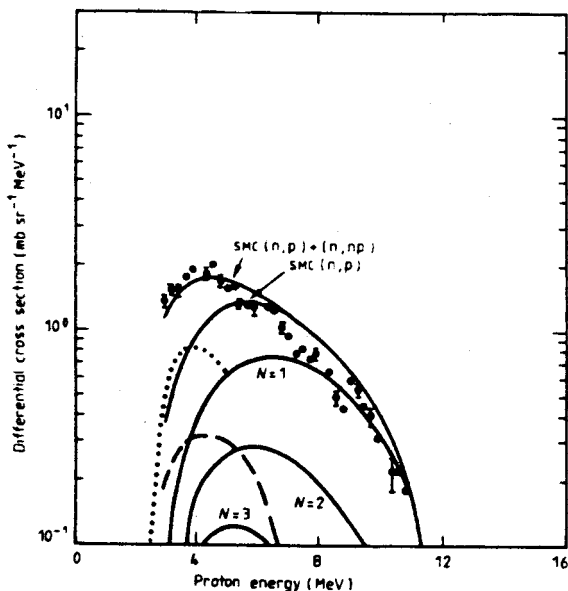


Fig. 4- Energy spectra of neutrons emitted at 30° and 150° from ⁵⁹Co at an incident neutron energy of 14 MeV. The curves labelled with the value of N show the contributions of N -step processes and the broken and dotted curves show those due to the residual r -stage processes for the (n,n') and the $(n,2n)+(n,pn)$ reactions respectively. The full curve gives the sum of these processes.

Fig. 5- Same as Fig. 4 for
 $^{59}\text{Co}(n,p)$ reaction.



IV. THE INTERPLAY BETWEEN SMC AND SMD AT DIFFERENT ENERGIES

The work at relatively low incident energy (about 14 MeV) has shown that SMC is able to reproduce data by itself. Indeed, empirical evaluation of the direct (or multistep direct) component at this energy by extraction of the anisotropic part of the angular distributions leads to conclude that such component is as high as 10% of the total cross section. At higher energies, the situation of course might change drastically due to the increasing probability that unbound states are populated. If the energy is therefore high enough, a situation will be reached in which on the other hand the cross section would be almost entirely given by SMD. To be more explicit, let us look at a case which was particularly studied, the $^{420}\text{Sn}(p,n)$ reaction. At 45 MeV the angular distributions of the continuum are extremely forward peaked. Therefore it is expected that SMD should

dominate. Indeed, a calculation using the expression

$$\frac{d^2\sigma}{dV d\Omega} = \sum_V \sum_n \int \frac{dk_1}{(2\pi)^3} \dots \int \frac{dk_V}{(2\pi)^3} \left[\frac{dW_{m,V}(k_1, k_V)}{dV_1 d\Omega_1} \right] \dots \left[\frac{dW_{2,1}(k_2, k_1)}{dV_2 d\Omega_2} \right] \frac{d^2\sigma_{el}(k_1, k_2)}{dV_1 d\Omega_1} \quad (8)$$

where

$$\frac{dW_{n,n-1}}{dV d\Omega} = 2\pi^2 \rho(k) \rho_2(V) |v_{n,n-1}|^2 \quad (9)$$

and where

$$\frac{d^2\sigma}{dV d\Omega} = \sum_L (2L+1) R_2(L) \rho_2(V) \left\langle \frac{d\sigma_L}{d\Omega} \right\rangle^{DW} \quad (10)$$

was able to fit quite well both angular distributions and neutron spectra (Fig. 6).

This calculation was done by assuming that the matrix elements in Eq. (9) were DWBA ones, $\langle \chi_n^- V_{n,n-1} \chi_{n-1}^+ \rangle$.

It was pointed out by M. Kawai that due to the biorthogonality of the distorted waves, one should use the expression $\langle \tilde{\chi}_n^+ V_{n,n-1} \chi_{n-1}^+ \rangle$ instead. We therefore repeated the calculations with the above expression (related to the previous one by the inverse of the elastic scattering matrix S). By using this choice, an unsatisfactory fit was obtained. However, Feshbach has recently shown ⁽⁷⁾ that the need for energy averaging of the distorted waves brings the latter expression in the DWBA form, thus justifying the first calculations.

To proceed in our discussion, it would be interesting to see what happens in "intermediate" energy cases, therefore at energies $14 \leq E \leq 45$. It is expected that in this energy interval both SMC and SMD contribute. We therefore choose the $\text{Sn}(p,n)$ reaction now at 25 MeV. The calculations have been done for the two mechanisms with the same parameters: Becchetti-Greenlees O.M. potential for the distorted waves, 1-fm Yukawa interaction for the two-body residual interaction with $V_0 = 25$ MeV; in addition, the bound states in SMC were calculated with an Harmonic oscillator potential and only bound levels were considered,

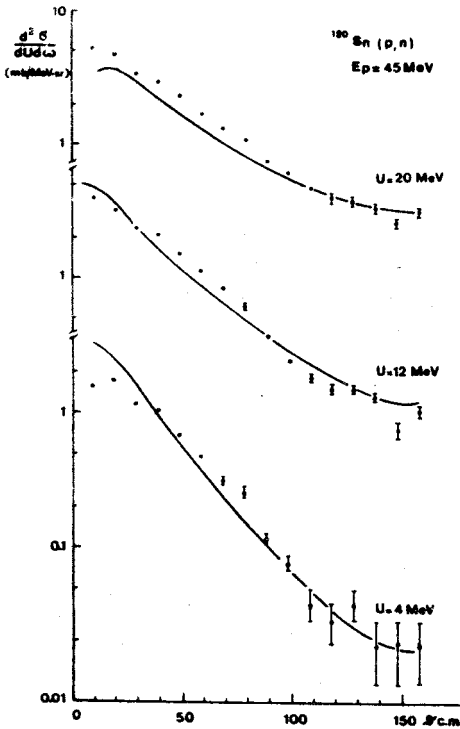
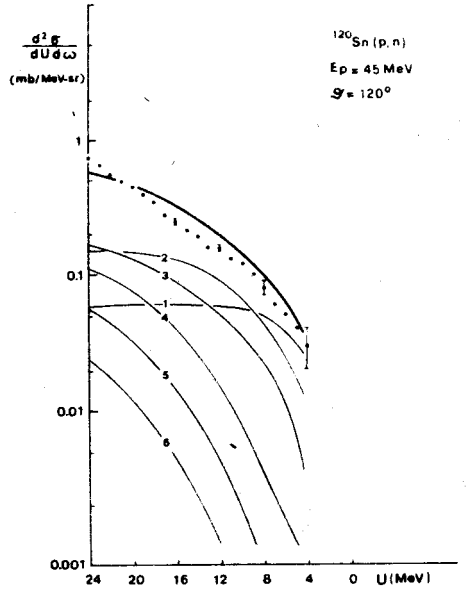
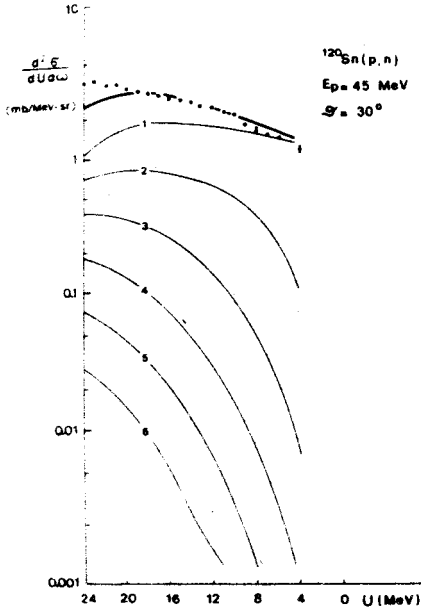


Fig. 6. Results of the SMD calculations on the $^{120}\text{Sn}(p,n)$ reactions at 45 MeV. The full line represents the sum of the different terms.

consistently with the basic assumption of SMC as discussed in Section II. This point is quite an important one. It was found that by using the traditional Ericson level density the quantity $\sum_{\ell} (2\pi r_1^{\ell}/D_{\ell})(2\ell+1)$ was about 3-4 times its theoretically expected upper limit given by $\sum_{\ell} T_{\ell}(2\ell+1)$, while by cutting the level density at the binding energy value the above quantity reduced to 10-20% of its upper limit. This correctly describes the well known decreasing importance of equilibrium and quasi-equilibrium processes with increasing incident energy. The results are shown in Fig. 7.

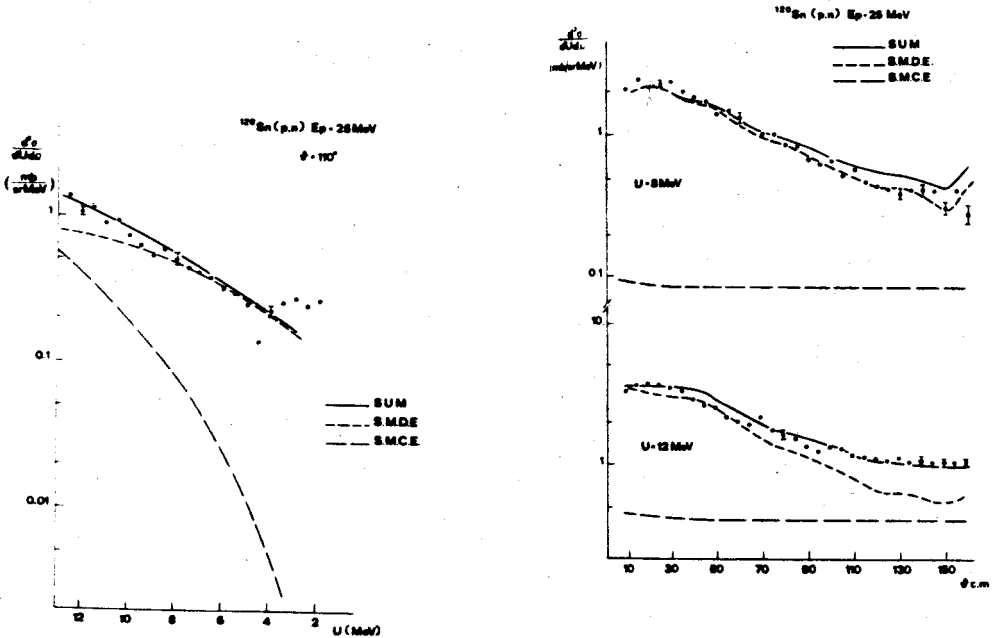


Fig. 7- Results of the SMC+SMD calculations on the $^{120}\text{Sn}(p,n)$ at 25 MeV.

The SMD process dominates in the angular distributions at low excitation energy and in the high energy part of the spectrum. The SMC, including the evaporation term, is important at backward angles and at lower neutron energies.

The same features are present in recent calculations on a series of (p,n) reactions on Mo isotopes⁽⁸⁾. In the case of $^{100}\text{Mo}(p,n)$ (Figs. 8 and 9) it is clear that in the intermediate part of the energy spectrum SMC and SMD contribute with comparable yield and must be both taken into account in order to fit the data, whereas at the high energy end (see the angular distribution) SMD alone is almost able by itself to explain the experimental cross section. This result quantitatively supports the qualitative features anticipated in Fig. 1. It seems now that these theories could be used with confidence to calculate more complicated reactions. Work on (p, α) and on light heavy-ion induced reactions is in progress.

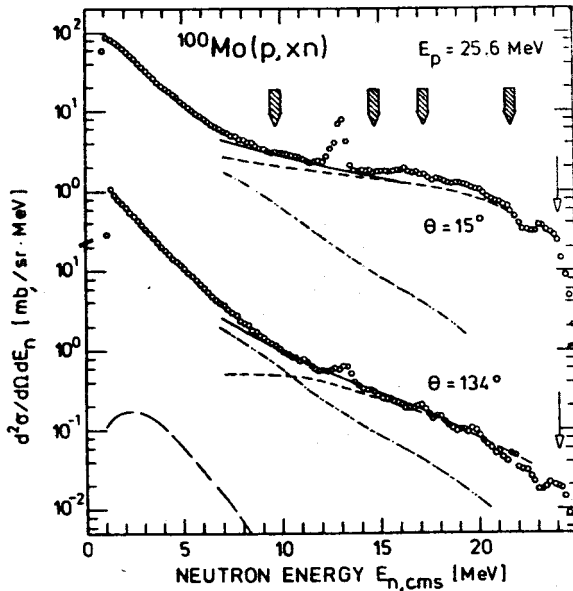


Fig. 8- Results of the SMC (dot-dashed line) and SMD (dashed line) calculations on the $^{100}\text{Mo}(p,n)$ reaction. The full line is the sum of the two processes.

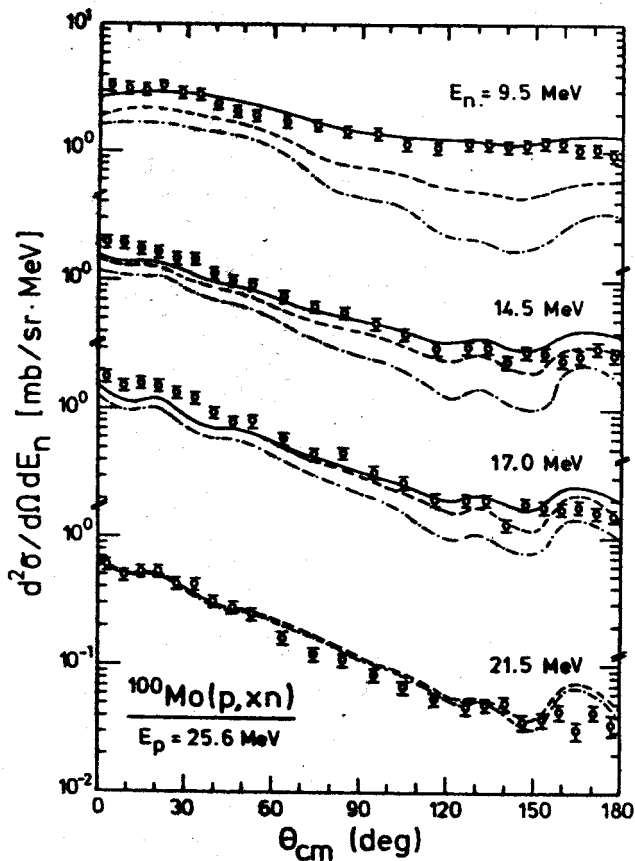


Fig. 9 - Same as Fig. 8 for the angular distributions.

REFERENCES

1. H. Fesbach, A. Kerman, S. Koonin, Ann. of Phys. 125(1980)429
2. R. Bonetti, L. Colli Milazzo, A. De Rosa, G. Inghima, E. Perillo, M. Sandoli, Phys. Rev. C21(1980),816
3. R. Bonetti, L. Colli Milazzo, M. Melanotte, Lett. Nuovo Cim. 31 (1981), 33
4. R. Bonetti, L. Colombo, Phys. Rev. C28(1983),980

5. R. Bonetti, L. Colli Milazzo, A. Garegnani, Lett. Nuovo Cim.
29(1980),496
6. G.M. Field, R. Bonetti, P.E. Hodgson, J. Phys. G:Nucl. Phys.,
12(1986),93
7. H. Feshbach, Ann. of Phys. 159(1985), 150
8. E. Mordhorst, M. Trabandt, A. Kaminsky, H. Krause, W. Scobel,
R. Bonetti, F. Crespi, Phys. Rev C, in press

MODEL CALCULATIONS OF FAST NEUTRON NONELASTIC CROSS SECTIONS

Andrzej Marcinkowski
Institute for Nuclear Studies
Hoża 69, 00-681 Warsaw, Poland

The semi-classical hybrid model and the quantum mechanical theories of pre-compound processes are used along with the Hauser-Feshbach theory to analyse the energy and angular distributions as well as the excitation curves for fast neutron induced reactions on target nuclei in the vicinity of $A=100$. The theory provides a fairly good understanding of the measured neutron cross sections.

1. INTRODUCTION

Quite recently an international effort has been undertaken to compare statistical nuclear reaction models and codes that calculate reaction cross sections, emission spectra and angular distributions with account for both the evaporation from the compound nucleus and for the pre-compound emission. These models and codes are widely used in nuclear data evaluations and in analyses of neutron induced reactions at energies from 0.5 MeV to 30 MeV. These limits exclude the resonance region on the low energy side, where the R-matrix theory finds application for description of the individual states of the compound nucleus, and the high energy region where the many open reaction channels make the calculations time consuming or even render consideration of individual channels impossible. The energies up to 30 MeV are of particular interest for testing nuclear models because the reaction mechanism changes in this range. Usually the interaction appears predominantly compound just above

the reaction threshold and changes with increasing energy to predominantly pre-compound or semi-direct and direct.

The compound nucleus cross sections are prescribed by the Hauser-Feshbach (H-F) theory, which accounts for angular momentum conservation and allows the cross sections for population of discrete excited levels of the product nucleus to be calculated. Codes, which use the H-F formalism and have contributed to the intercomparison exercise are listed in table 1.

Table 1. Contributions to model and code comparison

Code name	Contributor/Laboratory ⁺	Reference
STAPRE	S. Wilboolsak, B. Strohmaier M. Uhl / IRK	2
GNASH	P.G. Young / LAS K. Shibata / JAE	3
HAUSER-V	S.B. Garg, A. Sinha / TRM	4
PERRINI	H. Gruppelaar, H.A.J. Van der Kamp / ECN	5
TNG	C.Y. Fu / ORL	6
EMPIRE	M. Herman / IBJ	7

⁺ CINDA convention

These codes (classified according to ref.¹⁾ as class A codes) are applicable over wide energy range but are also time consuming and require large computer memory. Some of them calculate the angular distributions (TNG and an auxiliary of GNASH). All but one use the exciton model with internal transition rates from refs.^{8,9)} for calculation of the pre-compound emission. EMPIRE uses the angular

momentum and geometry dependent hybrid model GDH⁷⁾, with the intra-nuclear transition rates calculated optionally from the imaginary optical potential¹⁰⁾. In TNG, PERINNI and EMPIRE the pre-compound emission affects the spin population of final states by assuming an exciton number dependent spin cut-off parameter¹¹⁾. Additional refinements of the particle-hole state density, like pairing corrections¹³⁾ or yrast states for the exciton configurations¹²⁾ are included occasionally. Not all of these codes calculate the pre-compound contributions to discrete final levels and the composite-particle emission, e.g. alpha emission is treated within the exciton models but not in the hybrid model. Inverse reaction cross sections are used in the pre-compound emission rates except for the last three codes in table 1. Most codes provide particle-product spectra and the nonelastic reaction cross sections. Multi-particle emission and γ -ray production cross sections are also available.

The overall results of the computations are quite consistent for the neutron scattering reactions (n,n') and $(n,2n)$, though deviations exist between different calculations and/or experiment at the low and the high energy ends of the neutron spectra (see-fig. 1). These deviations are related to energy grid size, pairing energy shifts, geometry effects and effects due to excitation of individual excited levels. The GDH model seems to describe better the high energy tail of the spectra, which contain considerable amount of collective excitations.

For the much smaller (n,p) and (n,α) cross sections large deviations were established. In this case there is no significant difference between the results of the more sophisticated and time consuming codes and those using the Weisskopf-Ewing theory and/or the master equation or some simpler formulations of the exciton model. More details

of the comparison are given in the final report¹).

All the codes considered here are particularly suitable for complete data evaluations like the one shown in fig. 2 for the neutron induced reactions on ^{92}Mo . The requirement that many different reaction channels are fitted simultaneously imposes much higher constraints on the parametrisation of the models involved. Such complete analyses can be carried out or depending on whether the objective is to obtain a good fit to a chosen data set, or whether it is to describe a wide-range of data with the least number of parameters. The latter method is often used in neutron data evaluation, though it usually fails in providing adequate details like e.g. cross sections for sequences of isotopes of a particular element.

The aim of the present paper is to describe a possibly complete analysis of neutron induced reactions on nuclei, which are supposed to be constituents of structural materials for fusion reactors and therefore gained the interest of the IAEA Project on Measurements and Analysis of 14 MeV Neutron Nuclear Data. The studied target nuclei were isotopes of molybdenum, zirconium and niobium, all lying close to the atomic mass $A=100$. For completeness neutron capture and inelastic scattering at low incident energies on ^{114}Cd and ^{115}In are also discussed. All the calculations have been performed with use of the EMPIRE code⁷).

2. COMPOUND NUCLEUS AND PRE-COMPOUND CALCULATIONS

The main task in performing the calculations is a consistent parametrisation of (i) the optical model potentials, which provide the penetrability coefficients, (ii) the level densities and (iii) the radiative strength functions.

The partial wave penetrabilities were calculated

using both global and individually fitted potentials for neutrons, protons and alphas. The latter ones were used after it was found that the global potentials do not prescribe satisfactorily the cross sections for the zirconium isotopes used as targets. The global potentials applied were those of Moldauer¹⁴⁾ for neutrons, Björklund et al.¹⁵⁾ for neutrons and protons, and of Mc Fadden and Satchler¹⁶⁾ for alpha particles. When preference has been given to optical potentials, which have been determined systematically over a small range of nuclei near $A=100$, the one reported by Lagrange¹⁷⁾ for neutrons, by Johnsson¹⁸⁾ for protons and by Park et al.¹⁹⁾ for alphas have been chosen in accordance with the extensive evaluation of ref.²⁰⁾.

The compound nucleus calculations were conducted according to the H-F theory. For the lowest neutron energies where only few particle-emission channels are open the width fluctuations affect particularly the capture cross sections. This effect was accounted for by applying the formalism developed by Tepel et al.²¹⁾ with the elastic enhancement factor taken from ref.²²⁾. The width fluctuation correction lowers the capture cross section below the inelastic scattering threshold and enhances it above the threshold by up to 30%. By such a smoothing of the calculated excitation curve the width fluctuations bring the theory into a better agreement with experiment²³⁾. For heavy targets where many inelastic channels are open this effect is negligible. In fig. 3 it is shown that the H-F theory describes the radiative, weak channels fairly well up to 5-6 MeV incident neutron energy²⁴⁾.

The individual final states after scattering of low energy neutrons may be resolved experimentally and compared with the prescription of the theory. This method has been used often for the identification of spins of the low lying excited states in the target nucleus²⁵⁾.

At higher excitation energies where the separate levels merge into a continuum of states the four parameter level density formula proposed by Cameron and Gilbert²⁶⁾ was used to describe the level spectrum. The parameters systematized by Reffo²⁷⁾ have been adopted. The radiative strength function was assumed to be a superposition of the Weisskopf single-particle strength and giant dipole resonance.

The pre-compound emission was calculated using the GDH model, as described in ref.⁷⁾, with the particle-hole state densities obtained by Williams⁸⁾ and the intra-nuclear transition rates calculated from the imaginary optical potential.

The results of calculations are displayed in figs. 4 and 5, in which the proton spectrum from the $^{92}\text{Mo} + n$ reaction at 14.7 MeV and the excitation function for the $^{92}\text{Mo}(n,p)^{92m}\text{Y}$ reaction are compared with experimental results. The untypically high cross sections for the $^{92}\text{Mo}(n,np)^{91}\text{Y}$ reaction (see fig. 1) were confirmed by the analysis of the proton spectrum measured by Haight et al.²⁸⁾. The agreement between theory and experiment is rather good and the contributions of the compound nucleus and of the pre-compound emission derived from the analysis of the proton spectrum and from the analysis of the excitation curve are consistent. The compound nucleus mechanism at incident neutron energies up to 14-15 MeV. For the heavier molybdenum isotopes the excitation curves do not show the broad maximum typical for the decay of compound nucleus, instead the cross sections increase monotonically with energy reaching much lower values, at saturation, in agreement with experiment²⁹⁾. In case of the $^{92}\text{Mo}(n,\alpha)^{89}\text{Zr}$ reaction the analyses of the emission spectrum and of the excitation curve gives contradictory results. The compound nucleus decay fails to describe the shape of emitted alpha-particle

spectrum²⁸) whilst providing accidentally a quite satisfactory excitation curve²⁹).

Similar calculations were conducted for the (n,p) reaction on zirconium isotopes using global optical potentials. For the lightest target ⁹⁰Zr the theory reproduces the experimental proton spectrum and the excitation curve fairly well, figs. 6 and 7. In contrary for the remaining isotopes significant discrepancies are observed, which may be due to the failure of the global potentials in describing the isotopic behaviour. Abnormal behaviour of the isospin term in the optical potential for Zr isotopes has been already indicated by Hodgson³⁰).

3. STATISTICAL MULTI-STEP COMPOUND AND MULTI-STEP DIRECT CALCULATIONS OF PRE-COMPOUND REACTIONS

The statistical theory of Feshbach, Kerman and Koonin³¹) (FKK) introduces two parallel reaction types to account for pre-compound emission. The first, referred to as the statistical multi-step compound (MSC) reaction, describes the flow of the flux through a series of doorway states of increasing complexity, each of them containing only bound nucleons. After numerous successful calculations, implementing the MSC theory, conducted by the Milan-Naple group^{32,40}) quite recently the formulation of some basic quantities entering the model calculations have been derived, i. e. the X-functions, which are the weighting factors in the emission and damping widths, due to angular momentum conservation, have been generalized for the case of spin 1/2 particles³³) and analytical formulae for the particle-hole states densities (having all particles bound) were reported^{34,35}). Simultaneously the related Y-functions, which are the densities of states available in the different intra-nuclear transitions modes were

derived^{35,36}). These modifications facilitate the calculations to a large extent, thus providing an easily available theoretical tool. The application of this model has been extended to another area, where one may expect the MSC reactions to contribute significantly to the pre-compound emission, namely to the $(n,2n)$ reaction, which involves the soft part of the neutron emission spectrum and therefore should not be affected to greater extent by simpler processes, e.g. by the statistical multi-step direct (MSD) reactions. The latter process, which involves a chain of states with at least one particle in the continuum, has been introduced by FKK in order to account for the forward-peaked portion of the angular distributions observed. The MSC calculations have been incorporated into the EMPIRE code and the results for the $^{93}\text{Nb}(n,2n)^{92}\text{Nb}$ and $^{93}\text{Nb}(n,p)^{93}\text{Zr}$ reactions as well as for some heavy targets appeared very encouraging³³). These calculations have been done with the radial overlap integrals evaluated by assuming constant wavefunctions inside the nucleus for the four single-particle orbitals involved in an intranuclear two-body interaction. Similar method has been used for calculation of double-differential cross sections for the $^{93}\text{Nb} + n$ reaction at 14 MeV by Field et al.³⁷). It has been shown that at lower energies where few open channels contribute it is possible to determine the effective interaction strength V_0 directly by normalizing the sum of the cross sections in all channels to the total reaction cross section given by the optical model. Here the equilibrium component was evaluated within the SMC theory as its last step (the so called r-stage). In the light of the realistic calculations performed by Bonetti and Colombo³⁹) the constant wavefunctions approximation seems to be crude but still providing satisfactory results³³).

Wavefunctions generated in a harmonic oscillator po -

tential have been used also by Stankiewicz⁴⁰). Energy conservation has been taken into account whilst angular momentum effects were averaged out in preliminary calculation. The result is not yet satisfactory as one may see in fig. 8. Computations, which accept only angular momentum conserving transitions are in progress. In all our calculations the compound nucleus component is evaluated according to the H-F theory. This way seems to be superior because of the much better parametrisation of the H-F calculations.

The Milan-Naple group has also made the calculations implementing the MSD theory of FKK^{39,41}). Another treatment as multi-step direct reactions in distorted-wave Born approximation has been developed by Tamura et al.⁴²).

Despite of a controversy in the calculation of the matrix elements of the residual interaction both theories provided numerous cross sections in rather good agreement with experimental data for (p,p') , (p,n) , (n,p) , (n,n') and (p,α) reactions⁴¹⁻⁴⁴). These analyses indicate that the multi-step processes grow in importance with respect to the single-step one with increasing projectile energy, as well as with increasing emission angle and residual excitation energy. Practically up to about 25 MeV incident energy the single-step process is sufficient to describe the measured forward-backward asymmetry.

On the other hand some difficulties met in interpreting experimental data have been reported recently. Traxler et al.⁴⁵) present an analysis of double-differential cross sections for the $^{93}\text{Nb}(n,p)^{93}\text{Zr}$ reaction at 14 MeV based on the use of the ORION-TRISTAR-1 code⁴⁶). The single-step calculations reproduced well the shape of the angular distributions of protons but the absolute cross sections for excitation of states lying well in the continuum appeared by far too small. A similar result has been obtained by the author, who applied the model calcu-

lations described by Bonetti et al.⁴²⁾ to the description of angular distributions of neutrons scattered inelastically on ^{27}Al and ^{184}W at incident neutron energies 11.5 MeV and 26.0 MeV. The single-step direct calculations gave cross sections by one order of magnitude too low. Accounting for any symmetric or isotropic contributions can not remove the large discrepancy between theory and experiment. It has been found that the so called typical transitions, which do not involve spin-flip and/or transitions between orbitals with different main quantum numbers, provide similar angular distributions, whereas the remaining ones give rise to angular distributions, which may differ dramatically in both the shape and the absolute values of the cross sections. In these calculations the zero-spin transfer was assumed and the strength of the 1 fm range Yukawa effective interaction was set $V_0=25$ MeV.

4. CONCLUSIONS

The available optical potentials and parametrisations of level densities make possible the calculations of fast neutron cross sections with fair accuracy. The shapes of the spectra of emitted nucleons are well reproduced by superposition of the compound nucleus and pre-compound emission contributions, as calculated from the H-F theory and e.g. the GDH model. The description of isotopic effects in cross sections requires appropriate non-global optical potentials. Realistic quantum-mechanical calculations allow of the experimental forward-backward asymmetry of the angular distributions.

5. REFERENCES

1. Gruppelaar, H. and Nagel, P., Report on Internatio-

- nal Nuclear Model and Code Comparison on Pre-Equilibrium Effects, NEANDC-204 U, NEA Data Bank 1985
2. Strohmaier, B. and Uhl, M., Nuclear Theory for Applications, IAEA-SMR 43, 313 (1980)
3. Young, P.G. and Arthur, E.D., Los Alamos Report LA-6947
4. Mann, F.M., HEDL-TME-78-83 (1979)
5. Gruppelaar, H., unpublished
6. Fu, C.Y., Int. Conf. on Nuclear Cross-Sections for Technology NBS-Sp 594, 757 (1979); Brookhaven Report BNL-NCS-51245, Vol 2, 675 (1980)
7. Herman, M. et al., Comp. Phys. Comm. 33, 373 (1984)
8. Williams, F.C., Nucl. Phys. A166, 231 (1971)
9. Oblozinsky, P. et al., Nucl. Phys. A226, 347 (1974)
10. Blann, M., Nucl. Phys. A213, 570 (1973)
11. Fu, C.Y., Nucl. Sci. Eng. 92, 440 (1986)
12. Reffo, G. and Herman, M., Lett. Nuovo Cim. 34, 261 (1982)
13. Fu, C.Y., Nucl. Sci. Eng. 86, 344 (1984)
14. Moldauer, P.A., Nucl. Phys. 47, 65 (1963)
15. Björklund, P. and Fernbach, S., Phys. Rev. 109, 1295 (1958)
16. Mc Fadden, L. and Satchler, G.R., Nucl. Phys. 84, 177 (1966)
17. Lagrange, Ch., in Neutron Data of Structural Materials for Fast Reactors, Bockhoff, K.H. ed. , p 756, Oxford Pergamon Press 1979
18. Johnsson, C.H., Phys. Rev. C16, 2238 (1977)
19. Park, Y.S. et al., Phys. Rev. C4, 778 (1971)
20. Ivascu, M. et al., Final Report IAEA on Contract 2983/RB, NP-28-1983, Bucharest, Romania
21. Tepel, J.W. et al., Phys. Lett. 49B, 1 (1974)
22. Hofmann, H.M. et al., Z. Phys. A297, 153 (1980)
23. Herman, M. and Marcinkowski, A., Nucl. Phys. A357,

- 1 (1981)
24. Andersson, P. et al., Nucl. Phys. A443, 404 (1985)
25. Marcinkowski, A. et al., Nucl. Phys. A179, 781 (1972)
26. Cameron, A.G.W. and Gilbert, G., Can. J. Phys. 43, 1446 (1965)
27. Reffo, G., CNEN Report RT/FI/78/11, Bologna, 1978
28. Haight, R.C. et al., Phys. Rev. C23, 700 (1981)
29. Marcinkowski, A. et al., Z. Phys. 4323, 91 (1986)
30. Hodgson, P.E., University of Oxford Report 14/84
31. Feshbach, H., Kerman, A. and Koonin, S., Ann. Phys. 125, 429 (1980)
32. Bonetti, R. et al., Phys. Rev. C21, 816 (1980)
33. Herman, M. et al., Nucl. Phys. A435, ~~859~~ (1985)
34. Zhivopishev, F.A. et al., Izv. Acad. Sci. USSR (ser. fiz.) 46, 885 (1982)
35. Stankiewicz, K. et al., Nucl. Phys. A435, 67 (1985)
36. Oblozinsky, P., Nucl. Phys. A453, 127 (1986)
37. Field, G.M. et al., J. Phys. G: Nucl. Phys., in print
38. Bonetti, R. et al., Lett. Nuovo Cim. 31, 33 (1981)
39. Bonetti, R. and Colombo, L., Phys. Rev. C28, 980 (1983)
40. Stankiewicz, K., private communication
41. Bonetti, R. et al., Phys. Rev. C24, 71 (1981)
42. Tamura, T. et al., Phys. Rev. C26, 379 (1982)
43. Holler, Y. et al., Nucl. Phys. A442, 79 (1985)
44. Tamura, T., Proc. of Int. Conf. on Neutron Induced Reactions, Smolenice, CSR, 1985
45. Traxler, G. et al., Nucl. Sci. Eng. 90, 174 (1985)
46. Tamura, T. et al., Comp. Phys. Comm. 29, 391 (1983)
47. Marcinkowski, A. et al., Nucl. Phys. A402, 220 (1983)
48. Ikeda, Y. et al., Progr. Rep. Japan Atomic Energy Res. Institute, INDC JPN -102/U
49. Bormann, M. et al., in Handbook on Nuclear Activation Cross Sections, IAEA Techn. Rep. 156, Vienna 1974
50. Takahashi, A. et al., OKTAVIAN Report A-83-01, Osaka

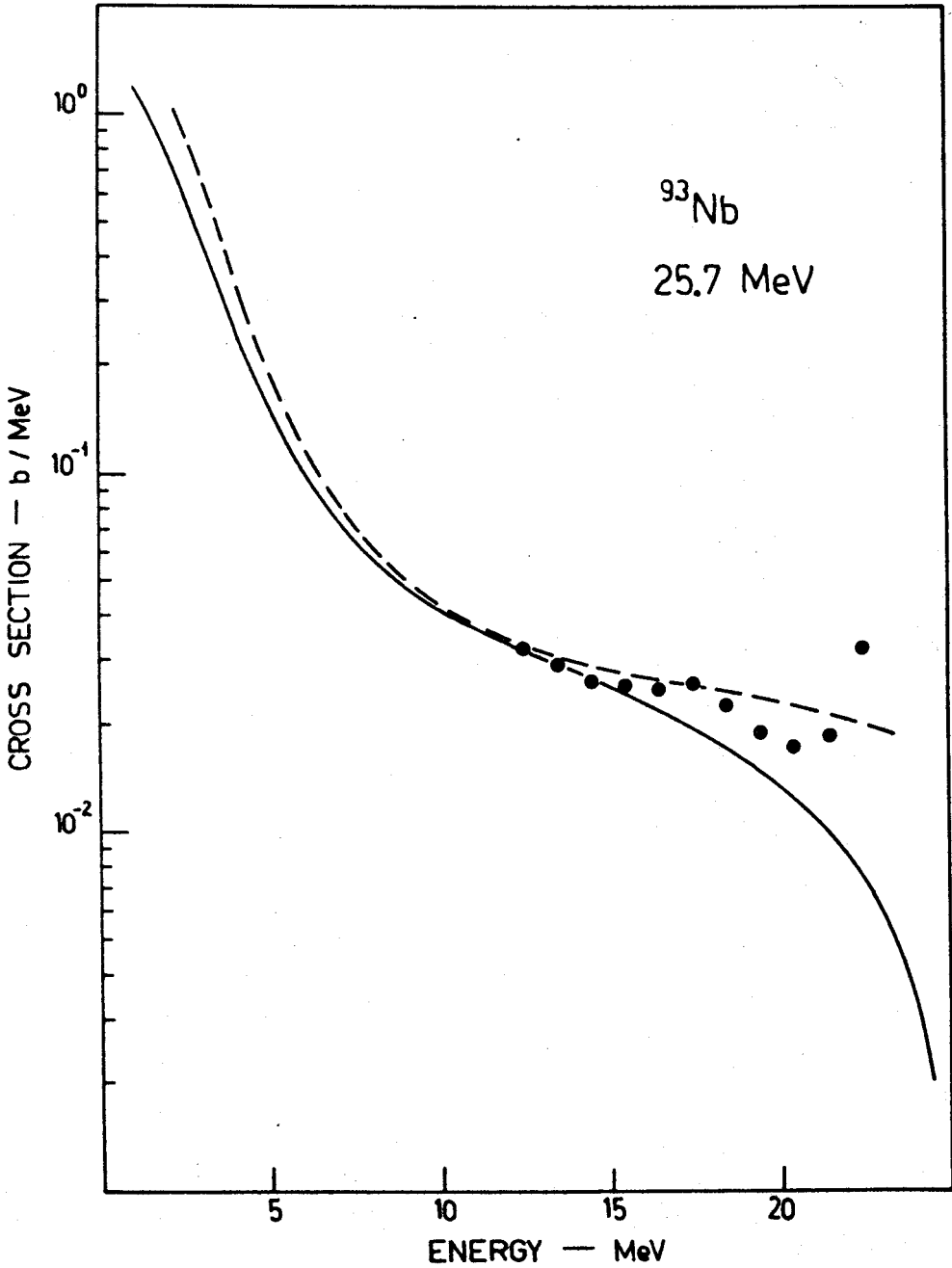


Fig. 1 Neutron spectrum from the $^{93}\text{Nb}+n$ reaction at 25.7 MeV ⁴⁷⁾ compared with calculations. Solid line Gnash code³⁾, dashed EMPIRE⁷⁾.

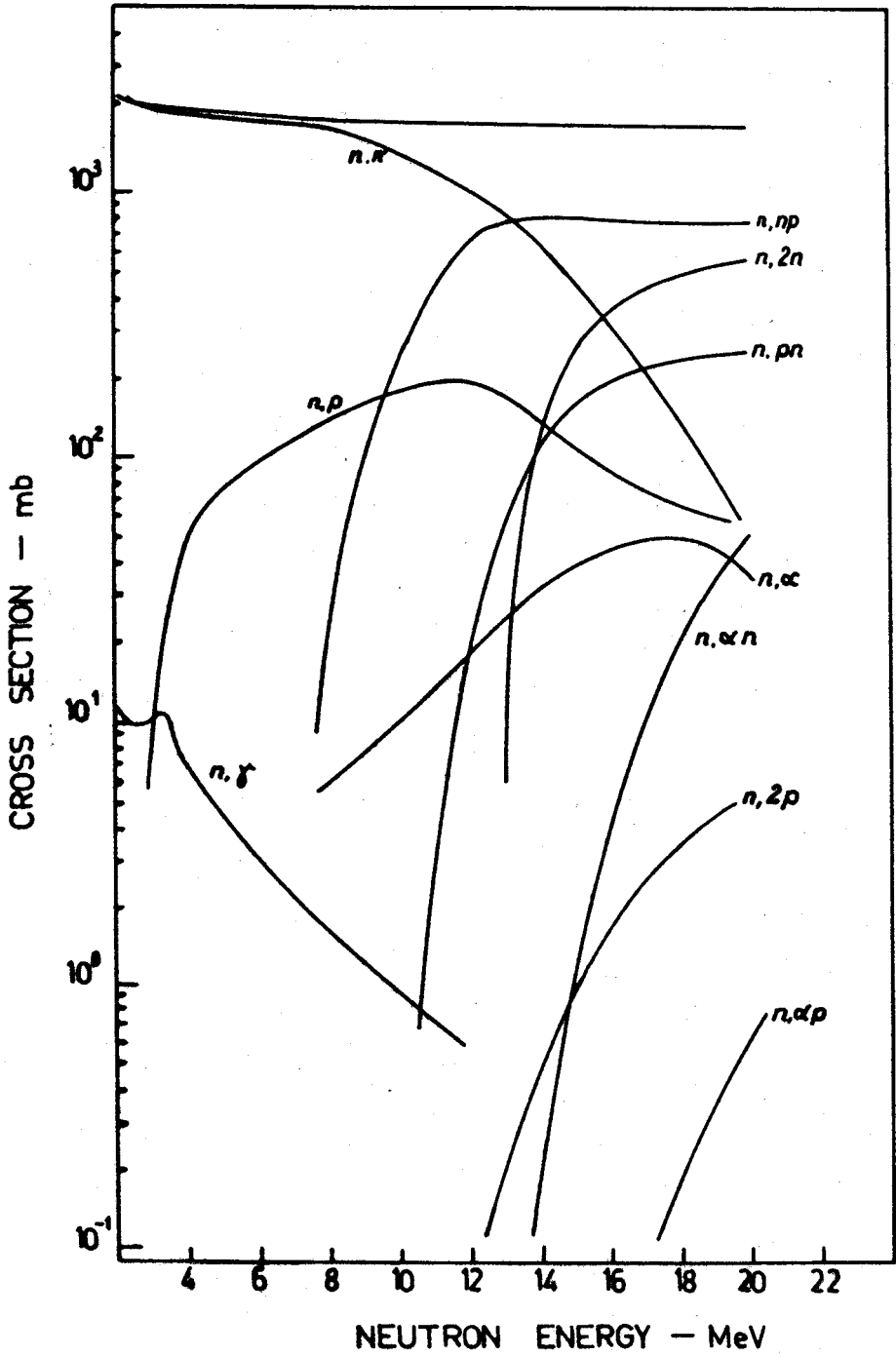


Fig. 2 Total cross sections for reactions induced by fast neutrons on ^{92}Mo calculated with the H-F theory.

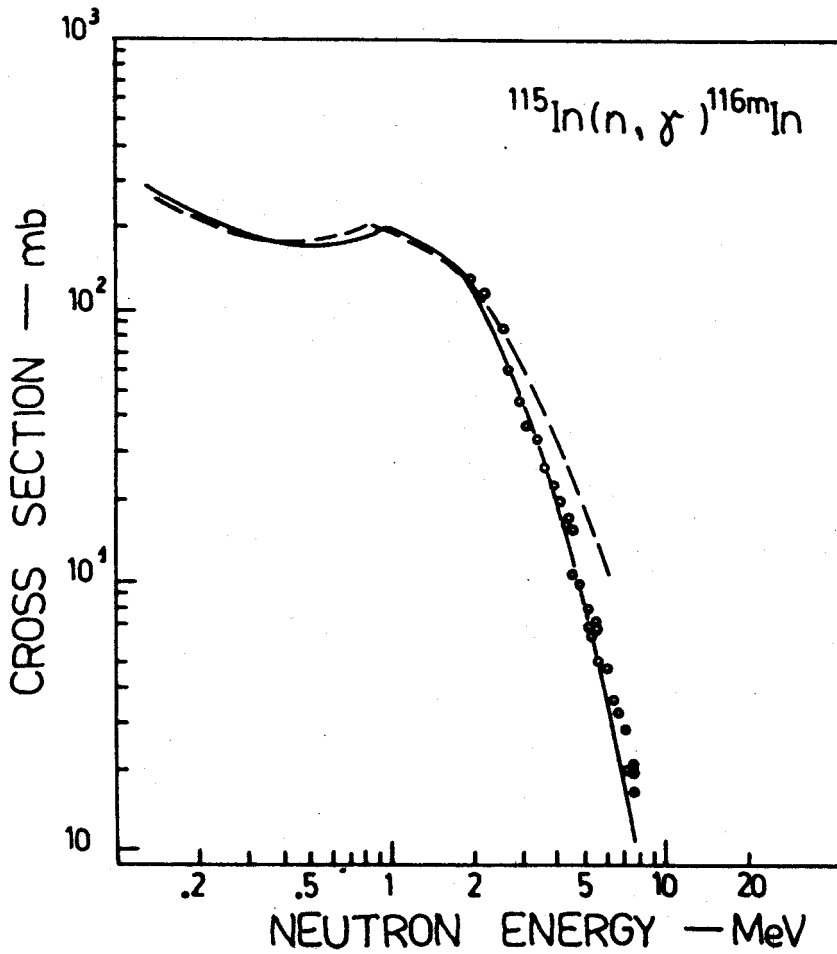


Fig. 3 Neutron capture cross sections for ^{115}In from ref.²⁴) compared with the H-F theory (solid line). Dashed line is the ENDFB-IV evaluation.

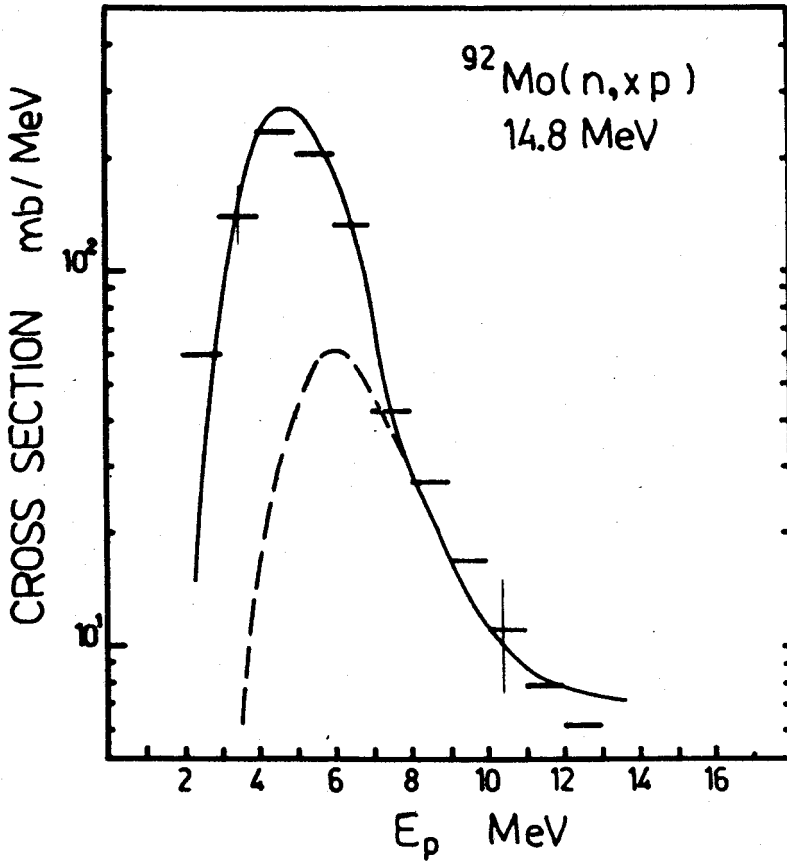


Fig. 4 Comparison of proton spectrum from the $^{92}\text{Mo}+n$ reaction measured at 14.8 MeV incident energy²⁸⁾ with H-F and GDH models. Dashed line shows the primary protons. Solid line accounts for the secondary protons, which are mainly due to the (n, np) reaction.

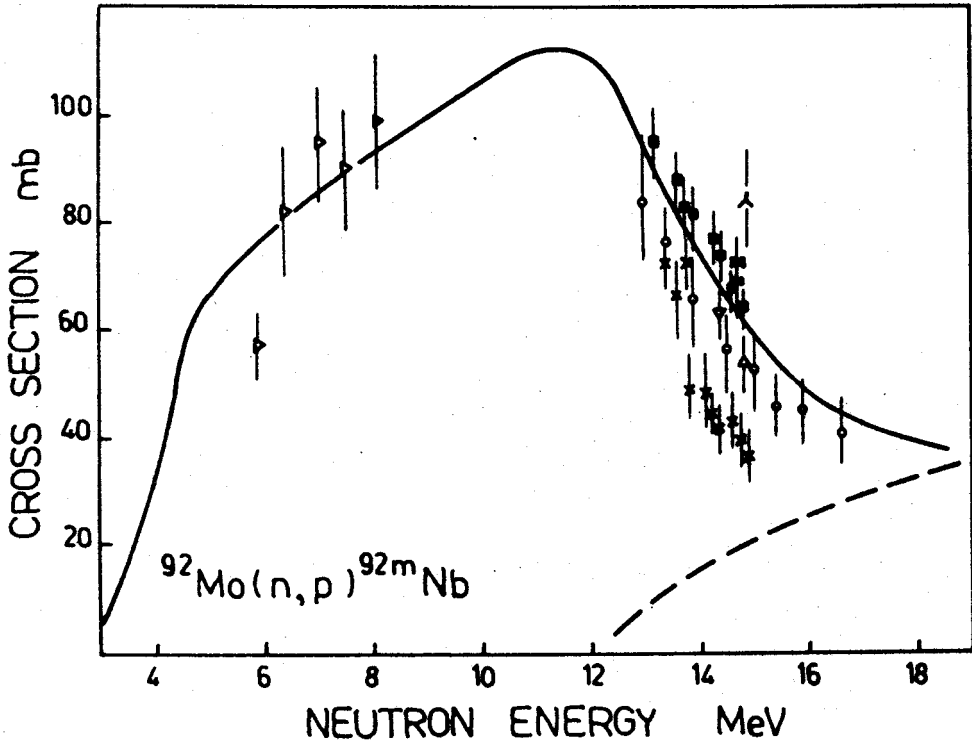


Fig. 5 Experimental and calculated excitation curves for the $^{92}\text{Mo}(n,p)^{92\text{m}}\text{Nb}$ reaction. Solid line denotes the sum of H-F and GDH predictions. The Pre-compound contribution (GDH) is shown separately by the dashed line. The experimental data indicated by squares are from ref.⁴⁸). For rest of the data see ref.²⁹).

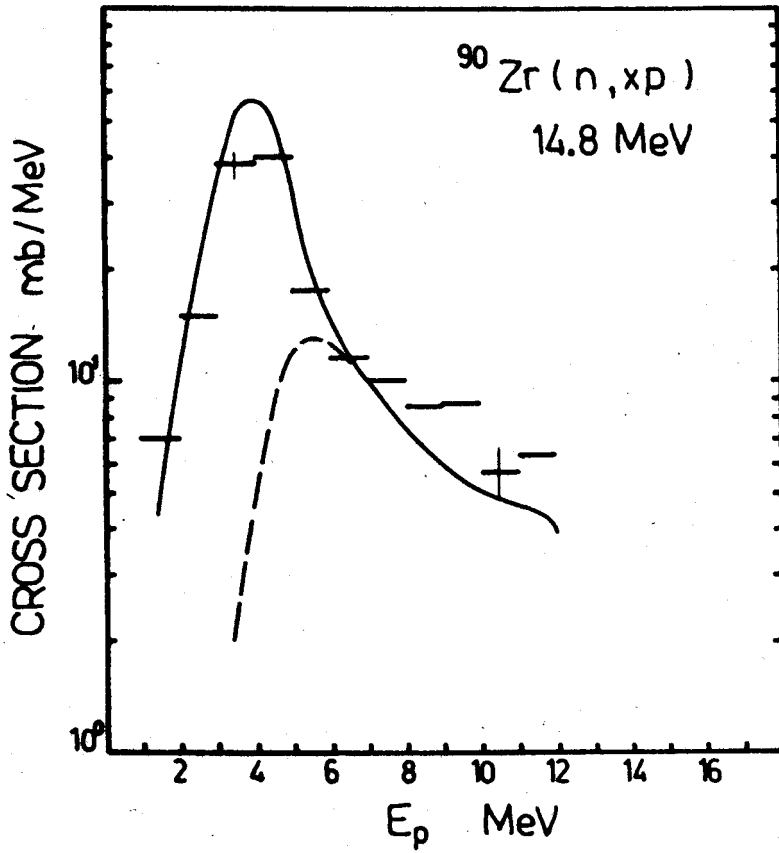


Fig. 6 The same as in fig. 4 but for the $^{90}\text{Zr}+n$ reaction.

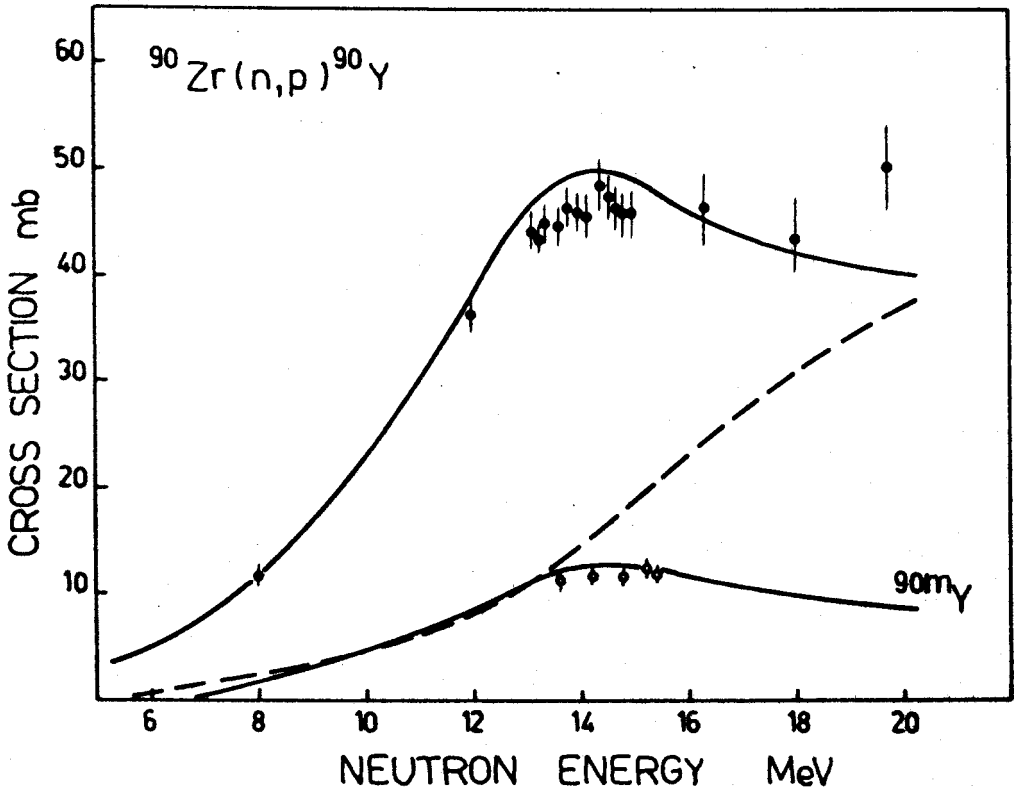


Fig. 7 The same as in fig. 5 but for the $^{90}\text{Zr}(n,p)^{90}\text{Y}$ reaction. The excitation curve for population of the isomeric state ^{90m}Y is also shown. Closed circles are from ref.⁴⁹, open circles are from a contribution to this conference.

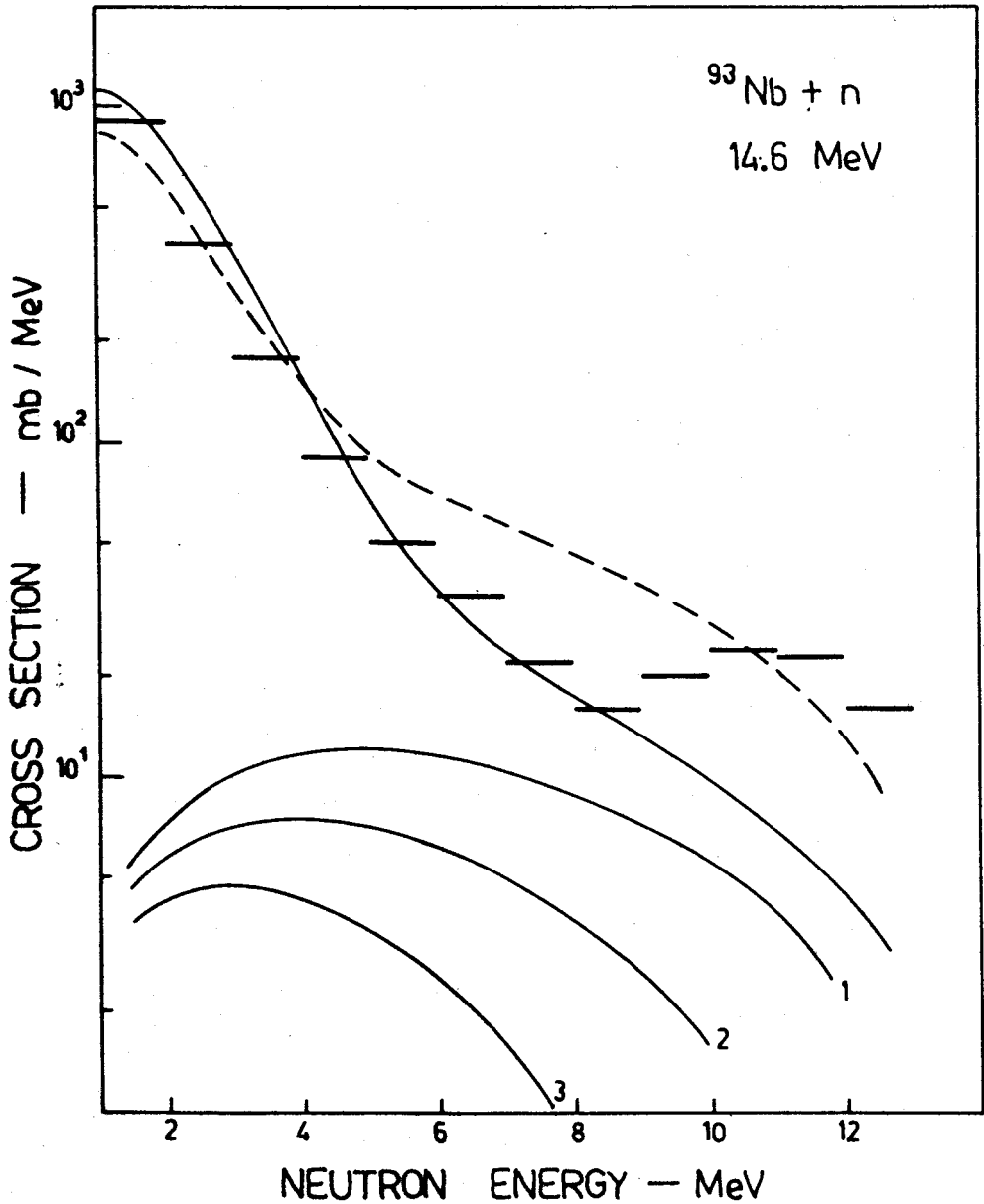


Fig. 8 Comparison of the calculated (H-F plus MSC) neutron spectrum with symmetric portion of angular distributions (horizontal bars) measured for the $^{93}\text{Nb}+n$ reaction at 14.6 MeV⁵⁰). Solid line is with Ericsson state densities and harmonic oscillator wavefunctions. Dashed line shows the effect of bound configurations.

ISOTOPIC EFFECTS IN NEUTRON INDUCED REACTIONS AND PREEQUILIBRIUM PARTICLE EMISSION*

Roman Čaplar

Rudjer Bošković Institute, P.O.B.1016, 41001 Zagreb
YUGOSLAVIA

The recent results showing the importance of preequilibrium particle emission for a proper description of isotopic effects in fast neutron induced reactions are presented. The reaction Q -value is identified as a relevant physical quantity responsible for the observed (n,p) isotopic trends both for lighter and heavier nuclei. The analysis of isotopic effects as well as the systematic analysis of neutron induced reactions on a number of nuclei ($A=45-209$) show that the principal transition rate in the preequilibrium exciton-model calculations λ_+ does not exhibit structure effects.

1. INTRODUCTION

The systematic dependence of various $(n, \text{particle(s)})$ cross sections on the neutron number of isotopes (isotopic effects) in reactions induced by fast neutrons was noticed in the early days of nuclear physics and has since represented a challenging and fruitful field of investigation. This long-standing interest in isotopic effects can be explained on the ground of importance of these effects from both scientific and practical point of view. On the scientific side, the investigation of isotopic effects allows a very stringent test of model predictions, owing to the systematic and, sometimes, large changes of input parameter values across the valley of stability, as compared with the usual investigations on high-abundance

* supported in part by the IAEA, Vienna.

isotopes along the valley of stability. On the practical side, the complete understanding of isotopic effects allows us to obtain reliable cross sections which are otherwise difficult to measure or even inaccessible to the measurement.

Pioneering papers^{1,2)} on the subject tried to establish phenomenological and/or semiphenomenological formulas in order to describe the observed isotopic trends. The semi-empirical approaches were of course based on the statistical evaporation model³⁾. However, more precise measurements with modern experimental techniques⁴⁾ yielded data (including low (~ 1 mb) cross sections on a number of low-abundance isotopes) which showed that the statistical evaporation model alone is not able to describe isotopic effects all over the periodic table. Subsequent work⁵⁻⁷⁾ clearly showed that the introduction of preequilibrium particle emission is necessary in order to describe the observed systematic trends. This fact is of course most readily recognized in the reactions where the Coulomb barrier suppresses the evaporation contribution.

Let me conclude this introduction with a notice that in this talk I am going to concentrate on the recent achievements in our understanding of the isotopic effects due to the inclusion of preequilibrium particle emission in the description of fast neutron induced reactions, rather than to give a complete overview and collection of formulas for calculating the cross sections themselves. Also, I will not discuss the isotopic trends in the cases where the evaporation mechanism is a dominant one as there has been a number of excellent papers and conference talks on the subject⁸⁾.

2. ISOTOPIC EFFECTS IN (n,p) REACTION CROSS SECTIONS

In this work I am going to pay special attention to the isotopic effects in (n,p) reactions. There are several reasons for it:

(i) the (n,p) cross sections show clear isotopic effects all over the periodic table. The (n,p) cross sections for a given element generally decrease with the increasing neutron number of an isotope. Also, variations connected with the character of residual nucleus (odd-odd or odd-even) are observed.

(ii) the (n,p) reaction has a simple outgoing channel (one nucleon), and no complications connected with the description of cluster emission do appear.

(iii) the (n,p) reaction mechanism, due to the increase of the Coulomb barrier, changes from evaporation to preequilibrium emission going from light to heavy targets. This offers us a good opportunity to investigate similarities and differences in the (n,p) isotopic trends connected with reaction mechanism.

According to the height of the Coulomb barrier and the associated reaction mechanism three different regions of targets can be roughly defined: (i) light targets, (ii) heavy targets and (iii) intermediate region of medium-heavy targets where contributions both from evaporation and preequilibrium emission are of importance. Early papers on the isotopic effects were concerned with larger (n,p) cross sections measured on light targets. A number of empirical and semiempirical formulas for estimating these cross sections were proposed^{1,2}. They proved to be successful in predicting the absolute cross sections and in describing the isotopic effects on these elements.

During the last decade the development of experimental techniques and methods has led to a more reliable experimental values of rather small (n,p) cross sections including, in some cases, data on a whole series of isotopes of heavy elements. These data show qualitative similarity in decreasing cross section with increasing mass number of an isotope but with a markedly less steep slope than for lighter nuclei. This

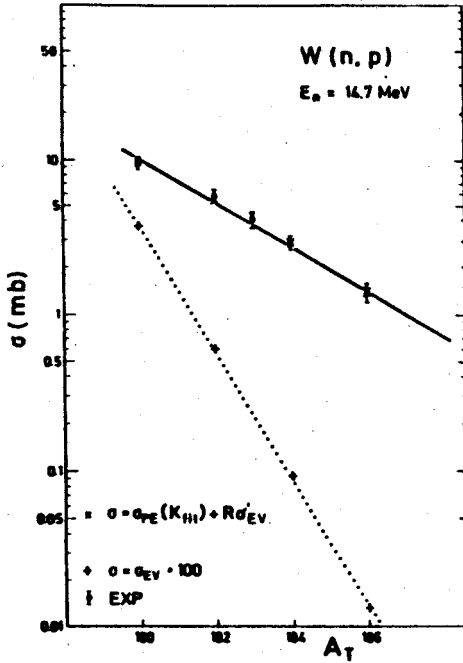


Fig. 1

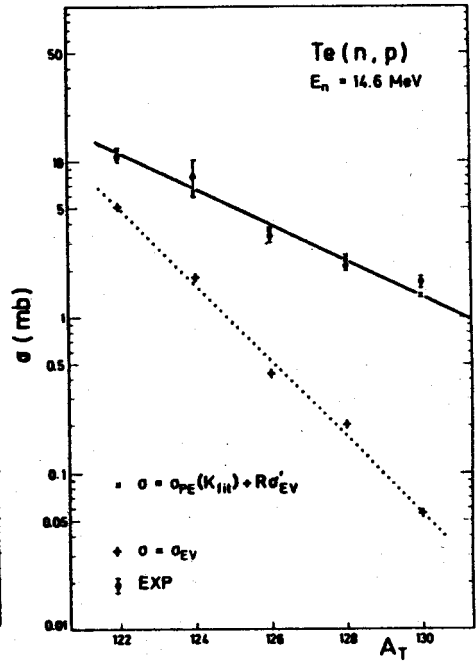


Fig. 2

Fig.1 : Comparison of experimental data on W isotopes with the predictions of the evaporation (multiplied by 100) and preequilibrium exciton models. The preequilibrium calculations were performed using a smoothly varying level-density parameter a ($a = A/8$) and the same value $K_{fit} = 400 \text{ MeV}^3$ for all the isotopes. The lines in the Figure are to guide the eye.

Fig.2 : The same as Fig. 1, for Te isotopes; $K_{fit} = 500 \text{ MeV}^3$.

is illustrated in Fig.1 in the case of tungsten(W), where experimental (n,p) cross sections on five isotopes measured by Qaim's group⁹⁾ are compared with calculations. The evaporation calculations (marked with +, dotted line is to guide the eye) predict cross sections which are orders of magnitude smaller than the experimental values. Furthermore, the evaporation calculations predict far too steep slope of the mass dependence of (n,p) cross sections on different isotopes. On the other hand, the preequilibrium calculations (marked with x, solid line is to guide the eye) reproduce very well the observed isotopic dependence. Before discussing in detail the preequilibrium calculations and the input parameters used, let us show the data for the medium-heavy Te isotopes (Fig.2). Now, evaporation contributions are not so much off in absolute value as in W case (lower Coulomb barrier for Te) especially for neutron-deficient isotopes (^{122}Te , ^{124}Te) but once more the evaporation calculations do not predict the isotopic dependence correctly. The preequilibrium emission (with addition of evaporation contribution) once again reproduces measured isotopic trend very nicely.

It should be pointed out here, that the balance of the evaporation and preequilibrium contributions is, in addition to the target - charge and neutron number, also dependent on the incoming energy. This energy dependence was investigated on a series of Mo isotopes in the recent work of Marcinkowski et al.¹⁰⁾

3. ISOTOPIC EFFECTS AND RELEVANT PHYSICAL QUANTITIES

3.1. Preequilibrium Emission and Model

In preceding sections, the important role of preequilibrium emission in describing properly isotopic effects in fast neutron induced reactions has been clearly demonstrated.

It has been shown that, depending on the reaction channel and incoming energy, the preequilibrium emission can represent a dominant part of the cross section (as for example in (n,p) reaction on heavier targets at 14 MeV). Let us now discuss physical quantities responsible for the observed isotopic effects in the cases where preequilibrium emission prevails. Although, nowadays, more elaborate approaches exist to calculate preequilibrium emission as reviewed by Bonetti¹¹⁾, we will use here for the discussion purpose, the closed form of exciton model due to its physical transparency and simplicity. The details of the model are given elsewhere, hereby only the formulas of direct significance for our discussion are quoted.

The closed-form exciton model cross section is given by

$$\sigma(\alpha, \beta) = \sigma_{CS}(\alpha, E_1) \int_0^{\epsilon_{\beta\max}} \sum_{\substack{n=n_0 \\ \Delta n=2}}^{\bar{n}} W_{\beta}(n, E, \epsilon_{\beta}) T(n, E) \quad (1)$$

where $\sigma_{CS}(\alpha, E_1)$ is the cross section for the formation of the composite system, $W_{\beta}(n, E, \epsilon_{\beta})$ is the emission rate and $T(n, E)$ is the time the system spends in an n -exciton state. The emission rate $W_{\beta}(n, E, \epsilon_{\beta})$ of particles β with energy ϵ_{β} and reduced mass μ_{β} from an n -exciton state (p , particles; h , holes) is given by

$$W_{\beta}(n, E, \epsilon_{\beta}) = \frac{2s_{\beta} + 1}{\pi^2 \hbar^3} \mu_{\beta} \epsilon_{\beta} \sigma_{\beta}(\epsilon_{\beta}) Q_{\beta}(p) \frac{\omega^{EP}(p-p_{\beta}, h, U)}{\omega^{EP}(p, h, E)} \quad (2)$$

where ω^{EP} are Ericson state densities corrected for Pauli principle, E and U are the excitation energies of composite and residual nuclei, respectively, and $\sigma_{\beta}(\epsilon_{\beta})$ is the cross section for the inverse process. The factor $Q_{\beta}(p)$ which contains the proton-neutron distinguishability makes it pos-

sible to use one-Fermion-type density of exciton states. An approximate expression for $T(n,E)$ reads as follows

$$T(n,E) = \tau(n,E) \prod_{\substack{i=n-2 \\ i=n_0 \\ \Delta i=+2}} \lambda_+(i,E) \tau(i,E) + \tau(n,E) \delta_{nn_0} \quad (3)$$

$\tau(n,E)$ being the mean lifetime of an n -exciton state. The transition rates λ_{\pm} are proportional to the averaged squared matrix element which is expected to behave approximately as

$$|M|^2 = K \cdot A^{-3} E^{-1} \quad (4)$$

3.2. Q-value Effect

On the basis of the preequilibrium calculations performed and the formulas given above it is straightforward to identify the (n,p) reaction Q -value as the principal physical quantity responsible for the observed isotopic behaviour for heavier targets. Namely, for a given isotopic chain, the Coulomb barrier and the cross section for the formation of the composite system change only slightly. The level-density parameter was assumed to vary smoothly (we will later on discuss the choice $a = a_{GC}^{12}$) and the parameter K defining the transition matrix element was kept constant in the calculations shown in Figs. 1 and 2. The neutron-proton composition of the target isotope is taken into account via the neutron-proton distinguishability factor $Q_p(p)$ of the composite system. On the other hand, the Q -value for (n,p) reaction varies systematically

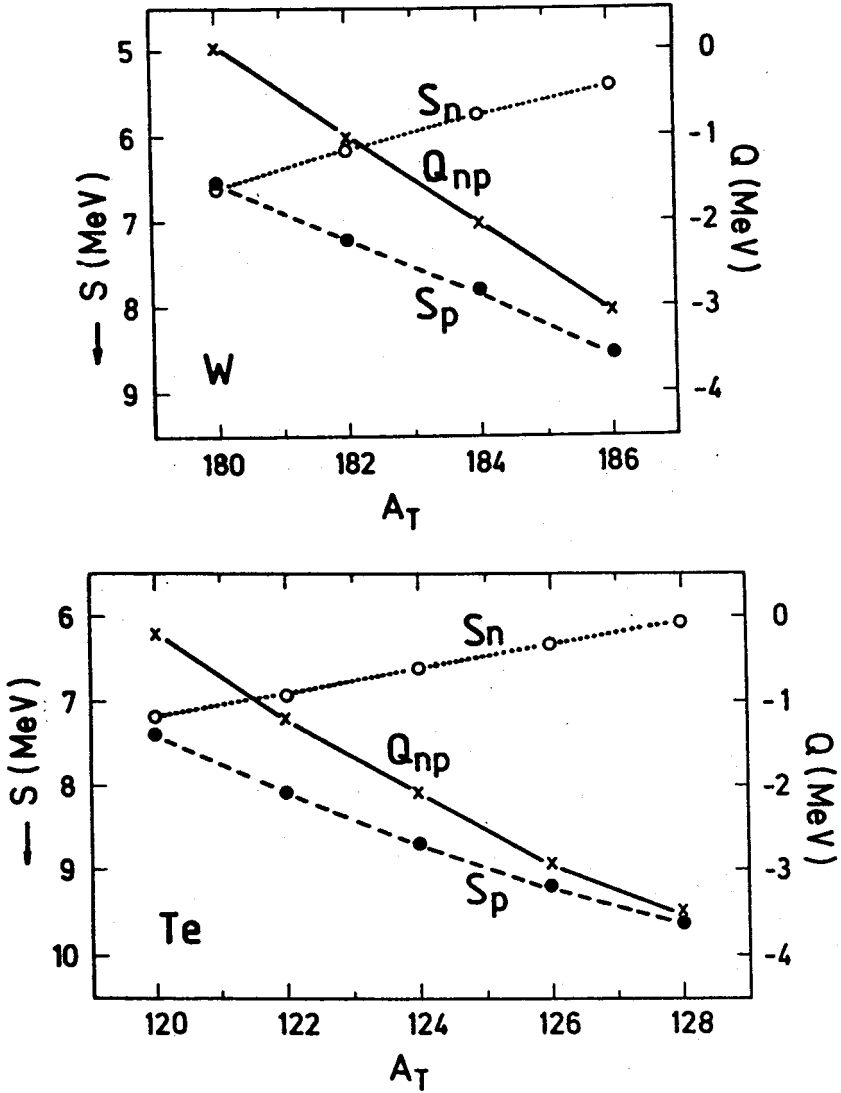


Fig.3

Fig.3 : Illustration of the systematic dependence of the neutron and proton separation energies and the (n,p) reaction Q-value on the mass number of the isotope.

for isotopes of a given element when the neutron number is increased by two. This is illustrated in Fig. 3 for the Te and W isotopes. The calculations show, and this can be qualitatively understood from Eq. 1 that the systematic variations of the Q-value are responsible for the observed isotopic trends (odd-even effects are discussed in Refs. 7 and 14). Namely, the total cross section for the emission of the first proton is calculated by integrating the proton spectrum up to the maximum proton energy given by $\epsilon_{\beta\max} = E_1 + Q_{np}$ and thus depends strongly and systematically on the Q-value.

The identification of the Q-value as the principal quantity which governs the preequilibrium isotopic trends presents the basis of the practical method for extrapolating the cross sections to energy domains where the measurements were not performed.¹³⁾ From Eq. 1 it follows that for the two isotopes of the same heavy element the relation

$$\left[\frac{\sigma_{np}(E_2')}{\sigma_{np}(E_1')} \right]_{Z,A'} = \left[\frac{\sigma_{np}(E_2)}{\sigma_{np}(E_1)} \right]_{Z,A} \quad (5)$$

should be valid. In the above equation, $\sigma_{np}(E)$ is the (n,p) cross section at energy E on the isotope (Z,A). The energies are connected by $E_{1,2}' = E_{1,2} + \Delta Q_{np}$, where ΔQ_{np} is the difference between the Q-values for the two isotopes. Thus, by measuring three cross sections experimentally, one can calculate the fourth one and determine σ_{np} for one of two nuclei in the eventually inaccessible domain of neutron energy. The application of Eq. 5, i.e. using the ratios of the cross sections improves the reliability of the extrapolation as compared with the simple one $\sigma_{np}(E + \Delta Q_{np}, Z, A') = \sigma_{np}(E, Z, A)$. This is due to the presence of other effects (dependence of the state densities $W(p, h, U)$ and $W(p, h, E)$ on the Q-value and

the neutron separation energy, respectively, in addition to the dominant (Q-value) effect.

3.3. Structure Effects

The systematic variation of the (n,p) cross section over a given isotopic chain of heavy element represents a sensitive test for determining the parameters of the pre-equilibrium model. I will illustrate it on the example of the choice of the level-density parameter a ($a = A/8$ structure independent and $a = a_{GC}^{12)}$ structure dependent). In Fig.4 the calculations using these two choices of level-density parameter and the same value of K for all Te isotopes are compared with the data. While the calculations with $a = A/8$ and $K = 500 \text{ MeV}^3$ fit the data correctly, the calculations with $a = a_{GC}$ and $K = 500 \text{ MeV}^3$ can not reproduce the observed isotopic trend at all. The preequilibrium cross sections are in the first approximation inversely proportional to the dominant transition rate which in turn is proportional (at given energy) to the product of the level-density parameter a and K . Thus, the comparison with experimental data shows (for details see Ref. 7) that only calculations performed with structure-independent transition rate not depending on a specific isotope (nuclei across the valley of stability) are able to reproduce the observed isotopic effect. The same conclusion, i.e. that structure-independent transition rate λ_+ should be used in the preequilibrium calculations, was drawn from our systematic analysis⁶⁾ of neutron induced reactions (n,n'), (n,p), (n,2n), (n,3n) on a number of targets (⁴⁵Sc, ⁵⁵Mn, ⁵⁶Fe, ⁵⁹Co, ⁹³Nb, ⁸⁹Y, ¹⁰³Rh, ¹⁶⁹Tm, ¹⁷⁵Lu, ¹⁸¹Ta, ¹⁹⁷Au, ²⁰⁹Bi) along the valley of stability.

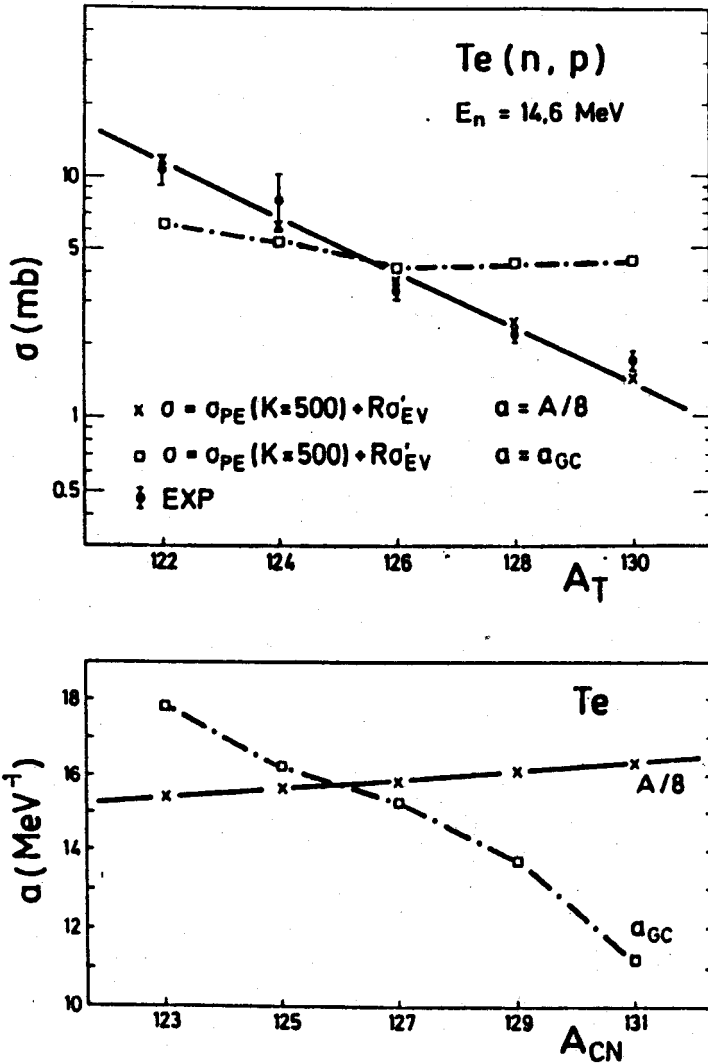


Fig.4.a. Measured (n,p) cross sections on even Te isotopes and predictions of the preequilibrium model with $K = 500$ MeV³ for all the isotopes considered, and two choices of the level-density parameter, $a = A/8$ and $a = a_{GC}$ ¹²⁾

- b. The dependence of the level-density parameters $a = A/8$ and $a = a_{GC}$ on the composite system formed in the n+Te reaction.

3.4. Isotopic Effects and Angular Distributions

The data discussed so far comprised the total cross sections. Recently, the angular distributions of the pre-equilibrium particles on a series of isotopes were measured by Scobel and his collaborators¹⁴⁾. The results of these detailed and precise measurements of the (p,n) reaction on the series of Mo isotopes at $E_p = 25.6$ MeV are summarized in Fig.5.

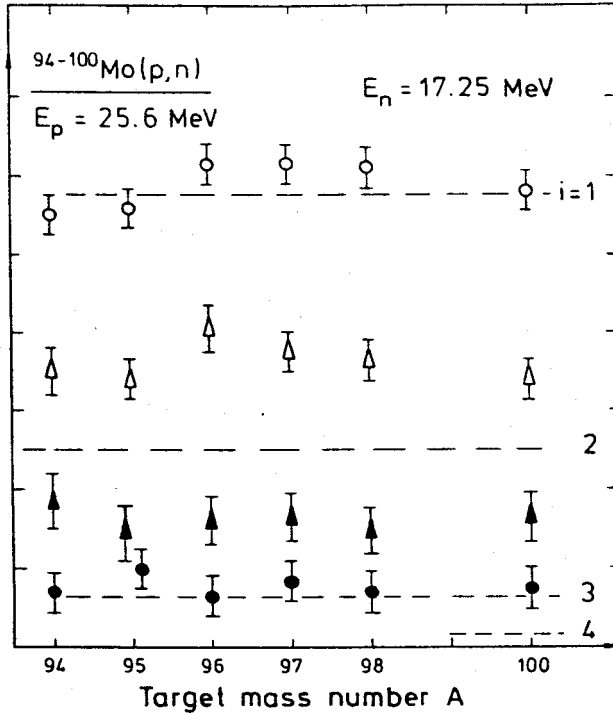


Fig.5 : Reduced coefficients a_1/a_0 of Legendre-polynomial fit (Eq.6) of the preequilibrium angular distributions of the (p,n) reaction ($E_p = 25.6$ MeV, $E_n = 17.25$ MeV) on a series of Mo isotopes. From Ref.14.

In this Figure the coefficients of the Legendre-polynomial fit of the differential cross sections

$$\frac{d^2 \sigma}{d\Omega d\epsilon_n} = \sum_{i=0}^{i_{\max}} a_v(\epsilon_i, A) \cdot P_i(\cos \theta) \quad (6)$$

are plotted as a function of the mass number of the target-isotope. From Fig.5 it is obvious that the angular distributions of preequilibrium particles are independent of the detailed structure of the isotope. This independence of the angular distributions on the mass number of an isotope renders additional confidence in the interpretation of the total(nucleon,nucleon) preequilibrium cross sections on a series of isotopes in terms of simple physical parameters.

4. SUMMARY AND CONCLUSIONS

This talk was devoted to the studies of isotopic effects in fast neutron induced reactions. The studies of isotopic effects (parameters change across the valley of stability) are complementary to the investigations of global systematics on nuclei along the valley of stability and thus add a valuable information to our understanding of the relevant physical processes and quantities.

Particular attention has been paid to the recent results on the role of preequilibrium emission mechanism in describing isotopic dependence of (n,p) cross sections on heavier targets. It has been shown that the isotopic trend of the (n,p) cross sections on heavier nuclei (preequilibrium emission is dominant), is caused

by the systematic variation of neutron and proton separation energies, i.e. the reaction Q-value. Thus, the same physical quantity (Q-value) determines the observed (n,p) isotopic trend over the whole periodic table, regardless of the fact that, in going from lighter to heavier nuclei, the reaction mechanism changes from evaporation to pre-equilibrium.

Furthermore, it has been demonstrated how isotopic effects can be used to select relevant parameters of the preequilibrium model. The main result here, which came out from analyzing (n,p) isotopic trends on heavy nuclei is that the dominant transition rate in preequilibrium calculations λ_+ does not exhibit structure effects, i.e. does not depend on the detailed structure of an isotope. This conclusion, i.e. that λ_+ does not exhibit structure effect, is in agreement with another our results obtained from the global analysis of neutron induced reactions on a number of nuclei ranging from ^{45}Sc to ^{209}Bi .

Let me conclude with a remark that the recent results (based on the inclusion of preequilibrium emission) show that isotopic trends in fast neutron induced reactions can be generally understood in the framework of existing nuclear reaction models and on the basis of the systematics of nuclear binding energies.

References

1. Gardner, D.G., Nucl. Phys. 29, 373 (1962)
2. Levkovskii, N., Sov. Phys. JETP 18, 213 (1964)
3. Pai, H.L. and Andrews, D.G., Can. J. Phys. 56, 944 (1978)
4. Qaim, S.M., Proc. Internatl. Conf. on Neutron Physics and Nuclear Data, p. 1088, Harwell 1978
5. Holub, E. and Cindro, N., Phys. Lett. 56B, 143 (1975)
6. Holub, E., Počanić, D., Čaplar, R. and Cindro, N., Z. Phys. A - Atoms and Nuclei 296, 341 (1980)
7. Čaplar, R., Udovičić, Lj., Holub, E., Počanić, D. and Cindro, N., Z. Phys. A - Atoms and Nuclei 313, 227 (1983)
8. Gardner, M.A., in Proc. of the Conf. on Nuclear Data Evaluation and Methods, Upton 1980, Nat. Nucl. Data Center, Vol.2. and references therein.
9. Graca, C. and Qaim, S.M., Nucl. Phys. A242, 317 (1975)
10. Marcinkowski, A., Stankiewicz, K., Garuska, U. and Herman, M., Z. Phys. A - Atoms and Nuclei 323, 91 (1986)
11. Bonetti, R., Invited talk, this conference
12. Gilbert, A. and Cameron, A.G.W., Can. J. Phys. 43, 1446 (1965)
13. Belovitskii, G.E., Sov. J. Nucl. Phys. 25, 282 (1977)
14. Mordhorst, E., Trabandt, M., Kaminsky, A., Krause, H., Scobel, W., Bonetti, R. and Crespi, F., Phys. Rev. C, to be published.

MODELS FOR RADIATIVE NEUTRON CAPTURE IN NUCLEAR GIANT RESONANCE REGION

Milan Potokar

"J. Stefan" Institute, E. Kardelj University of Ljubljana,
Ljubljana, Yugoslavia

Abstract

Macroscopic and microscopic semidirect models for radiative neutron capture in the nuclear giant resonance region are briefly presented, discussed and compared.

1. INTRODUCTION

In the region of the nuclear giant resonance the cross section for radiative neutron capture is a few orders of magnitude lower than the cross section of most other neutron induced reactions, at least for lighter nuclei. Yet radiative capture is a very attractive reaction for study since it provides an ideal ground for learning in detail the dynamic interplay between the collective and single particle modes of nuclear motion. This knowledge is needed to fully understand the dynamics of many other neutron induced reactions.

The uniqueness of radiative capture stems from the beneficial properties of the electromagnetic interaction responsible for the reaction. This interaction is weak, and therefore the cross section can be calculated with sufficient accuracy within the first - order perturbation theory. It is also very selective; i.e. it excites only a few specific types of nucleon motion. And finally, it is well known. It is due to these properties that from the matrix elements obtained from the experimental data, we can rather directly (using a model) study the components of the nuclear wave function in the continuum, reflecting the interplay of the fundamental modes of nuclear motion mentioned above.

2. RELATION OF THE EXPERIMENTAL DATA TO THEORETICAL QUANTITIES

"The building block" of each observed quantity in a radiative capture experiment is the differential cross section corresponding to the transition from the initial state $|i\rangle$ in which asymptotically the incoming neutron has the momentum \vec{k}_n and the spin orientation \vec{s} and the target nucleus is in the ground state of the angular momentum J_0 , its "z" component M_0 and parity Π_0 , into the final state $|f\rangle$ in which the residual nucleus is in the state $|\Psi_f\rangle$ with quantum numbers J_f , M_f and Π_f , and the emitted photon has the momentum \vec{k}_γ and helicity λ . Thus

$$\begin{aligned} \frac{d\sigma}{d\Omega}(i: J_0 M_0 \Pi_0, \vec{k}_n \vec{s}; \infty \rightarrow f: J_f M_f \Pi_f; \vec{k}_\gamma \lambda) \\ \cong \frac{1}{j_n} \cdot \frac{2\pi}{\hbar} |\langle \Psi_f | \langle \vec{k}_\gamma \lambda | H_{int} | 00 \rangle | \Psi_E^{(in)} \rangle|^2 \rho_{ph} \quad (1) \\ = \frac{1}{j_n} \frac{2\pi}{\hbar} |\langle \Psi_f | H_\gamma | \Psi_E^{(in)} \rangle|^2 \left(\frac{k_\gamma}{\hbar c}\right)^2 \end{aligned}$$

Here j_n is the flux of incident neutrons, ρ_{ph} is the density of the final photon states, and H_γ is the electromagnetic interaction defined by the matrix element of the interaction Hamiltonian H_{int} and the two photon states

$$H_\gamma = \langle \vec{k}_\gamma \lambda | H_{int} | 00 \rangle \quad (2)$$

In the experiment usually the initial magnetic substates M_0 are equally populated (i.e., the target nucleus is unpolarised) and the polarisation of the residual nucleus and the outgoing γ -ray not observed. Therefore the measured cross section is the cross section of eq.(1) averaged over M_0 and summed over M_f and λ . The polarised incident neutrons may eventually be available. The measured quantities are usually presented as the differential cross section

$$\begin{aligned} \sigma(E, \theta) &= \frac{1}{2} [\sigma^\uparrow(E, \theta) + \sigma^\downarrow(E, \theta)] \quad (3) \\ &= A_0(E) \left[1 + \sum_k a_k(E) P_k(\cos \theta) \right] \end{aligned}$$

and the analysing power $A(E, \theta)$, defined by

$$\begin{aligned} \sigma(E, \theta) A(E, \theta) &= \frac{1}{2} [\sigma^{\uparrow}(E, \theta) - \sigma^{\downarrow}(E, \theta)] \\ &= A_0(E) \left[\sum_k b_k(E) P_k^1(\cos \theta) \right] \end{aligned} \quad (4)$$

In these two expressions σ^{\uparrow} and σ^{\downarrow} are the cross sections obtained for the incident neutrons with spin polarised up and down perpendicular to the reaction plane and θ is the angle between the direction of the incoming neutron and the outgoing γ -ray (Fig. 1). P_k

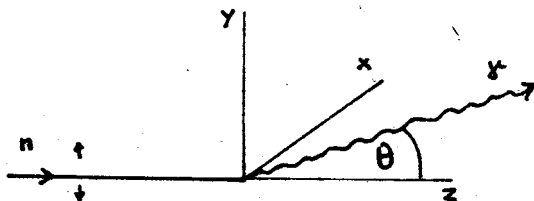


Fig.1: A schematic of a radiative neutron capture reaction.

and P_k^1 are Legendre and associated Legendre polynomials, respectively, of the k -order which is limited by $k \leq J + J'$ where J and J' refer to the interfering multipoles. The coefficient $A_0(E)$, defined by $A(E) = \sigma_{\text{tot}}(E)/4$, and the angular distribution coefficients a_k and b_k are expressible as bilinear combinations of the reaction amplitudes (transition matrix elements) of the type $\langle \Psi_f | H_{\gamma} | \Psi_{E,i}^{(n)} \rangle$. From Eqs.(1),(3), and (4) it is clear that by determining the coefficients A_0 , a_k , and b_k from measured angular distributions the possible ranges for the values of transition matrix elements are obtained. In the special cases of neutron capture by a target nucleus with angular momentum $J = 0^+ (\frac{1}{2}^+)$ to form a nucleus with $J = \frac{1}{2}^+ (0^+)$ and when, for example, only dipole and quadrupole transitions contribute, the problem is even overdetermined. From the experiment 9 angular distribution coefficients can be obtained, while there are only 7 unknowns: 2 dipole amplitudes, 2 quadrupole amplitudes and 3 relative phases. Such an example is the reaction $^{207}\text{Pb}(n, \gamma_0)$.

3. REACTION MODELS

In the case of radiative neutron capture in the nuclear resonance region, the reaction model is essentially determined by the model wave function, which enters the (energy averaged) transition amplitude and approximates the exact ("energy averaged") continuum wave function, $|\Psi_E^{(+)}\rangle$. The aim is to include explicitly in the play those components of the continuum wave function which are expected to give such transition amplitudes which lead to a satisfactory reproduction of the experimental data. Let us note here, that only in the case when all the particular amplitudes responsible for the observed features of the studied reaction are determined from the experimental data, can the reaction model be really fully tested. (For the sake of simplicity, in this work we assume that either the target or the residual nucleus is spherical.)

The reaction models range from the macroscopic to the microscopic ones, the particular type being determined by the way of "selecting" the important components of $|\Psi_E^{(+)}\rangle$ and by the approximations applied in expressing them, i.e. in solving the Schroedinger equation

$$(E - H)|\Psi_E^{(+)}\rangle = 0 \quad (5)$$

The representative of the macroscopic or phenomenological models, most frequently used in data analysis, is the original direct - semidirect (DSD) model /1,2,3/ with the complex particle vibration coupling /4/. Few other models, like the pure - semidirect (PSD) model /5,6/ or the extended pure-resonance model /7/, and its approximation, the pure - resonance (PR) model /8/, have been discussed recently. Here we shall present mainly the DSD model, since the other models describe the same physics and only employ somewhat modified model ingredients. To find the details the reader is referred to refs. /5-8/.

A fully microscopic model would require the complete diagonalisation of the nuclear Hamiltonian H in the basis of single particle wave functions including the continuum ones. As such a

calculation is not feasible, one uses the procedure in which the effects of selected configurations are incorporated and the modified residual interaction used. It is believed that the best procedure to treat the giant resonances is the random phase approximation (RPA). Therefore we shall describe here the continuum RPA model /9,10/ for radiative neutron capture. The models based on the coupled - channels formalism /11,12/ will not be discussed, as they are more appropriate for lower energies and light nuclei.

A few models in between, the so called semimicroscopic models, have been tried /13,14/. They are conceptually very close to the semidirect models. We shall present the results of a semimicroscopic DSD model in comparison with the CRPA model results.

1) DIRECT - SEMIDIRECT MODEL

The original DSD model is basically a two state model. It assumes that only two components of the wave function $|\Psi_E^{(u)}\rangle$ are important enough to be taken into account explicitly in the model. Thus, the ansatz to be included in the Schroedinger equation is:

$$|\bar{\Psi}_E^{(u)}\rangle \approx |t_0\rangle |\Psi_{opt}^{(u)}\rangle + F_1 \cdot |t_1\rangle |\Psi_f\rangle \quad (6)$$

The first term is the optical model wave function, with $|t_0\rangle$ being the ground state of the target nucleus and $|\Psi_{opt}^{(u)}\rangle$ the single particle optical model wave function describing the neutron elastic scattering. The second term is proportional to the dipole collective component of the wave function, with $|t_1\rangle$ being the giant dipole vibration state of the target nucleus and $|\Psi_f\rangle$ the single particle bound state (of the energy ϵ_f) into which the incident neutron is captured.

Solving the Schroedinger equation (5) with the ansatz (6) the Schroedinger equation for the single particle state $|\Psi_{opt}^{(u)}\rangle$ is obtained and the following expression for the factor F_1 :

$$F_1 \cdot |t_1\rangle |\Psi_f\rangle = \frac{1}{E - (\epsilon_{t_1} + \epsilon_f)} |t_1\rangle |\Psi_f\rangle \langle\langle \Psi_f | K t_1 | H | t_0 \rangle |\Psi_{opt}^{(u)}\rangle \quad (7)$$

Usually, the giant - dipole state $|t_1\rangle$ is described by the schematic model of Brown and Bolsterli /15/,

$$|t_1\rangle = \frac{D_0 |t_0\rangle}{\langle t_0 | D_0^2 | t_0 \rangle^{1/2}} \quad (8)$$

where D_0 is the isovector part of the dipole operator for the target nucleus. The residual interaction H' , however, is taken to be the sum of the third components of the isospin - dependent part of the residual zero-range interaction between the incident neutron and the nucleons in the target nucleus,

$$H' = \sum_{i=1}^A v_{01} \tau_{i3} \tau_3 \cdot \delta(\vec{r}_i - \vec{r}_0) \quad (9)$$

The target nucleus matrix element $\langle t_1 | H' | t_0 \rangle$ presents the transition potential, V_{tr} , which causes the scattering of the incoming neutron into a bound single particle state. It is usual to introduce the so called particle - vibration coupling interaction or the form factor, $h(r)$, which is defined by:

$$\begin{aligned} V_{tr}^{1M}(\vec{r}) &= \langle t_1 | H' | t_0 \rangle \\ &\cong -\kappa \langle t_0 | D_0^2 | t_0 \rangle^{1/2} \cdot \tau_3 \cdot v_{01} \cdot \kappa \rho(r) Y_{1M}^{\dagger}(\hat{r}) \\ &= \langle t_0 | D_0^2 | t_0 \rangle^{-1/2} \cdot \left(-\frac{\kappa}{A}\right) \cdot h(r) \cdot Y_{1M}^{\dagger}(\hat{r}) \end{aligned} \quad (10)$$

Here, κ is a constant and $\rho(r)$ the density of the target nucleus in the ground state.

The singularity present in the equation (7) at $E = E_n + E_f$ in fact does not exist. Namely, one has to include in the ansatz (6) also the rest of the configurations, when solving the Schroedinger equation for the two wave function components which explicitly enter the model. The effects of this rest of the wave function $|\Psi_E^{(0)}\rangle$ is incorporated in the effective operators determining the two components. The consequences are:

- i) in the Schroedinger equation for $|\Psi_{tr}^{(0)}\rangle$ the single particle

potential may indeed be approximated by the optical model potential.

ii) the energy denominator in eq. (7) becomes complex, so that the singularity has gone

$$E_{t_1} \rightarrow E_{t_1} + \Delta E_{t_1} - \frac{i}{2} \Gamma_{t_1} = E_{t_1} - \frac{i}{2} \Gamma_{t_1} \quad (11)$$

The energy E_{t_1} may well be approximated by the position of the GDR in the target nucleus, and Γ_{t_1} by its width.

iii) The residual interaction becomes complex, i.e. $H \rightarrow \mathcal{H}'$. The approximation used above may therefore be extended /4/ to

$$\mathcal{H}' = \sum_{i=1}^A v_{0i} \tau_{i3} \tau_{03} (1 - iI(r)) \delta(\vec{r}_i - \vec{r}_0) \quad (12)$$

Obviously the transition potential (10) and therefore the form factor become complex:

$$h'(r) \rightarrow h(r) + ik(r) \quad (13)$$

An useful approximation /4/ is

$$h(r) + ik(r) \sim r \cdot \left(\frac{V_1}{4} \cdot f_R(r) - i \frac{W_1}{4} 4b \frac{d}{dr} f_I(r) \right) \quad (14)$$

where V_1 and W_1 are the strengths of the real and imaginary part of the symmetry optical model potential and $f_R(r)$, $f_I(r)$ the corresponding Woods - Saxon form factors.

Writing the isovector dipole operator of the final nucleus, D , as the sum of the dipole operator for the incident neutron, d_0 , and the dipole operator for the target nucleus, D_0 , i.e.

$$D = d_0 + D_0 \quad (15)$$

the DSD model transition amplitude may be expressed as

$$\begin{aligned} T_{DSD}^{1M} &= \langle \langle \psi_f | K | \psi_i \rangle | D^{1M} | \text{ansatz (6)} \rangle \quad (16) \\ &= \langle \psi_f | d_0^{1M} | \psi_{opt}^{(u)} \rangle + \frac{1}{E - E_{t_1} + i\Gamma_{t_1}} \langle \psi_f | (-\frac{r}{A}) (h(r) + ik(r)) Y_{1M}^{\dagger}(\hat{r}) | \psi_{opt}^{(u)} \rangle \end{aligned}$$

Here the first term describes the direct capture in which the incoming neutron experiences a direct dipole radiative transition from its scattering state to a bound single particle state of the residual nucleus. The second term describes a two step process. The target

nucleus is first brought to the dipole collective state by the incident neutron scattering into a bound single particle state, and is then deexcited by a dipole photon.

From the expression (16) it is apparent that the model ingredients are:

- i) the bound single particle state potential
- ii) the optical model potential (consistent with the bound state potential) describing the neutron elastic scattering
- iii) the energy parameters of the giant collective state (also referred to as doorway state)
- iv) the transition potential or the form factor.

As the first three model ingredients are usually relatively well known (the energy parameters at least for the dipole capture), the form factor - its strength, shape, and character - may be studied. This is probably the primary role of the model and the obtained informations are certainly most interesting ones for the study of the other fast neutron induced reactions.

Most experimental data have been analysed on the basis of the DSD model. The values for V_1 have always been in reasonable agreement with the values obtained from analysis of other experimental data. For example in Fig. 2 we present an analysis of the $^{40}\text{Ca}(n, \gamma)^{41}\text{Ca}$ reaction [16, 17]. The long dashed curve corresponds to the values $V_1 \approx 80$ MeV and $W_1 \approx 40$ MeV which are both in good agreement with the result from

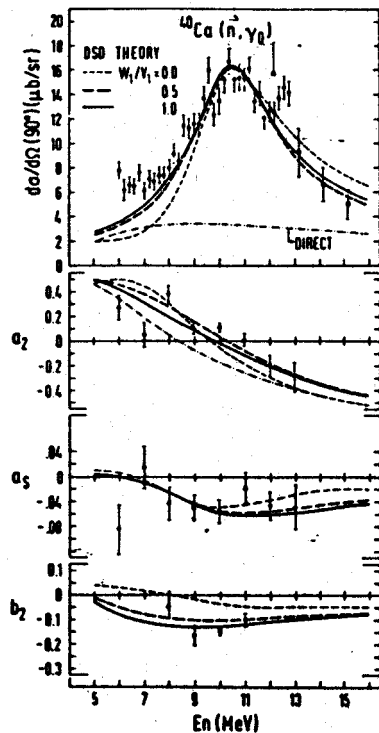


Fig.2: The DSD model results for the reaction $^{40}\text{Ca}(n, \gamma)^{41}\text{Ca}$. The experimental data from refs. [15, 17].

charge exchange reactions of ref./18/. However, the solid curve, for which $V_1 = W_1$, is also an acceptable fit. This case indicates that the imaginary coupling interaction cannot be determined reliably unless the real one is well known.

The real part of the transition potential or the real form factor is well understood. It is determined by the target nucleus transition density, ρ_{tr} , folded with the effective two-body residual interaction, $v(\vec{r}-\vec{r}')$,

$$\begin{aligned} V_{tr}^{JM}(\vec{r}) &= \langle t_{JM} | H' | t_0 \rangle \\ &= \int d\vec{r}' v(\vec{r}-\vec{r}') \rho_{tr}^{JO}(\vec{r}') \end{aligned} \quad (17)$$

For a zero - range interaction, like in (10), V_{tr} is simply proportional to the transition density (in the case of the schematic model, to $\rho(r)$). We believe that due to the improving knowledge on the models for giant vibrations and on the effective two-body interactions the real part of the form factor will be more or less fixed in the near future.

For the time being the imaginary part of the transition potential is still poorly known with regards to both its phenomenological parametrization and its microscopic origin. As we have discussed already, the complex nature of the form factor can readily be justified formally. This was done in the framework of Feshbach's unified reaction theory /20/ in refs./5,6,19/. It is understood that an imaginary part of the form factor is the consequence of the indirect excitations of the giant vibration, however no attempt has been done yet to find out what fraction of the phenomenological imaginary interaction is of this origin. It would be of great importance to perform such a study as this problem is closely connected to the problem of the particle decay of giant resonances.

Early analysis showed that the values of W_1 from radiative neutron capture are in agreement with the values obtained from charge exchange reaction for medium-weight nuclei, but that they tend to increase with the mass of nucleus. In the case of $^{208}\text{Pb}(n, \gamma)$ the

result $W_1 \approx 1.7 \cdot V_1$ was obtained. This observation has not been changed over the last years. Only recently a careful reanalysis /21/ of the $^{208}\text{Pb}(n, \gamma)$ data /22/ showed, that the values for the form factor parameters V_1 and W_1 might be close to those obtained from the phenomenological analysis of the data for other reactions. This interesting analysis of the $^{208}\text{Pb}(n, \gamma)$

data is shown in Fig.3. The DSD model ingredients in these calculations were chosen in an as consistent way as possible on the basis of the existing relevant experimental and theoretical data. The bound single particle potential which reproduces the experimental rms radii in ^{208}Pb was used as a starting point. The optical model potential of Rapaport et al /23/ was then reparametrized into a kind of natural extension of the bound potential. For the real part of the form factor an analytical function $(n^3 \rho(r))$ was used, which closely resembles the RPA transition density (calculated on the basis of the same bound state potentials) folded by an effective two - body interaction with the range of ~ 0.8 fm. And, finally, the applied values for V_1 and W_1 were determined from a consistent reanalysis of the proton and neutron elastic scattering data

(the uncertainty range for W_1 was from $W_1^<$ to $W_1^>$). Thus in this calculation no parameter was adjusted to fit the capture data. An important observation of this study is that it is essential to use the mentioned radial shape for the real form factor in order to reproduce the angular distribution coefficient a_2 .

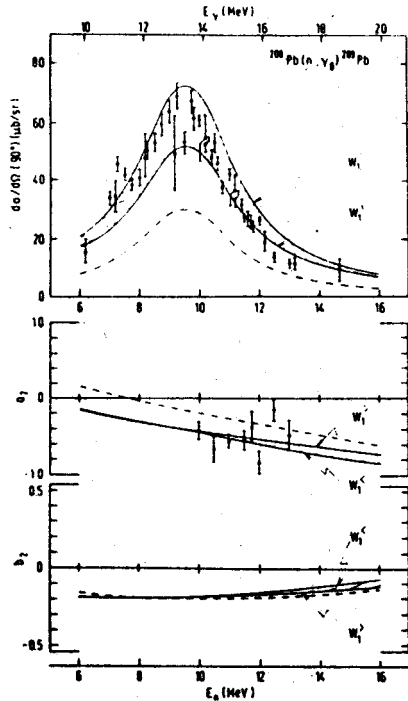


Fig.3: $d\sigma/d\Omega(90^\circ)$ cross section and a_2 angular distribution coefficient for the reaction $^{208}\text{Pb}(n, \gamma)$ /22/ compared with the predictions of the DSD model using consistent model ingredients /21/.

The DSD model may also be applied to describe the radiative capture processes, proceeding through excitations of higher multipoles than the electric dipole one. As these reflect themselves practically only through interference effects, the role of the DSD model here is to detect, confirm and possibly to locate the corresponding giant resonances rather than to study the details of the form factors.

In Fig. 4 we present the observed fore - aft asymmetry in the yield of γ - rays from the reaction $^{40}\text{Ca}(n, \gamma)^{41}\text{Ca}$ /16,24/. The DSD model analysis suggests the excitation of an isoscalar quadrupole giant resonance at ~ 18 MeV and the lower isospin component of the isovector quadrupole giant resonance at ~ 32 MeV.

ii) CONTINUUM RPA MODEL

Roughly speaking we may say that the continuum RPA model is a kind of microscopic direct - semidirect or, better, a pure - semidirect model. It assumes that the state $|\Psi_{\mathcal{E}}^{(\lambda)}\rangle$ can be satisfactorily described within particle - hole basis states. The effects of the truncated basis states are roughly incorporated by the use of a modified nucleon - nucleon interaction which is a zero range density dependent force. This force is not complex, which means that effects of most of the rest space are indeed not taken into account even in an averaged way. Therefore it is understandable that the approach does not include the scattering state corresponding to an optical model potential.

As in the macroscopic pure - semidirect model, also here only those nuclear wave function components which correspond to the giant vibration of the residual nucleus enter the transition amplitude explicitly. In contrast to the DSD model, now the part of the incident particle continuum state that may radiatively decay to the

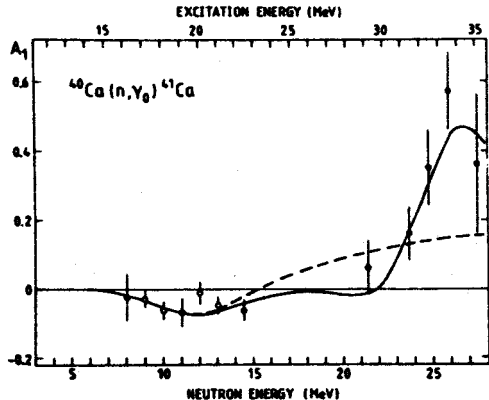


Fig.4: The fore-aft asymmetry of the $^{40}\text{Ca}(n, \gamma)^{41}\text{Ca}$ /16,24/. The full curve presents the results of the DSD model including an isoscalar and an isovector GQR. The dashed curve presents results with only direct quadrupole transitions included in the calculation.

final bound state is included in the semidirect term. So, the giant vibration state in the residual nucleus is considered, rather than the one in the target nucleus. For capture to a closed shell nucleus /10/

$$|\Psi_{E,c}^{(u)}\rangle \approx \sum_{c'=[p,h]} \int d\varepsilon' \left\{ X_{c,c'}(E+\varepsilon_f, J, \Pi; \varepsilon') [a_p^\dagger(\varepsilon') b_h^\dagger]_J^J - Y_{c,c'}(E+\varepsilon_f, J, \Pi; \varepsilon') [b_h, a_p(\varepsilon')]_J^J \right\} |10\rangle \quad (18)$$

Here $E + \varepsilon_f$ is the excitation energy of the nucleus, J is the total angular momentum and Π the parity of the corresponding multipole vibration, a^\dagger and b^\dagger are creation operators for the particle and the hole, respectively, a and b corresponding destructive operators, ε' is the single particle energy and $c = [p, h]$ is the (decay) channel characterized by the quantum numbers of the particle and the hole state involved. The expansion coefficients X and Y are determined by solving the continuum RPA equations with proper boundary conditions and by taking into account the adequate reaction specifications.

In Fig.5 we present the analysis /25/ of the data for the reaction $^{16}\text{O}(\gamma, p_0)^{15}\text{N}$. In fact $^{15}\text{N}(\bar{p}, \chi^+)$ reaction data /26,27/ are used. The unperturbed Hamiltonian is expressed by the sum of Woods - Saxon single particle potentials, the residual particle - hole interaction used is the zero - range density - dependent Landau - Migdal force with parametrisation given by Rinker and Speth /28/. The basis continuum states were included up to the $j_{1/2}$, $j_{3/2}$ waves.

The agreement with the gross features of the experimental data is very good. This indicates that in a light nucleus like ^{16}O the basic reaction mechanism is well described within the $1p - 1h$ basis and using a

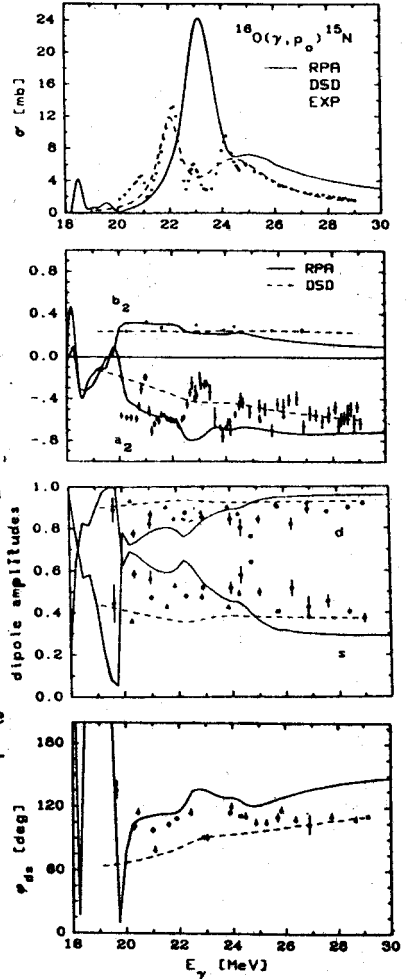


Fig. 5: Experimental data /26,27/ for the reaction $^{16}\text{O}(\gamma, p_0)^{15}\text{N}$ compared to the predictions of the continuum RPA model (solid line) and of the semimicroscopic DSD model (dashed line).

zero-range force. Such a result cannot be expected for heavier nuclei where the spreading width is larger than the decay width. In the case, for example, of the photoabsorption cross section of ^{208}Pb , the inclusion of the 2p-2h basis states is indispensable /29/. In general, the zero-range force is also an inadequate effective residual interaction and ignorance of long range correlations a deficiency.

In Fig.5 the results of a semimicroscopic DSD model are also presented. Here special care was taken to use consistent bound and scattering single particle states, two doorway states were included, and the particle-vibration coupling was determined by folding the corresponding bound RPA transition densities with the isovector part of the effective interaction of ref. /30/. The agreement with the CRPA model results is not surprising because, as we have stated already, the physics contained in the two models is essentially the same. Above the GDR the a_2 angular distribution coefficient seems to be better reproduced by the DSD model. The reason lies probably in the fact that in the optical model scattering state the effects of 2p-2h and other more complicated configurations are at least phenomenologically taken into account.

Both models also reproduce quite well the relative absolute values of the two dipole transition amplitudes and their relative phase, data which have been extracted from A_0, a_2 , and b_2 coefficients. It is evident that this analysis presents a convincing positive test of the models.

Good agreement with experimental data is obtained also with the original DSD model which is including the phenomenological particle - vibration coupling. However, this might not be the case for the quadrupole amplitudes.

4. SUMMARY AND OUTLOOK

Analysis of the data for the $^{15}\text{N}(\bar{p}, \gamma_0)$ reaction shows that the two models, the continuum RPA model and the direct - semidirect model, well describe the reaction mechanism; the CRPA model despite the fact that it invokes only 1p-1h basis states and a zero-range residual interaction. This microscopic model is of course not suitable for the extraction of the gross properties of the giant vibration states from the experimental data. However, it may lead to excellent reproduction of the data when using a more adequate effective residual interaction and a better ground state and when including the effects of the 2p-2h configurations. Because the imaginary coupling is small or even ignorable for light nuclei, the DSD model can well be applied for locating and evaluating the multipole strength, but, so it seems, with the provision that a microscopically founded transition potential and consistent (unified) bound state and optical model potentials are used. The transition potentials and other gross properties of giant vibrations obtained from DSD model analysis of radiative capture data certainly present valuable ingredients for the analysis of other neutron induced reactions.

In the case of heavier and, especially, heavy nuclei, the CRPA model has to be improved with regard to the basis, the ground state, and the effective residual interaction. Also, the DSD model obtains a serious deficiency. The imaginary part of the transition potential or the particle - vibration coupling interaction increases with the mass number. Fortunately, knowledge of the real part of this interaction is improving, so it is reasonable to hope that phenomenological parametrisation of the imaginary term will become much better known in the near future. The investigation of the microscopic origin of this term remains a challenging problem, closely connected to the problem of the particle decay of giant resonances.

Acknowledgements

I would like to acknowledge the collaboration of G. Co, V. Klemt and S. Krewald in the work with microscopic models and the help of A. Ramsak in most of the computing and technical work. I thank also The International Bureau at KFA, Juelich, for valuable financial support and the colleagues at The Institute for Nuclear Physics at Juelich, for their kind hospitality during my stay in Juelich.

REFERENCES

1. G.E.Brown, Nucl. Phys. 57(1964)339
2. A.A.Lushnikov and D.F.Zaretsky, Nucl. Phys. 66(1965)35
3. C.F.Clement, A.M.Lane and J.A.Rook, Nucl.Phys. 66(1965)273,293
4. M.Potokar, Phys. Lett. 46B(1973)346
5. M.Potokar, Phys. Lett. 92B(1980) 1
6. M.Potokar, In Neutron-Capture Gamma - Ray Spectroscopy and Related Topics 1981, V. von Egidy, F.Goennenwein and B.Maier, eds. (The Institute of Physics, Bristol and London, 1981), p. 477
7. F.S.Dietrich, in Capture Gamma-Ray Spectroscopy and Related Topics - 84, S.Raman, ed., (American Institute of Physics, New York, 1985),p.445
8. F.S.Dietrich and A.K.Kerman, Phys. Rev. Lett. 43(1979)114
9. M.Cavinato, M.Marangoni, P.L.Ottaviani and A.M.Saruis, Nucl. Phys. A373(1982)445
10. G.Co and S.Krewald, Phys. Lett. 137B(1984)145; Nucl. Phys. A433(1985)392
11. B.Buck and A.D.Hill, Nucl.Phys. A95(1967)271
12. M.Marangoni, P.L.Ottaviani, and A.M.Saruis, Nucl. Phys. A277(1977)239, and references therein.
13. W.L.Wang and C.M.Shakin, Phys. Rev. C5(1972)1898
14. B.Castel and M.Micklinghoff, in Neutron Capture Gamma-Ray Spectroscopy, R.Chrien and W.Kane, eds. (Plenum, N.Y., 1979), p.285
15. G.E.Brown and M.Bolsterli, Phys. Rev. Lett. 3(1960)472
16. S.A.Wender, N.R.Roberson, M.Potokar, and H.R.Weller, Phys. Rev. Lett. 41(1978)1217
17. H.R.Weller, private information
18. J.D.Carlson, D.A.Lind and C.D.Zafiratos, Phys. Rev. Lett. 30(1973)99
19. M.Potokar, Ph.D.thesis, E.Kardelj University of Ljubljana, 1974, unpublished
20. M.Potokar, 1976-177 Progress Report, Stanford University, unpublished
21. H.Feshbach, Ann. Phys. (N.Y.) 19(1962)287
22. M.Potokar and A.Ramsak, to be published
23. S.E.King, M.Potokar, N.R.Roberson and H.R.Weller, Nucl. Phys. A384(1982)129
24. J.Rapaport, T.S.Cheema, D.E.Bainum, R.W.Finlay and J.D.Carlson, Nucl. Phys. A296(1978)95
25. I.Bergqvist, R.Zorro, A.Hakansson, A.Lindholm, L.Nilson, N.Olsson, and A.Likar, Nucl. Phys. A419(1984)509
26. M.Potokar, A.Ramsak, G.Co and S.Krewald, to be published
27. W.J.O Connell and S.S.Hanna, Phys. Rev. C17(1978)892
28. S.S.Hanna, H.F.Glavish, R.Avida, J.R.Calarco, E.Kuhlmann and R.LaCanna, Phys. Rev. Lett. 32(1974)114
29. G.A.Rinker and J.Speth, Nucl. Phys. A306(1978)360
30. J.Wambach, Lecture presented at the International School on Nuclear Structure, Alushta, 1985, USSR
31. J.P.Jeukenne, A.Lejeune, and C.Mahaux, Phys. Rev C16(1977)80

INVESTIGATION OF SPIN EFFECTS IN EXCITON MODEL CODES

H. Gruppelaar, J.M. Akkermans, Shi Xiangjun*

Netherlands Energy Research Foundation ECN

P.O. Box 1, 1755 ZG Petten, The Netherlands

ABSTRACT

Various options to introduce spin effects into the pre-equilibrium exciton model are considered. These options have an approximate nature, but are such that they do satisfy basic consistency requirements. Calculations show that, firstly, the neutron spectrum is somewhat hardened due to spin effects and, secondly, there is a dependence on the ground-state spin.

1. INTRODUCTION

A draw-back of the usual exciton model (EM) is that it does not take into account the spins and parities of the nuclear states involved in the reaction process. The exciton model yields in the pure equilibrium limit the same results as the Weisskopf-Ewing (WE) formula. A generalization of the EM to include spin and parity is relatively easy, as has been shown e.g. in Ref. [1]. The main difference with the usual EM is that all quantities (internal transition rates λ , emission rates W , occupation probabilities q , mean life times τ , etc.) become a function of the composite-nucleus spin and parity J and Π , respectively.

It is fair to require that in the pure-equilibrium limit the continuum Hauser-Feshbach formula (HF) is obtained. The relation between HF and WE is such that ignoring the channel-spin dependence of the transmission coefficients and assuming a $(2J+1)$ -dependence and an even parity distribution the HF formula leads to WE. Similarly, we may require that the same assumptions should transform the spin-dependent exciton model into the usual EM. These consistency requirements imply that there must be a close relation between the mean lifetimes $\tau^{\text{spin}}(n)$ and $\tau(n)$ of these models, for each value of the exciton number n . In this paper some relations between these two quantities are postulated. They define different (approximate) spin-dependent exciton models. The differences between the spin-dependent and spin-independent models are investigated. In order to perform this intercomparison the two models have been made identical except for the dependences of spin and parity.

2. A SIMPLE UNIFIED MODEL

Without any loss of generality it can be shown that the spin-dependent exciton model can be obtained from the usual HF model by

* On leave from the Institute of Atomic Energy, Beijing, China.

means of the following substitution for the level density [3]

$$\rho(I, \pi, E^*) \rightarrow \sum_n \frac{\rho^{I\pi}(n-b', E^*)}{\rho^{J\Pi}(n, E)} Q_b(n) \tau^{J\Pi}(n), \quad (1)$$

where E^* refer to the residual nucleus formed by the reaction (a, b) with $Q_b(n)$ as defined in [2] ($Q_b \rightarrow 1$ at equilibrium); b' is the mass number of b . For the spin and parity dependence of $\tau^{J\Pi}$ we formally write

$$\tau^{J\Pi}(n) = s^{J\Pi}(n) \tau(n). \quad (2)$$

It is easy to show [1,3] that due to conservation of probability the following equation is strictly valid

$$\sum_n \tau^{J\Pi}(n) W_t^{J\Pi}(n) = \sigma_a^{J\Pi} / \sum_{J\Pi} \sigma_a^{J\Pi}, \quad (3)$$

where $W_t^{J\Pi}$ is the total emission rate and $\sigma_a^{J\Pi}$ the composite formation cross section as a function of J and Π . This is an extension of

$$\sum_n \tau(n) W_t(n) = 1. \quad (4)$$

Neglecting the weak $(J\Pi)$ -dependence of $W_t^{J\Pi}$ these relations lead to the approximation

$$s^{J\Pi}(n) = \sigma_a^{J\Pi} / \sum_{J\Pi} \sigma_a^{J\Pi}, \quad (5)$$

i.e., independent of n . This means that substitution (1) modifies to

$$\rho(I, \pi, E^*) \rightarrow \sum_n \frac{\rho^{I\pi}(n-b', E^*)}{\rho^{J\Pi}(n, E)} Q_b(n) \tau(n). \quad (6)$$

A further simplification is possible if it is assumed that the spin distribution of the level density is independent of n :

$$\rho(I, \pi, E^*) \rightarrow \sum_n \frac{R^{I\pi}(E^*) \omega(n-b', E^*)}{\omega_c(n, E)} Q_b(n) \tau(n). \quad (7)$$

Another assumption made in literature [4] postulates $s^{J\Pi}(n) = R^{J\Pi}(n, E)$, which actually is only true at equilibrium. It leads to

$$\rho(I, \pi, E^*) \rightarrow \sum_n \frac{\rho^{I\pi}(n-b', E^*)}{\omega_c(n, E)} Q_b(n) \tau(n). \quad (8)$$

In this paper the effects of the substitutions (6) to (8) based upon approximation (5) are studied. It is noted that substitution (7) is an attempt to describe the precompound option of a code like GNASH [5] in a more consistent way. We have introduced substitutions (7) and (8) into GNASH and substitutions (6) to (8) into ERINNI [6]. The new versions are referred to as GNASH-ECN and PERINNI (recently extended with a spectrum option). It was checked that by inserting the equilibrium conditions

$$\tau(n) = \omega_c(n, E), \quad Q_b(n) = 1 \quad (9)$$

the HF results are recovered, whereas with

$$R^{I\pi}(E^*) = 2I+1, \quad T_{kj} \rightarrow T_k \quad (10)$$

the spin-independent exciton-model [7] results were reproduced. The combination of (9) and (10) leads to the WE formula.

3. RESULTS AND CONCLUSIONS

Some results of the calculations for incident 14.6 MeV neutrons on Nb are shown in Figs. 1 and 2. In Fig. 1 we compare the spin-dependent options (6) to (8) with a spin-independent EM calculation. A first conclusion is that pre-equilibrium spin effects lead to a somewhat harder (first-emitted) neutron spectrum as compared to the spin-independent case. The second conclusion is that the numerical results of various spin assumptions in EM are quite close, although their physical background may be quite different. Thirdly, as demonstrated in Fig. 2, there is a clear ground-state spin dependence. Fig. 2 was produced by a change of the ground-state spin from 9/2 to the fictitious value 1/2, keeping all other parameters exactly the same.

Summarizing, we note that spin effects are of some importance in pre-equilibrium processes. The spin dependence of τ^{II} should be studied in more rigorous detail [3].

Acknowledgement: This work has been supported by the International Atomic Energy Agency, Vienna.

REFERENCES

- [1] Gruppelaar, H., in Proc. IAEA Adv. Group Meeting on Basic and Applied Problems of Nuclear Level Densities, Report BNL-NCS-51694, p. 143, Brookhaven National Laboratory, 1983.
- [2] Kalbach, C., Z. Phys. A283 (1977) 401.
- [3] Shi Xiangjun, Akkermans, J.M., Gruppelaar, H., to be published.
- [4] Fu, C.Y., in Proceedings Int. Conf. on Nuclear Cross Sections for Technology, Report NBS-Sp-594, p. 757, National Bureau of Standards, 1980.
- [5] Young, P.G., Arthur, E.D., GNASH: A pre-equilibrium statistical nuclear model code for calculation of cross sections and emission spectra, Report LA-6947, Los Alamos National Laboratory 1977.
- [6] Fabbri, F., Reffo, G., ERINNI nuclear model code, Report RT/F1 (77)4, ENEA, Bologna 1977.
- [7] Gruppelaar, H., Akkermans, J.M., The GRAPE code system for the calculation of precompound nuclear reactions - GRYPHON code description and manual -, ECN-164 (1985).

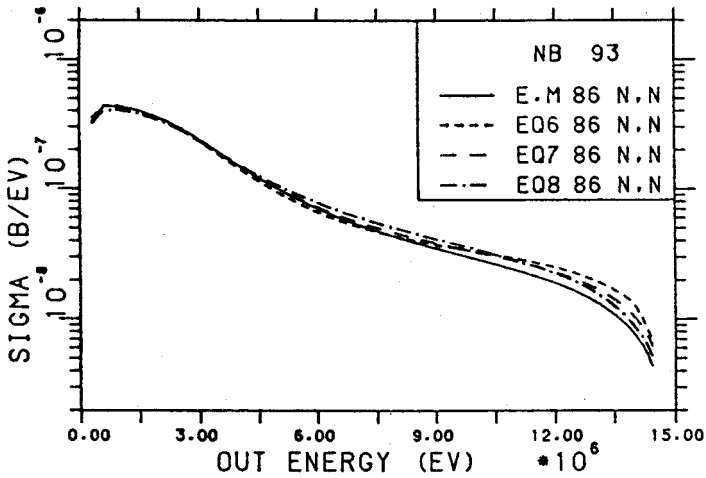


Fig. 1. Comparison between the unified model (3 options) and the normal exciton model for the reaction $^{93}\text{Nb}(n,n'x)$.

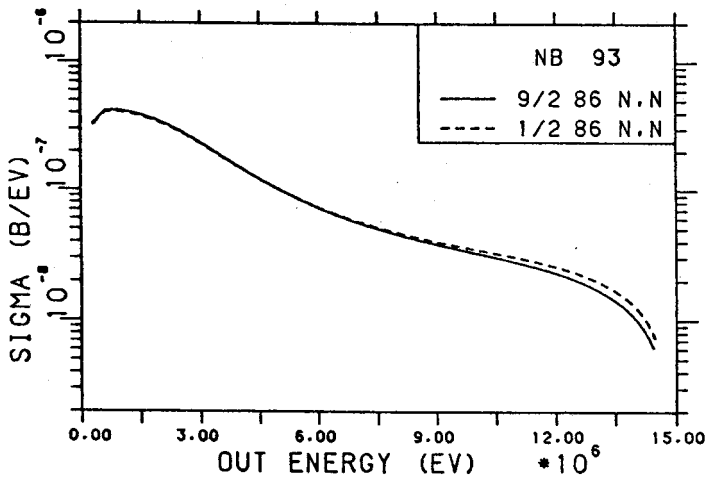


Fig. 2. Ground-state spin dependence ($J=9/2$, full line, versus $J=1/2$, dotted line) for the same reaction as in Fig. 1. The spin option chosen is Eq. (7).

NUCLEAR MODEL ANALYSIS OF THE (n,p) REACTION CROSS SECTION ISOTOPE EFFECT FOR THE TITANIUM ISOTOPES

Marilena Avrigeanu, Marin Ivascu and Vlad Avrigeanu
Institute for Nuclear Physics and Engineering,
P.O.Box MG-6, R-76900, Bucharest-Magurele,
ROMANIA

The proton emission data for the stable titanium isotopes in the energy range from threshold to 20 MeV have been consistently described through geometry-dependent hybrid (GDH) and Hauser-Feshbach model calculations. The single-particle level density used in the preequilibrium emission calculations has been related to the energy dependent level density parameter of the Hauser-Feshbach model, resulting in lower preequilibrium emission fractions. The isotope effect of the (n,p) reaction cross sections has been analysed in the frame of both reaction mechanisms.

1. INTRODUCTION

A modern trend of nuclear model calculations is the use of consistent sets of input parameters, determined or validated by means of various independent types of experimental data, in conjunction with developed computer codes. The unitary account of a whole body of related data for an isotope chain as well as the unitary use of the common parameters of the preequilibrium and equilibrium processes provide more confidence in the calculated results. Therefore, the present analysis involves all the proton emission data for the $^{46-50}\text{Ti}$ isotopes, performed by means of the Hauser-Feshbach code STAPRE¹⁾ including the GDH model HYBRID subroutine²⁾.

2. PREEQUILIBRIUM EMISSION

Taking advantage of the realistic³⁾ level density parameter $a(E)$ assumed in the Hauser-Feshbach calculations, the single-particle level density $g = (6/\pi^2) \cdot \underline{a}$ has been used in the GDH model. As a result of the present approach⁴⁾ the necessary consistency of the nuclear level density and the equivalent particle-hole state density has been achieved. However, the main consequence is the decrease of the

preequilibrium emission fractions $f_n = \sigma_n^{\text{PE}} / \sigma_R$ and $f_p = \sigma_p^{\text{PE}} / \sigma_R$, given as functions of the composite system excitation energy in Fig.1 (the dashed lines correspond to the constant $g=A/20$). At the same composite excitation energy of the nucleon preequilibrium emission fractions are closely

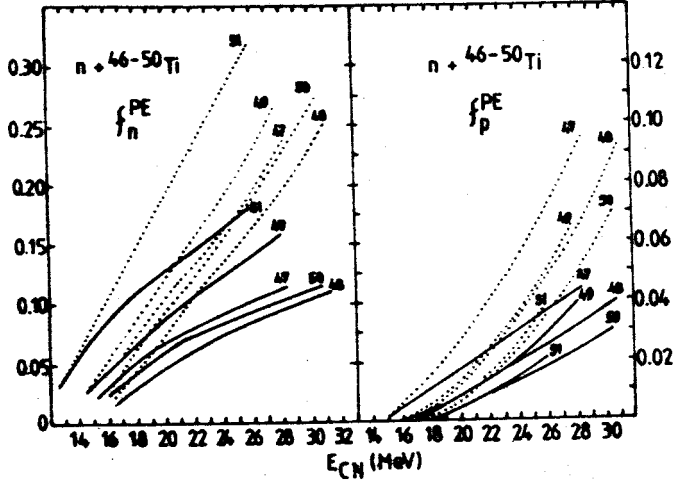


Fig.1.

related to the smallness of the nucleon binding energies S (fig.2a). The asymmetry parameter $(N-Z)/A$ dependence of the last ones gives the neutron excess dependence of f_X , too.

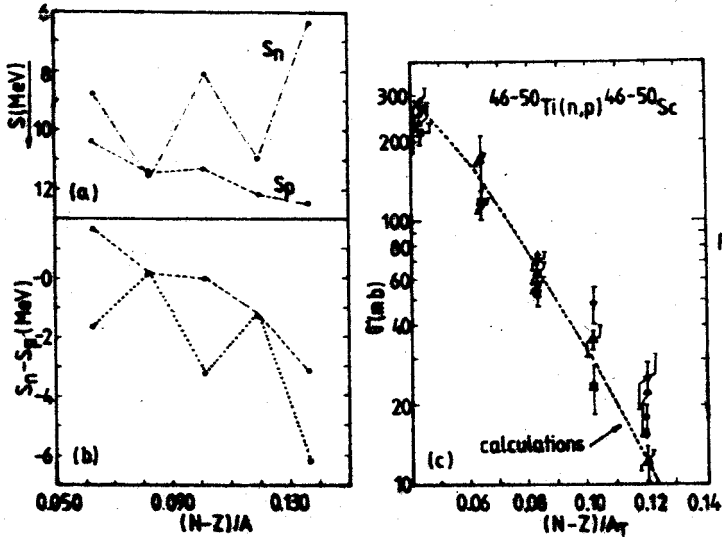


Fig.2.

3. THE ISOTOPE EFFECT FOR TITANIUM (n,p) REACTION CROSS SECTIONS

In spite of the f_p diminishing with the increase of the asymmetry parameter, the preequilibrium contribution to the (n,p) reaction cross section increases steadily (fig.3 for the stable Ti isotope extremes). The faster decrease of the compound cross sections seems to be due to

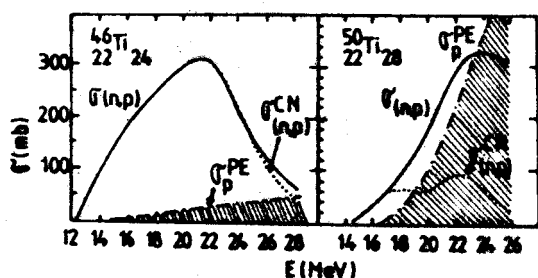


Fig.3.

its most important level density dependence and the nucleon binding energy trends versus the asymmetry parameter. In fig.2b there are shown (full squares) the differences

$S_n - S_p$ between the neutron and proton binding energies for the compound nuclei $^{47-51}\text{Ti}$. Taking into account the sum of the binding energy and the pairing energy corrections, the corresponding "effective" binding energy differences (open squares) give the differences between excitation energy regions of rather equal nuclear level densities in the neutron and proton channels. The linear decrease of this effective difference versus the asymmetry parameter could be correlated to an exponential decrease of the (n,p) reaction cross sections, according to the exponential energy dependence of the level density. Although this comment is rather qualitative, it corroborates well the "effective" binding energy difference trend with the dependence of the (n,p) reaction cross sections on Ti isotopes, at 14.8 MeV, on the target asymmetry parameter (fig.2c). The last dependence, known as the isotope effect and greatly discussed by Molla and Qaim⁵⁾ and Čaplar et al.⁶⁾, has therefore to be analysed in the frame of both preequilibrium emission and compound nucleus mechanisms.

1. Stöhmaier, B. and Uhl, M., IAEA-SMR-43 (1980), p.313
2. Blann, M., COO-3494-10 (1973)
3. Ignatyuk, A.V., Smirenkin, G.N. and Tishin, A.S., Yad.Fiz. 21 255 (1975)
4. Ivaşcu, M., Avrigeanu, M. and Avrigeanu, V., NP-43-1985 (1985)
5. Molla, N.I. and Qaim, S.M., Nucl.Phys. A283, 269 (1977)
6. Čaplar, R., Udovičić, Ly., Holub, E., Počanic, D. and Cindro, N., Z.Phys. A313, 227 (1983).

PREEQUILIBRIUM γ RAYS WITH ANGULAR-MOMENTUM COUPLING

P. Obložinský

Institute of Physics, Electro-Physical Research Centre
of the Slovak Academy of Sciences, 842 28 Bratislava,
CZECHOSLOVAKIA

Spin-dependent relation is suggested for the emission rate of preequilibrium γ rays in the framework of the exciton model. The approach is illustrated on the ^{56}Fe (n, γ) spectrum at 14.6 MeV.

Angular-momentum effects are commonly neglected in the preequilibrium nuclear reaction models such as the exciton model. Preequilibrium γ ray emission, in particular, remained unsatisfactorily solved even in the non-spin formulations of the model. Recent plausible non-spin γ ray emission rate by Akkermans and Gruppelaar¹⁾ motivated us to develop fully spin-dependent relations for γ emission. Present communication briefly summarizes essential results of this development.

We consider single-particle transitions of the electric dipole ^{type} between two levels (E, J) and (U, S). The number of excitons is changed by $\Delta n = 0, -2$ due to emitted γ ray, and by $\Delta n = 0, +2$ due to its absorption. The Brink-Axel hypothesis implies for the absorption of a γ ray of energy E and multipolarity λ

$$\sigma_n^{abs}(U, S \xrightarrow{E\lambda} E, J) = \sigma_{g.s.}^{abs}(E) \frac{2J+1}{3(2S+1)} \quad (1)$$

Then, the preequilibrium γ ray emission rate with the angular-momentum coupling can be expressed as

$$W_m^S(EJ \xrightarrow{E1} uS) = \frac{E^2 \tilde{\sigma}_{a.s.}^{ab}(\epsilon)}{3x^2 \hbar^3 c^2} \frac{\omega_{m-2}(u, S) b_{m-2}^{mJ} + \omega_m(u, S) b_m^{mJ}}{\omega_m(E, J)}, \quad (2)$$

where

$$b_{m-2}^{mJ} = \frac{y_{m-2}^m x_{m-2}^{mJ}}{y_{m-2}^m x_{m-2}^{mJ} + y_{m-2}^m x_{m-2}^{mJ}}, \quad (3)$$

$$b_m^{mJ} = \frac{y_m^m x_m^{mJ}}{y_m^m x_m^{mJ} + y_m^{m+2} x_m^{m+2J}}$$

are the branching ratios for absorption. The y -functions refer to energy structure of the absorption

$$y^+ \equiv y_m^{m+2} = q^2 \epsilon, \quad y^0 \equiv y_m^m = q m, \quad (4)$$

while the x -functions keep all the angular-momentum dependence of the process. They can be obtained from the spin part of the $E1$ transition matrix element by summing over final levels and by averaging over initial levels. The result for $\Delta n = 0$, see fig.1, is

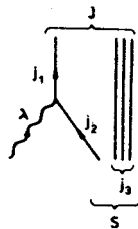


Fig.1. Diagram of the x^0 function.

$$x^0 \equiv x_m^{mJ} = \frac{\hat{\lambda} \hat{J}}{R_m(S)} \sum_{j_1 j_2 j_3} \hat{j}_1 R_1(j_1) \hat{j}_2 R_2(j_2) R_{m-1}(j_3) \left(\begin{matrix} j_2 & \lambda & j_1 \\ \frac{1}{2} & 0 & -\frac{1}{2} \end{matrix} \right)^2 \left\{ \begin{matrix} j_2 & j_3 & S \\ J & \lambda & j_1 \end{matrix} \right\}^2, \quad (5)$$

and the result for $\Delta n = +2$ analogically is

$$X^{\uparrow} \equiv X_{mS}^{m+2J} = \frac{\hat{J}}{\hat{S}} \sum_{j_1 j_2} \hat{j}_1 R_1(j_1) \hat{j}_2 R_2(j_2) \left(\begin{matrix} j_2 & j_1 & 1 \\ \frac{1}{2} & -\frac{1}{2} & 0 \end{matrix} \right)^2 \Delta(S, J). \quad (6)$$

Here, $\hat{J} = 2j+1$ and the angular-momentum distribution function reads²⁾

$$R_m(J) = \frac{2J+1}{2\sqrt{2\pi} \sigma_m^3} e^{-\frac{(J+\frac{1}{2})^2}{2\sigma_m^2}}, \quad (7)$$

where $\sigma_m^2 = m\sigma^2$. Our W_n^k readily leads to the usual equilibrium limit and it is in accord with the non-spin rate of ref.¹⁾.

The spin-dependent formulation of the exciton model is completed by the appropriate nucleon and damping emission rates. The former is obtained straightforwardly from the detailed balance, and the latter from the Golden rule as

$$W_{mJ}^{\downarrow} = \frac{2\tilde{\omega}}{\hbar} |M_m^{m+2}|^2 Y_m^{\downarrow} X_{mJ}^{\downarrow}, \quad (8)$$

where $Y_n^{\downarrow} = \frac{1}{2} g^3 E^2 / (n+1)$ and the angular-momentum term is

$$X_{mJ}^{\downarrow} = \frac{1}{R_m(J)} \sum_{j_1 j_2} R_1(j_1) \tilde{F}(Q) R_2(j_2). \quad (9)$$

The function $\tilde{F}(Q)$ is spelled out in full in ref.³⁾. The intranuclear transition matrix element $|M_m^{m+2}|^2$ can be related to the usual non-spin value $KA^{-3}E^{-1n}$ as

$$|M_m^{m+2}|^2 = \frac{m+1}{4 \langle X_{3J}^{\downarrow} \rangle} \frac{K}{A^3 E}. \quad (10)$$

As an example we studied the primary γ ray spectrum of

$^{56}\text{Fe}(n, \gamma)$ at 14.6 MeV as measured in refs.^{4,5}. All parameters used in calculations were standard. Thus, $g=A/13$, $G^2 = 0.28 A^{2/3}$, $K = 190 \text{ MeV}^3$, the GDR γ ray strength function was taken with $E_R = 18.3 \text{ MeV}$ and $\Gamma_R = 5 \text{ MeV}$. Spin-dependent γ ray widths, $\Gamma_{\lambda J}^{\gamma} = \hbar \sum_{\gamma} W_{\gamma}^{\gamma} dE$, are compared with the non-spin values in fig.2. Then, the spectra are shown in fig.3. The impact of the angular-momentum coupling on the shape of the spectrum is rather small. The non-spin result is somewhat higher than the spin one basically due to the $n=1$ term since $\langle X_{3J} \rangle = 0.0208$ rather than $\langle X_{1J} \rangle = 0.0163$ was applied in eq.(10). Importance of the lowest n terms is essential in the preequilibrium γ ray emission involving presumably low J and $\Delta n = 0$ transitions.

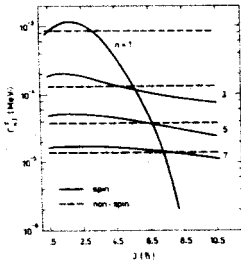


Fig.2. $\Gamma_{\lambda J}^{\gamma}$ as a function of angular momentum.

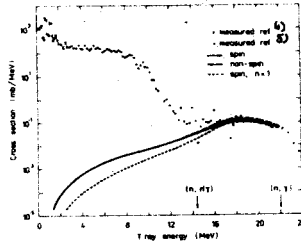


Fig.3. Calculated (n, γ) spectra are compared with measured cross sections.

References

1. Akkermans J.M. and Gruppelaar H., Phys. Lett. 157B, 95(1985)
2. Feshbach H. et al., Ann. Phys. (NY) 125, 429(1980)
3. Herman M. et al., Nucl. Phys. A430, 69(1984)
4. Hlaváč S. and Obložinský P., Report INDC(CSR)-5/GI, IAEA, Vienna, 1983
5. Budnar M. et al., Report INDC(YUG)-6/L, IAEA, Vienna, 1979

COUPLED-CHANNEL ANALYSIS OF NEUTRON SCATTERING

FROM ^{12}C BETWEEN 9 and 15 MeV

L. F. Hansen

Lawrence Livermore National Laboratory, Livermore, CA 94550, U.S.A.

A. S. Meigooni

Therapeutic Radiology Dept., Yale University, New Haven, CT 06510,
U.S.A.

A deformed and energy dependent phenomenological optical model potential and coupled-channel formalism for deformed nuclei have been used in the analysis of elastic and inelastic ($Q = -4.439$ MeV) scattering, and analyzing power for neutrons scattered from ^{12}C in the energy range of 9 to 15 MeV.

Measurements¹⁻³ of the angular distributions for the (n, n_0) and $(n, n')_{4.44}$ secondary neutrons and for the analyzing power $A(\theta)$ of polarized neutrons scattered from these two levels were analyzed using deformed optical model potentials (DOMP). The coupled-channel (CC) calculations were done with the code ECIS using deformed central and spin orbit potentials. The main objectives of these calculations were, 1) to find an energy dependent DOMP (EDDOMP) that will give reasonable fits to the scattering and analyzing power data and 2) to investigate the importance of a rotation-vibration interaction at these energies by coupling the levels of the ground state (GS) rotational band $K = 0^+$ to those of the first octupole band $K = 3^-$.

There are two earlier CC analyses^{2,3} of some of the data included in this work but both have their limitations. In Ref. 3 the authors did not obtain an EDDOMP from the analysis of their polarization measurements and scattering data⁴. Furthermore, the latter has recently been reanalyzed⁵ and although systematic differences with the earlier data have not been found, there are changes in the values of the cross sections. In Ref. 2 the prescribed EDDOMP (set A & B) were obtained from a CC analysis that only included elastic and inelastic neutron scattering data. As a result these DOMP give poor fits to the analyzing power data of Ref. 3.

Starting from the DOMP given² by set B, a search procedure was done to optimize the fits to both the scattering and analyzing power angular distributions from the GS and 4.44 MeV level. The CC calculations shown in Fig. 1 include the GS(0^+), 4.439 MeV(2^+) and 14.08 MeV (4^+) levels of the GS band. The central potential (V_R and W_D) and the real spin orbit potential, V_{SO} , are deformed (see Table I for the values of the parameters). No improvement in the fits to the data was found by introducing an imaginary spin orbit potential

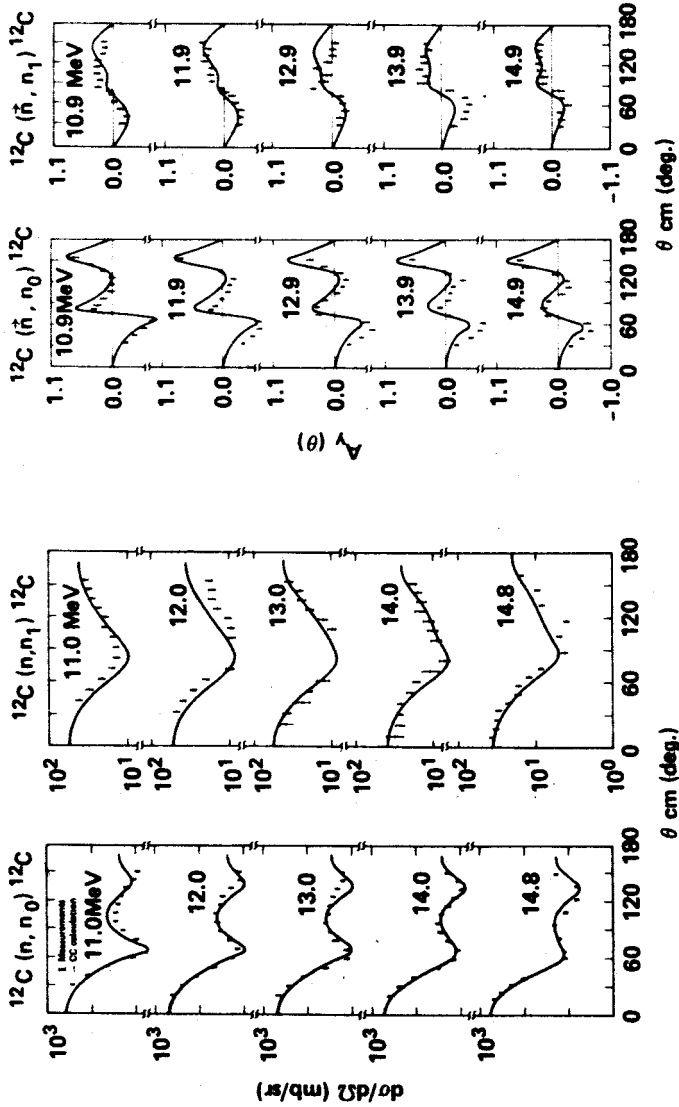


Fig. 1. Coupled-channel calculations carried out with the DOMP given in Table I. Measurements of the neutron elastic and inelastic (4.44 MeV level) differential cross sections^{1,2} and respective analyzing power³. The fits to the 9 and 10 MeV data are not shown to avoid overcrowding the figures, but they are comparable in quality to the ones seen here.

TABLE I. Parameters for the DOMP used in the present calculations.

$V_R = 59.80 - 0.34E$ MeV	$r_V = 1.06$ fm	$a_R = 0.540$ fm
$W_V = 0$		
$W_D = 0.66E - 4.60$ MeV	$r_W = 1.25$ fm	$a_W = 0.280$ fm
$V_{SO} = 9.67 - 0.38E$ MeV	$r_{SO} = 0.86$ fm	$a_{SO} = 0.360$ fm
$\beta_2 = 0.640$	$\beta_4 = 0.200$	$\beta_3 = 0.227$

A second calculation was done where the GS and 4.44 levels were coupled to each other and to the 9.64 MeV 3^- level (rotational-vibrational model). Starting from the DOMP given in Table I, the interband and intraband transitions potentials were calculated using the formalism derived by Meigooni *et al.*⁶. In these calculations only the central potential is deformed and a real, spherical V_{SO} is included only in the calculation of the intraband potentials (codes OCTOVIB and EXTERNAL written by A. S. Meigooni were used to calculate the potentials to be input into ECIS). The CC results showed that if only the 0^+-3^- interband coupling was included, the agreement with the data was comparable to that shown in Fig. 1, although systematically worse. The fits were similar to those obtained with the $0^+-2^+-4^+$ coupling with a spherical V_{SO} . However when the 2^+-3^- ($\lambda = 3, 5$) couplings were also included the fits to the 2^+ inelastic scattering and $A(\theta)_V$ data deteriorated completely (the limited space of this presentation does not allow to show the results of these calculations). In order to reproduce the measurements the interband potential for the 2^+-3^- coupling has to be changed drastically from the values predicted⁶ by the calculations. Since these changes affected also the values of the cross sections for the 3^- level and they could not be tested due to the lack of data for this level in this energy region, it was felt that we did not have enough information to have a meaningful interband calculation.

In summary, neutron scattering data from ^{12}C in the 9-15 MeV energy range is well reproduced by CC calculations where the target is described by a pure rotational model. The complexities of the calculations required to couple the GS rotational band to the octupole band were not justified by the quality of the fits to the data. At this stage it is not clear if the rotational-vibrational description is needed at these energies, or if the approximations in the calculations of the potentials must be revised before proceeding any further.

REFERENCES

1. G. Haouat *et al.*, Nucl. Sci. Eng. **65**, 331 (1978).
2. L. F. Hansen *et al.*, AIP Conf. Proc. **124**, 314, (1984).
3. E. Woye *et al.*, Nucl. Phys. **A394**, 134 (1983).
4. D. W. Glasgow *et al.*, Nucl. Sci. Eng. **61**, 521 (1976).
5. C. Gould (private communication) (1986).
6. A. S. Meigooni *et al.*, Nucl. Phys. **A445**, 304 (1985).

FAST POLARIZED NEUTRON SCATTERING ON ^{40}Ca , ^{40}Ar , ^{89}Y AND ^{163}Tm FOR COUPLED-CHANNELS OPTICAL MODEL ANALYSIS

J. W. Hammer, W. Grum, K.-W. Hoffmann, H. Postner,
G. Schleußner and G. Schreder

(Institut für Strahlenphysik, Universität Stuttgart)

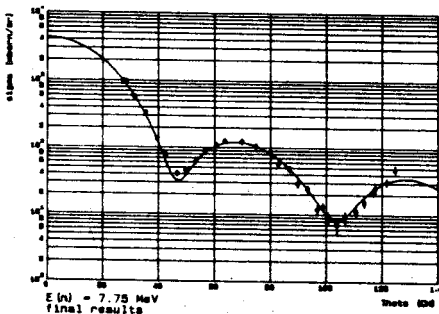
P. A. Owono

(Departement de Physique, Université de Yaounde, Kamerun)

The phenomenological optical model is a mighty tool to work out systematic properties of the nuclei. Additionally it reduces the large variety of experimental data to some significant parameters, which can serve as the data base for theoretical nuclear models. The investigation of a large number of nuclides is necessary to get a proper insight into the behaviour of nuclear matter. At the Stuttgart 'SCORPION' facility angular distributions of the neutron differential cross section and the analysing power of several nuclei at the typical energy of 7.75 MeV have been measured during the past few years. Yttrium is a typical candidate for supporting the convenience of the simple spherical optical model (OM). A potential without an imaginary volume term was used:

$$U(r) = -V_R f(r, R_V, a_V) + 4ia_S W \frac{d}{dr} f(r, R_S, a_S) + \lambda \frac{1}{2} 2V_{so} \frac{1}{r} \frac{d}{dr} f(r, R_{so}, a_{so}) \vec{I} \cdot \vec{S},$$

Diff. Cross-Section of Yttrium



Analysing Power of Yttrium

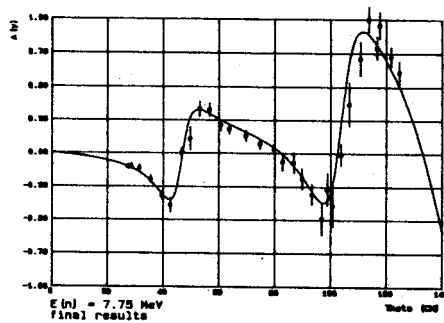


Fig. 1: Experimental data for yttrium together with the OM-results.

where f is the usual Woods-Saxon form factor. The experimental data and the OM-results are shown in Fig. 1, the parameter set is given in Table 1. The strongly deformed thulium has been approached through the

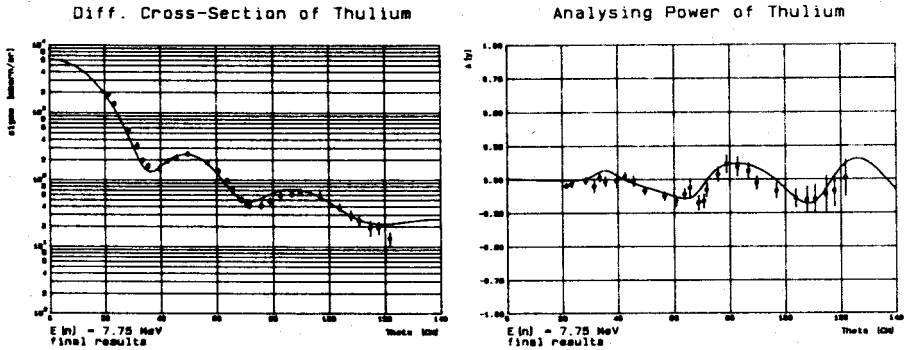


Fig. 2: Experimental data for thulium together with the CC-results.

Table 1: Parameter sets for yttrium, thulium, calcium and argon at $E_n = 7.75$ MeV.

parameter	Y	Tm	Ca	Ar
V_R (MeV)	47.33	44.93	51.31	52.61
r_V (fm)	1.24	1.27	1.22	1.17
a_V (fm)	0.62	0.63	0.69	0.73
W_I (MeV)	5.75	7.18	3.72	2.19
r_W (fm)	1.26	1.27	1.22	1.26
a_W (fm)	0.58	0.48	0.58	0.58
V_{so} (MeV)	7.845	6.0	5.87	6.1
r_{so} (fm)	1.147	1.07	0.81	1.02
a_{so} (fm)	0.488	0.63	0.68	0.58
B_2	-	+0.31	0.18	0.30
B_3	-	-	0.49	-
B_4	-	+0.01	-	-

rotational model in terms of the Coupled-Channels formalism (CC). The deformation is introduced by an expansion of the radius parameters in Spherical Harmonics. The fit shown in Fig. 2 has been achieved by superposing the angular distributions of the experimentally unresolved inelastic states of the ground state band. The parameters are given in Table 1. The analysis of the calcium data led to the investigation of the neighbouring nucleus argon. For this measure-

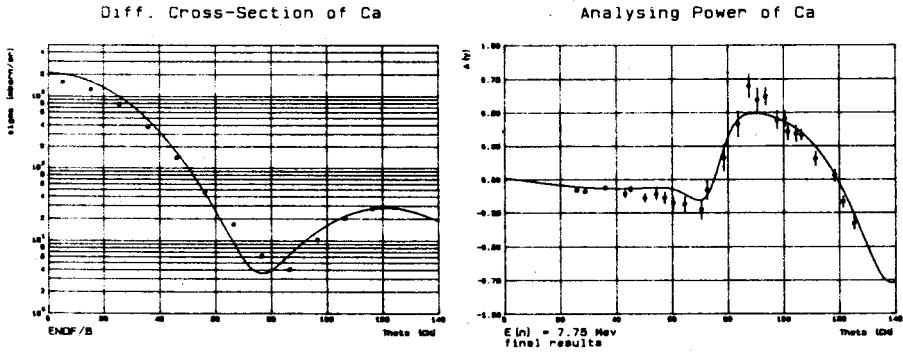


Fig. 3: Experimental data for calcium together with the CC-results.

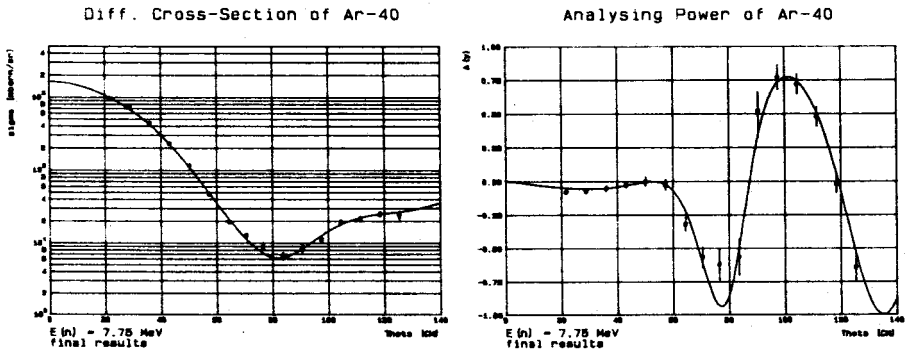


Fig. 4: Experimental data for argon together with the CC-results.

ment a cryogenic liquid sample in a thin-walled Dewar was used. Both nuclei have been studied with a vibrational Coupled-Channels approach. The analysis of polarized data results in a great reduction of the freedom of the model parameters. The evaluation of the calcium differential cross section is in progress, therefore the CC-results for a model fit of the analysing power data is compared with the corresponding ENDF/B values. The angular distributions are shown in Figs. 3 and 4, the parameters are given in Table 1. The strong octupole coupling in calcium will be subject to further investigations.

MICROSCOPIC AND CONVENTIONAL OPTICAL MODEL ANALYSIS OF
21.6 MeV NEUTRON ELASTIC SCATTERING FROM Mg TO Bi

N. Olsson, B. Trostell, E. Ramström and B. Holmqvist

The Studsvik Science Research Laboratory, S-61182 Nyköping, Sweden

F.S. Dietrich

Lawrence Livermore National Laboratory, Livermore, CA 94550, USA

Calculations of neutron elastic scattering cross sections at 21.6 MeV over a wide mass range have been performed using a phenomenological optical model as well as different microscopic folding models. The results are compared with recently measured Studsvik data.

Fast neutron elastic scattering angular distributions have been measured at 21.6 MeV with an energy resolution of 0.5 MeV for the natural elements Mg, Al, Si, S, Ca, Cr, Fe, Co, Ni, Y, Ce, Pb_r (radio-genic lead) and Bi by using the Studsvik pulsed beam time-of-flight facility¹⁾.

The experimental data have been analysed in terms of a standard phenomenological spherical optical model. The potential depths and geometry parameters of the real and imaginary central potential parts were least squares fitted to each angular distribution, while the spin-orbit potential part was kept constant. The results of these analyses are shown in fig. 1, where they are compared with the experimental data. As shown in the figure the agreement is in general very good.

Microscopic folding models for the optical potential according to Jeukenne, Lejeune and Mahaux (JLM)²⁾, Brieda and Rook³⁾, and Yamaguchi et al.⁴⁾ have been tested by calculating angular distributions for all the elements studied. In these calculations the central and spin-orbit parts of the optical potential were generated by folding ground-state nucleon densities with energy- and density-dependent effective interactions as described in refs. ^{5,6,7)}. A 'midpoint' local density approximation⁵⁾ was used. The spin-orbit potential was calculated with interactions taken from the work of Bertsch et al.⁸⁾.

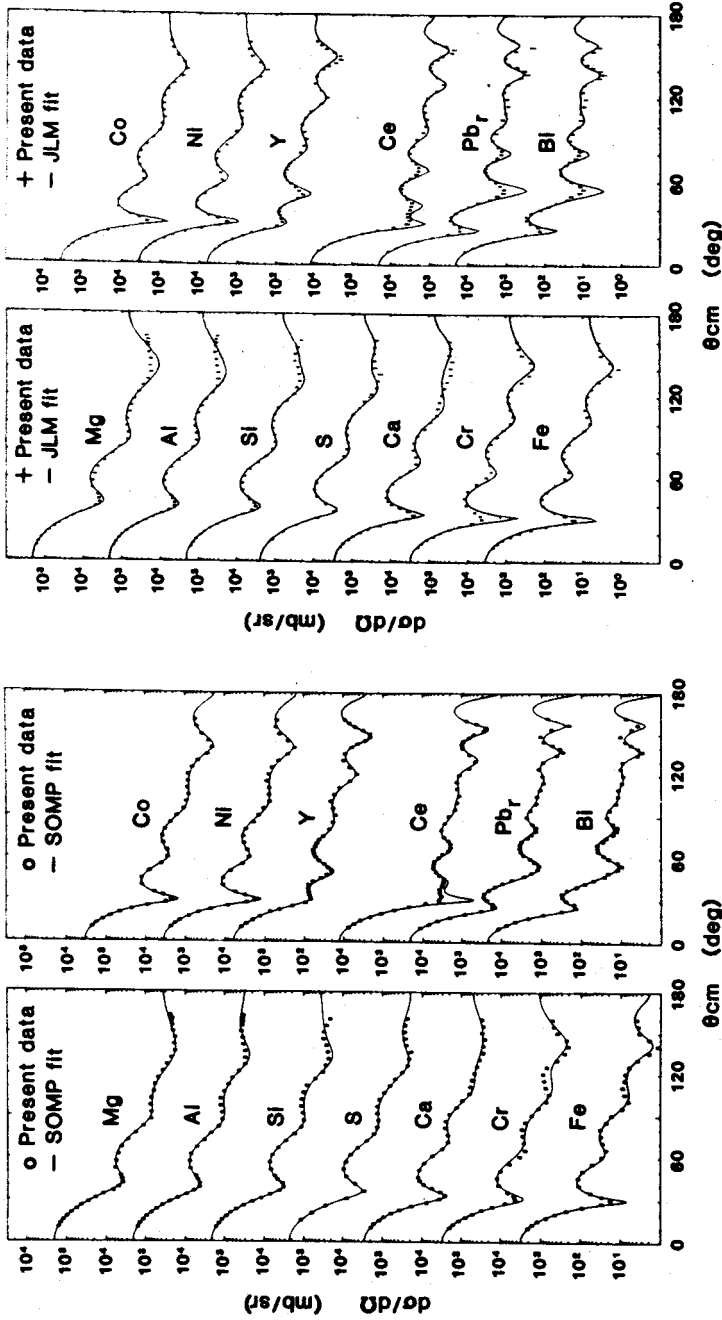


Fig. 1. Corrected differential neutron elastic scattering cross sections at 21.6 MeV for Mg to Bi in the centre of mass system plotted versus the scattering angle. The solid curves are the results of individual best fit optical model calculations.

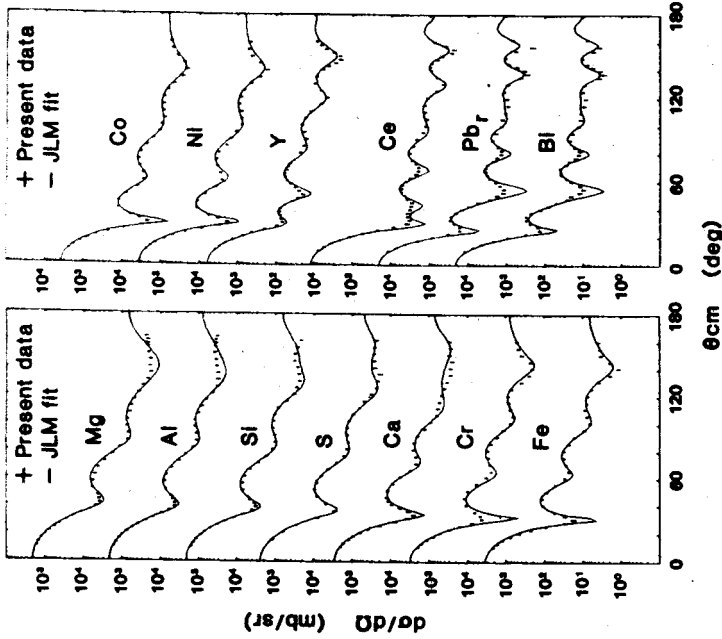


Fig. 2. Corrected differential neutron elastic scattering cross sections at 21.6 MeV for Mg to Bi in the centre of mass system plotted versus the scattering angle. The solid curves are the results of JLM microscopic model calculations.

The results of the calculations with the different microscopic models have been intercompared by studying introduced normalizing constants λ_v and λ_w of the real and imaginary central potential parts, respectively. These constants were determined from least squares fits to the experimental data. Best description of the experimental data is obtained with the JLM potential, where λ_v and λ_w seem to be within 5 % and 15 % of unity, respectively, for all the elements studied. Angular distributions calculated with this model are shown in fig. 2 together with the experimental data. The agreement is good except at the minima in the $20^\circ - 60^\circ$ range in medium to heavy nuclei, where the model seems to underpredict the cross sections. The results of the calculations with the Yamaguchi potential are slightly worse, whereas the Brieva-Rook model yields poorer agreement. For these interactions the real normalizing constants are within 10 % of unity, while the imaginary potential part is underpredicted by 35 % in the Brieva-Rook model and overpredicted by a similar amount in the Yamaguchi model.

Furthermore, as can be seen when comparing figs. 1 and 2, the angular distributions calculated with the JLM model describe the data nearly as well as the individual best fits calculated with the phenomenological model.

Volume integrals of the real and imaginary potential parts calculated with the JLM model are in good agreement with those of the phenomenological analyses. The corresponding values obtained with the models of Brieva-Rook and Yamaguchi et al. show reasonable agreement.

REFERENCES

1. N. Olsson and B. Trostell, Nucl. Instr. Meth. (to be published)
2. J.-P. Jeukenne et al., Phys. Rev. C15(1977)10, C16(1977)80.
3. F.A. Brieva and J.R. Rook, Nucl. Phys. A291(1977)299,317, Yukawa parameterization of interaction by H.V. von Geramb.
4. N. Yamaguchi et al., Prog. Theor. Phys. 70(1983)459.
5. S. Mellema et al., Phys. Rev. C28(1983)2267.
6. F.S. Dietrich et al., Phys. Rev. Lett. 51(1983)1629.
7. L.F. Hansen et al., Phys. Rev. C31(1985)111.
8. G. Bertsch et al., Nucl. Phys. A284(1977)399.

PHENOMENOLOGY OF ANGULAR DISTRIBUTIONS OF
FAST NEUTRON-INDUCED PARTICLE EMISSION
CROSS SECTIONS

D Hermsdorf, H Kalka, D Seeliger, U Steininger
Technische Universität, Sektion Physik
Mommsenstr. 13, 8027 Dresden
GDR

Experimental emission cross sections for n, p and α -particles induced by fast neutrons have been analysed systematically. In the paper it is shown that by two simple models, the GEM and the Kalbach-Mann formalism, the main features of experimentally verified angular distributions can be interpreted very well.

1. SYSTEMATICS OF EXPERIMENTAL DATA

Generally, the energy and angular dependences of fast neutron-induced particle emission cross sections (DDX) are favourably represented in terms of Legendre polynomials using reduced coefficients $a_1 = f_1/f_0$ and the normalization conditions $a_0 = 1$ and $f_0 = dG/dE'/G(E)$.

A systematical analysis of the reduced coefficients a_1 carried out by Briseno et al.¹⁾ yields following results in accordance with other investigations:

- i) independence on the target nucleus mass number A in the range $30 < A < 200$;
- ii) independence on the incidence energy in the range $5 < E < 60 \text{ MeV}^{1,2)}$ (see fig. 1 for the coefficients a_1);
- iii) independence on the kind of incidence and emitted particle (at least for neutrons and protons)^{1,2)} (see fig. 2 for the coefficient a_1).

2. THEORETICAL MODELS

At present, quite different theoretical models exist for prediction and interpretation of Legendre' moments a_1 and their dependencies on A , E and E' .

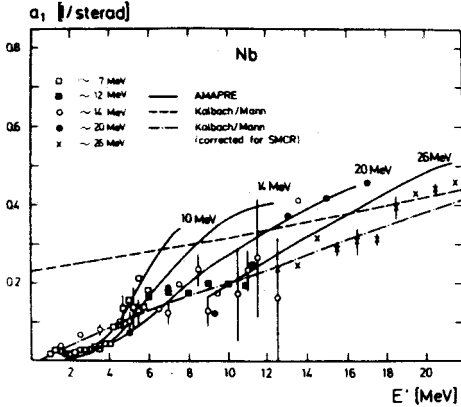


Fig. 1:

Coefficient $a_1(E')$ for $93\text{-Nb}(n,n')$ at different incidence energies. Experimental data are compared to model predictions.

At present, two simple approaches have been applied very successfully:

- i) the "Leading-Particle-Model" derived by Mantzouranis et al.³⁾. This model has been implemented into the Generalized Exciton Model (GEM)⁴⁾;
- ii) the semi-empirical formula of Kalbach and Mann (KM)²⁾ predicting the Legendre' momenta a_1 by

$$a_1 = 1/(1 + \exp(A_1(B_1 - E')) \quad (1).$$

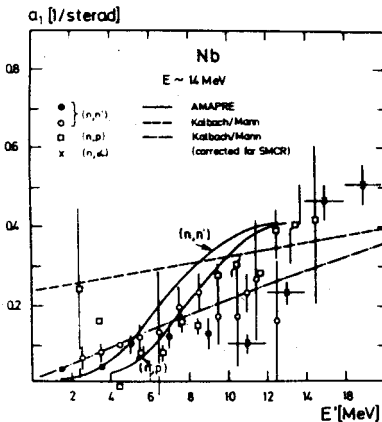


Fig. 2:

Coefficient $a_1(E')$ for $93\text{-Nb}(n,n')$, (n,p) and (n,α) at 14 MeV. Experimental data are compared to model predictions.

The parameters A_1 , B_1 have been extracted from an analysis of DDX at high energies and are therefore valid in the absence of compound reactions only. Obviously, equ. 1 also reflects the independencies concluded from the systematics of experimental data.

3. APPLICATION OF MODELS

Generally, the validity of GEM is restricted to $E > 6$ MeV roughly. Therefore, any application at 14 MeV should yield reliable results.

But, the KM formalism has to be modified to account for contributions from CR which will become the dominant reaction mechanism in the energy region $E < 20$ MeV.

This correction concerns the odd-valued coefficients only because CR results in symmetrical angular distributions by basic rules of reaction theories. In the assumption of isotropic CR all odd coefficients a_1 ($l \leq 1$) have to be reduced by a factor $r(E')$ defined as relative contributions of direct reactions (DI) to the total emission cross section. So, in this factor all informations on the nuclear structure and reaction mechanisms are included.

4. RESULTS

Calculations in the frame of GEM for (n, n') and (n, p) have been done using the code AMAPRE⁵⁾ by fitting only one parameter (the transition rate λ_0^+) to achieve best agreement with experimental data.

Results obtained for $^{93}\text{Nb}+n$ at different incidence energies are given in figs. 1 and 2 demonstrating the excellent description of experimental values for both (n, n') and (n, p) reaction.

Applying a reduction factor r averaged over energy and reaction type also the KM formalism is able to interpret the experimental data (compare figs. 1 and 2 also) with surprisingly accuracy.

5. REFERENCES

1. Briseno-Galvez, J., Hermsdorf, D., Kalka, H., Report ZfK-559, 45 (1985)
2. Kalbach, C., Mann, F.M., Phys. Rev. C23, 112 (1981)
3. Mantzouranis, G. et al., Phys. Lett. 57B, 220 (1975), Z. Physik A276, 145 (1976)
4. Akkermans, J.M. et al., Phys. Rev. C22, 73 (1980)
5. Hermsdorf, D. et al., Proc. 6-th Conf. on Neutron Physics, Kiev, 1983, Vol. I, 131 (1984)



Chapter II

NUCLEAR DATA FOR BIOMEDICAL APPLICATIONS

DOSIMETRY OF FAST NEUTRONS WITH ENERGIES BELOW 20 MEV

G. Dietze

Physikalisch-Technische Bundesanstalt Braunschweig,
FEDERAL REPUBLIC OF GERMANY

Dosimetry in intense neutron fields used for radiotherapy or radiobiological research is often performed with tissue-equivalent (TE) ionization chambers, low-pressure TE proportional counters or calorimeters. Due to the difference in the atomic composition of tissue and TE plastic, if the absorbed dose in tissue is to be determined, corrections must be applied which include atomic data and kerma factor ratios and depend on the neutron energy distribution. Hence the uncertainty of absorbed dose measurements in tissue is related to the uncertainty of these data. The problems are discussed with respect to the application of atomic and nuclear data. Some results are given for neutron fields used in practice, e.g. $d + Be$ and $p + Be$.

1. INTRODUCTION

The determination of the absorbed dose in tissue is an important topic in the field of radiotherapy and radiation protection. While in radiation protection dosimetry an overall accuracy of 10 to 30 % is usually sufficient, in radiotherapy an accuracy of 2 to 5 % for the determination of the absorbed dose in tissue is desired in order to optimize the treatment of cancer.

For high-LET neutron radiation, this aim has not yet been achieved. The main reasons for this are the strong energy dependence of the neutron cross sections, the different types of secondary charged particles produced in neutron-induced nuclear reactions and the uncertainty of the atomic data required. To date, all methods for the determination of the absorbed dose from neutron radiation require additional information on the neutron spectrum if an accuracy below about 6 % is desired. In the following, the methods using a cavity

chamber or a calorimeter will be discussed, in particular with respect to the nuclear data applied.

The restriction to neutron energies below 20 MeV is not based on physical properties. Today, in neutron radiotherapy the energy range has been extended up to 80 MeV, but the mean neutron energy of such broad therapy beams is about 15 to 30 MeV. Table 1 shows that even for high energy beams the neutrons below 20 MeV significantly contribute to the absorbed dose or kerma in tissue. In addition, for the energy range up to 20 MeV, large nuclear data files like ENDF/B-V¹⁾ exist which are very helpful in calculating correction factors or estimating absorbed dose values also in materials other than standard tissue.

Table 1: Mean neutron energy \bar{E}_n and standard tissue kerma K per incident beam charge Q at a distance of 1 m from a thick Be target bombarded by protons or deuterons with energy E.

Reaction	E MeV	\bar{E}_n MeV	K/Q Gy · C ⁻¹	K($E_n < 20$ MeV)/K %
d + Be	13	4.5	99.0	100
	16	6.1	181.6	100
	33	12.9	1605	76
	50	19.7	5605	56
	23	5.1	109	90
p + Be	41	14.6	430	55
	41, filtered	19.5	210	43
	60	26.0	680	40

2. ABSORBED DOSE DETERMINATION

The neutron absorbed dose in tissue is mostly measured using techniques similar to those used in photon dosimetry either with instruments based on the cavity chamber principle or calorimetric methods²⁾.

2.1 Cavity Chamber

Cavity chambers are either ionization chambers or low-pressure proportional counters of tissue-equivalent (TE) material, chiefly A150 plastic³⁾, with tissue-equivalent gas in the cavity, often methane-based TE gas or Sirdoc gas⁴⁾, where the wall thickness is chosen to

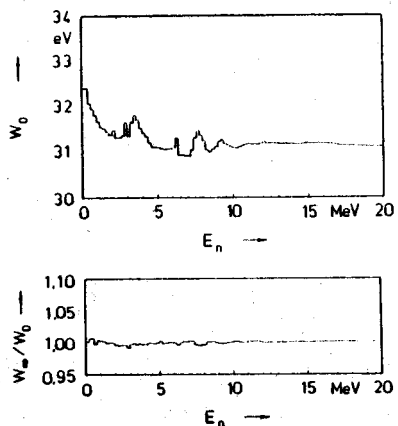
achieve secondary charged particle equilibrium within the small cavity of the chamber. The measured quantity is the charge Q produced in the cavity through ionization by those secondary charged particles passing, entering or starting within the gas cavity. If a photon contribution is ignored, the determination of the absorbed dose in tissue (t), which for neutrons is almost equal to the kerma, can be described by the expression:

$$D_t = \frac{K_t}{K_m} \cdot r_{m,g} \cdot \frac{W_N}{e} \cdot \frac{Q}{M_g} \quad (1)$$

M_g is the mass of the gas in the cavity which is usually determined by indirect methods, e.g. by an additional calibration in a well-known photon field. Due to the quality of modern electrometers or amplifiers, Q can be determined with an uncertainty smaller than 1 % (1 standard deviation) and therefore the experimental uncertainty of Q/M_g may be estimated to be about 2 %, if saturation and polarity effects are corrected. The main contribution to the overall uncertainty of D_t comes from the three correction factors in eq. (1).

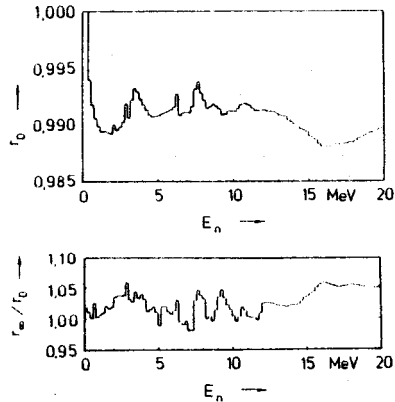
W_N is the mean energy needed to create an ion pair in the gas averaged over all secondary charged particles in the gas contributing to the charge Q and e is the electron charge. Siebert and Coyne⁵⁾ calculated W_N for a TE chamber of an infinitesimal and an infinite cavity size for monoenergetic neutrons from thermal up to 20 MeV (see Fig. 1).

Fig. 1: Mean energy W_0 for methane-based TE gas in a cavity of infinitesimal volume in A150 plastic and ratio of W -values of an infinitesimal chamber (W_0) and an infinite chamber (W_∞) versus neutron energy E_n (from ref. 5)



The dependence of W_N on cavity size is small ($< 1\%$), while for energies above 2 MeV the variation with energy is assumed to be about 2 - 3 %. The correction factor $r_{m,g}$ is the ratio of the absorbed dose or kerma in the chamber wall (m) to the mean specific energy released in the gas. $r_{m,g}$ varies with the neutron energy and the cavity size (see Fig. 2).

Fig. 2: Conversion factor r_o for an infinitesimal cavity and ratio of conversion factors for infinitesimal (r_o) and infinite (r_∞) cavities versus neutron energy E_n (from ref. 5)



For an infinitesimal chamber size $r_{m,g}$ is equal to the stopping power ratio S_g/S_m which has been recently calculated by Makarewicz et al.⁶⁾ again for a methane-based TE gas and A150 plastic. Their results deviate from data published by the ICRU⁷⁾ in 1983 by 2 - 3 % for neutron energies above 1 MeV and from earlier data of Bichsel and Rubach⁸⁾. While for E_n above 2 MeV the ratio S_g/S_m shows a small variation with energy, the dependence of $r_{m,g}$ on cavity size remains strong⁵⁾. Hence for high neutron energies an uncertainty of about 4 % may be a realistic estimate, but it increases for low energies. W_N and $r_{m,g}$ depend mainly on atomic data and only indirectly via the charged particle spectra on neutron cross sections. The third correction factor in Eq. 1 transfers the absorbed dose in the wall material to the absorbed dose in tissue and this factor is usually approximated by the kerma ratio K_t/K_m , which to date contributes strongly to the uncertainty of this method, in particular for neutron energies above 10 MeV. Details will be discussed in section 3. In Table 2 the achieved and desired uncertainties typical of this type of measurement are presented. However, an additional uncertainty appears

Table 2: Uncertainties (1 s.d.) corresponding to the measurement of neutron absorbed dose in tissue by a cavity chamber

Uncertainty	Q	M _g	W	r _{m,g}	K _t /K _m	total
typical	1 %	2 %	2-3 %	3-4 %	3-10 %	5-12 %
desired	0.5 %	1 %	1 %	2 %	2 %	3.3 %

if the neutron spectrum at the position of interest is not well known. Also a photon absorbed dose component of the field requires the use of a second neutron insensitive detector if an ionization chamber is applied. However, with a single tissue-equivalent proportional counter of the Rossi type⁹⁾ the photon and neutron dose components can be determined immediately.

2.3 Calorimeters

In photon dosimetry, calorimeters are often used for the precise measurement of absorbed dose¹⁰⁾. In neutron dosimetry calorimeters made of A150 plastic¹¹⁾ or using water¹²⁾ have been developed, but to date, the application is limited to intense neutron fields with a dose rate of at least 0.2 Gy min⁻¹.

When a temperature rise ΔT is measured in a material m with the specific heat c_m , the absorbed dose in tissue at the calorimeter position can be determined by

$$D_t = \frac{K_t}{K_m} \cdot \frac{1}{r} \cdot c_m \cdot \Delta T \quad (2)$$

The correction factor r corresponds to the heat defect due to a loss of imparted energy by endothermic radio-chemical reactions or the trapping of nuclei into interstitial sites of the material. This factor can be positive or negative within some percent and contributes significantly to the uncertainty of this method. Nevertheless, the main contribution comes from the kerma ratio K_t/K_m , as in the method discussed before. This favours the use of a water calorimeter, as will be shown in section 3. In principle, a calorimeter always

measures the total absorbed dose. Hence, for the determination of the neutron absorbed dose, a two detector technique with an additional neutron insensitive chamber must be applied.

3. KERMA RATIO

The determination of the neutron absorbed dose in tissue in fields with a broad energy distribution requires an energy averaging of the correction factors.

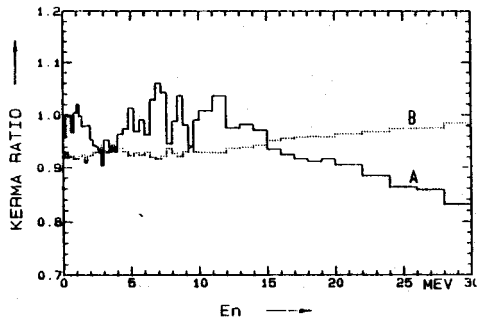
$$D_t = \frac{Q}{M_g} \cdot \frac{1}{K_m} \cdot \int_0^{E_{\max}} \left(\frac{K_t}{K_m} \right)_E \cdot r_{m,g}(E) \cdot \frac{W_N(E)}{e} \cdot K_{E,m}(E) dE \quad (3a)$$

$K_{E,m}(E)$ is the spectral kerma in the wall material (m) which is equal to $k_m(E) \cdot \phi_E(E)$, where k_m is the kerma factor and ϕ_E the neutron spectral fluence. Eq. (3a) can be written as

$$D_t = \frac{Q}{M_g} \int_0^{E_{\max}} k_t(E) \cdot \phi_E(E) \cdot r_{m,g}(E) \cdot \frac{W_n(E)}{e} dE / \int_0^{E_{\max}} k_m(E) \cdot \phi_E dE \quad (3b)$$

This expression shows that not only the kerma ratios but also the kerma factor values are of importance in order to accurately determine the neutron absorbed dose in tissue.

Fig. 3: Kerma ratio of ICRU muscle tissue to A150 plastic (A) and water (B) versus neutron energy



In Fig. 3 the kerma ratios of ICRU muscle tissue to A150 plastic

and to water (s. Table 2) are presented which were obtained from the kerma factor data published by Caswell and Coyne¹³⁾. The data below 20 MeV are calculated using neutron cross section data from the ENDF/B-V nuclear data file which are mainly based on the evaluation of experimental data, while the kerma factors above 20 MeV were estimated from smooth interpolations between the small amount of existing data and some additional theoretical approaches. Up to 12 MeV the ratio K_{TE}/K_{A150} oscillates around a mean value of about 0.98 to 1.0. For higher neutron energies this ratio decreases down to about 0.83 at 30 MeV. Hence, in a neutron field with a broad energy distribution, e.g. from Be + d, the mean kerma ratio may not strongly depend on the details of the energy distribution and the mean neutron energy if this energy is far below 10 MeV. For such neutron fields with mean energies above 12 MeV the energy dependence of the kerma ratio obviously becomes more important.

The tissue to water kerma ratio is much more stable and shows only an increase of about 6 % between 5 and 30 MeV. Nevertheless, this situation demonstrates that a discussion of the uncertainty in measurements of the absorbed dose must consider both the uncertainty of kerma factor values and the uncertainty due to incomplete knowledge of the neutron spectrum at the point of interest. Both aspects will be discussed in the following.

4. KERMA FACTORS

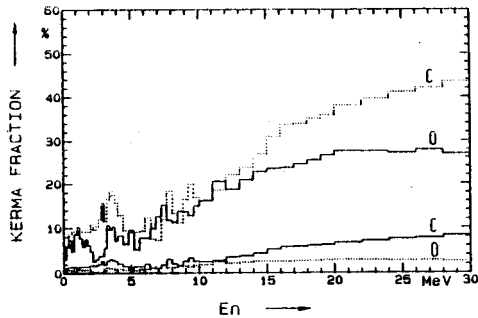
In ICRU muscle tissue, A150 plastic and water, the kerma factors of hydrogen, carbon and oxygen are most important (see Table 3), while

	Composition in percentage by mass			
	H	C	N	O
ICRU Muscle Tissue	10.2	12.3	3.5	74.0*)
A150 Plastic	10.1	77.6	3.5	8.8
H ₂ O	11.2	-	-	88.8

Table 3: Atomic composition in percentage by mass of various materials
*) other nuclides are treated as oxygen

the small amount of nitrogen is significant for low neutron energies only, due to the reaction $^{14}\text{N}(n,p)^{14}\text{C}$. The $\text{H}(n,n)\text{H}$ cross section and therefore the hydrogen kerma factor is well known with an uncertainty lower than 1 %¹⁴⁾. Hence the main uncertainty stems from carbon and oxygen. Fig. 4 shows the contribution of these nuclides to the kerma of tissue and A150 plastic which adds up to 30 - 50 % of the total kerma for $E_n > 15$ MeV.

Fig. 4: Relative kerma contribution of carbon and oxygen to the total kerma in ICRU muscle tissue (full) and A150 plastic (dotted) versus neutron energy E_n



Various methods were applied for the determination of kerma factors, e.g. for carbon, including:

1. the measurement of the absorbed dose in carbon with a cavity chamber, usually a low-pressure graphite proportional counter, together with a precise fluence determination^{15,16)}
2. the measurement of the absorbed dose in carbon with a calorimeter together with a precise fluence determination¹⁷⁾
3. the calculation of kerma factors from neutron cross sections¹³⁾

$$k_f = N_c \cdot \sum_J \bar{E}_J \cdot \sigma_J$$

where N_c is the number of nuclides per unit of volume and the sum is performed over all neutron induced reactions on the nuclide to be considered. σ_J is the partial cross section and \bar{E}_J is the mean energy transferred to charged particles via a reaction channel J

4. the calculation of kerma factors using secondary charged particle spectra¹⁸⁾ with

$$k_f = N_i \cdot \sum_i \int_0^{\infty} \frac{d\sigma_i}{dE} \cdot E \cdot dE$$

where the sum must be performed over all types of secondary charged particles produced by the neutron reactions to be considered and $d\sigma_i$ is the cross section for the emission of a charged particle of type i with an energy between E and $E + dE$.

While there are only few measurements available regarding methods (1) and (2), most of the kerma factors were determined from neutron cross sections either by using evaluated data files, e.g. ENDF/B-V or by estimating cross sections from theoretical nuclear reaction models. For light nuclei like carbon, nitrogen and oxygen the application of theoretical models for the calculation of particle emission cross sections - e.g. an evaporation model¹⁹⁾ combined with precompound corrections²⁰⁾ or the intra-nuclear cascade model²¹⁾ - are to date restricted to incident neutron energies above 15 - 20 MeV, therefore for lower energies the cross section data files evaluated from experimental data are most important.

For energies above 20 MeV the number of possible reaction channels increases more and more. With increasing energy it therefore becomes even more difficult to determine all cross sections by experiment, which emphasizes the importance of reliable theoretical models for the prediction of neutron cross sections in this energy range.

In Fig. 5 and 6 the contribution of various reaction channels to the kerma is shown for carbon and oxygen. Below 10 MeV the elastic scattering and the (n,α) reaction contribute most of the kerma, while above 14 MeV the $(n,n'\alpha)$ reaction on carbon and the $(n,n'\alpha)$ reaction on oxygen are most important. For elastic scattering the mean energy of the recoil nucleus strongly depends on the angular distribution of the scattered neutrons, and even if the differential cross section at backward angles is small compared with the cross section at 0° to the direction of the incident neutron, this angular range is most important for the kerma factor determination. This must be taken into

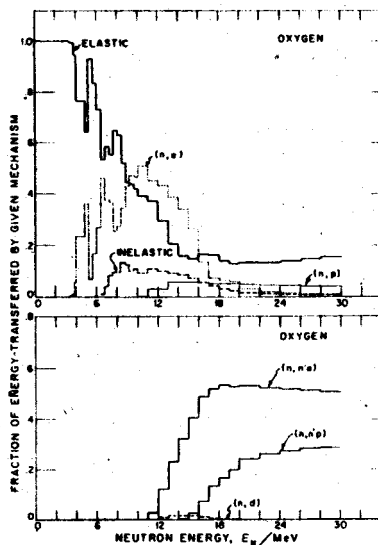
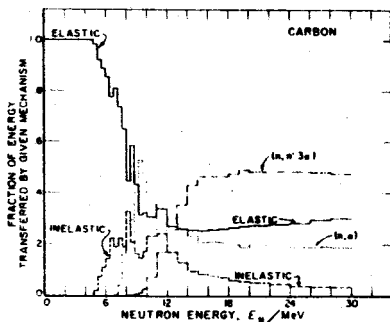


Fig. 5 and 6:
Fraction of energy transferred by
the various neutron induced reac-
tions on carbon and oxygen versus
neutron energy
(from ICRU report 26³¹⁾)

account when discussing the uncertainty of kerma factors. For example, the result of the precise differential cross section measurements on carbon for neutrons with energy of 13.75 MeV at the PTB²²⁾ differs from the ENDF/B-V data only by 2.5 % for the partial cross section, but by about 11 % for the partial kerma factor.

The mean energy transferred to secondary charged particles by the $(n,n'3\alpha)$ and $(n,n'\alpha)$ reactions is correlated to the mean energy of the emitted neutron which depends on the excitation of the various subchannels of these reactions. It is, therefore, not sufficient to determine the partial cross section of $^{12}\text{C}(n,n'3\alpha)$ or $^{16}\text{O}(n,n'\alpha)^{12}\text{C}$, and a detailed analysis of the reaction mechanism is also necessary in order to calculate kerma factors more precisely. For the $(n,n'3\alpha)$ reaction this has been done by Antelkevic et al.²³⁾ and also in recent measurements which have been discussed in detail during this conference²⁴⁾. For the $(n,n'\alpha)$ reaction on oxygen, much less information is available²⁵⁾. Because of the strong contribution of this reaction to the oxygen kerma factor, experimental investigations

would also be very useful.

Fig. 7: Kerma factor of carbon obtained from Caswell (1), Wells (2), Behrooz (3), Dimbylow (4) and Brenner (5) versus neutron energy E_n

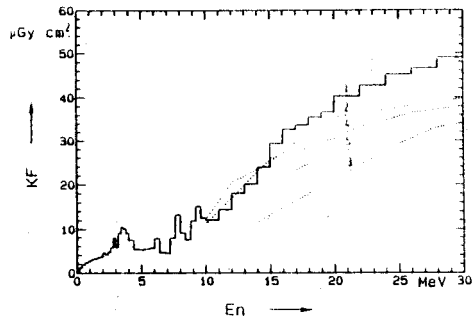
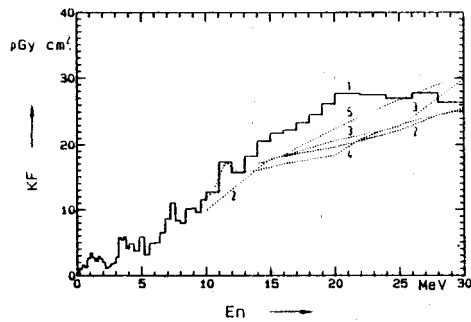


Fig. 8: Kerma factor of oxygen obtained from Caswell (1), Wells (2), Behrooz (3), Dimbylow (4) and Brenner (5) versus neutron energy E_n



In Fig. 7 and 8 the kerma factors for carbon and oxygen calculated by Caswell et al.¹³⁾ using the data file 'ENDF/B-V are compared with an analysis of Wells²⁶⁾ and Behrooz et al.²⁷⁾, with the data of Dimbylow²⁰⁾ obtained from a theoretical evaporation model including precompound contributions and with Brenner's data²¹⁾ using an intra-nuclear cascade model for the calculation of all subchannel contributions.

It seems inappropriate to estimate an uncertainty from the variation of these data, but in the following the data of Caswell, Dimbylov and Brenner will be used to study the influence of different functions on the kerma factor ratios.

5. DISCUSSION OF KERMA RATIOS

The energy dependence of the tissue to A150 plastic kerma ratio is shown in Fig. 9. The ratios calculated from theoretical models show a much smaller energy dependence than that from Caswell et al.¹³⁾ and the discrepancy increases with energy up to 14 % at 30 MeV.

Fig. 9: Kerma ratio of ICRU muscle tissue to A150 plastic versus neutron energy E_n with data from Caswell (1), Dimbylov (2) and Brenner (3)

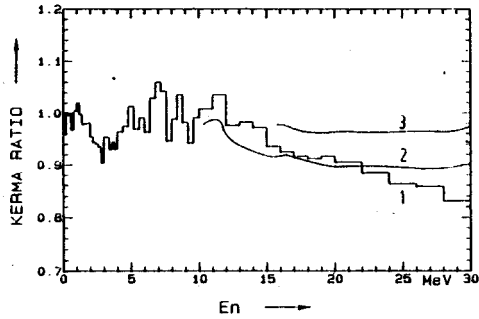
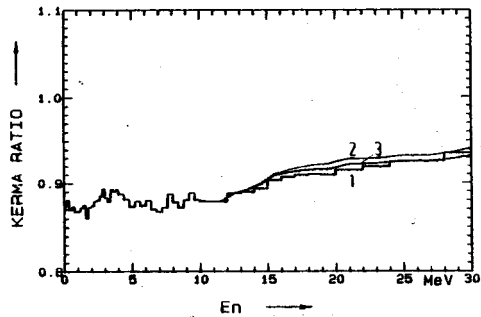


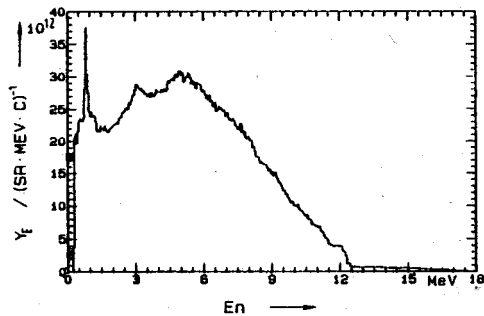
Fig. 10: Kerma ratio of ICRU muscle tissue to water versus neutron energy E_n with data from Caswell (1), Dimbylov (2) and Brenner (3)



In Fig. 10 the same relations are shown for the tissue-to-water kerma ratio. Obviously, the sensitivity to changes of the oxygen kerma factor is much lower, a fact which would favour the use of a water calorimeter. There remains a change of the ratio from about 0.88 at 10 MeV to about 0.92 at 20 MeV, hence neutron spectral information could not be totally ignored even in this case.

With the exception of 14 MeV neutron beams from $T(d,n)^4He$ all other intense fast neutron sources produce beams with a broad neutron

Fig. 11: Neutron spectral yield Y_E from $d(13\text{ MeV}) + Be$ at 0 degrees to the incident beam direction versus neutron energy E_n



spectrum. Neutron spectra from a d + Be source with a thick Be target were measured, e.g. by Meulders²⁸⁾ at various deuteron energies and more precisely by Lone et al.²⁹⁾ at 12 MeV and Brede et al.³⁰⁾ from 9.5 MeV to 13.3 MeV (see Fig. 11). The neutron spectrum shows a strong peak at about 0.8 MeV due to the reaction ${}^9\text{Be}(d,d'){}^9\text{Be}^*_{2.43} \rightarrow {}^8\text{Be} + n$, but below this energy no increase in the neutron yield has been measured by Brede contrary to the data of Lone. Mean kerma factor ratios were calculated for d (12 MeV) + Be and d (33 MeV) + Be (see Table 4) using the different kerma factors mentioned above. Due to the

Neutron Source	Ref.	Mean Kerma Factor Ratio, Data from		
		Caswell (13)	Dimbylov (20)	Brenner (21)
d (12 MeV) + Be	(29)	0.981	-	-
	(30)	0.980	0.978	0.980
d (33 MeV) + Be	(28)	0.942	0.933	0.979
p (23 MeV) + Be	(29)	0.959	0.956	0.978
filtered	-	0.966	-	-

Table 4: Mean ICRU muscle tissue to A150 plastic kerma ratios calculated for various neutron spectra and kerma factors from different authors

low mean neutron energy of about 4.2 MeV the kerma factor ratio for the neutron field from 12 MeV deuterons remains practically uninfluenced by the ratio for neutrons above 12 MeV, and therefore by the (n,n'3 α) and (n,n' α) reaction cross sections. The uncertainty for this field stems chiefly from the elastic scattering and the (n, α) reaction cross sections on carbon and oxygen. For 33 MeV deuterons the situation changes and the ratio varies by about 4 %. Nevertheless, the neutrons below 10 MeV remain important. This also holds true for the reaction p (23 MeV) + Be. Its neutron spectrum shows a strong rise at low energies and polyethylene filters are sometimes used in order to reduce this low energy contribution.

Mean ratios were calculated for the undisturbed neutron field and for a filtered beam simulated by reducing the low energy contribution. Variations of the kerma factor of up to 2.5 % were obtained with the different assumptions on kerma factors. It should be mentioned, however, that a realistic analysis of the total uncertainty of the kerma factor ratio must include the uncertainty of all cross sections to be considered.

REFERENCES

1. NNCSC, Evaluated Nuclear Data File ENDF/B-V, BNL, Upton (1979)
2. Attix, F.H., Roesch, W.C. and Tochillin, E. (Ed.), Radiation Dosimetry Vol. II, Instrumentation (1966)
3. Goodman, L.J., Phys. Med. Biol. 23, 753 (1978)
4. Sirdoc, D., Rad. Res. 43, 302 (1970)
5. Siebert, B.R.L. and Coyne, J.J., Rad. Prot. Dos. 9, 215 (1984)
6. Makarewicz, M., Burger, G. Bichsel, H., Phys. Med. Biol. 31, 281 (1986)
7. ICRU, Microdosimetry, Report 36, ICRU Publications, Bethesda (1983)
8. Bichsel, H. and Rubach, A., Phys. Med. Biol. 27, 1003 (1982)
9. Rossi, H.H. and Rosenzweig, W., Radiobiology 64, 404 (1955)
10. Doman, S.R. and Lamperti, P.J., J. of Res. NBS 78A, 595 (1974)
11. McDonald, J.C., Laughlin, J.S. and Freeman, R.E., Med. Phys. 3, 80 (1976)
12. Galloway, G. Greening, J.R. and Williams, J.R., Phys. Med. Biol. 31, 397 (1986)
13. Caswell, R.S., Coyne, J.J. and Randolph, M.L., Rad. Res. 83, 217 (1980)
14. Larson, D.C., Symp. on Neutron Cross Sections, NEANDC(US)-208/L (1980)
15. Bühler, G., Menzel, H.G., Schuhmacher, H. and Dietze, G., Rad. Prot. Dos. 13, 13 (1985)
16. Deluca, P.M., Barschall, H.H., Haight, R.C. and McDonald, J.C. Rad. Res. 100, 78 (1984)
17. McDonald, J.C., Rad. Res. (1986) submitted
18. Brady, F.P., Romero, J.L. and Subramanian, T.S., Proc. Intern. Conf. on Nuclear Data for Science and Technology, Reidel Publ. Comp., Dordrecht, p. 922 (1983)
19. Dimbylow, P.J., Phys. Med. Biol. 25, 637 (1980)
20. Dimbylow, P.J., Phys. Med. Biol. 27, 989 (1982)
21. Brenner, D.J., Phys. Med. Biol. 29, 437 (1983)
22. Böttger, R., Brede, H.J., Klein, H., Schölemann, H. and Siebert, B.R.L., Conf. on Data for Basic and Applied Science, Santa Fe (1985) to be published
23. Antolkovic, B., Slaus, J. Plenkovic, D., Macq, P. and Meulders, J.P., Nucl. Phys. A394, 87 (1983)
24. Antolkovic, B., (this proceedings)
25. Brenner, D.J., in "Nuclear and Atomic Data for Radiotherapy and Radiobiology", IAEA Panel Series (1986) (to be published)
26. Wells, A.H., Rad. Res. 80, 1 (1979)
27. Behrooz, M.A., Phys. Med. Biol. 26, 507 (1981)
28. Meulders, J.P., Leloux, P., Macq, P.C. and Pirart, C., Phys. Med. Biol. 20, 235 (1975)
29. Lone, M.A. Ferguson, A.J. and Robertson, B.C., Nucl. Instr. Meth. 189, 515 (1981)
30. Brede, H.J., Dietze, G., Schlegel-Bickmann, D. and Kujo, K., Fifth Symp. Neutron Dosimetry, Vol. II, EUR 9762, 907 (1985)
31. ICRU, Neutron Dosimetry for Biology and Medicine, Report 26, ICRU publications, Washington (1977)

PARTIAL KERMA FACTORS FOR ELASTIC AND INELASTIC NEUTRON SCATTERING
FROM TISSUE-ABUNDANT ELEMENTS*

Roger W. Finlay⁺ and M.S. Islam
Ohio University
Athens, Ohio 45701, USA

ABSTRACT

Recent measurements of elastic and inelastic neutron scattering from C, N, O and Ca at $18 < E_n < 26$ MeV are discussed. The heavy-ion-recoil contribution to kerma is obtained directly from the data at each energy. These data, together with earlier measurements of total and reaction cross sections, are used to construct model potentials that may be used to calculate various quantities of interest in neutron dosimetry over a broad energy range typically 20 - 60 MeV. The use of proton inelastic scattering data in this application is discussed.

1. INTRODUCTION

Continuing interest in the use of high energy neutrons for cancer radiotherapy has focussed attention on the generally meager data base of neutron cross sections in the energy region above 20 MeV. In a recent survey¹⁾ of this problem, an IAEA advisory group described the needed data as including all cross sections, secondary particle spectra and angular distributions from the interaction of high energy neutrons in all of the tissue-abundant elements. Since the world-wide number of facilities that are capable of providing these data is small (and decreasing !), it is clear that extensive recourse to use of theoretical models for the calculation of the quantities of interest will be required. Current efforts can best be directed toward selective measurements which test the calculational models as well as fill immediate gaps in the tabulated data files. The present contribution is made in that spirit, i.e. new measurements of dif-

ferential elastic and inelastic scattering above 18 MeV at Ohio University are combined with earlier data from many sources in order to build calculational models for nuclei of interest in neutron dosimetry.

The principal quantity of interest in neutron dosimetry is the kerma factor, and many recent attempts have been made to calculate this quantity in terms of the underlying nuclear reaction cross sections or to measure it directly with special-purpose instruments such as tissue-equivalent proportional counters. Present knowledge of the kerma factor is thought not to be adequate for the needs of clinical radiotherapy. However, enough is known to convince us that the partial kerma factors produced by recoiling target nuclei are relatively small above 20 MeV. Considerably larger contributions to kerma are associated with secondary charged-particle production $[(n, xp), (n, x\alpha)$ etc.] which are experimentally much more difficult to measure. Where the present measurements and models may prove to be of greatest value is in the related areas of transport theory (depth-dose distributions, treatment planning, shielding etc.) and also in the interpretation of ionization yield spectra in microdosimetry. The very high LET region of these spectra ($\sim 10^3$ keV/ μ) can in principle be related to the energy distribution of recoiling target nuclei measured and calculated in the present work.

2. EXPERIMENTAL DATA

The Ohio University beam swinger facility was used to measure elastic and inelastic scattering of neutrons by C, O, N and Ca at various energies between 18 and 26 MeV. The facility has been described in detail previously, and the reader is referred to ref.²⁾ for details. A portion of the present results has also been discussed in a different context in ref.³⁾.

Table 1 lists the target nuclei and incident neutron energies at which differential cross section data have been obtained for the present analysis.

Table 1
Energies of Differential Cross Section Data

^{12}C :	$E_n = 20.8, 22, 24, 26, 40^*\text{MeV}$
^{14}N :	$E_n = 20, 25\text{ MeV}$
^{16}O :	$E_n = 18, 20, 22, 24^+, 24.5, 26\text{ MeV}$
^{40}Ca :	$E_n = 19, 21.7, 25.5, 30.3^*, 40^*\text{MeV}$

* Ref.4

+ Ref.5.

In addition to these measurements, the final data set included measurements of total cross sections for C by Lisowski et al.⁶⁾, for O and Ca by Larson⁷⁾ and for N by Peterson et al.⁸⁾ and by Auman et al.⁹⁾.

Since the measured and calculated values for the partial kerma factors for C have been previously published^{10,11)}, this important case is listed in Table 1 only for completeness. Detailed discussion will not be repeated here, and the reader is directed to ref.¹¹⁾ for the final results of model calculations.

3. THE PHENOMENOLOGICAL OPTICAL POTENTIAL

The framework for the theoretical interpretation of elastic scattering - the optical potential model - is very well established for heavy nuclei and can be successfully applied to the light nuclei of interest in dosimetry provided that a large enough base of high quality data is available. In this model the interaction between the incident nucleon and a target nucleus is represented by a complex potential:

$$U(r) = -V_R(E) f(r) - i [W_V(E) - 4W_D(E) a_1 \frac{d}{dr}] g(r) + 4 \frac{V_{SO}}{r} \frac{d}{dr} f_{SO}(r) \vec{S} \cdot \vec{r}$$

Where $f(r)$ and $g(r)$ are taken to be Woods-Saxon radial form factors, e.g.

$$f_i(r) = [1 + \exp(r - R_i)/a_i]^{-1}.$$

In the present analysis of elastic scattering from O, N and Ca we assume a spherical optical model (SOM) in contrast to the earlier analysis of C for which a deformed optical potential was required and coupled-channel effects were very important^{10,11}). Inelastic scattering is then described in terms of surface vibrations about a spherical equilibrium shape (i.e. in DWBA). Strong coupling effects can still be included in this model, and they were found to be of possible importance for Ca (see section 4.2).

The optical model as given in eq.(1) requires a large number of parameters for its complete specification at each energy, so the model is only useful when the number of parameters can be reduced. In this analysis, we assume that the geometrical parameters (r_i , a_i) are not functions of energy and that the potential well depths depend smoothly on the incident energy. Historically, the light nuclei are not easily fit into this mold, and some compromises are required in the analysis. One source of difficulty is that the competing compound nucleus reaction mechanism is not entirely negligible at the lower end of the energy region of interest. A second problem - which is quite pathological for these three nuclei - is the appearance of a deep minimum in the differential elastic scattering cross section near 120° . Many explanations for this phenomenon have been proposed¹²), but the approach taken in the present work is to ignore the effect and to fit the differential cross section data only up to 110° . Detailed calculations showed that inclusion of the back-angle data resulted in a deterioration of the fits at forward angles and a generally less systematic behaviour of the potential parameters. The effect of this approximation on the accuracy of the derived partial kerma factors will be discussed in the next section.

The optical model search code OPSTAT¹³⁾ was used to calculate simultaneously the differential cross sections at each energy and the total cross section over the entire available energy range above 20 MeV. Fits to the total cross section for each element are shown in fig.1 and the resultant potential parameters are given in Table 2.

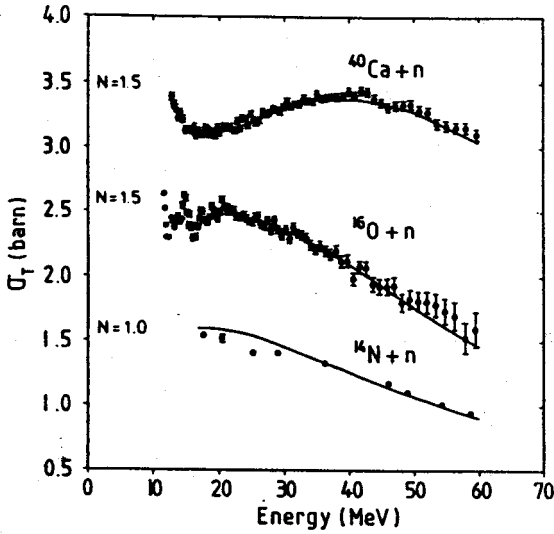


Fig.1: Spherical optical model fits to the total cross section data.

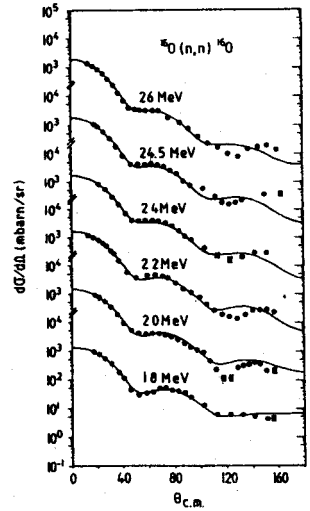


Fig.2: Spherical optical model fits to elastic scattering from Oxygen.

Table 2
Spherical Optical Model (SOM) Parameters
 $18 \leq E \leq 60$ MeV

 ^{16}O :

$$\begin{aligned}
 V_R &= 53.5 - 0.297 E \\
 W_V &= -3.5 + 0.167 E & E > 21 \text{ MeV} \\
 &= 0 & E \leq 21 \text{ MeV} \\
 W_D &= 6.5 - 0.31 (21-E) & E \leq 21 \text{ MeV} \\
 &= 10.0 - 0.166 E & E > 21 \text{ MeV} \\
 V_{\text{So}} &= 4.31 \\
 r_R &= 1.153 \quad r_I = 1.376 & r_{\text{So}} = 1.11 \\
 a_R &= 0.646 \quad a_I = 0.473 & a_{\text{So}} = 0.450
 \end{aligned}$$

 ^{40}Ca :

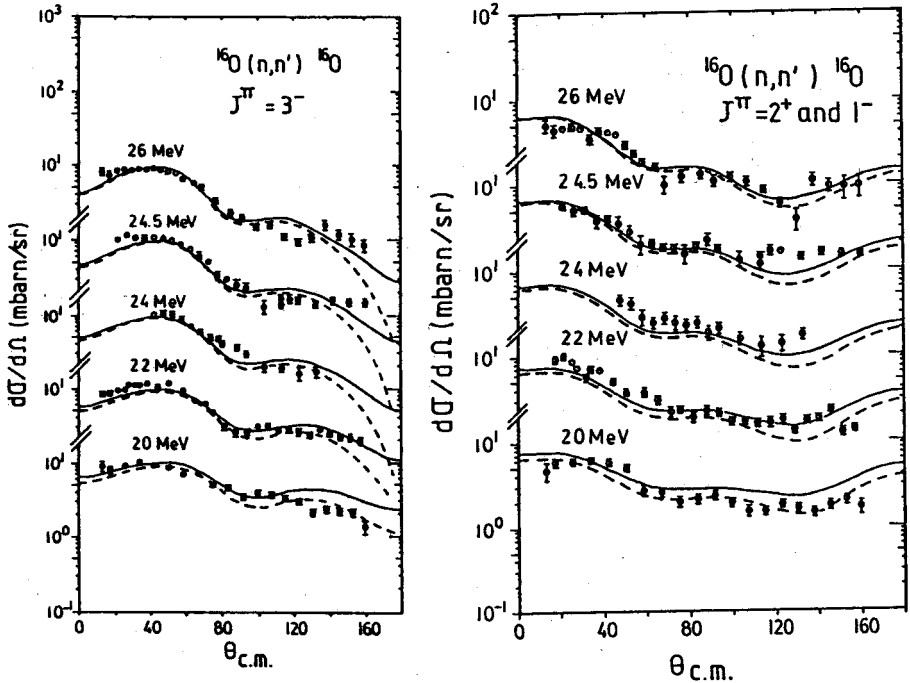
$$\begin{aligned}
 V_R &= 52.13 - 0.282 E \\
 W_V &= -4.32 + 0.216 E & E > 20 \text{ MeV} \\
 &= 0 & E \leq 20 \text{ MeV} \\
 W_D &= 7.91 & E \leq 20 \text{ MeV} \\
 &= 10.95 - 0.152 E & E > 20 \text{ MeV} \\
 V_{\text{So}} &= 6.2 \\
 r_R &= 1.198 \quad r_I = 1.325 & r_{\text{So}} = 1.010 \\
 a_R &= 0.710 \quad a_I = 0.528 & a_{\text{So}} = 0.750
 \end{aligned}$$

 ^{14}N :

$$\begin{aligned}
 V_R &= 52.4 - 0.29 E \\
 W_V &= -5.86 + 0.267 E & E > 22 \text{ MeV} \\
 &= 0 & E \leq 22 \text{ MeV} \\
 W_D &= 5.43 - 0.16 (22-E) & E \leq 22 \text{ MeV} \\
 &= 8.64 - 0.145 E & E > 22 \text{ MeV} \\
 V_{\text{So}} &= 6.0 \\
 r_R &= 1.197 \quad r_I = 1.388 & r_{\text{So}} = 1.010 \\
 a_R &= 0.593 \quad a_I = 0.449 & a_{\text{So}} = 0.500
 \end{aligned}$$

3.1 Elastic and Inelastic Scattering from Oxygen

Fits to the measured differential elastic scattering cross sections for ^{16}O are shown in fig.2. Of course, the dip in the cross section near 120° is not fitted in this approach. The same potential parameters, plus the familiar Coulomb correction term for the real part of the potential, provide a very good description of proton elastic scattering from 23 to 65 MeV (see ref.¹⁴).



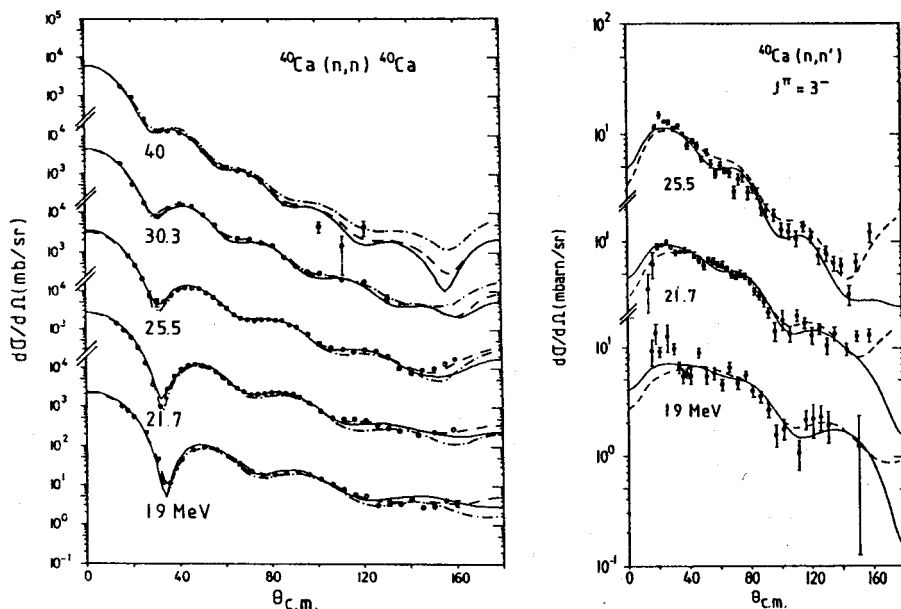
Figs.3+4: Measurements and DWBA calculations of inelastic neutron scattering to particle-stable states in ^{16}O . The solid (dashed) lines are with (without) compound nucleus contributions.

DWBA calculations of the inelastic scattering cross sections for the 3^- (6.13 MeV) state and for the unresolved 2^+ (6.92 MeV) and

1^- (7.12 MeV) doublet are shown in figs. 3 + 4. Deformation parameters for the vibrational model were held constant at $\beta_3 = 0.537$, $\beta_2 = 0.23$ and $\delta_1 = 0.062$. Full coupled channel calculations were also carried out for these transitions, but the net effects were not large, and so the simpler model is reported here.

3.2 Elastic and Inelastic Scattering from Calcium

Differential elastic scattering cross sections for Ca are shown in fig.5. The solid lines are the spherical optical model calculations performed with the potential given in Table 2. The dash-dot lines are the results of coupled-channel calculations using a potential recently given by Honoré et al.¹⁵⁾ and the dashed lines are individual best fit calculations by Alarcon¹⁶⁾ using a spherical optical model. Clearly, all three potentials do comparably well at describing the data.



Figs.5+6: Elastic and inelastic neutron scattering from Calcium.

See text for a description of the calculations.

Differential inelastic scattering cross sections for the 3^- (3.74 MeV) state in ^{40}Ca are shown for three energies in fig.6. The solid lines are the results of DWBA vibrational model calculations using the potential of Table 2 and the dashed lines are coupled-channel calculations with the potential of Honore et al.¹⁵⁾. For all calculations, the deformation parameter was $\delta_3 = 0.329$. Both types of calculation are in good qualitative agreement with the data, the DWBA calculation being somewhat better at forward angles and the coupled-channel calculation doing considerably better at the very backward angles.

3.3 Elastic scattering from N

The total data set for N is considerably smaller than for O and Ca consisting of only two differential cross section measurements and 9 total cross section values. The potential was assumed to have the same functional form as for the other two nuclei and the entire data set was used to obtain the parameters shown in Table 2. The fits are shown as solid lines in fig.1 and 7. The dashed lines in fig.7 are the

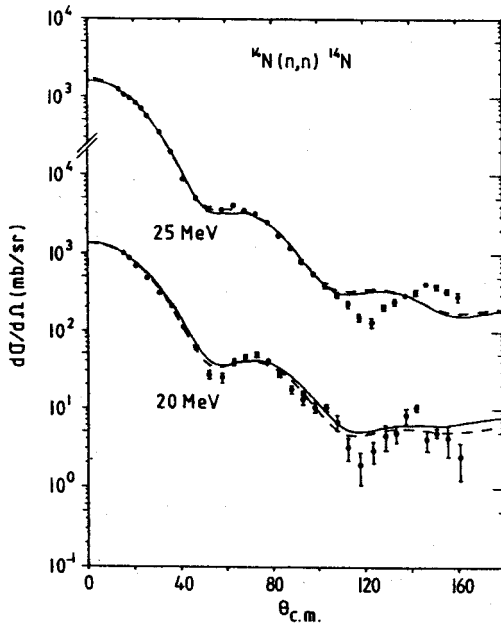


Fig.7: Elastic neutron scattering from Nitrogen. See text for a description of the calculations.

individual best fits to the data at 20 and 25 MeV at $\theta < 110^\circ$ from Petler et al.³⁾. The fits obtained in ref.³⁾ are, of course, somewhat better, but the energy dependent potential model of Table 2 lends itself to extrapolation. For nitrogen, no inelastic scattering cross sections were obtained.

4. KERMA FACTORS

The kerma K , the kerma factor k_F and the fluence ϕ are related by

$$K(E_n) = k_F(E_n)\phi$$

The kerma factor is related to the underlying reaction cross sections by

$$k_F = \sum_{ij} N_i \int E_{ij}(E_n, \theta_{cm}) \sigma_{ij}(E_n, \theta_{cm}) d\Omega$$

where N_i is the number of nuclei of the i -th element per gram, j specifies the type of nuclear interaction, $E_{ij}(E_n, \theta_{cm})$ is the energy of the charged particle in a collision whose cross section is $\sigma_{ij}(E_n, \theta_{cm})$ at incident neutron energy E_n and center-of-mass angle θ_{cm} . In the present work we consider each element separately and evaluate only two types of reaction channels, i.e. heavy ion recoil following 1) elastic scattering and, 2) inelastic scattering to bound final states. Numerical values of the partial kerma factors are obtained from the data and from the model calculations by using the Legendre polynomial expansion technique of Caswell et al.¹⁷⁾.

4.1 Elastic Scattering

Kerma factors for elastic scattering are shown in fig.8. The circles with error bars are obtained from the Legendre series

expansion to the measured data. The solid lines are obtained from optical model calculations using the potentials of Table 2. The extent

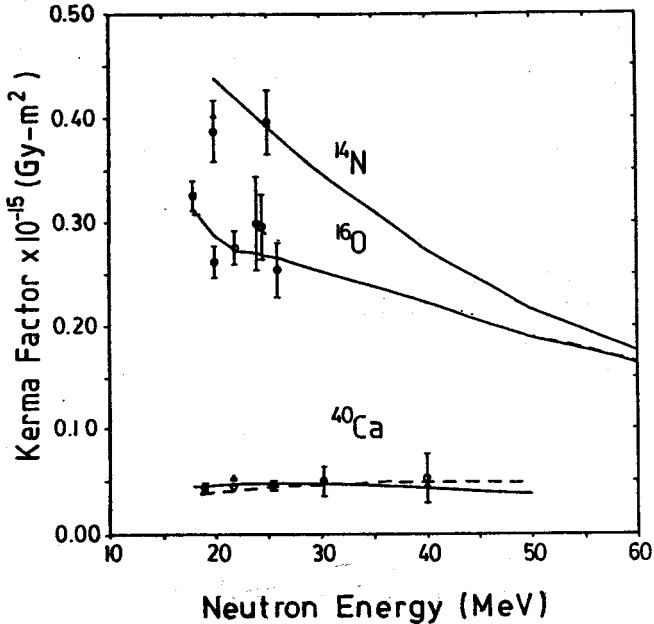


Fig.8: Recoil Kerma values for elastic scattering vs. neutron energy. Circles are from Legendre fits to the measurements. Triangles (for N and Ca) are individual best OMP fits. Solid line: calculations with OMP of Table 2. Dashed line (Ca): coupled channel calculations.

to which the data point differs from the line is a measure of the error that results from not fitting the scattering cross sections at large angles with these potentials. The triangles are calculations based on the individual best fit potentials of Petler³⁾ and of Alarcon¹⁶⁾. It can be seen that for Ca little error is introduced by using the spherical potential model instead of the best fit potentials or the measured values. For the lighter nuclei (N and O) the fluctuations in the measured values with respect to the optical model predictions might be attributable to an incomplete description of the

reaction mechanism. The extracted kerma values are very sensitive to the detailed shape of the differential cross section which is only represented in an average way by the optical model. The compound nucleus mechanism dies away rapidly above 25 MeV. Since the potential for O does an excellent job of predicting proton differential cross sections and neutron reaction cross sections above 25 MeV¹⁴⁾, the values in Table 2 are recommended for use up to 60 MeV.

The potential for N is less well established, but the values given in Table 2 are considered to be a reasonable representation of the limited data available.

The dashed line for Ca in fig.8 is from the coupled-channel potential of Honoré et al.¹⁵⁾.

4.2 Inelastic Scattering

Partial kerma factors for recoiling target nuclei obtained in the present work are summarized in fig.9. The data points with error bars are obtained with the Legendre fitting procedure described earlier. The solid lines are the results of DWBA-calculations using the vibrational model and the potentials of Table 2. In the experiments, the 3^- state in ^{16}O was not resolved from the weakly excited 0^+ state at 6.05 MeV and the 3^- state for ^{40}Ca was not resolved from the neighboring state at 3.9 MeV. In both cases, the measured cross sections were analyzed as if only the 3^- state were present. The 2^+ , 1^- doublet near 7.0 MeV in ^{16}O was also not resolved in the measurements, but the cross sections for each excitation were considered in detail¹⁴⁾ and the sum of the two contributions is plotted in fig.9. For convenience in plotting, the kerma values multiplied by the stated normalization factors before plotting. Also shown on fig.9 are the analogous quantities for inelastic proton scattering for ^{16}O .

It should also be emphasized that the quantities plotted in fig.9 represent only the direct reaction component of the inelastic scattering to these states. The calculated¹⁴⁾ compound nucleus contributions were subtracted from the differential cross section data

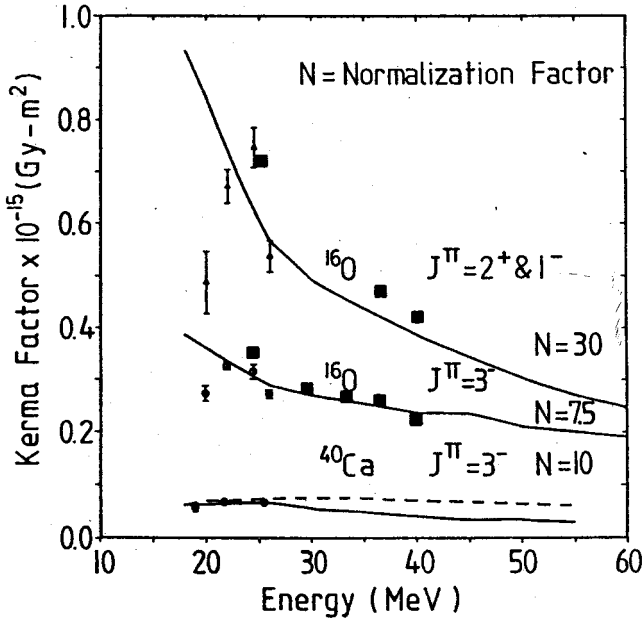


Fig.9: Recoil Kerma values for inelastic neutron scattering to the indicated states. Solid line: DWBA calculations with OMP from Table 2. Deashed line: coupled channel calculation. Squares are the analogous quantities from inelastic proton scattering.

before the experimental kerma factors were extracted. For ^{40}Ca , the compound nucleus effect is negligible at all energies under consideration, but for ^{16}O a correction to fig.9 is required. At 18 MeV the kerma factors from fig.9 should be multiplied by 1.25 and 1.35 respectively for the 3^- and the $2^+, 1^-$ doublet. These correction factors decrease to 1.10 and 1.15 at 26 MeV and to 1.0 at 30 MeV and above. The correction factors themselves are considered to be uncertain below 30 MeV by $\pm 30\%$.

One sees in fig.9 that the calculations are in reasonable overall agreement with the measurements. Fluctuations in the measured values for ^{16}O are again probably due to an incomplete description of

the reaction mechanism. The compound nucleus calculations mentioned above are energy averages and do not include local resonances the presence at which is clearly suggested by the fluctuations in the total cross section (fig.1) near 20 MeV.

Confidence in the model for the $^{16}\text{O}(n,n')$ reaction would clearly be strengthened by inclusion of inelastic scattering data at higher energy. Unfortunately, no such data exists. In this case, it is extremely valuable to observe that the high precision, well resolved proton inelastic scattering data¹⁸⁾ are well described by the model.

Inelastic neutron scattering from ^{40}Ca is very well described by the DWBA calculations using the spherical optical model of Table 2 and by the coupled-channels potential of ref.15. Above the region of the data ($E_n > 25.5\text{MeV}$) the calculations diverge. The potential of ref.15 was used with good success to describe inelastic proton scattering up to 40 MeV, and, for that reason, this potential is probably preferred whenever precise calculations of this quantity are required.

5. CONCLUSIONS

1. The data base for elastic and inelastic scattering of neutrons from tissue-abundant elements has been greatly expanded for neutron energies above 18 MeV.
2. Optical model potentials have been developed that provide good descriptions of all of the available cross section data in this energy region. These models can be used for transport calculations and for analysis of microdosimetry spectra up to 60 MeV.
3. Kerma factors have been extracted from the data and compared with the model calculations with varying degrees of success. The model calculations are generally most reliable at higher energy where resonance and compound nucleus effects are smallest.

4. High resolution proton scattering data is a valuable source of information for verifying the proposed models.

The authors wish to acknowledge the many valuable contributions to this work of R.Alarcon, J.S.Petler and J.Rapaport.

*This investigation was supported by PHS Grant Number CA-25193 awarded by the National Cancer Institute, Department of Health and Human Services.

+On leave at Kernforschungszentrum Karlsruhe, Institut für Kernphysik I, Postfach 3640, D-7500 Karlsruhe, BRD.

REFERENCES

- 1) Okamoto, K. ed. Proc. IAEA Advisory Group Meeting on Nuclear and Atomic Data for Radiotherapy and Related Radiobiology, INDC (NDS)-175/L+MO, Nov. 1985
- 2) Finlay, R.W., Brient, C.E., Carter, D.E., Marcinkowski, A., Mellema, S., Randers-Pehrson, G. and Rapaport, J., Nucl. Instrum. Methods 198, 197 (1982).
- 3) Petler, J.S., Islam, M.S., Finlay, R.W. and Dietrich, F.S., Phys. Rev. C32, 673 (1985).
- 4) DeVito, R.P., Ph.D. thesis Michigan State University 1979 (unpublished) and DeVito, R.P., Austin, S.M., Sterrenburg, W. and Berg, U.E.P. Phys. Rev. Lett. 47, 628 (1981).
- 5) Grabmayr, P., Rapaport, J. and Finlay, R.W., Nucl. Phys. A350, 167 (1980).
- 6) Lisowski, P.W., Moore, M.S., Morgan G.L. and Shamu, R.E. in Proc. Int. Conf. on Neutron Cross Sections for Technology eds. J.L. Fowler, C.H. Johnson and C.D. Bowman, NBS Special Publication SP-594524 (1980).
- 7) Larson, D.C., Hetrick, D.M. and Harvey, J.A., Bull. Am. Phys. Soc. 25, 543 (1980).
- 8) Peterson, J.M., Bratenahl, A and Stoering, J.P., Phys. Rev. 120, 521 (1960).
- 9) Auman, M., Brady, F.P., Jungerman, J.A., Knox, W.J., McGie, M.R. and Montgomery, T.C., Phys. Rev. C5, 1 (1972).
- 10) Meigooni, A.S., Petler, J.S. and Finlay, R.W., Phys. Med. Biol. 29, 643 (1984).
- 11) Finlay, R.W., Meigooni, A.S., Petler, J.S. and Delaroche, J.P. Nucl. Instrum. Methods B10/11, 396 (1985).
- 12) Delaroche, J.P., Islam, M.S. and Finlay, R.W., Phys. Rev. C (in press).
- 13) Annand, J.R.M.. The code OPSTAT, Ohio University (1983).
- 14) Islam, M.S., Finlay, R.W., Petler, J.S., Rapaport, J. and Alarcon R. (to be published) and Islam, M.S., Ph.D. Dissertation, Ohio University, 1986 (unpublished).
- 15) Honoré, G.M., Tornow, W., Howell, C.R., Pedroni, R.S., Byrd, R.C. and Walter, R.L., Phys. Rev. C33, 1129 (1986)
- 16) Alarcon, R., Rapaport, J. and Finlay, R.W., submitted to Nucl. Phys. and Alarcon, R., Ph.D. Dissertation, Ohio University, 1985 (unpublished).
- 17) Caswell, R.S. and Coyne, J.J., Rad. Res. 52, 448 (1972).
- 18) Bayers, D., Ph.D. Dissertation, Michigan State Univ., 1970 (unpublished)

REFINEMENT OF NEUTRON ENERGY DEPOSITION AND MICRODOSIMETRY CALCULATIONS*

Randall S. Caswell, J. Joseph Coyne,
Henry M. Gerstenberg, and Robert B. Schwartz
National Bureau of Standards
Gaithersburg, Maryland 20899
UNITED STATES OF AMERICA

Calculations describing the deposition of energy by neutrons in tissue-like materials are usually carried out by the "analytic method" or the "Monte Carlo method".

Extensions of the equations of the analytic method to include thin walls as well as thick walls are now available. Furthermore, inclusion of straggling effects in the analytic method is relatively simple and has been programmed for computer calculations.

The first step in the analytic method is the calculation of the "initial" spectra of secondary charged particles generated by the neutrons. We are preparing tables of initial spectra below 20 MeV. Two main problems exist in the preparation of these tables: (1) At low neutron energies the charged particle spectra consist of two very different parts, a very low energy component due to elastically scattered recoils from neutrons, and a much higher energy component due to protons and carbon recoils produced by the $^{14}\text{N}(n,p)^{14}\text{C}$ reaction. (2) Above 5 MeV the carbon and oxygen neutron cross sections are controversial, particularly for the $^{12}\text{C}(n,n'\alpha)$ reaction. This is expected to be an important topic of the present meeting.

The calculation of "lineal energy" or "y" spectra for neutrons is of interest for microdosimetry. New measurements of y spectra using filtered reactor beams of 144 keV and 25 keV show good agreement with calculations, if one accounts for the presence of higher-energy neutrons in the filtered beams. At 2 keV, however, there is a major discrepancy between experiment and analytic method calculations which we do not yet understand.

The possibility of carrying out microdosimetric calculations on a nanometer scale using track structure information generated by Wilson and Paretzke is being pursued jointly with Walt Wilson of the Pacific Northwest Laboratory.

A Monte Carlo code is being generated using the same data base as our analytic method codes. Although straggling is included in this code, the chief advantage of the Monte Carlo code is in the correct handling of events where two or three correlated charged particles are emitted. Some results of microdosimetric calculations including straggling will be given.

*Supported in part by the Office of Health and Environmental Research, U.S. Department of Energy.

1. INTRODUCTION

Two calculational methods are usually used to provide physical information on the process by which neutrons transfer their energy to tissue-like materials: The "analytic method,"^{1-4]} and the "Monte Carlo method".^{4-7]} Both methods are very much dependent on neutron cross section data in light elements — a major subject of this meeting — and on stopping-power data. Since other papers will cover the neutron data aspects, it is our intention in this paper to address the two calculational methods, and new more sophisticated versions of these methods which should lead to improved microdosimetry calculations.

2. ANALYTIC METHOD

2.1 Initial and Slowing-Down Spectra and Kerma

The analytic method starts from two secondary-particle spectra: the initial spectrum, $n(E)$, of the secondary charged particles as generated by neutron interactions; and the slowing-down spectrum, $\phi(E)$, of the same particles. The slowing-down spectrum is the average spectrum of the particles after slowing down in the matter in which the interactions take place. E is the energy of the charged particles. These two spectra are related by the equation

$$\phi(E) = \frac{1}{S(E)} \int_E^{E_{\max}} n(E') dE' \quad (1)$$

which states that the slowed-down particles at a given energy, E , come from those in the initial spectra which started at higher energies, and that the fluence in the spectrum at a given energy is inversely proportional to the stopping power. Note also that the kerma, K , is given by

$$K = \int_0^{E_{\max}} E n(E) dE = \int_0^{E_{\max}} S(E) \phi(E) dE \quad (2)$$

Kerma factors (kerma per unit neutron fluence), k_f , are usually not determined from explicit calculations of initial spectra as in Eq. (2), but from cross sections and average energy transfer:^{8]}

$$k_f(E_n) = \sum_L N_L [\sum_J \bar{E}_{LJ}(E_n) \sigma_{LJ}(E_n)] \quad (3)$$

The index L identifies the element or nuclide, J is the type of nuclear reactions, N_L is the number of nuclei per gram, and $\bar{E}_{LJ}(E_n)$ is the average amount of energy transferred to kinetic energy of charged particles in a reaction or scattering with cross section $\sigma_{LJ}(E_n)$. Equation (3) shows clearly where problems can come in the determination of kerma factors. First, the cross section, $\sigma_{LJ}(E_n)$ may be wrong. Secondly, the data required to determine $\bar{E}_{LJ}(E_n)$ — such as angular distributions, excitation of intermediate and final states, energy spectra of charged particles — may be in error or, more often, not available. Considerable activity has taken place in the last few years concerning the cross sections and charged-particle energy distributions of carbon above 10 MeV. Carbon is easier to investigate experimentally than oxygen, which is the other key element for dosimetry applications for which the data are not as good as desired. In particular, the kerma factor values in this energy region are generally being reported lower than in reference 8] which was based on ENDF/B-V. Some representative values of kerma factors in carbon in the range 14-15 MeV are given in Table 1.

Table 1. Some kerma factors for carbon in the neutron energy range 14.1-14.6 MeV.

Neutron energy/MeV	$k_f/(10^{-15} \text{ Gy m}^2)$	Method	Reference
14.1	1.78 ± 0.1	C proportional counter	9]
14.1	1.84 ± 0.19	Magnetic alpha spectrometer	10]
14.6	1.81 ± 0.15	C Calorimeter	11]
14.1	$2.24 \pm 10\%$	Calculated, based on ENDF/B-V	8]

In view of the consistency of the kerma factors given here and elsewhere using different experimental methods, the question immediately arises, can something be wrong with the calculated value? Brenner *et al.*,^{12]} argue that the $^{12}\text{C}(n,n')3\alpha$ cross section is probably too high, particularly around 16-18 MeV, due to the subtraction technique used for evaluating the cross section and due to over-reliance on old nuclear emulsion data. Also, in the evaluation of \bar{E}_{LJ} , use of a nuclear reaction model gives strong forward peaking of the emitted neutron with the neutron carrying away more energy than previously assumed, leaving less energy available for the alpha particles, and consequently smaller kerma. Confirming this general view are TEPC measurements using absolutely determined neutron fluences by Bühler *et al.*,^{13]} which show smaller alpha-particle production than do microdosimetry calculations using the data base in reference 8].

The study of various reaction mechanisms is important in determining \bar{E}_{LJ} . This has been pursued particularly by Antolkovic and Dolenec at 14.4 MeV^{14]} and by Antolkovic, Šlaus, and Plenkovic for neutron energies up to 35 MeV^{15]} using cyclotron neutrons. Detailed theoretical analyses of the effect of reaction mechanisms on initial spectra for $^{12}\text{C}(n,n')3\alpha$ under the assumption of isotropic neutron emission have been carried out by Coyne *et al.*^{16]}. These are now being extended to anisotropic inelastic neutron emission.

Before leaving the subject of the initial energy given to charged particles, we should mention that we are actively working on preparing tables of initial charged-particle spectra, $n(E)$, for neutron energies below 20 MeV, and have printed out a number of sample tables. Two main problems exist: (1) The problem discussed above of what should one take for the carbon and oxygen partial cross section data above 5 MeV — perhaps the present meeting will shed light on this problem. (2) The problem of tabulating the particle spectra over widely dispersed energy regions while keeping a reasonable number of energy bins. At low neutron energies, say, below 1 keV, the charged-particle spectra consist of two parts, a very low energy component, tens of eV, due to

elastically scattered recoils from neutrons, and a second component that consists of an almost monoenergetic proton peak near 0.58 MeV, and a carbon peak near 0.04 MeV, both from the $^{14}\text{N}(n,p)^{14}\text{C}$ reaction. Our proposed solution to this latter problem is to tabulate two spectra in the energy range where both components are important, since no single energy grid will serve for both. It is planned to make the initial spectra tables available in both book and floppy-disk form for reading by computers. Elements covered will be H, C, N, and O, and of course the tables will be valid for tissues and dosimetry materials in which these elements are dominant.

2.2 Conventional Analytic Method

We now come to the subject of microdosimetry calculations for neutrons using the analytic method. The assumptions of the conventional analytic method are indicated in Figure 1.

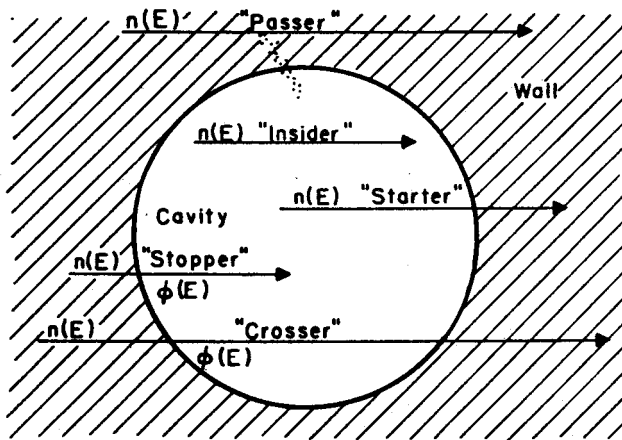


Fig 1. Classes of neutron-induced charged particle interactions with a cavity.

In this analytic method, the charged particles in the cavity are ejected with the distribution of energies corresponding to the initial spectrum, $n(E)$. Those in the wall, which is assumed thicker than the maximum range of the charged particles, start in the wall with the initial spectrum of energies. By the time they reach the cavity they have an equilibrium spectrum with lower average energy; we call this the slowing-down spectrum, $\phi(E)$. The cavity is assumed spherical which leads to a simple chord length distribution, $C(L)$. The charged particles are assumed to move in straight lines, delta-ray effects are neglected, and the particles are assumed to lose energy according to the continuous-slowing-down approximation (c.s.d.a.). Since delta-ray effects are ignored, events such as "passers" shown in Figure 1 are ignored. Based on these assumptions, the distributions of energy deposited, ϵ , for the four classes of events in the cavity are (neglecting normalization):

$$n_{INS}(\epsilon) = n(E) \frac{2}{3} D \int_{R(\epsilon)}^D I(\ell) d\ell \quad (4)$$

$$n_{STR}(\epsilon) = \frac{2}{3} D \int_{\epsilon}^{E_{max}} n(E) I(\ell) \frac{dE}{S(E-\epsilon)} \quad (5)$$

$$n_{STP}(\epsilon) = \phi(\epsilon) \int_{R(\epsilon)}^D C(L) dL \quad (6)$$

$$n_{CR}(\epsilon) = \int_{\epsilon}^{E_{max}} \phi(E) C(L) \frac{dE}{S(E-\epsilon)} \quad (7)$$

where $I(\ell)$ is the inside chord length distribution for particles starting at random in the sphere, and for $I(\ell)$ in Eq. (5) and $C(L)$ in Eq. (7) the length must equal $R(E) - R(E-\epsilon)$.

Because of the importance of neutrons in the keV energy region for personnel protection, we have carried out some measurements of "lineal energy" or "y" spectra for filtered reactor beams at 144 keV and 25 keV, which are compared to conventional analytic calculations in

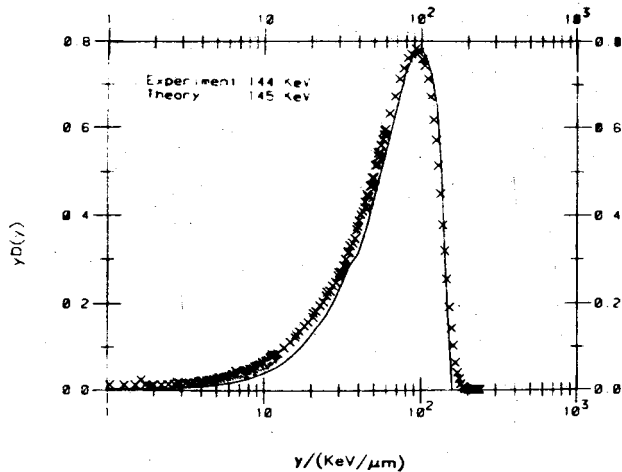


Fig. 2. Lineal energy spectra (crosses) for 144-keV filtered reactor beam neutrons compared to conventional analytic calculations (solid line). Cavity size is $1.7 \mu\text{m}$ for both measurements and calculation.

Figure 2 and 3. In Figure 2 note the generally satisfactory agreement between experiment and theory. In Figure 3 for 24 keV neutron energy there is general agreement below about 20 keV per micron, although the experimental curve is somewhat broader than the calculated curve. This broadening is probably due to the resolution in the proportional counter. The area above 25 keV/ μm in the spectrum is 15% of the area between 1 and 25 keV/ μm ; this is consistent with spectral measurements of the contamination of the 24 keV beam with higher energy neutrons (at 74, 135, 280, and 360 keV neutron energies). Some measurements were attempted at 2 keV neutron energy, which give rather different results from the calculation. We do not yet understand this discrepancy.

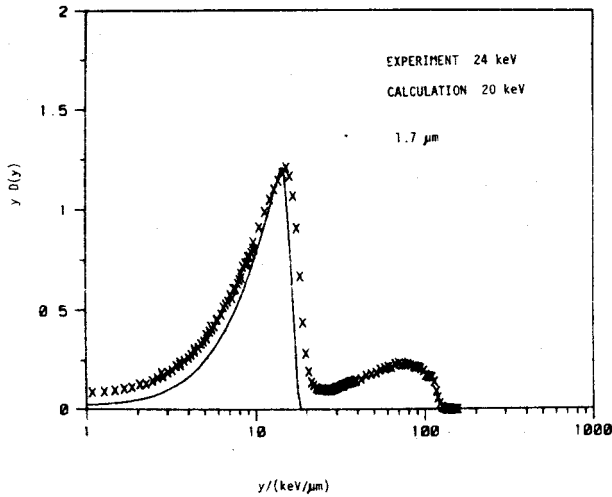


Fig. 3. Lineal energy spectrum for 24-keV filtered reactor beam neutrons compared to conventional analytic calculations for 1.7 μm cavity size. Points were normalized to peak value of calculation. Calculation used a single energy bin extending from 14 keV to 26 keV.

2.2 Analytic Method for Thin-Walled Cavities

The conventional analytic method assumes that the walls are thicker than the maximum range of the secondary charged particles ejected by the neutrons. Milavickas and Wu^{17]} have modified Eq. (6) and (7) so that only protons starting out to a thickness x (a function of the displacement from the center or eccentricity) are considered. Equations (6) and (7) become, in the integrated form for a spherical cavity:

$$n_{STP}(\epsilon) = \int_0^{E_{\max}} n(E) \frac{[C^2 - R(\epsilon)^2]}{S(\epsilon) D^2} dE \quad (8)$$

$$n_{CR}(\epsilon) = \int_0^{E_{\max}} n(E') \int_{\epsilon}^{E'} \frac{1}{S(E_r)} \frac{2[R(E_r) - R(E_r - \epsilon)]}{D^2 S(E_r - \epsilon)} dE_r dE' \quad (9)$$

These equations are not as simple as they appear. For example, C in Eq. (8) is a function of E and ϵ , not a simple constant. In Eq. (9) $R(E_r) - R(E_r - \epsilon)$ is zero unless it is less than C . The results of these calculations yield a slower buildup of cavity response with wall thickness than is found experimentally. Further investigation is therefore needed. However, the extension of the analytic method to the thin wall case is indeed very interesting.

2.3 Inclusion of Straggling in the Analytic Method

At high neutron energies, for example, 14 MeV, the analytic method fails to some extent because of the neglect of straggling of protons. Although it is difficult to see how to handle delta-ray effects in the analytic method, straggling can be handled, in principle, with another integration. If we use a straggling function, $P(E, \bar{\epsilon}, \epsilon)$ which gives the probability that a proton of energy E having an average energy loss $\bar{\epsilon}$ in the given chord length, will in a particular event lose energy ϵ , then the integrated form of Eq. (7) becomes to a good approximation:

$$n_{CR}(\epsilon) = \int_{\epsilon}^{E_{\max}} \phi(E) \int P(E, \bar{\epsilon}, \epsilon) \frac{2[R(E) - R(E - \bar{\epsilon})]}{D^2} \frac{dE}{S(E - \bar{\epsilon})} d\bar{\epsilon} \quad (10)$$

It is then possible to put in appropriate unit-normalized scattering distribution functions $P(E, \bar{\epsilon}, \epsilon)$ from Landau or Vavilov theory, or those based on the track structure calculations of Wilson and Paretzke.^{18]} We are now collaborating with W. Wilson in calculations of the latter type, which can also be extended to nanometer cavity sizes.

At present we are using a triangular straggling distribution. This enables us to check consistency and energy balance in the calculation. Some results of this kind are shown in Figure 4. The straggled curve is in the correct sense based on comparisons of conventional analytic calculations with experimental results. We are encouraged by the results so far, but clearly, realistic straggling functions need to be used before serious comparison is made with experiment.

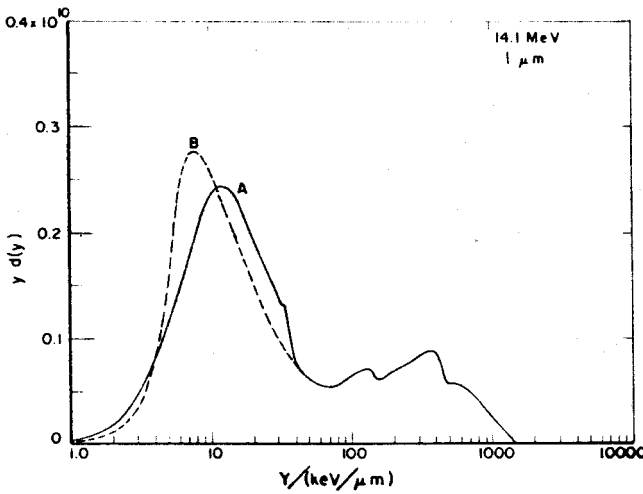


Fig. 4. Effect of straggling of protons on $y d(y)$ lineal energy distribution at 14.1 MeV neutron energy. Curve A is the straggled distribution, and curve B is the conventional analytic calculation (c.s.d.a.).

3. MONTE CARLO METHOD

We are developing a Monte Carlo neutron energy deposition code using the same data base of neutron cross sections and stopping power as is used for the analytic calculations. We have been able to demonstrate that the Monte Carlo code and the analytic code give nearly identical results for cases for which both are valid; for example, see Figure 5.

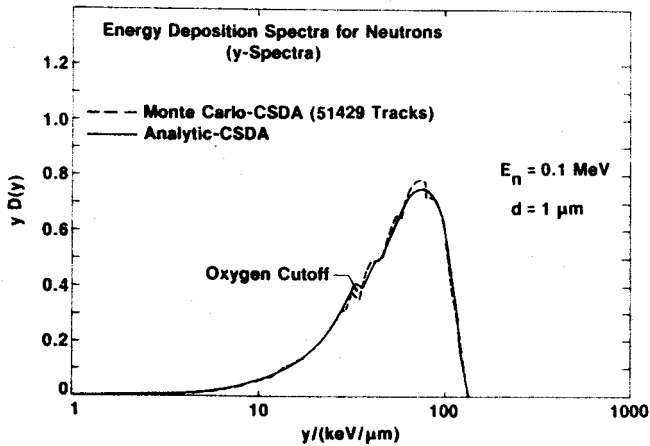


Fig. 5. Comparison of energy deposition spectra for neutrons analytic versus Monte Carlo, both using c.s.d.a.

An example of the inclusion of straggling, in this case a truncated Landau distribution which permits consistency with c.s.d.a. in the total amount of energy deposited, is shown in Figure 6. The agreement with experiment^{19]} is slightly better than that obtained with the analytic method.

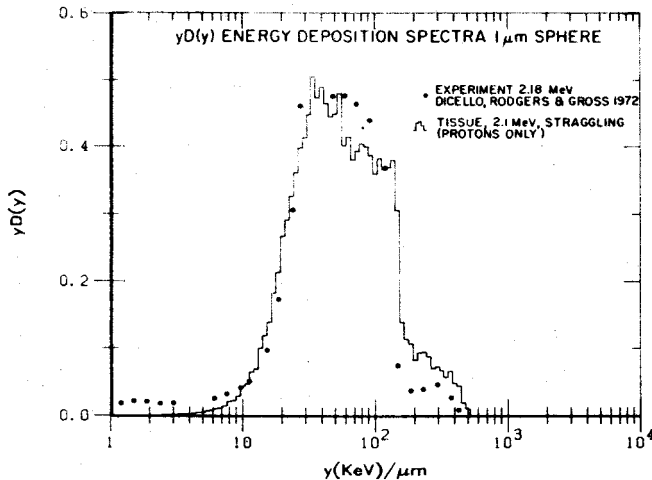


Fig. 6. Comparison of energy deposition spectra for neutrons of about 2.1 MeV energy, experiment¹⁹⁾ versus Monte Carlo straggling.

However the chief advantage of the Monte Carlo code is probably not in terms of the possibility of handling straggling or delta-ray effects, but rather to handle correctly events where two or three correlated charged particles are emitted. A code for this purpose is under development, but we do not yet have results.

4. SUMMARY

Many interesting developments are underway which should lead to more accurate calculations of the neutron energy deposition process. In the case of kerma factors for neutrons, improved and verified nuclear data is the primary need. For calculations of neutron energy deposition spectra, increasingly sophisticated calculational methods should make a major contribution.

4. REFERENCES

1. Caswell, R. S., Rad. Res. 27, 92 (1966).
2. Caswell, R. S. and Coyne, J. J., Rad. Res. 52, 448 (1972).
3. Edwards, A. A. and Dennis, J. A., Phys. Med. Biol. 20, 395 (1975).
4. International Commission on Radiation Units and Measurements, Microdosimetry, Report 36, 1983.
5. Oldenburg, U. and Booz, J., Rad. Res. 51, 551 (1972).
6. Booz, J. and Coppola, M., Proc. Fourth Symp. Microdosimetry, Report EUR 5122 (1974) p. 983.
7. Brenner, D. J., Prael, R. E., Dicello, J. F., and Zaider, M., Proc. Fourth Symposium Neutron Dosimetry, EUR 7448, Vol. 2, p. 103 (1981).
8. Caswell, R. S., Coyne, J. J., and Randolph, M. L., Rad. Res. 83, 217 (1980).
9. DeLuca, P. M. Jr., Barschall, H. H., Haight, R. C., and McDonald, J. C., Rad. Res. 100, 78 (1984).
10. Haight, R. C., Grimes, S. M., Johnson, R. G., and Barschall, H. H., Nucl. Sci. Eng. 87, 41 (1984).
11. McDonald, J. C., Rad. Res. (Submitted 1986).
12. Brenner, D. J., Coyne, J. J., Menzel, H. G., and Zaider, M., Radiation Research Society Las Vegas Meeting, paper Dk-5, April 12-17, 1986.
13. Böhler, G., Menzel, H. G., Schumacher, H., and Dietze, G., Proc. Ninth Symposium Microdosimetry, Radiation Protection Dosimetry (in press 1986).
14. Antolković, B. and Dolenc, Z., Nucl. Phys. A237, 235 (1975).
15. Antolković, B., Šlaus, I., and Plenković, D., Rad. Res. 97, 253 (1984).
16. Coyne, J. J., Gerstenberg, H. M., and Hennen, L. A., Proc. IAEA Advisory Group Meeting on Nuclear and Atomic Data for Radiotherapy and Radiobiology, Rijswijk, The Netherlands, Sept. 1985 (in press).
17. Milavickas, L. R. and Wu, C. S., "Calculation of Proton Buildup for Fast Neutrons," submitted for publication, 1986.
18. Wilson, W. E. and Paretzke, H. G., Rad. Res. 87, 521 (1981).
19. Rodgers, R. C. and Gross, W., Proc. Fourth Symp. Microdosimetry, Report EUR 5122 (1974) p. 1027.

KERMA FACTOR OF CARBON FOR NEUTRONS OF ENERGIES
BETWEEN 14 AND 20 MEV*

H.H. Barschall and P.M. DeLuca
University of Wisconsin-Madison

and

R.C. Haight
Lawrence Livermore National Laboratory and
Los Alamos National Laboratory

For applications in dosimetry and in fusion technology a knowledge of the kerma factor of carbon for fast neutrons is needed. Fast neutron kerma factors are usually calculated from microscopic cross sections. For carbon the microscopic cross sections around 14 MeV are not well known. Recent measurement of the $^{12}\text{C}(n,n'\alpha)$ reaction cross section, which contributes about a third to the kerma factor of carbon, differ by a factor of three.

In the present measurement kerma factors are determined directly by observing the distribution of charged-particle energy depositions in a small graphite-walled proportional counter. The counter consists of a 1.3 cm diameter spherical cavity surrounded by a 1.3 mm thick wall filled with a mixture of Ar and CO_2 at 60 Torr.

Neutron fluence was determined primarily by measuring activities produced in the reactions $^{19}\text{F}(n,2n)$, $^{27}\text{Al}(n,\alpha)$, and $^{197}\text{Au}(n,2n)$. In addition, an ionization chamber with A-150 plastic walls served as a

fluence monitor. Since the plastic contains carbon, an iterative procedure was applied to correct the kerma factor of the plastic.

Measurements at 14.1 and 15.0 MeV neutron energy were performed at Lawrence Livermore National Laboratory where a rotating target which contained tritium absorbed in titanium was bombarded by low-energy deuterons. The measurements at 17.9 and 19.8 MeV neutron energy were performed with deuterons accelerated in an electrostatic accelerator at the University of Wisconsin where a tritium gas target was used.

The measured kerma factors increased from 1.8×10^{-15} Gy m² at 14.1 MeV to 3.6×10^{-15} Gy m² at 19.8 MeV with uncertainties between 6 and 10%. At the lower energies the measurements are about 20% lower than the values calculated from microscopic cross sections by Caswell et al.¹⁾, but at the highest energy the measured and calculated values agree well. The measurements are consistent with the cross section measurement at 14.1 MeV by Haight et al.²⁾, and with the recent calorimetric kerma factor measurement at 14.6 MeV by McDonald.³⁾

References

* Work supported by the U.S. Department of Energy.

1. R.L. Caswell, J.J. Coyne, and M.L. Randolph, Radiat. Res. 83, 217 (1980).
2. R.C. Haight, S.M. Grimes, R.G. Johnson, and H.H. Barschall, Nucl. Sci. Eng. 87, 41 (1984).
3. J.C. McDonald, Radiat. Res., to be published.

CROSS SECTIONS FOR FAST NEUTRON INDUCED REACTIONS ON CARBON

B. Antolković^{*}, G. Dietze^{*} and H. Klein^{*}^{*}Ruder Bošković Institute, Zagreb^{*}Physikalisch-Technische Bundesanstalt, Braunschweig

Twin experiments were performed with a liquid scintillator and nuclear emulsion to measure the reaction cross section on carbon in the energy range from 11.5 to 19 MeV. The total reaction cross sections were determined with an uncertainty of about $\pm 4\%$, while the partial breakup cross sections are given with uncertainties of 15 to 5 %, improving with energy. The results are compared with the ENDF/B-V data.

1. INTRODUCTION

As carbon is the major component of tissue-equivalent fast neutron dosimeters and organic scintillation detectors reliable fast neutron induced reaction cross sections are required for many applications (calculation of the response spectra, KERMA factors etc.). The evaluation of these cross sections was chiefly based on the difference between total and scattering cross sections¹⁾ as experimental reaction data are scarce. In this paper we describe an experiment where the scintillator method²⁾ and the nuclear emulsion technique³⁾ were simultaneously applied. A liquid scintillator and the emulsions, both acting as a carbon target and a 4π detector, were irradiated with monoenergetic neutrons between 11.5 MeV and 19 MeV produced via the $D(d,n)^3He$ and $T(d,n)^4He$ reactions at the PTB's fast neutron facilities.

2. SCINTILLATION METHOD

Multiparameter analysis was performed for any NE 213 scintillation event in order to discriminate between photons and background neutrons. Measurements with different gains delivered scintillation spectra with a dynamic range of about 800:1. The detector response was simulated by Monte Carlo methods for the neutron spectrum actually used but considering only the scattering on hydrogen and carbon. The

upper part of the spectrum chiefly originates from proton recoils and precisely yields the neutron fluence. Above the lowest part of the spectrum due to carbon recoils a considerable fraction remains which is attributed to all reactions kinematically allowed, except for the sequential decay $^{12}\text{C}(n,n')^{12}\text{C}^*$ (7.62 MeV) 3α which cannot be distinguished from carbon recoil events. The resulting cross sections are compared with the evaluated excitation function in fig. 1. The target thicknesses caused the energy width, while the uncertainties summed up from statistics ($\leq 1\%$), n/γ discrimination procedure ($\sim 1.5\%$), determination of zero intercept and carbon light output ($\sim 1.5\%$) and systematic uncertainties of the MC simulation (estimated to 2%).

3. NUCLEAR EMULSION TECHNIQUE

Nuclear emulsions were irradiated in a neutron field the fluence of which was measured with a proton recoil telescope (uncertainty $\sim 2\%$) and/or the scintillator (uncertainty $\sim 2.5\%$).

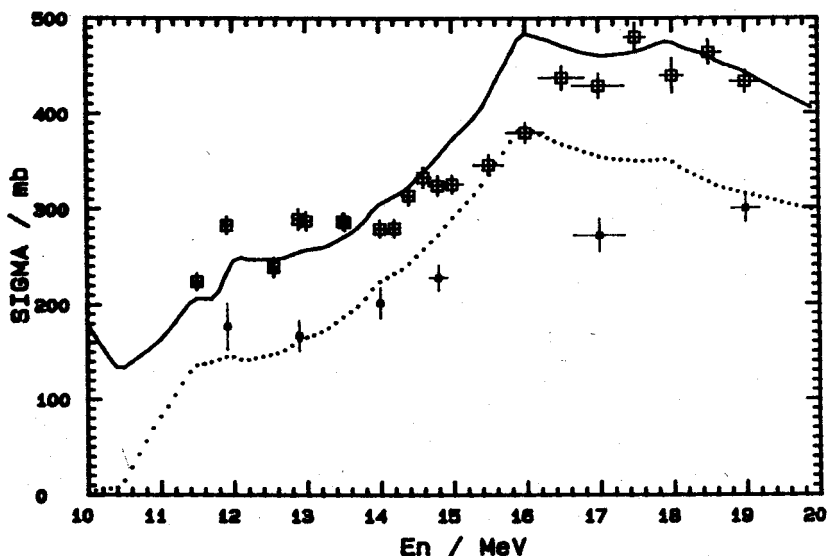


Fig. 1: Carbon cross sections for total neutron induced reactions (□ experimental data, full line evaluated data) and b) $(n,n'3\alpha)$ breakup (○ experimental data, dotted line evaluated data)

The emulsions were scanned in a standard way³⁾. Background events pertaining to the reaction $^{14}\text{N}(n, \alpha \ ^7\text{Li})\alpha$ have been omitted on the basis of the conservation laws (uncertainty $\sim 3\%$). The 3α and 2α correlations obtained by the eventwise analysis of the raw data yield information on the intermediate state excitations of the decay sequence $^{12}\text{C}(n, n')^{12}\text{C}^*(\alpha)^8\text{Be}^*(\alpha)\alpha$.

To correct for the loss of events due to the low energy threshold ($E_{\text{th}} = 0.45$ MeV) the Monte Carlo simulation has been applied, assuming a three step sequential decay mechanism with branching ratios for various decay chains experimentally obtained. The uncertainty of the correction factor is estimated to be 15 % (due to the uncertainty in the reaction mechanism assumed) and is the main uncertainty in the low energy region. The statistical uncertainty is less than 4 %.

The cross section data for the reaction $^{12}\text{C}(n, n' 3\alpha)$ (including the reaction $^{12}\text{C}(n, \alpha_1)^9\text{Be}_{2,4}(n, 2\alpha)$, but excluding the transition via the 7.6 MeV level of ^{12}C) are presented in fig. 1.

4. CONCLUSION

For neutron energies from 11.5 to 19 MeV the summed cross section of all reactions leading to charged particle emission as well as the partial cross section for the breakup reaction $^{12}\text{C}(n, n' 3\alpha)$ without the transition via the 7.6 MeV level of ^{12}C were determined. The present results deviate from the ENDF/B-V evaluation¹⁾ and recent experimental data⁴⁾. For the breakup reaction the branching ratios of various sequential decay chains were also extracted. This information as well as reliable angular distribution parameters for all contributing reactions are needed before simulated MC-spectra can satisfactorily be fitted to the scintillator spectra in order to extract the partial cross sections.

5. REFERENCES

- 1 ENDF/B-V, BNL, Upton New York (1978)
2. Dietze, G. et al., Proc. Antwerp Conference, p. 930 (1982)
2. Antolkovic, B. et al., Nucl. Phys. A394, 87 (1983)
3. Haight, B. et al., NSE 87, 41 (1984)

This work was supported within the framework of the Yugoslav-German bilateral agreement.

FAST NEUTRON INTERACTION DATA FROM MEASUREMENTS WITH LOW PRESSURE PROPORTIONAL COUNTERS

Hans-Georg Menzel and Helmut Schuhmacher
FR Biophysik und physikalische Grundlagen der Medizin
Universität des Saarlandes, D-6650 Homburg (Saar), FRG

Low pressure proportional counters were used to measure kerma factors for the tissue substitute material "A-150", graphite, aluminium and magnesium in well defined beams of monoenergetic neutrons from 13.9 MeV to 19 MeV. A high accuracy was achieved by application of the cavity chamber principle. The measured pulse height spectra provide additional information on the charged particles released in neutron interactions.

1. INTRODUCTION

Dosimetry of fast neutrons for biomedical applications requires the knowledge of basic data for interactions of neutrons with low Z nuclei. A principal quantity in dosimetry of uncharged particles is the kerma, K , defined as the kinetic energy transferred in interactions to charged particles. The ratio of kerma and neutron fluence is called kerma factor k_f :

$$k_f = K/\Phi = \sum_l N_l \sum_j \epsilon_{lj} \sigma_{lj}$$

l identifies the nuclide, j the type of nuclear interaction, N_l is the number of nuclides of type l per unit mass, ϵ_{lj} is the average energy transferred to kinetic energy of charged particles in an interaction whose cross-section is $\sigma_{lj}^{(1)}$. The quantity measured with a proportional counter is absorbed dose which differs in concept from kerma by implicitly accounting for the energy transport by secondary charged particles. In many practical cases, however, both quantities are numerically equal. The conditions to be met are existence of charged particle equilibrium and negligible attenuation of the primary beam. The pulse height spectra measured with a low pressure proportional counter (PC) are determined by the energy loss of charged particles in the gas cavity which have been released in single primary interactions of neutrons with mainly the detector material. The spectral information can be used to distinguish kerma contributions from different types of charged particles.

2. METHOD

The PC-method offers two principal advantages for the determination of kerma factors and interaction data for neutrons if compared to ionisation chambers being the more frequently applied cavity chamber. (1) The frequency of primary interactions within the cavity is low due to the low mass of the gas. This is essential for the accuracy with which the absorbed dose to the gas can be converted into the absorbed dose (= kerma) to the wall. (2) The cavity acts like a ΔE -detector for charged particles with ranges in excess of $10^{-4} \text{ g cm}^{-2}$. The resulting energy loss spectra can be used to identify different types of charged particles due to their different stopping power. Calculations for the tissue equivalent proportional counter (TEPC) show that the spectra are composed of dose contributions by elastically scattered protons, alpha particles from non-elastic reactions mainly in carbon and elastically scattered heavy recoils⁽²⁾. The exact separation of these contributions in a measured spectrum requires unfolding using calculations. Approximate separations, however, can be achieved by simple empirical methods.

3. RESULTS

PC measurements with counter walls made of A-150, graphite, aluminium and magnesium have been performed in the well defined beams of monoenergetic neutrons at PTB, Braunschweig^(3,4,5). The uncertainty achieved in the determination of kerma factors was about 5 % for A-150 and 7-9 % for the other materials. As an example fluence normalised spectra are shown for 17 MeV neutrons and for A-150, C and Al in Fig. 1. The quantity lineal energy $y^{(6)}$ is the quotient of energy transferred to the gas cavity and the mean chord length of the cavity (expressed for a density of 1 g cm^{-3}). The area under each curve corresponds to the respective kerma factor. Fig. 1 illustrates the large difference in kerma factors between the different materials, the absence of recoil protons for the carbon counter and protons from (n,p) and α particles from (n, α) reactions in aluminium.

The comparison of the measured kerma factors to tabulated values has revealed some discrepancies to ENDF/B based data for example for carbon. The comparison of measured spectra and calculated distributions has shown that this is mainly due to non-elastic reactions such as $^{12}\text{C}(n,n')3\alpha$ ^(4,7).

4. CONCLUSION

The PC-method to measure kerma factors for high energy neutrons^(3,8) provides relevant data for neutron dosimetry in biomedical applications. This is important because at high neutron energies kerma is influenced strongly by non-elastic reactions with low-Z nuclei for which the cross sections and charged particle spectra are often not well known. The analysis of the measured spectra by means of comparison to calculated distributions may provide the possibility to assess basic physical data such as cross sections.

This work is supported by the Commission of the European Communities (contract BI-6-0010-D)

5. REFERENCES

1. ICRU Report No. 33, Quantities and Units, ICRU, Washington (1980)
2. Caswell, R.S. and Coyne, J.J., Proc. 5th Symp. Microdosimetry, (1975)
3. Menzel, H.G. et al., Phys. Med. Biol. 29, 1537 (1984)
4. Bühler, G. et al., Radiat. Prot. Dosim. 13, 13 (1985)
5. Bühler, G. et al., Phys. Med. Biol., 31 (in press)
6. ICRU Report No. 36, Microdosimetry, ICRU, Washington (1983)
7. Schuhmacher, H. et al., Proc. 5th Symp. Neutron Dosimetry, 213 (1985)
8. DeLuca, P.M. et al., Radiat. Res. 100, 78 (1984)

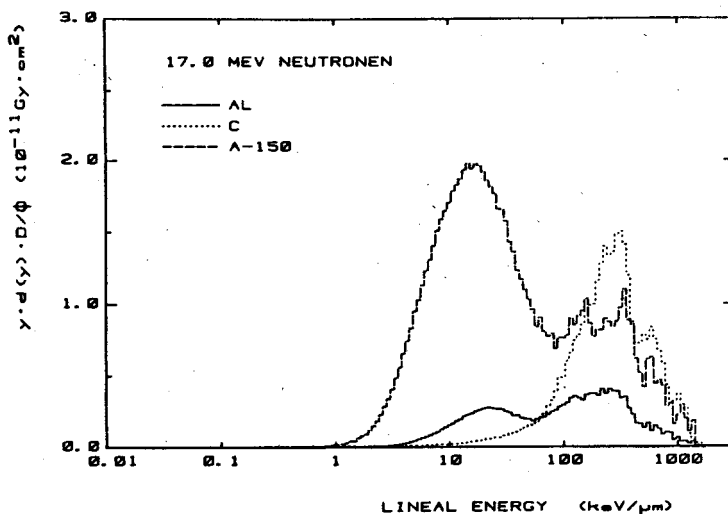


Fig. 1: Measured and fluence normalised dose distributions as a function of lineal energy for 17.0 MeV neutrons and A-150, graphite and aluminium counters

Chapter III

FEW BODY SYSTEMS

SCATTERING THEORY AND NUMERICAL RESULTS FOR FEW-NUCLEON SYSTEMS

W. Glöckle

Institut für Theoretische Physik
Ruhr-Universität Bochum
D 4630 Bochum 1, West Germany

The theory for three-body scattering is sketched and applications are shown to elastic and scattering and breakup reactions. The complexity of the four nucleon system is described and first results are shown.

1. INTRODUCTION

Few-nucleon systems are ideal to test nuclear dynamics, since with modern computers few-body equations can be solved. The two-nucleon force cannot yet be calculated neither in conventional field theoretical models for nucleons, deltas, pions, ... nor on the more fundamental level of quarks and gluons. However, the theoretical picture of meson exchanges between nucleons has led to two-nucleon force models, the one- or two-meson exchange potential ¹⁾ and the Paris potential ²⁾, which provide expressions with only a few open parameters. They can be fitted to the rich set of two-nucleon data, differential cross sections, polarisations, depolarisations, spin correlations and deuteron properties. A potential describing these data, usually given mainly in form of phase shift parameters, is called "realistic". The interesting question is then, whether the realistic potentials also describe three-, four-, ... nucleon systems quantitatively. With the advent of the Faddeev equations for three particles ³⁾ and the Yakubovsky ⁴⁾ or Alt, Grassberger, Sandhas (AGS) ⁵⁾ equations for four and more particles the Schrödinger equation could be rewritten into a form, which clarified and opened the way for its solution and initiated a great number of studies, theoretically and experimentally.

While a two-particle system has only one asymptotic geometric configuration a three-particle system has in general four. Two particles can be bound together or all three are free. The first case leads to

three asymptotic configurations with two fragments, the second case is called the break-up configuration. The three two-body fragmentations are illustrated in Fig. 1 which introduces also the convenient usual channel notation.

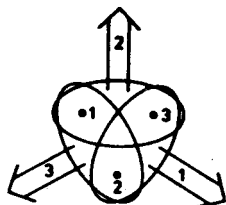


Fig. 1: The three two-body fragmentation channels

Four particles have in general seven two-body fragmentation channels of the type i,jkl and ij,kl , six three-body fragmentation channels ij,k,l and of course the total break-up channel. That rich structure cannot yet be controlled sufficiently accurately with available computing facilities, therefore we shall describe only the three-nucleon system in some detail and mention only some first results for four nucleons.

2. THEORY ⁶⁾ AND RESULTS

The description of scattering based on a time dependent formulation leads to Möller-wave operators, which map states of noninteracting fragments in relative motion onto scattering solutions of the Schrödinger equation. Analysing the scattering solution for large times leads to transition amplitudes into energetically allowed final channels. They have the general structure

$$T_{fi} = \langle \phi_f | V^f | \Psi_i^{(+)} \rangle \quad (1)$$

Here the final channel state ϕ_f is a product of bound states for the fragments and of momentum states of relative motion. It obeys

$$(H_0 + V_f - E) \phi_f = 0 \quad (2)$$

where H_0 is the kinetic energy and V_f the interaction which binds the fragments. The interaction V^f acts between the fragments and is

therefore in terms of the total interaction V

$$V^f \equiv V - V_f \quad (3)$$

Finally the scattering state initiated in channel i is determined by the Möller-wave operator

$$\Psi_i^{(+)} = \lim_{\epsilon \rightarrow 0} \frac{i\epsilon}{E + i\epsilon - H} \phi_i \quad (4)$$

with the total Hamiltonian $H = H_0 + V$.

For two nucleons $V_i = V_f = 0$ and $\phi_{i,f}$ are momentum eigenstates. Using the resolvent identity

$$\frac{1}{z - H} = \frac{1}{z - H_0} + \frac{1}{z - H_0} V \frac{1}{z - H} \quad (5)$$

eqn.(4) leads to the Lippmann Schwinger equation (LSE) for the two-nucleon scattering state

$$\Psi^{(+)} = \phi + G_0 V \Psi^{(+)} \quad (6)$$

Here and in the following the resolvent operators are always taken on the upper rim of the cut like

$$G_0 \equiv \lim_{\epsilon \rightarrow 0} \frac{1}{E + i\epsilon - H_0} \quad (7)$$

Inserting (6) into (1) and using the spectral decomposition of G_0 in terms of momentum states ϕ leads to the LSE for the two-body T-matrix

$$T = V + V G_0 T \quad (8)$$

One solves eqn.(8) conveniently by using the basis states $|p(ls)j\rangle$. The quantum numbers are the magnitude of the relative momentum p , the orbital-, spin-, and total angular momenta l , s , and j , respectively. In that basis eqn.(8) decomposes for each j into coupled (tensor force) or uncoupled integral equations in one variable.

Three nucleons allow two relative motions usually expressed in terms of Jacobi momenta

$$\begin{aligned} \vec{p}_1 &= \frac{1}{2} (\vec{k}_2 - \vec{k}_3) \\ \vec{q}_1 &= \frac{2}{3} \left(\vec{k}_1 - \frac{1}{2} (\vec{k}_2 + \vec{k}_3) \right) \end{aligned} \quad (9)$$

or the two cyclical permuted pairs (\vec{p}_2, \vec{q}_2) and (\vec{p}_3, \vec{q}_3) . The kinetic

energy is

$$H_0 = \vec{p}_i^2 + \frac{3}{4} \vec{q}_i^2 ; i=1,2,3 \quad (10)$$

(We put $\hbar^2/m = 1$). It is convenient to denote the pair interactions by $V_i \equiv V_{jk}$. The three channel Hamiltonians describing two-body fragmentations are

$$H_i = H_0 + V_i ; i=1,2,3 \quad (11)$$

and the corresponding channel eigenstates are

$$\phi_i = |\varphi_i\rangle |\vec{q}_i\rangle \quad (12)$$

In the two-nucleon system there is only one two-body bound state .

Let us regard a scattering state initiated in channel 1

$$\Psi_1^{(+)} = \lim_{\epsilon \rightarrow 0} \frac{i\epsilon}{E + i\epsilon - H} \phi_1 \quad (13)$$

From eqn.(13) one can derive integral equations with the help of resolvent identities

$$\frac{1}{z - H} = \frac{1}{z - H_i} + \frac{1}{z - H_i} (V_j + V_k) \frac{1}{z - H} \quad (14)$$

Choosing $i = 1, 2, 3$ we get in obvious notation

$$\Psi_1^{(+)} = \phi_1 + G_1 (V_2 + V_3) \Psi_1^{(+)} \quad (15a)$$

$$\Psi_1^{(+)} = \lim_{\epsilon \rightarrow 0} i\epsilon G_2 \phi_1 + G_2 (V_3 + V_1) \Psi_1^{(+)} \quad (15b)$$

$$\Psi_1^{(+)} = \lim_{\epsilon \rightarrow 0} i\epsilon G_3 \phi_1 + G_3 (V_1 + V_2) \Psi_1^{(+)} \quad (15c)$$

Since ϕ_1 is neither a discrete eigenstate of H_2 nor H_3 the driving terms in (15b,c) vanish in the limit $\epsilon \rightarrow 0$. We get the triad of LSE's, one inhomogeneous and two homogeneous ones ⁷⁾. Obviously if we had chosen the initial channel 2 to determine the scattering state $\Psi_2^{(+)}$ eqn.(15b) would have been the inhomogeneous one and (15c) for the state $\Psi_3^{(+)}$. As a clear consequence (15a) alone allows the solution

$$\Psi = \Psi_1^{(+)} + \alpha \Psi_2^{(+)} + \beta \Psi_3^{(+)} \quad (16)$$

with α, β arbitrary. If we require that Ψ should also solve eqn.(15b) then α has to be zero and similarly β in the case of eqn.(15c). Now every solution of the set (15a-c) is a solution of the Schrödinger equation. Are there additional solutions to a given energy E ? For $E > 0$ a fourth type of scattering state exists which is initiated in the break-up channel, $\Psi_0^{(4)}$. It is easy to see that it always obeys inhomogeneous equations. Therefore the triad is necessary and sufficient to define $\Psi_1^{(4)}$ uniquely ⁷⁾. This is now a convenient basis to derive the Faddeev equations for scattering states or the AGS equations ⁸⁾ for transition operators U_{ij} . The elastic and rearrangement transition amplitudes in accordance with eqn.(1) are given as

$$\begin{aligned} (\phi_1 | U_{11} | \phi_1) &\equiv (\phi_1 | V_2 + V_3 | \Psi_1^{(4)}) \\ (\phi_2 | U_{21} | \phi_1) &\equiv (\phi_2 | V_3 + V_1 | \Psi_1^{(4)}) \\ (\phi_3 | U_{31} | \phi_1) &\equiv (\phi_3 | V_1 + V_2 | \Psi_1^{(4)}) \end{aligned} \quad (17)$$

Using the set (15a-c) in a proper manner we deduce immediately

$$\begin{aligned} U_{11} \phi_1 &= V_2 G_2 U_{21} \phi_1 + V_3 G_3 U_{31} \phi_1 \\ U_{21} \phi_1 &= V_3 G_3 U_{31} \phi_1 + V_1 G_1 U_{11} \phi_1 + V_1 \phi_1 \\ U_{31} \phi_1 &= V_1 G_1 U_{11} \phi_1 + V_2 G_2 U_{21} \phi_1 + V_2 \phi_1 \end{aligned} \quad (18)$$

This set links all three two-fragmentation channels. We use $V_i \phi_i = G_0^{-1} \phi_i$ and $V_k G_k \equiv T_k G_0$, which introduces the two-body T-matrix embedded in the three-particle space

$$T_k = V_k + V_k G_0 T_k \quad (19)$$

Clearly T_k sums up the pair interaction V_k to infinite order. This explains the typical Faddeev structure of the kernel in (18), namely only to link U_{i1} to U_{j1} with $i \neq j$. For a general initial channel and keeping in mind that the operators should be applied onto channel states ϕ_l we get the standard form of the AGS-equations

$$U_{kl} = \delta_{kl} G_0^{-1} + \sum_{m \neq k} T_m G_0 U_{ml} \quad (20)$$

Their physical content is very transparent by iterating (20) which yields the multiple scattering series: consecutive scattering events between different pairs

$$U_{k\ell} = \delta_{k\ell}^{-1} G_0^{-1} + \sum_{\substack{u_1 \neq k \\ u_1 \neq \ell}} T_{u_1} + \sum_{u_1 \neq k} T_{u_1} G_0 \sum_{\substack{u_2 \neq u_1 \\ u_2 \neq \ell}} T_{u_2} + \dots \quad (21)$$

From eqn.(1) the transition amplitude into the break-up channel is

$$(\phi_0 | U_{01} | \phi_1) \equiv (\phi_0 | V_1 + V_2 + V_3 | \Psi_1^{(+)}) \quad (22)$$

Here the channel state ϕ_0 , eigenstate to H_0 , is clearly

$$\phi_0 = |\vec{p}_i\rangle |\vec{q}_i\rangle \quad ; \quad i = 1, 2, 3 \quad (23)$$

Using again the basic set (15a-c) we read off (for general 1)

$$U_{0\ell} = G_0^{-1} + \sum_k T_k G_0 U_{k\ell} \quad (24)$$

Therefore the break-up operator can be calculated by quadrature in terms of the $U_{k\ell}$.

For identical particles the three two-fragmentation channels are indistinguishable experimentally and rearrangement operators are simply gained from the direct (elastic) one by permuting particles. If we define

$$U | \phi_1 \rangle \equiv (V_2 + V_3) | \Psi_s^{(+)} \rangle \quad (25)$$

in terms of the symmetrised scattering state initiated in the two-fragmentation channel then (20) can be rewritten as

$$U = P G_0^{-1} + P T G_0 U \quad (26)$$

where $P = P_{12} P_{23} + P_{13} P_{23}$ leads from channel 1 to channels 2 and 3.

After angular momentum decomposition the set (20) or eqn.(26) still poses a severe problem in two continuous variables $|\vec{p}|$ and $|\vec{q}|$. The exploration of three particle dynamics in the beginning was therefore only possible once the AGS equations were converted into effective multichannel LSE's for the relative motion of two fragments⁹⁾. Then after angular momentum decomposition they are one-dimensional.

A simple way to achieve this is based on two-body forces of finite rank

$$V = \sum_n |g_n\rangle \lambda_n \langle g_n| \quad (27)$$

To illustrate the basic structure a separable potential (rank 1) is sufficient. The off-shell two-body T-matrix can be determined algebraically from (19) with the result

$$T(z) = |g\rangle \tau(z) \langle g| \equiv |g\rangle \left(\frac{1}{\lambda} - \langle g| G_0(z) |g\rangle \right)^{-1} \langle g| \quad (28)$$

The two-body bound state with binding energy ϵ_b obeys

$$|\psi\rangle = \frac{1}{\epsilon_b - \hat{p}^2} V |\psi\rangle \propto \frac{1}{\epsilon_b - \hat{p}^2} |g\rangle \quad (29)$$

Consequently the channel state can be represented as

$$|\phi\rangle \propto G_0 |g\rangle |\vec{q}\rangle \quad \Big| \quad \text{on shell} \quad (30),$$

when on shell means $E = \epsilon_b + \frac{3}{4} \vec{q}^2$. The transition amplitude can therefore be written as

$$\langle \vec{q}' | X | \vec{q} \rangle \equiv \langle \vec{q}' | (g | G_0 U G_0 | g) | \vec{q} \rangle \quad (31)$$

and obeys, as should be obvious from (26) and (31), the Lovelace equation

$$\begin{aligned} \langle \vec{q} | X | \vec{q}' \rangle &= \langle \vec{q} | Z | \vec{q}' \rangle \\ &+ \int d^3 \vec{q}'' \langle \vec{q} | Z | \vec{q}'' \rangle \tau(E - \frac{3}{4} \vec{q}''^2) \langle \vec{q}'' | X | \vec{q}' \rangle \end{aligned} \quad (32)$$

The "potential" Z is nonlocal and describes the exchange of a particle between formfactors g of different pairs:

$$\langle \vec{q}' | Z | \vec{q} \rangle \equiv \langle \vec{q}' | (g | P G_0 | g) | \vec{q} \rangle \quad (33)$$

That driving term is often pictured as

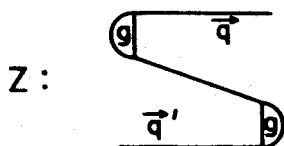


Fig. 2: The driving term in (32) is a one-particle exchange process.

The function $\tau(\mathbf{z})$ from (28) plays the role of the propagator in the two-fragmentation channels which is manifest near its pole $Z = \epsilon_b$:

$$\tau(E - \frac{3}{4}q^2) \sim \frac{1}{E - \frac{3}{4}q^2 - \epsilon_b} \quad (34)$$

The pioneering work by Amado¹⁰⁾ and following calculations demonstrated that the elastic and break-up nd processes could qualitatively be quite well reproduced. These first calculations¹¹⁾ were carried through with spin dependent separable potentials which moreover act only in s-states. We show in Fig. 3 an example for a kinematically complete break-up experiment, in which two nucleons are measured under fixed solid angles (ϑ_1, ϑ_2). Energy and momentum conservation impose 4 conditions which leave 5 independent variables. Therefore the energies E_1 and E_2 are not independent. Events against the arc length of the kinematically allowed curve in the E_1 - E_2 plane are shown.

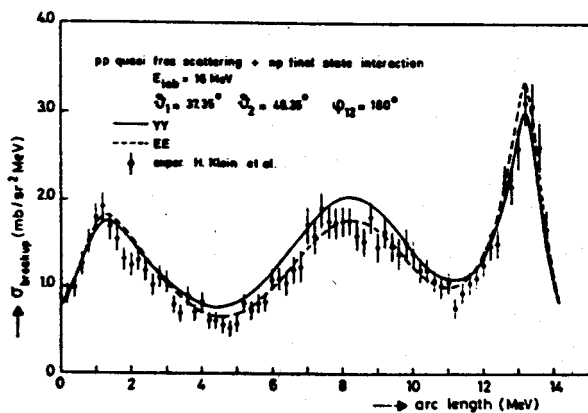


Fig. 3: The pd break-up reaction at $E_p = 16$ MeV.

We recognize quasi free scattering and final state interaction peaks. The two curves use different shapes of $g(p)$. (The Coulomb force is theoretically not included).

Inasmuch meson exchanges are responsible for the NN force local potentials should be used. A first step was done with the spin-dependent Malfliet-Tjon potentials ¹²⁾ constructed for s-waves, which were used by Kloet and Tjon ¹³⁾. In Fig. 4 we show a comparison with a proton energy spectrum (kinematically incomplete). The structures are due to n-n and n-p final state interactions.

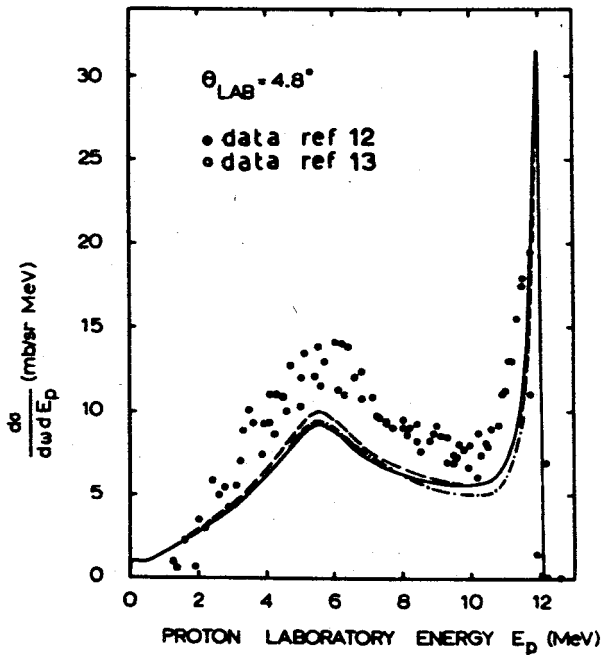


Fig. 4:

Proton-energy spectrum for $E_n^{\text{lab}} = 14.4$ MeV. The solid and dashed curves are for Malfliet-Tjon potentials and the dash-dotted curve for the separable Yamaguchi potential.

One recognizes that the simple separable Yamaguchi potential yield similar results in this case. However a systematic search in the entire three-nucleon phase space revealed regions where the cross sections depend very much on the potential used.

A next step was the inclusion of p-wave and tensor forces. This was undertaken by the Grenoble group ¹⁴⁾ with the realistic local soft core potential of de Tournelle and Sprung ¹⁵⁾. They calculated

elastic nd scattering and several spin observables at $E_n=14.1$ MeV. A rather good agreement for the differential cross section can be seen in Fig. 5, while some spin observables like the deuteron vector polarisation in not well reproduced, see Fig. 6.

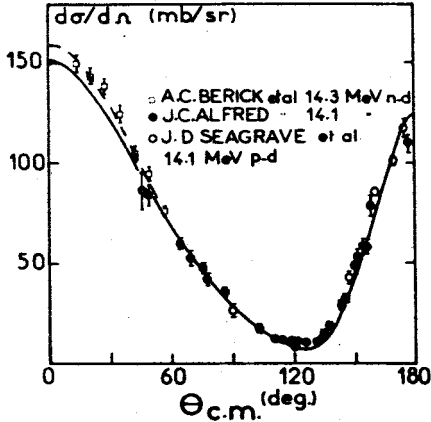


Fig. 5: Differential cross section for n-d scattering

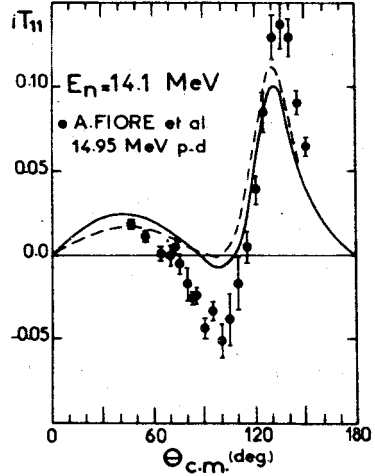


Fig. 6: Deuteron vector polarisation

Calculations of similar sophistication based on finite rank potentials by Doleshall and Koike describe n-d elastic scattering data equally well. We show in the table total nd cross sections from ref. ¹⁶⁾ in comparison with experiment.

Table: The total nd cross section for various energies

E_n^{lab} (MeV)	$\sigma_{\text{exp}}^{\text{tot}}$	$\sigma_{\text{th}}^{\text{tot}}$
3	2.202 ± 0.02	2.193
5	1.639 ± 0.02	1.649
7	1.337 ± 0.01	1.348
9	1.128 ± 0.01	1.145
14	0.824 ± 0.01	0.823
20	0.603 ± 0.006	0.601

There is however still room for improvement as is seen from the total break-up cross section ¹⁶⁾ shown in Fig. 7.

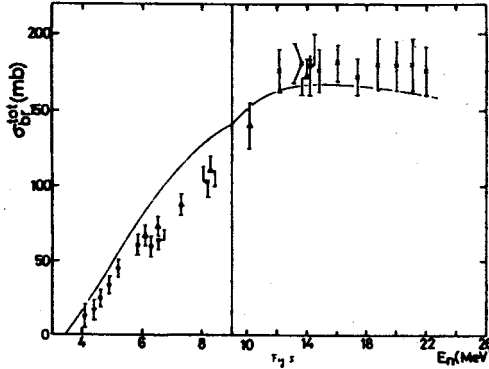


Fig. 7: The total n-d break-up cross section from Ref. ¹⁶⁾.

A set of differential nd cross sections in comparison to calculations by Doleshall ¹⁷⁾ are shown in Fig. 8.

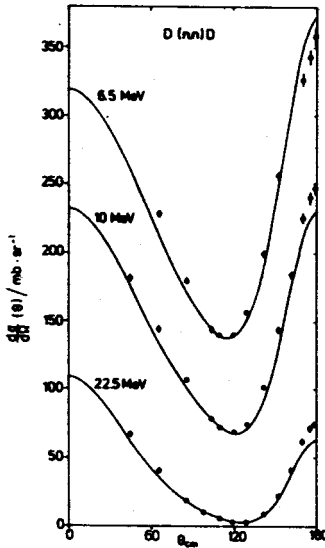


Fig. 8:
Differential nd cross
sections.

A recent review on separable interactions can be found in Ref. ¹⁸⁾, which also discusses finite rank approximations to meson-exchange NN potentials.

Equally serious studies on the break-up process have already appeared ¹⁹⁾ and are underway ²⁰⁾. There is good reason to expect that agreement between experiment and theory will be equally good. However, one also hopes ²¹⁾ that certain kinematical configurations may show the effect of a three-nucleon force, which is needed to understand the triton binding energy. Realistic two-nucleon forces alone underbind the triton by 1 to 1.5 MeV ²²⁾ and first results ²³⁾ with the 2π -exchange three-nucleon force give an encouraging additional binding energy.

Let us now regard the four nucleon system. Faddeev equations have been generalized by Yakubowsky ⁴⁾ and AGS ⁵⁾ to $N = 4$ and more particles. For $N = 4$ it result 18 coupled equations. This number, $4 \times 3 + 3 \times 2$, counts the number of possibilities of selecting an internal pair in the seven-two-fragmentation clusters. The 18 different chains of decomposition into subcluster partitions can also be visualised by Yakubowsky trees

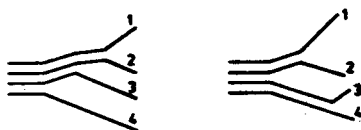


Fig. 9: Yakubowsky trees for the chains

$(1234) \rightarrow (123)4 \rightarrow (12)34 \rightarrow 1234$ and $(1234) \rightarrow (12)(34) \rightarrow (34)12 \rightarrow 1234$.

Using finite rank approximations these 4-body equations are under study ²⁵⁾ but due to obvious complexities realistic results comparable to the three-nucleon system have not yet been achieved. We show in Figs 10, 11 results ²⁵⁾ based on separable potentials and various approximation schemes.

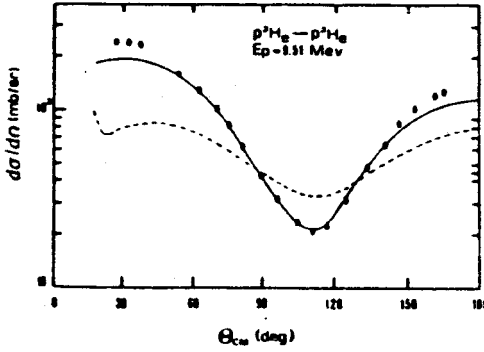


Fig. 10: Differential cross section for
 $p + {}^3\text{He} \rightarrow p + {}^3\text{He}$

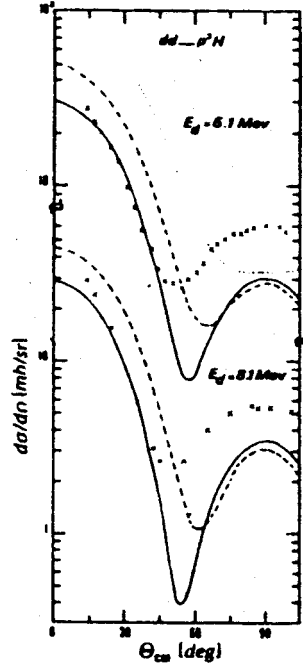


Fig. 11: Differential cross sections for $dd \rightarrow p + {}^3\text{He}$

I want to illustrate the complexity of the four-body system by showing the Sloan equations ²⁶⁾. They can very easily be derived by using L.S.E's. ⁶⁾. According to eqn. (1) transition operators between two-fragmentation channels, denoted by $a_2, b_2 \dots$ are defined by

$$U_{b_2 a_2} |\phi_{a_2}\rangle \equiv \sum_{b_3 \notin b_2} V_{b_3} |\Psi_{a_2}^{(4)}\rangle \quad (35)$$

Here ϕ_{a_2} is a two-fragmentation channel state and $\Psi_{a_2}^{(4)}$ the scattering state initiated in channel a_2 . Obviously pairs characterize three-fragmentation channels and are consequently denoted by a_3, b_3, \dots . Then $b_3 \notin b_2$ means that the pair b_3 does not occur within a cluster of b_2 . The Sloan equations couple the seven transition operators

$$\begin{aligned}
 U^{b_2 a_2} = & \overline{\delta_{b_2 a_2}} (E - H_0 - V_{a_2 b_2}) \\
 & + \sum_{b_3 \neq b_2} V_{b_3} G_{b_3} \sum_{c_2 \supset b_3} V_{c_2}^{b_3} G_{c_2} U^{c_2 a_2}
 \end{aligned}
 \tag{36}$$

The resolvent operators G_{b_3} and G_{c_2} include the internal interactions for fragmentations b_3 and c_2 , respectively. In deriving (36) one uses the identity

$$\sum_{c_3 \neq b_3} V_{c_3} = \sum_{b_2 \supset b_3} (V_{b_2} - V_{b_3}) \equiv \sum_{b_2 \supset b_3} V_{b_2}^{b_3}
 \tag{37}$$

The kernel in (36) requires the know how to handle all the subsystems for 4 particles. Finally $V_{a_2 b_2}$ is the sum of pair interactions common to a_2 and b_2 .

Analysing the richer variety of four nucleon reactions in the future will consolidate our understanding of nuclear dynamics gained for three nucleons or may bring up surprises.

REFERENCES

1. Machleidt, R., and Holinde, K., Proc. of the 10th Intern. Conf. on few-body problems, 1983, (Zeitnitz, B., ed.) p. 57.
Amsterdam: North-Holland 1984
2. Lacombe, M., Richard, M., Vinh Mau, R., Côté, J., Pirés, P., and de Tourreil, R., Phys.Rev.C21,861(1980)
3. Faddeev, L.D., Sov.Phys. JETP 12, 411(1961)
4. Yakubovsky, O.A., Sov.J.Nucl.Phys.5,937(1967)
5. Grassberger, P., and Sandhas, W., Nucl.Phys.B2,181(1967);
Alt, E.O., Grassberger, P., and Sandhas, W., Joint institute for nuclear research institute Report Nr. E4-6688,1972
6. Glöckle, W., The quantum-mechanical few-body problem (Springer, Berlin 1983)
7. Glöckle, W., Nucl.Phys.A141,620(1970)
8. Alt, E.O. Grassberger, P., and Sandhas, W., Nucl.Phys.B2,167(1967)
9. Lovelace, C., Phys.Rev.B135,1125(1964)
10. Amado, R.D., Phys.Rev.132,485(1963); Aaron, R.A., and Amado, R.D., Phys.Rev. 150,857(1966)
11. Bruinsma, J., Eberhöf, W., Stuivenberg, J.H., and van Wageningen, R., Nucl.Phys.A228,52(1974)
12. Malfliet, R.A., and Tjon, J.A. Nucl.Phys.A127,161(1969)
13. Kloet, W.M., and Tjon, J.A., Nucl.Phys.A210,380(1973)
14. Benayoun, J.J., Chauvin, J., Gignoux, C., and Laverne, A., Phy.Rev.Lett. 36,1438(1976)
15. de Tourreil, R., and Sprung, D.W.L., Nucl.Phys.A201,193(1973)
16. Koike, Y., and Taniguchi, Y., Few-body systems 1,13(1986)
17. see Schwarz, P., Klages, H.O., Doll, P., Haesner, B., Wilczynski, J., and Zeitnitz, B., Nucl.Phys.A398, 1(1983)
18. Plessas, W., in few-body methods in atomic, molecular, and nuclear physics and chemistry, Proc. of the internat. Symposium Nanning (P.R. China), 1985 (World Scientific, Singapore), to appear
19. Stolk, C., and Tjon, J.A., Nucl.Phys.A319, 1(1979)
20. private communications by R. Brandenburg and T. Sasakawa

21. Meier, W., and Glöckle, W., Phys.Lett.B138, 329(1984)
22. Friar, J.J., Gibson, B.F., and Payne, G.L., Ann.Rev.Nucl.Part. Sc.34, 403(1984)
23. Ishikawa, S., Sasakawa, T., Sawada, T., and Ueda, T., Phys.Rev.Lett. 53, 1877(1984);
Wiringa, R.B., Friar, J.L., Gibson, B.F., Payne, G.L., and Chen, C.R., Phys.Lett. B134, 273(1984)
Bömelburg, A., preprint Bochum, 1986
24. Tjon, J.A., Nucl.Phys.A353, 47C (1981)
25. Fonseca, A.C., in few-body methods in atomic, molecular, and nuclear physics and chemistry, Proc.of the internat. Symposium Nanning (P.R. China), 1985 (World Scientific, Singapore), to appear
26. Sloan, I.H., Phys.Rev. C6, 1945(1972)

RECENT MEASUREMENTS OF THE n-p CAPTURE CROSS SECTION

P. Leleux

Catholic University of Louvain
Louvain-la-Neuve, Belgium

1. INTRODUCTION

The neutron-proton capture and its inverse reaction, the deuteron photodisintegration are in principle attractive phenomena, mostly because the interaction responsible for this very simple reaction is electro-magnetic ; this interaction has two nice features : first it is well-known and second it is weak which means that the perturbation theory at first order is certainly valid to describe the reaction. We should be thus in a position to learn something about the neutron-proton scattering states and the deuteron wave function, i.e. about the nucleon-nucleon strong interaction. In fact, some important problems are remaining, as we will see.

As the talk will be mostly devoted to the description of n-p capture experiments (up to an incident energy of 80 MeV) it is necessary to say first a few words about the kinematics of the reaction.

2. KINEMATICS

It is clear that, apart from the deuteron binding energy, half of the incident neutron energy is used to move the center-of-mass ; the other half is available as the reaction energy, and is thus partitioned between the gamma-ray and the deuteron. Because of the very unequal masses of the reaction products, the deuteron takes away a very small amount of kinetic energy in the c.m. and as a consequence the deuteron is restricted to very small angles in the lab (e.g. for $E_n = 61$ MeV, $\theta^{\max} = 5.5^\circ$). At each lab angle correspond two c.m. angles, the first one for a forward and the second one for a backward c.m. emission (e.g. at 0° in the lab. one finds the 0° and 180° c.m. deuterons, at θ^{\max} one finds the 90° c.m. deuterons). The

deuteron energy is the lab. is peaked around $(-\frac{E_n}{2})$ with a variation of $\pm 20\%$ around this value.

One should note that this capture kinematics is very different from the inverse reaction, the deuteron photodisintegration ; in the latter, apart from the deuteron binding energy, lab. and c.m. systems coincide, and the neutron and the proton are not restricted to any angular region in the lab. Both reactions can be related by the detailed balance theorem which in this case is implied by the fact that the electromagnetic interaction is invariant under time reversal. In the following, this theorem will always be used.

3. THE EXTREME ANGLE DIFFERENTIAL CROSS SECTION

This is a very interesting observable in the following sense : suppose one does an experiment in an energy range where the initial n-p state is mostly a P state ; then if the deuteron was a purely symmetric object (an 3S_1 state), the only electromagnetic transition would be an E1 transition which should give an angular distribution proportional to $\sin^2\theta$: the cross section at 0° and 180° c.m. should then be zero ; it is only the presence of the 3D_1 component in the deuteron that gives a nonzero cross section. Calculations had been done long before, particularly in the decisive work of Partovi ¹⁾. It was thus a great surprise when in 1976 a measurement done at Mainz ²⁾ was found in disagreement with "the theory" (figure 1). This work was later confirmed by n-p capture measurements done at Louvain-la-Neuve ³⁾ and Indiana ⁴⁾.

I am coming now to the description of a recent measurement of the 0° and 180° cross section at 61 MeV done at Louvain-la-Neuve. The set-up is depicted in figure 2. Neutrons are produced by the Li(p,n) reaction at 0° induced by 65 MeV protons hitting a 1 cm-thick natural lithium target. A 0.7 cm diameter carbon collimator defines the beam spot on target. Behind the target, protons are bent downstairs by a few cm by a dipole magnet and they are stopped in an isolated Carbon beam dump where are integrated.

The neutrons are limited at 0° by a 2 m long conical collimator with a 0.8 cm entrance diameter and a 2 cm exit diameter. The proton target is a liquid hydrogen cell of 2.5 cm diameter and 0.5 cm thickness, closed by thin (6 μm) aluminized mylar windows. The target region is surveyed by two plastic scintillators : upstream of the target, a 100 μm thick detector (VETO) fires on charged particles contaminating the neutron beam, and downstream of the target a 50 μm thick detector (START) triggers on charged particles from the target ; the latter detector is also used to select monoenergetic neutrons from the ${}^7\text{Li}(p,n){}^7\text{Be}$ reaction : for this purpose the time-of-flight between START detector and a capacitive beam pick-off upstream of the Li target is recorded.

Charged particles from the hydrogen target at 0° are selected by a 4.6 cm diameter collimator at 1.15 m from the target, then they enter a magnetic spectrograph composed of a quadrupole doublet and a dipole magnet, of 27° bending angle. In the focal plane of the spectrograph, at 5 m from the target, detectors are located : first a 0.1 cm thick rectangular (50 x 20 cm^2) scintillator (STOP), then a hodoscope (H) made of 23 vertical scintillators (20 cm high, 1, 2 or 3 cm wide depending on their position, and 0.5 or 1 cm thick) and finally a 0.2 cm thick rectangular scintillator (50 x 20 cm^2) (ANTI).

The data taking proceeds as follows : a 25 μA , 65 MeV proton beam from the Louvain cyclotron bombards the Li target ; the bursts width is reduced to 1 ns using a slit near the cyclotron center. The TOF between the START detector and the BPO, as well as the TOF between the START and the STOP detector are recorded. The amplitude of each detector is also registered. All parameters are stored on magnetic tape via a CAMAC interface coupled to a computer. A CAMAC gate is defined as $\text{START} \times \text{BPO} \times \text{STOP} \times \text{H} \times \overline{\text{ANTI}}$ for a "deuteron" (not only capture deuterons and bremsstrahlung protons are selected this way, but also charged particules from neutron reactions on the target windows and on the START detector), and as $\text{START} \times \text{BPO} \times \text{H} \times \text{ANTI}$ for a "proton" (mostly n+p elastic protons at 180° c.m. are selected by this gate, and used for the normalization). Runs are alternated

between hydrogen and empty target ; the monitor is the integrated current in the carbon beam stopper. The spectrometer acceptance $e(\theta)$ inside the collimator is calculated by a Monte-Carlo method, for backward and forward deuterons and for elastic protons. The transmission was checked using elastic protons through different collimator diameters.

The data analysis starts by selecting the monoenergetic neutrons from the START-BPO spectrum ; then two bidimensional spectra are reconstructed : the START-STOP TOF versus the hodoscope scintillator (or the particle momentum), and the STOP amplitude versus the hodoscope scintillator ; both are used to discriminate between protons and deuterons. The selected deuterons are integrated in the hodoscope amplitude spectra, yielding the backward and forward deuteron peaks (figure 3), for which the signal over background ratio is respectively 0.3 and 0.5. Protons for the normalization are obtained from the "proton" gate runs, with a S/B ratio of 40.

Cross sections are extracted the following way : the measurement yields the two ratios $\frac{D_f}{P}$ and $\frac{D_b}{P}$, each one being equal to a cross section ratio :

$$\frac{D_f}{P} = \frac{\int_0^{\theta_{\max}^f} (d\sigma/d\Omega)_c(\theta) d\Omega e_f(\theta)}{\int_0^{\theta_{\max}^f} (d\sigma/d\Omega)_{el}(\theta) d\Omega e_p(\theta)}$$

and

$$\frac{D_b}{P} = \frac{\int_{\theta_{\max}^b}^{\pi} (d\sigma/d\Omega)_c(\theta) d\Omega e_b(\theta)}{\int_{\theta_{\max}^b}^{\pi} (d\sigma/d\Omega)_{el}(\theta) d\Omega e_p(\theta)}$$

the f, b and p indices stand respectively for forward and backward deuterons and for protons ; $(d\sigma/d\Omega)_c(\theta)$ is the capture cross section ; $(d\sigma/d\Omega)_e(\theta)$ is the n-p elastic cross section ; $e(\theta)$ is the computed spectrometer acceptance.

The elastic cross section is taken from a recent phase-shift analysis ⁵⁾. The capture cross section is translated into the inverse reaction in the c.m. system, and it is expressed ¹⁾ as :

$$\frac{d\sigma}{d\Omega}(\theta) = a + b \sin^2\theta + c \cos\theta + d \sin^2\cos\theta + e \sin^4\theta$$

The coefficients b, d and e are taken from a global fit of all the previous experimental data ⁶⁾ : one can then extract (a+c) and (a-c) which are the 0° and 180° cross section values.

The final result is

$$\frac{d\sigma}{d\Omega}(0^\circ) = 4.70 \pm 0.25 \text{ } \mu\text{b/sr}$$

$$\frac{d\sigma}{d\Omega}(180^\circ) = 3.90 \pm 0.40 \text{ } \mu\text{b/sr}.$$

The quoted error is purely statistical. Two other errors can be traced down :

- 1) The uncertainty on the fitted coefficients (b, d and e) has a very small effect on (a+c) and (a-c). The additional error is of the order of 0.05 $\mu\text{b/sr}$.
- 2) The normalization to the 180° n-p elastic cross section also brings some additional uncertainty. Our group has recently measured the back angle-over-90° cross section ratio ⁷⁾ for the n-p elastic scattering ; the measured ratio was in good agreement with a recent phase shift analysis ⁵⁾. As the 90° cross section absolute value is strongly constrained by the well known total cross section, the estimated error on the 180° cross section is about 3 % ⁸⁾.

The 0° measurement is compared at figure 1 with the other data. It is important to point out that the "c" coefficient is now positive, in good agreement with the global fit ⁶⁾.

Let us now quickly review some attempts to reproduce the data : as mentioned above, the "standard model" ¹⁾ used a Hamada-Johnston potential to calculate wave functions, the transition amplitude included terms up to the dipole-octupole interference and nucleons were supposed pointlike. Trying different potentials did not help ; an unphysical D-state percentage was requested to fit the data. Adding higher multipoles was of very small effect ⁹⁾. Coming to the third feature, it should be recalled that mesonic exchange currents are implicitly included in wave functions, for the electric transitions (Siegert theorem) : thus only the nucleonic electric charge density (ρ_1) enters the calculations. A promising way has been recently to add "relativistic corrections" to ρ_1 ¹⁰⁾ (see figure 1).

However, in view of the importance of those relativistic corrections, a fully relativistic theory should be developed (potentials e.g. are non-relativistic). For a complete description of the calculations see ref. 11.

4. THE TOTAL CROSS SECTION (σ_t)

The constant term in the angular distribution which is overestimated by all the calculations enters σ_t as a " $4\pi a$ " term. Unless there is some cancellation with other coefficients, calculations of σ_t should also be in disagreement with measurements.

In fact the situation is not clear : in the 20-100 MeV neutron energy range (corresponding to about 10-50 MeV γ -rays for the photodisintegration), calculations were very stable versus e.g. the nucleon-nucleon potential and differed by at most a few percent from the so called "pole cross section", which is the incoherent sum of a pure E1 and a pure M1 contribution using asymptotic wave functions, possibly with an effective range correction ¹²⁾. A fit of all the existing data ⁶⁾ until 1982 did not show a strong disagreement with calculations. Recently however, measurements done at Rossendorf ¹²⁾

and Louvain-la-Neuve ⁷⁾ were not in agreement with the calculations, whereas a photodisintegration measurement performed at Frascati ¹³⁾ showed no contradiction with σ_{Pole} (figure 4). It is interesting to note that the introduction of the relativistic corrections into the electromagnetic operator (see 3.), had some influence also on the total cross section in the sense that calculations done with different potentials are now ¹⁰⁾ much more scattered than before.

A measurement of σ_t is presently underway at Louvain-la-Neuve. The principle is simple : a large scintillator ($65 \times 65 \text{ cm}^2$), viewed by 8 photomultipliers is located at 2 m from a liquid hydrogen target, in order to cover the entire solid angle of the deuterons. In this case, the neutron flight path from the lithium to the hydrogen target is larger (6.7 m) to ensure a better energy selection of the neutrons. Protons elastically scattered at a forward lab angle (7° , or 166° c.m.) are detected in a $3 \times 3 \text{ cm}^2$ scintillator and used for normalization. Deuterons are selected in a bidimensional spectrum, the amplitude of the E scintillator versus the time-of-flight between the hydrogen target (in fact, a thin scintillator downstream of the target) and the E scintillator.

5. THE HARD BREMSSTRAHLUNG

In a n-p "hard" bremsstrahlung ($n+p \rightarrow n+p+\gamma$), the γ -ray carries away as much energy as it is allowed by the kinematics (i.e. about half the neutron lab energy). This means that very little is left over as internal energy to the outgoing n-p pair, which simulates perfectly the unbound 1S_0 deuteron state (the so-called d^*).

Having a small relative energy, the n-p pair has also a small relative angle in the lab and both nucleons can be detected and localized in three successive sets of detector planes located around 0° . The first two are made of 10 x and 10 y $40 \times 4 \text{ cm}^2$ strips of 1 mm thick scintillator to locate protons. Neutrons are detected in third plane made of 100 plastic scintillator blocks ($4 \times 4 \text{ cm}^2$, 5 cm thickness). A coincidence is requested

between a neutron and a proton detector. Data were taken and are presently analyzed. They will also give more insight on the non-coplanar bremsstrahlung events which were not studied before.

ACKNOWLEDGEMENTS

I wish to thank my colleagues at Louvain-la-Neuve, C. Dupont, P. Lipnik, P. Macq, A. Ninane, Sindano W.K. and P. Wauters, for many useful discussions.

REFERENCES

1. Partovi, F., Ann. Phys. (N.Y.) 27, 79 (1964)
2. Hugues, R.J. et al., Nucl. Phys. A267, 329 (1976)
3. Gilot, J.F. et al., Phys. Rev. Lett. 47, 304 (1981)
4. Meyer, H.O. et al., Phys. Rev. C31, 309 (1985)
5. Arndt, R.A. and Roper, L.D., NN interactive program
6. De Pascale, M.P. et al., Phys. Lett. 119B, 30 (1982)
7. Bol, A. et al., Phys. Rev. C32, 308 (1985)
8. Dupont, C. et al., Nucl. Phys. A445, 13 (1985)
9. Friar, J.L. et al., Phys. Rev. C30, 441 (1984)
10. Cambi, A. et al., J. Phys. G10, L11 (1984) ;
Pandey, L.N. and Rustgi, M.L., Phys. Rev. C32, 1842 (1985)
11. Proc. of the Workshop on radiative processes in few nucleon systems,
Canad. J1 of Physics 62, 1019-1128 (1984)
12. Blatt, J.M. and Weisskopf, V.F., Theoretical nuclear physics (Springer,
Berlin 1979)
13. Stiehler, Th. et al., Phys. Lett. 151B, 185 (1985)
14. Bernabei, R. et al., Internal report LNF-86/3(P), (1986)

FIGURE CAPTIONS

Figure 1 : 0° deuteron photodisintegration cross section versus γ -ray energy. Black dots are from Mainz ²⁾ ; the remaining three data are n-p capture data translated into photodisintegration : cross (Louvain-la-Neuve ³⁾), triangle (Indiana ⁴⁾) and open dot (Louvain-la-Neuve, present work). The solid curve is Partovi's calculation, the dashed curve is from Cambi et al. ¹⁰⁾.

Figure 2 : a : Neutron source

b : Set-up for the measurement of the 0° and 180° n-p capture cross section.

Figure 3 : Backward and Forward deuterons from n-p capture after subtraction of the empty target contribution.

Figure 4 : Total capture or photodisintegration cross section versus γ -ray energy, normalized to $\sigma_{\text{pole}}^{12)}$. The hatched area is the result of a global fit to all data ⁶⁾ prior to 1982. Open dots are measurements at Louvain-la-Neuve ⁸⁾, crosses are photodisintegration data from Frascati ¹⁴⁾.

Fig. 1

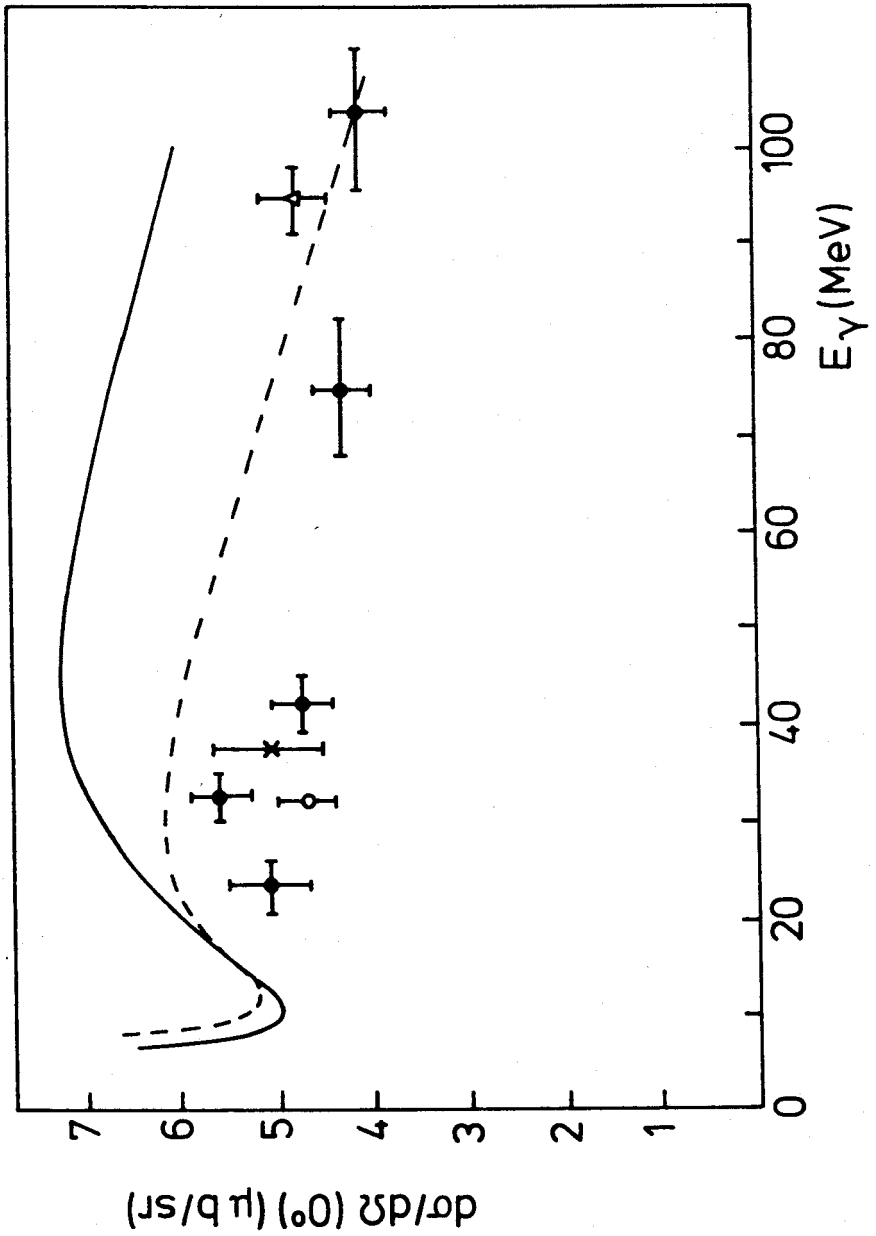


Fig. 2a

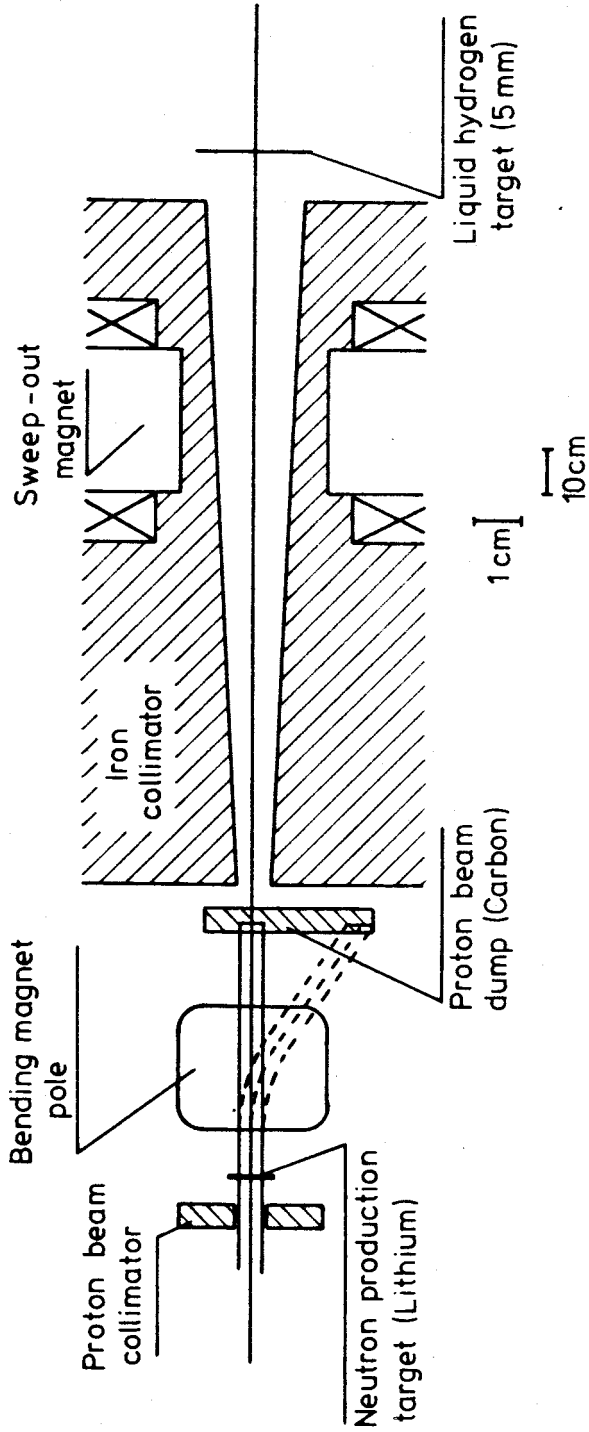


Fig. 2b

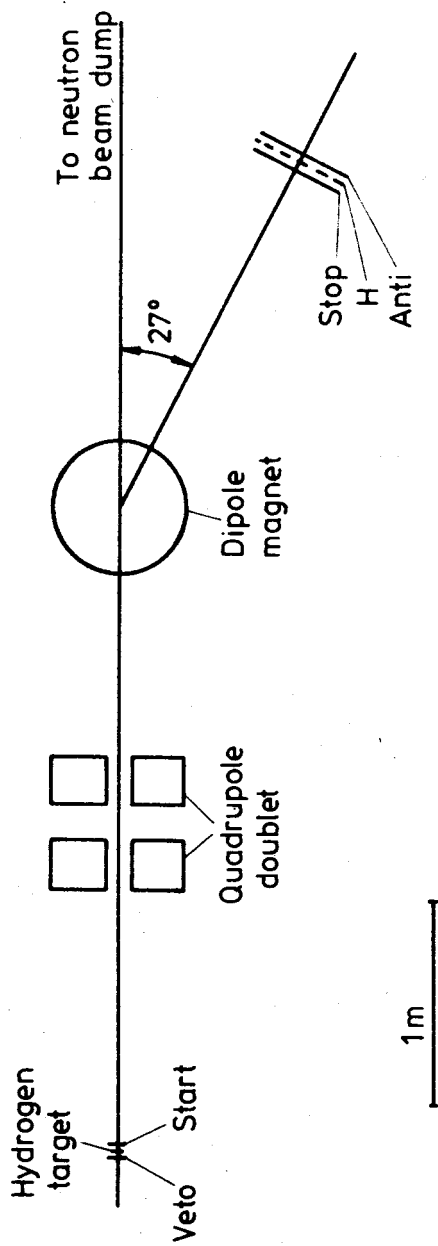


Fig. 3

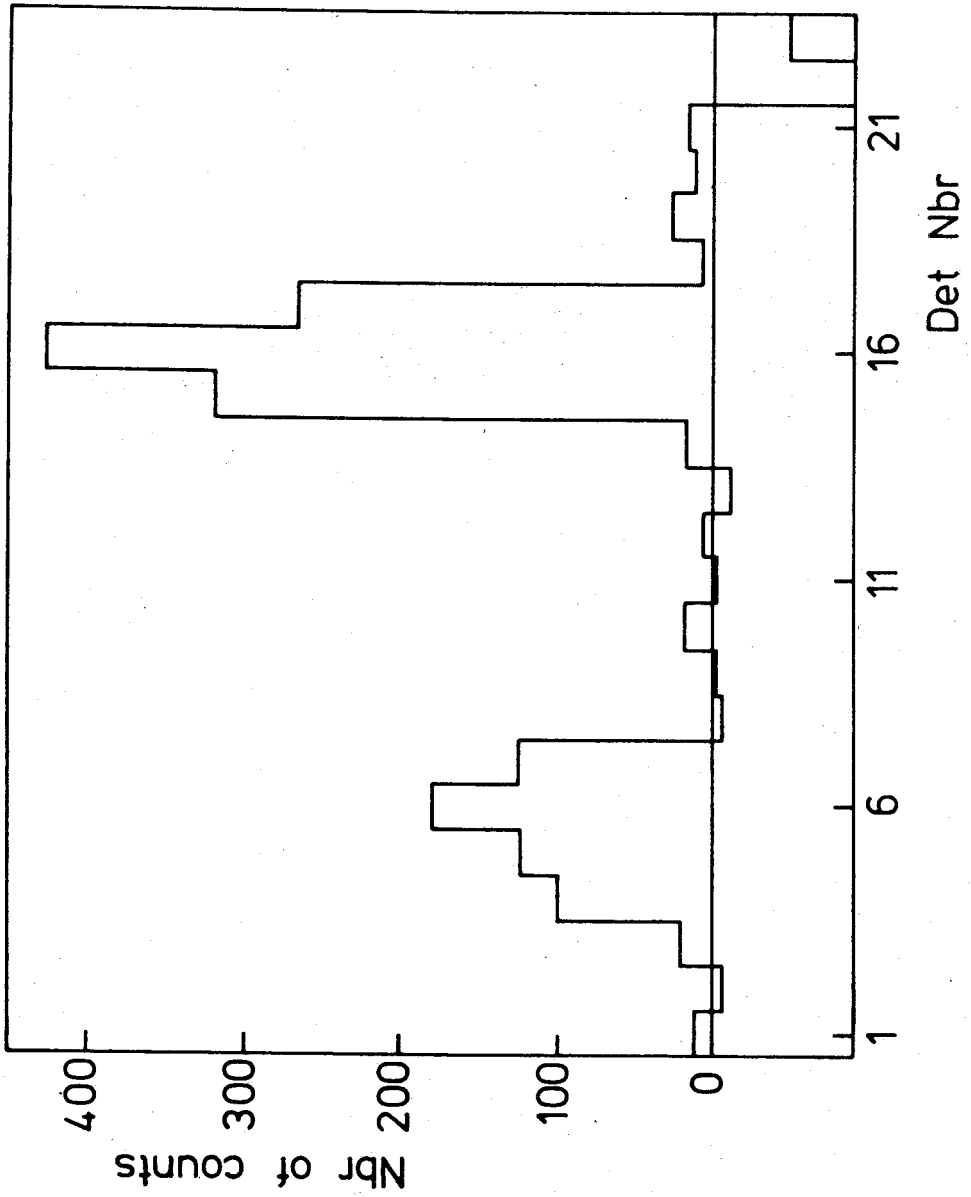
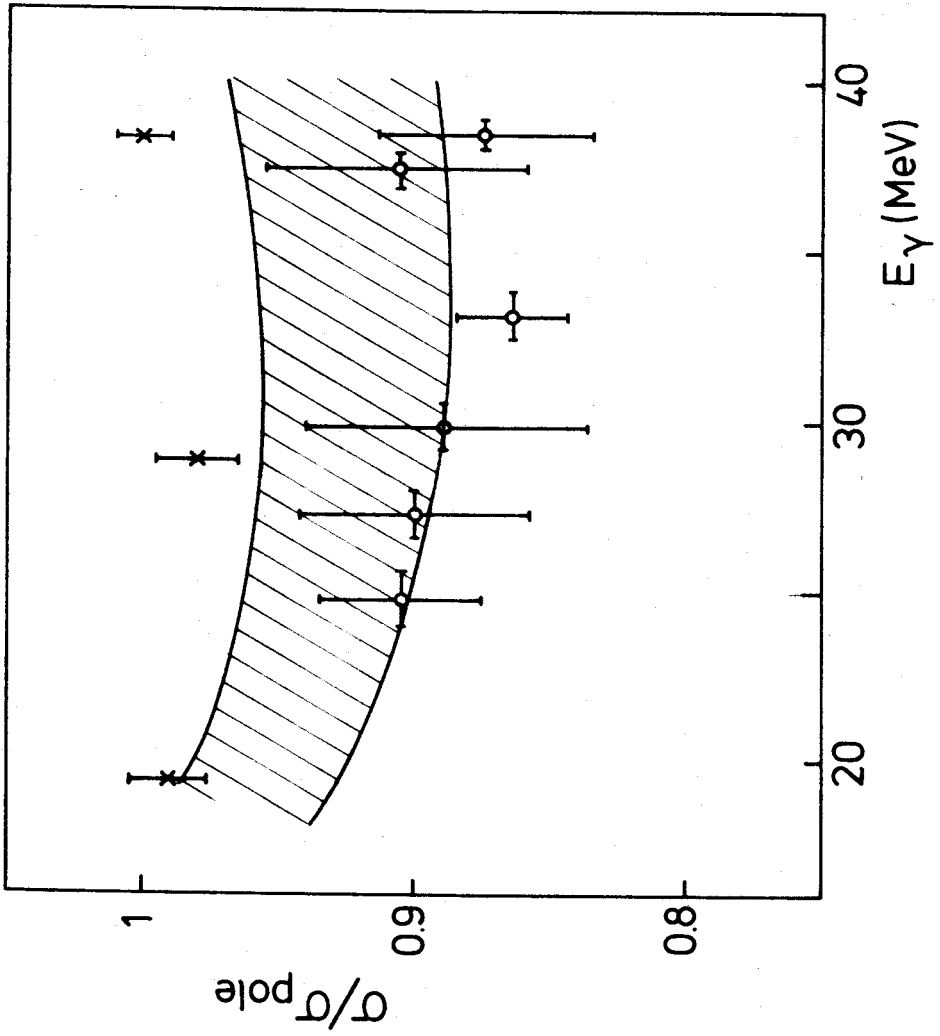


Fig. 4



A KINEMATICALLY COMPLETE n-D-BREAK-UP EXPERIMENT AT $E_n = 13 \text{ MeV}^+$)

K. Geißdörfer, R. Lin, A. Strate, J. Böttcher, J. Cub, E. Finckh, G. Fuchs, B. Kratz, S. Schindler, M. Seiter; W. Tornow*)

Physikal. Institut, Universität Erlangen-Nürnberg, Erlangen, West Germany

At the Erlangen Neutron Scattering Facility¹⁾ a well-collimated neutron beam is produced via the $D(d,n)^3\text{He}$ reaction. The iron collimator is embedded in a solid concrete wall of 120 cm thickness which completely separates the experimental hall from the neutron source. We are investigating the n-D-break-up reaction in a kinematically complete experiment. The proton energy is measured in a deuterated NE 232 target scintillator. After a flight path of 45 cm the two outgoing neutrons are detected by 22 NE 213 scintillators positioned symmetrically to the beam axis. This arrangement is necessary for the planned measurement of the analyzing power and doubles the count rate of the cross section measurement. Four of these detectors are placed out of plane, forming space star configurations with detectors in plane. More than 30 different break-up configurations including FSI, QFS, collinearity, space and coplanar star are measured simultaneously (see fig. 1).

in plane	130°	0	0		0	0	X	X	X	X	X
	110°	0	0	FSI		0	X	X	X	X	X
	90°						X	X	X	X	X
	75,5°							X	X	X	X
	62,5°				COLL			X	X	X	X
	50,5°				FSI	COLL			X	X	X
	50,5°	SST	SST	CST			COLL			0	0
	39°				QFS		FSI	COLL			0
	17°					CST				FSI	
	50,5°					SST				0	0
out of plane	50,5°					SST				0	0
		50,5°	50,5°	17°	39°	50,5°	62,5°	75,5°	90°	110°	130°
		above	below	in plane							

FSI: Final State Interaction
 COLL: Collinearity
 QFS: Quasi Free Scattering
 CST: Coplanar Star
 SST: Space Star
 0: one neutron energy below threshold ($\leq 400 \text{ keV}$)
 X: kinematically not allowed

The azimuth angle is $\phi = 180^\circ$ for all detector combinations in plane, $\phi = 120^\circ$ for a combination with one detector out of plane and $\phi = 60^\circ$ for two detectors out of plane.

Fig. 1:

Angular positions of the neutron detectors. Break-up events are simultaneously measured by each detector on the one side in coincidence with each detector on the other side and the central target detector.

+) supported by Deutsche Forschungsgemeinschaft

*) Universität Tübingen, now at Duke University, North Carolina, U.S.A.

For each break-up event the proton energy, the time-of-flight of both neutrons, their flight time difference and the proton recoil energies in the NE 213 detectors are recorded. Additionally the elastic n-D-scattering is measured for on-line control of the experiment and shall be used for normalization of the break-up cross section.

Due to effects of the finite geometry of the experimental set-up the data are spread around the exact kinematic curve (S-curve), see fig. 2. A Monte-Carlo code simulates all experimental uncertainties and calculates probability factors, which are used to reallocate the measured events back to the S-curve. In addition this method sets windows for the three particle energies, which further reduce the background of break-up events induced by low energy neutrons.

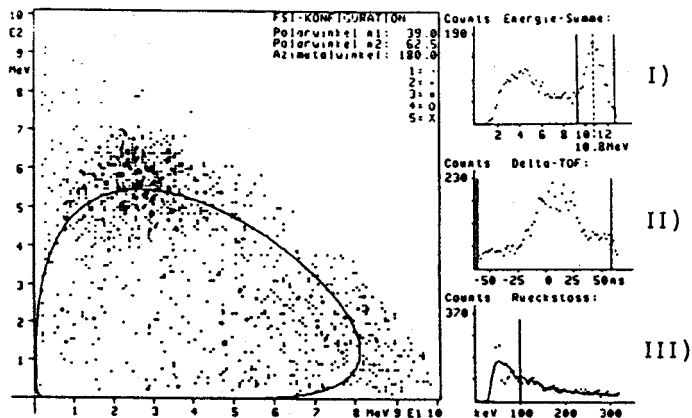


Fig. 2:

Break-up data of the np-FSI. Plotted is the energy of neutron 1 versus the energy of neutron 2. The solid line shows the exact kinematic curve.

- I) Energy sum of the three nucleon energies
- II) Time-of-flight difference of the two neutrons
- III) Proton recoil spectra of the neutron detectors

Fig. 3 shows preliminary differential cross sections of four special configurations. The data are corrected for flux attenuation in the target and for relative detector efficiencies. The cross section is normalized to a Fadeev calculation^{*)} based on a simple two nucleon potential (modified Bruinsma-Stuivenberg code). The size of the error bars results from statistics (about 120 hours beam time) and uncertainties due to detector efficiencies.

To obtain better energy resolution and to increase the count rate further measurements will be performed with a neutron flight path of 70 cm and larger detector volumes. Measurements of the analyzing power are in progress.

^{*)} We thank Dr. Krug and Dr. Lekkas, Bochum, for these calculations.

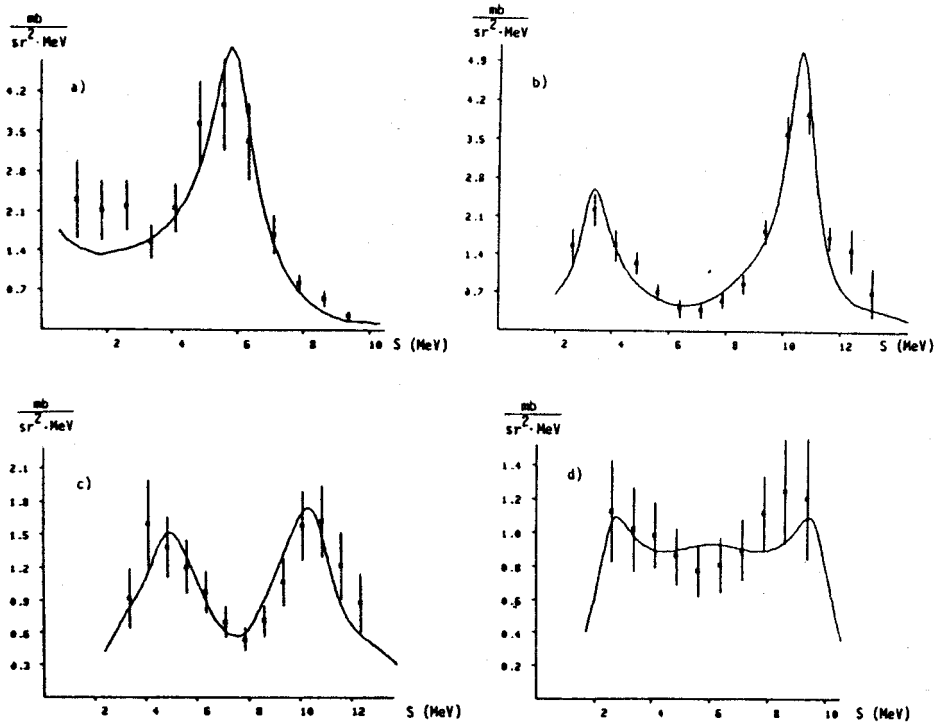


Fig. 3:

$\frac{d\sigma}{d\Omega_1 d\Omega_2 dS}$ of four special $D(n, nnp)$ configurations. Solid lines are Faddeev calculations (modified Bruinsma-Stuivenberg code).

- a) FSI: $\theta_1 = 17^\circ$, $\theta_2 = 110^\circ$, $\varphi = 180^\circ$
- b) FSI: $\theta_1 = 39^\circ$, $\theta_2 = 62.5^\circ$, $\varphi = 180^\circ$
- c) Coll.: $\theta_1 = 50.5^\circ$, $\theta_2 = 62.5^\circ$, $\varphi = 180^\circ$
- d) Space Star: $\theta_1 = \theta_2 = 50.5^\circ$, $\varphi = 120^\circ$

Reference

1. Blank H. et al., Nucl. Instr. and Meth. A240, 311 (1985)

EVIDENCE FOR A SIMULTANEOUS BREAKUP COMPONENT IN NUCLEON SCATTERING ON CARBON

B. Antolković

Ruder Bošković Institute, Zagreb, Yugoslavia

The continuum of the $^{12}\text{C}(p,p')$ and $^{12}\text{C}(n,n')$ energy spectra, underlying the peak structure is analysed in terms of the phase space spectra of the kinematically allowed three- and four-body final states: N,α , ^8Be and N,α,α,α . A good agreement obtained with the experimental data yields a strong evidence on the presence of the simultaneous breakup reaction mechanism in the nucleon scattering on carbon.

1. INTRODUCTION

The particle spectra from the interaction of light nuclei generally exhibit large continua which can be attributed to i) transitions to broad resonant levels, ii) peripheral phenomena (QFS and FSI) and iii) other phenomena resulting in several particles in the outgoing channel. The first two processes have been extensively studied, but the third one, though representing a large part of the continuum, has been treated as a background and more or less arbitrarily subtracted.

Recent studies of the continuous inclusive particle spectra from the reaction and particle scattering on light nuclei have shown that a considerable part of the total cross section is due to a simultaneous n-body breakup, a process with a constant matrix element and hence with a phase-space-like energy distribution¹⁻⁵⁾.

Since carbon is a light nucleus the energy spectra in nucleon scattering on ^{12}C have been analysed in terms of the simultaneous breakup mechanism, with the aim to investigate the role of this mechanism in reactions induced on carbon, and if so, to calculate the shape of the energy spectrum of the continuous contribution. This spectral shape is highly needed for correct subtraction of the continuum from the total spectrum in order to obtain proper data on the superimposed peaks.

2. DATA ANALYSIS

The energy spectra of protons⁶⁾ ($E_0 = 45$ MeV) and neutrons⁷⁾ ($E_0 = 24$ MeV) scattered on carbon are shown in Fig. 1. Both spectra show a dis-

tinct peak structure due to nucleon scattering via different ^{12}C states, but also a continuum starting with a steep rise beneath the second excited 7.65 MeV level of ^{12}C . The Q values for the $\text{N}, \alpha, {}^8\text{Be}$ and $\text{N}, \alpha, \alpha, \alpha$ breakup processes are -7.37 and -7.27 MeV, respectively. It is thus obvious that the onset of the continuum in the vicinity of the 7.63 MeV level is due to the 3-body and/or 4-body breakup.

In Fig. 1a the solid curve represents the phase space spectrum which is the sum of the 3- and 4-body phase spaces and the dashed curve is the phase space spectrum for the 3-body breakup alone. The wiggled solid curve in the first 10 MeV of the excitation range above the 3α threshold is the background as evaluated by the authors⁶⁾.

The neutron spectrum at $E_0 = 22$ MeV is shown on Fig. 1b with the full line indicating the evaluated continuous background. The spectrum represents the raw data (not corrected for the detector efficiency, etc.). The continuous component of the spectrum has been subsequently transformed to yield the ^{12}C excitation spectrum⁸⁾. This was done for a set of angles ($\theta = 20^\circ - 56^\circ$) and for $E_0 = 22$ and 24 MeV. Fig. 2. shows two typical ^{12}C excitation spectra and our fit to the experimental data with a combination of 3- and 4-body phase spaces. The fit describes satisfactorily all sets of angles, though it is only qualitative, due to a narrow energy interval of ^{12}C excitations available.

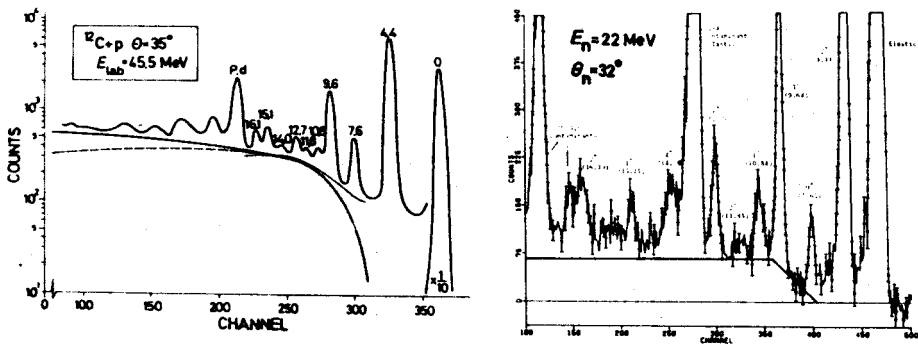


Fig. 1. Energy spectra of a) protons and b) neutrons.
For details see text.

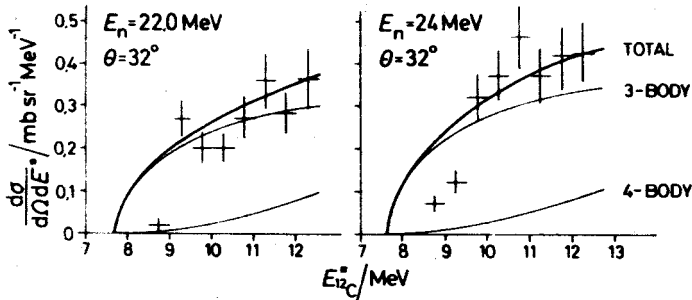


Fig. 2. Excitation spectrum of ^{12}C . For details see text.

3. CONCLUSION

A good fit obtained in the analysis of the energy continuum of the (p,p') and (n,n') scattering on carbon by a combination of 3- and 4-body phase spaces yields a strong evidence of the presence of the simultaneous breakup reaction mechanism in the nucleon scattering on carbon. The analysis also shows that special care should be taken in extracting the data for levels occurring near the 3-body threshold since a steep rise of the continuum contribution is present there. Experimental spectra in a larger range of excitations and angles are highly desirable to obtain quantitative data on the continuum component. This is of special interest when peaks of low intensities (obtained at backward angles) have to be unambiguously extracted.

REFERENCES

1. Paić, G., Antolković, B., Djaloeis A., Bojowald J., Mayer Börcke C., Phys. Rev. **C24**, 841 (1981)
2. Delbar Th., Gregoire Gh., Belery P. and Paić G., Phys. Rev. **C27**, 1876 (1983)
3. Antolković B., Paić G., Kadija K., to be published in Few Body Systems
4. Kadija K., PhD. thesis, Zagreb University, 1985.
5. Kadija K., Paić G., to be published in Phys. Rev. C.
6. Petersen E.L., Šlaus I., Verba J.W., Carlson R.F. and Richardson R., Nucl. Phys. **A102**, 145 (1967).
7. Meigooni Ali S., Petler J.S. and Finlay R.W., Phys. Med. Biol., **29**, 643 (1984)
8. Finlay R.W., private communication.

This work was supported in part by the NBS, JFP-688 Yu-US grant.

QUADRUPOLE SPECTROMETER MEASUREMENTS
OF (N, CHARGED PARTICLE) CROSS SECTIONS
OF BE, N, AND O AT $E_N = 14$ MEV*

Robert C. Haight

Los Alamos National Laboratory⁺ and
Lawrence Livermore National Laboratory
Los Alamos, New Mexico 87545, USA .

Neutron-induced reactions that result in charged particles are of importance in basic and applied nuclear physics. For light nuclei (e.g. $A < 20$), reaction models are more complicated because the level density of excited states does not allow statistical averaging over many final states. The matrix elements between many individual states must be known to calculate cross sections and seldom is this information available. Direct measurements of the cross sections are therefore necessary to provide data for applications. These (n, charged particle) cross sections are required for nuclear data bases in the calculations of fusion and fission reactor performance including neutron transport, heating, and radiation damage. They are also necessary for dosimetry.

The present measurements are a continuation of the program in (n, charged particle) reaction studies using a magnetic quadrupole spectrometer.¹⁻⁴⁾ Targets of Be, N and O were chosen because of the importance of these elements in fusion reactor design and, for N and O, in biological materials. We expected to observe charged particles with low energy since, for each target, there is a three- or four-body final state consisting of one or more alpha particles. The experimental arrangement was therefore similar to our previous study of the $^{12}\text{C}(n, n'\alpha)$ reaction.⁴⁾ Some details are that the targets were Be (0.25 mg/cm⁻² on a thin gold backing), N (in the form of TaN, 0.3 mg/cm⁻², on either thin Au or Ta

backings), and O (in the form of WO_3 on a Au backing). The angular range from 30 to 135 degrees was studied for alpha particles above 1 MeV.

The energy distribution of alpha particles detected at 30° from the beryllium target is shown in Fig. 1. Reactions leaving residual ^6He in the 1.8 MeV state are indicated by the resolved peak at 9.6 MeV alpha-particle energy. This particular reaction contributes only a small part of the total alpha particle production, the majority being continuum alphas from the four-body decay channel.

A much different spectral shape is found for alpha particles emitted from the nitrogen target, also at 30 degrees (Fig. 2). Here a large part of the total alpha-particle production is given by discrete transition to excited states of ^{11}B . Again there is an apparent continuum of alpha particles at low energy suggesting that multibody final states are contributing. This result is similar to that for oxygen where the transition to the ground state of ^{13}C constitutes a large part of the total alpha-particle production cross section.

These preliminary data are being reduced to angle-integrated cross sections where they will be compared with other (n,charged particle) data and with the total helium production as reported recently by Kneff *et al.*⁵⁾

1. S. M. Grimes, R. C. Haight, K. R. Alvar, H. H. Barschall, and R. R. Borchers, Phys. Rev. C 19, 2127 (1979).
2. K. R. Alvar, H. H. Barschall, R. R. Borchers, S. M. Grimes, and R. C. Haight, Nucl. Instrum. Methods 148, 303 (1978).
3. R. C. Haight, S. M. Grimes, R. G. Johnson, and H. H. Barschall, Phys. Rev. C. 23, 700 (1981).
4. R. C. Haight, S. M. Grimes, R. G. Johnson, and H. H. Barschall, Nucl. Sci. Eng. 87, 41 (1984).
5. D. W. Kneff, B. M. Oliver, H. Farrar, IV, and L. R.

Greenwood, Nucl. Sci. Eng. 92, 491 (1986).

* Work performed with Dr. S. M. Grimes under the auspices of the US Department of Energy, Office of Basic Energy Sciences.

+ Present address

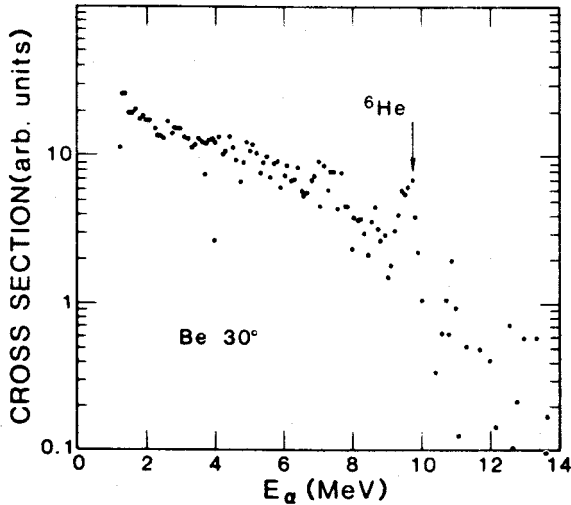


Figure 1 - Spectrum of alpha particles from 14-MeV neutron bombardment of beryllium.

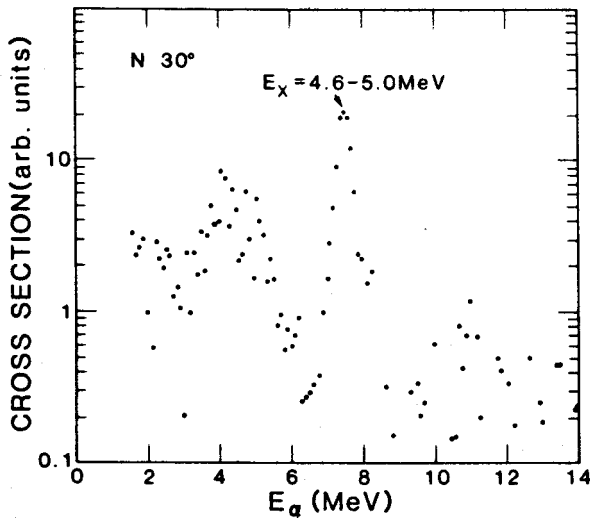


Figure 2 - Spectrum of alpha particles from 14-MeV neutron bombardment of nitrogen.

INTERACTION OF NEUTRONS WITH ^9Be AT 14.6 MeV - THE FOUR BODY BREAKUP $2n+2\alpha$

D. Ferenc, B. Antolković, G. Paić, M. Zadro and S. Blagus
Rudjer Bošković Institute, Zagreb, Yugoslavia

Measured alpha particle spectra in the angular range 0° - 100° and complementary neutron spectra from the literature have been analyzed in terms of a combination of sequential and simultaneous breakups. The results show that $\approx 50\%$ of the total inelastic cross section is due to simultaneous breakup $n+^9\text{Be} \rightarrow n+\alpha+^5\text{He}$, while the remainder is mainly due to neutron inelastic scattering to the three excited states of ^9Be : 2.43, 6.76 and 11.28 MeV.

1. INTRODUCTION

Nuclear data on neutron induced four body breakup $n+^9\text{Be} \rightarrow 2n+2\alpha$ are considered as high priority data for fusion reactor technology, specifically for blanket application. Besides the cross section, the reaction mechanism and the angular distributions of the outgoing particles should be known as well, since they both may influence considerably the spectrum of secondary particles.

So far, alpha particle spectra have been measured only with the aim to determine the contributions of α_0 and $^6\text{He}_{0,1}$ leading to the ground and 1.8 MeV excitation of ^6He . The alpha continuum has, however, not been studied in details. The present experiment was performed with the aim to measure the alpha particle spectrum and to make a comparative analysis of the measured α spectra and of neutron spectra from Takahashi et al.¹

2. EXPERIMENTAL PROCEDURE

The measurement was performed at 14.6 MeV. The alpha particles from the interaction of neutrons with ^9Be were detected using a standard telescope counter system consisting of two hydrogen filled proportional

ΔE -counters. A surface barrier Si detector was used to measure the residual energy. The ^9Be target was a 2.3 mg/cm^2 thick foil mounted onto a gold backing. The detection threshold for alpha particles starting in the middle of the target is 3 MeV. The residual energy spectra were corrected for energy losses in the target and ΔE counters, and further processed to obtain a linear energy scale.

3. ANALYSIS OF DATA

The α particle and neutron continuum of the $2\alpha+2n$ final state is due to the reaction channels proceeding via the particle unstable states of ^9Be , ^6He and ^5He , as well as to the 3-body $n, \alpha, ^5\text{He}$ (with subsequent decay $^5\text{He} \rightarrow \alpha + n$) and 4-body $2n, 2\alpha$ simultaneous breakup.

In course of the analysis it has been found that:

- The most important contribution to the neutron inelastic scattering is the transition to the 2.43 MeV state of ^9Be . All decay fragments occur in the low energy part of the alpha and neutron spectrum.

- The contribution of inelastic scattering to ^9Be levels above 2.43 MeV is relatively small and spread over a large energy region. It is thus unable to account for the continuum observed.

- The reaction $^9\text{Be}(n, ^5\text{He})$ may be assumed to have approximately the same cross section as the $^9\text{Be}(n, ^6\text{He})$ reaction ($\approx 10 \text{ mb}$), since both can be interpreted as pickup reactions of alpha or ^5He particle, respectively.

Based on the preceding statements, we conclude that the above mentioned reaction channels are responsible only for a fraction of the continuous alpha and neutron spectra and that a considerable part of the total cross section is due to a simultaneous breakup into the available phase space. Satisfactory fits to the experimental data may be obtained using only the 3-body breakup channel. The 3-body breakup was calculated by the Monte Carlo method simulating complete events in the simultaneous($n_1, \alpha_1, ^5\text{He}$)-sequential($^5\text{He} \rightarrow \alpha_2 + n_2$) decay chain. In fig. 1 we show a typical qualitative fit to a neutron spectrum with n_1 and n_2 components of the 3-body breakup channel and of the sequential decays $^9\text{Be}(n, n_1)^9\text{Be}_i(2\alpha, n_2)$ (i being the 2.43, 6.76 and 11.28 MeV level of

^9Be). Adopting the same criteria for alpha particle spectra, we have obtained similarly good qualitative fits.

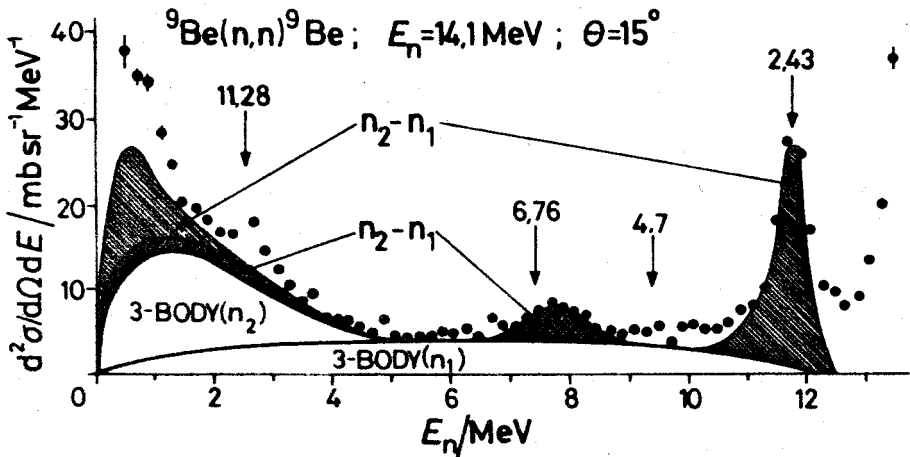


Fig. 1. Neutron spectrum. For details see text.

4. CONCLUSION

The analysis of alpha and neutron spectra created by interaction of 14 MeV neutrons with ^9Be has proved that a very satisfactory fit may be achieved invoking only direct processes to the 2.43, 6.76 and 11.28 MeV states of ^9Be , and the breakup of the $n+^9\text{Be}$ system into $n+\alpha+^5\text{He}$ in a statistical way. This is in contrast to the treatment of the same spectra attempted by Perkins et al.² introducing many different levels of ^9Be that are usually only weakly excited both in (p,p') and (n,n') . The contribution of the statistical breakup accounts for $\approx 50\%$ of the measured cross sections in the analyzed angular range.

This work was partially supported by the International Atomic Energy Agency (Contract No 3312/RB), Yu-US grant (NBS, JFP-688) and by SIZZR of SR Croatia (Contract No 07/NE).

REFERENCES

1. A. Takahashi, et al., Oktavian Report, Report A-83-01, Osaka University, Japan (1983).
2. S.T. Perkins, Nucl. Sci. Eng., 90, 83 (1985).

${}^4\text{H}$ AND $(n, \alpha x)$ REACTIONS ON ${}^6\text{Li}$ AND ${}^7\text{Li}^+$

D. Miljanić, S. Blagus, M. Zadro and D. Rendić

Rudjer Bošković Institute, POB 1016, 41001 Zagreb, Yugoslavia

The cross sections for the ${}^6\text{Li}(n, \alpha x)$ and ${}^7\text{Li}(n, \alpha x)$ reactions have been measured at 14.6 MeV by the detection of α -particles in coincidence with other charged particles (x). Prominent structures in the coincident α -particle energy spectra have been observed only in the case of ${}^7\text{Li}$. They could be attributed to the processes involving state(s) of ${}^4\text{H}$. A calculation using ${}^4\text{H}$ ground state parameters ($E_r=2.7$ MeV and $\gamma^2=2.3$ MeV) as obtained from the most complete study of the ${}^7\text{Li}(\pi^-, tt)n$ reaction fits satisfactorily the higher part of the spectra.

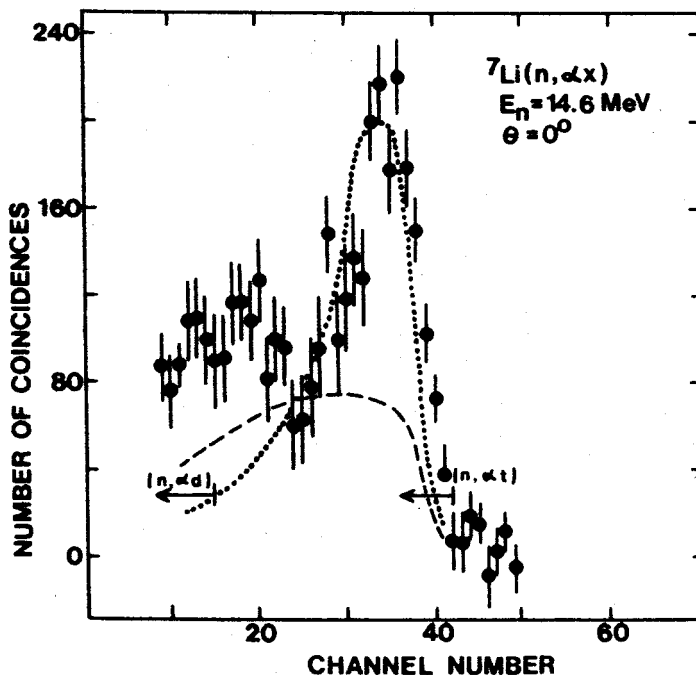


Fig. 1 Coincident α -particle spectrum from ${}^7\text{Li}(n, \alpha x)$ reaction

*The complete version is going to be published in Physical Review C.

Chapter IV

EXPERIMENTAL TECHNIQUES AND NEUTRON SOURCES

D-T NEUTRON SOURCES

H.H. Barschall

The University of Wisconsin, Madison, WI 53706 USA

An update of the status of D-T neutron sources is given, including some historical background and a review of recent developments in the construction, operation, and planning of D-T sources.

1. INTRODUCTION

In 1979 the present author reviewed D-T neutron sources. This review was published in 1983 as a chapter¹⁾ in the book "Neutron Sources for Basic Physics and Applications". In 1984 additional information about D-T sources, especially developments in Eastern Europe, was reported at a symposium held in Gaussig (GDR) under the heading "Neutron Generators and Application".²⁾

The present report is an attempt to provide some historical background and to review recent developments in the manufacturing, operation, and planning of D-T neutron sources.

D-T sources have the advantage over other neutron sources that they are relatively compact and intense and do not emit gamma rays. They have the advantage over radioactive sources that they can be turned off or pulsed and that they produce neutrons with a small energy spread. On the other hand, they have the disadvantage that for some applications the source strength cannot readily be made as high as is desirable, that the energy of the neutrons cannot be varied very easily, and that tritium is a hazardous material.

Until the relatively recent past the advantages of D-T neutron sources appeared to outweigh their disadvantages, but more recently the interest in D-T neutron sources has decreased to the extent that many of the commercial suppliers no longer manufacture such sources and many fewer D-T sources are operating now or are being planned for the future than ten years ago.

2. USE OF D-T SOURCES FOR NUCLEAR PHYSICS

Shortly after appreciable amounts of tritium became available, the first D-T neutron source was developed at Los Alamos early in 1948. It was immediately used to measure neutron interaction cross sections at 14 MeV. At the time, very little was known about the interactions of 14 MeV neutrons so that a large body of information could be gathered in a short time. As might be expected, the first experiment we did was to measure the angular distribution of 14 MeV neutrons scattered by protons, and this was published in 1949.³⁾

Now 14 MeV neutron sources are rarely used for studying the properties of nuclei, but there remains an active interest in measurements of the nuclear interactions of 14 MeV neutrons for applied problems. Even though D-T sources produce large fluxes of neutrons of known energy, the results of measurements are often surprisingly inconsistent. As an example, recent measurements^{4,5)} of the cross section for the reaction $^{12}\text{C}(n,\alpha)$ differ by a factor of almost three. This cross section is particularly important for applications. There are other important cross sections for which different measurements do not agree well. One reason for differences in the results of various measurements may be that the effective neutron energy may differ.⁶⁾ The effective neutron energy depends on the tritium distribution in the target if a solid target is used, and

on the beam composition if an unanalyzed deuteron beam is used. The interaction cross section, especially of light target nuclei, may vary rapidly with neutron energy, which may explain some of the inconsistencies. In spite of the importance of some of these cross sections, few such measurements are in progress.

3. ROTATING TARGET NEUTRON SOURCES - A BRIEF HISTORY

In 1969 the head of our radiotherapy department visited me to tell me about recent successes in the use of fast neutrons in the treatment of malignant disease. He had just returned from London, England, where a cyclotron was used as a neutron source, and he was wondering whether a D-T neutron source might be preferable.

I expressed doubt that a solid target could provide enough intensity, but mentioned the possibility of using a gas target. To my surprise I found out that this casual remark led to the construction of a gas target source at our university. This source is still in active use for radiobiological experiments, but it has never been used for therapy.

When I looked through the literature, I found a 1967 abstract⁷⁾ that described what was by far the most intense D-T source. It had been built by Rex Booth at Livermore and produced close to 2×10^{12} neutrons/sec. I visited Rex Booth and was impressed by the clever design of the rotating target that made the high source strength possible. Rex Booth was enthusiastic about working with me on trying to increase the source strength. One of the first experiments we tried was to see whether we could increase the source strength by using simultaneously atomic and molecular deuterium ions; only atomic ions were in use at the time. To our surprise, we found that even a

small admixture of molecular ions resulted in a rapid decrease in source strength. We quickly realized that the molecular ions displace tritium in the target at a depth where the atomic ions produce the highest neutron yield. This explained why the Livermore target lasted so much longer than targets at generators which used an unanalyzed deuteron beam. Although we published this observation⁸⁾ in 1972, it was not generally accepted. For example, the D-T generator built by Radiation Dynamics for the Eppendorf hospital in Hamburg used an unanalyzed beam in spite of the fact that I had tried to persuade them of the problems this would cause. More recently a small separation of the atomic and molecular beam on the target resulted in a six-fold increase in target life time.⁹⁾

To increase the output of the Livermore source we acquired a larger high voltage power supply which permitted the beam current to be increased from 8 to 25 mA. To maintain a good target life time the diameter of the rotating target was increased from 15 cm to 22 cm. With these changes a neutron source strength of $6 \times 10^{12}/\text{sec}$ was attained in 1975. This source strength should have been adequate for the use of this source for radiotherapy, but by that time the National Cancer Institute had been persuaded that the Cyclotron Corporation could manufacture a closed tube D-T source for therapy, and there was no interest in developing the Livermore design for hospital use.

When it became known that there was an intense D-T source available, material scientists interested in the fusion program began to use the source for studies of radiation damage produced by 14 MeV neutrons, but the available intensity was only marginally useful. We decided that a new facility built on the rotating target design could achieve an increase in source strength by a factor of five, and possibly even by a factor of ten. Even that was less than what was

needed to learn what would happen in a fusion reactor, but the cost of building a larger rotating target source was by one or two orders of magnitude less than the cost of building other facilities that were being proposed for materials test facilities for fusion reactors. In 1976 the U.S. Department of Energy authorized the construction of a new facility containing two high-intensity rotating target D-T sources at a cost of five million dollars. The first source became operational in 1978, the second in 1982 following an agreement with the Japanese government providing for joint funding of the operation of the source.

After this brief review of my own involvement in the use of D-T sources let me return to an overview of the applications of such sources.

4. APPLICATIONS OF D-T SOURCES

I have mentioned the use of D-T sources for obtaining nuclear data for pure and applied nuclear physics. A second area of application of D-T sources is in activation analysis to detect elements that do not readily produce observable activities with slow neutron irradiation, and for the detection of fissionable materials for safeguards applications. Although this is in principle a useful method, it does not appear to have wide uses. Whenever there are threats of explosives on airplanes, the discussion of the use of D-T sources for the detection of explosives in baggage resumes. The idea is to look for objects which have a high nitrogen content, but so far no such detection devices are in use.

A third area of applications of D-T sources is for geophysical exploration. Small diameter sealed tubes are widely used in boreholes, but probably this is of limited interest to nuclear physicists. Details about geophysical applications are often considered proprietary by exploration corporations and few details about this application are available in the scientific literature.

Ten years ago a promising application of D-T neutron generators appeared to be in radiotherapy. A compact neutron source that could be moved around the patient would have great advantages over a cyclotron which has a fixed beam. 14 MeV neutrons are more penetrating than the neutrons from 16 MeV deuterons on Be which had been used in England,¹⁰⁾ so that such neutrons could be used for treating more deep seated tumors. As a consequence, several manufacturers developed D-T neutron generators for radiotherapy which were installed in hospitals. All but one of these generators used sealed tubes to avoid the problem of having to handle tritium in a hospital. While it is relatively easy to build sealed-tube generators for low intensity applications, the problems with trying to get high intensity turned out to be much greater than the manufacturers had expected. In order to keep treatment times down to the order of 10 minutes, source strengths of the order of $5 \times 10^{12} \text{s}^{-1}$ are needed, and none of the D-T generators achieved such an intensity. At the same time radiotherapists became more interested in using neutrons of higher energy than 14 MeV in order to get even better penetration into tissue. The use of small superconducting cyclotrons appears to be a much more promising approach to obtaining high intensity and high-energy neutron sources than D-T generators.

The early successes of neutron therapy could not be reproduced at other hospitals, and the question what caused the difference has not

yet been resolved. While the present evidence does not indicate that neutrons have advantages over photons in treating all malignant diseases, there is good evidence that neutrons do have advantages in the treatment of some diseases, especially in cancers which grow slowly.¹¹⁾ There are several hospitals that will continue to use neutron radiotherapy, but only two or three centers, all in Germany, continue to use D-T neutrons.

Related to the interest in neutron therapy is a continuing effort to understand better the radiobiology that is basic to neutron therapy. For example, there is some evidence that combinations of neutron and photon treatment have advantages over either radiation alone, and there is a continuing effort to study the radiobiology of this effect. For such studies D-T sources could be used.

I have mentioned another application for which high-intensity D-T sources were desired, i.e., for the study of radiation damage caused by 14 MeV neutrons. This information is needed for the design of fusion reactors, since the first wall of a fusion reactor is bombarded by a very high flux of 14 MeV neutrons. How long the first wall of a reactor can be subjected to such a bombardment determines how long the reactor can operate without a major overhaul. The effect of 14 MeV neutrons is sufficiently different from that of fission neutrons that it appeared necessary to build intense sources that could produce neutrons of at least 14 MeV energy. Ten years ago there were several proposals to build intense neutron sources for fusion technology, and the construction of three of these was authorized in the U.S.: INS at Los Alamos, FMIT at Hanford, and RTNS II at Livermore. INS was cancelled several years ago, FMIT was cancelled more recently, and only RTNS II, the least ambitious of the three was completed. Although the RTNS II sources worked well and were used in

many radiation damage experiments, primarily carried out by Japanese scientists, the sources will be turned off shortly after the end of the current year. There are several reasons for this decision. The most important is probably that funding for fusion technology has been contracting in the U.S., largely because the energy problem appears less worisome and because fusion reactors do not appear a likely solution to the energy problem in the near future. In addition, many material scientists believe that they can obtain the needed information in other ways.

Nevertheless the Japanese scientists who have used RTNS II so successfully plan to build a similar source in Japan and to continue research with an intense source of D-T neutrons.

5. COMMERCIALY PRODUCED D-T GENERATORS

5.1 Deuteron Accelerators

Ten years ago there were several manufacturers who supplied accelerators in which several milliamperes of deuterons bombarded tritium, usually absorbed in titanium. These generators produced typically 10^{11} neutrons/sec although higher source strengths could be produced with a fresh target. Hundreds of such generators were sold for teaching, research, and applications. While I have no statistics, my impression is that not very many of them are now in operation, and no new generators are being manufactured as far as I have been able to learn. There is, however, a small company (Potentials Inc.) that buys used generators that were originally manufactured by Texas Nuclear. This company restores the machines to their original state and sells them as equivalent to new machines. Apparently several generators are bought and sold by this company every year.

5.2 Sealed Tube Generators

Two types of sealed tube generators have been available commercially: Tubes intended for high intensities and continuous operation, and low-intensity sources intended primarily for pulsed operation.

Tubes for high-intensity ($\geq 10^{12}\text{s}^{-1}$) operation have been manufactured in the U.K., Holland, Switzerland, and the U.S. Of these only the Swiss manufacturer may still offer such a system. All the units manufactured by the other companies have been shut down.

Kaman manufactures a sealed tube generator that produces up to 10^{11} D-T neutrons/sec. This tube is advertised to have more than 50% of its initial yield after 100 hours of operation, but the cost of replacing the tube is over \$15,000.

There are several manufacturers who sell closed tubes for pulsed operation, typically delivering 10^8 neutrons per pulse. Such tubes are manufactured by Sodern in France, GEC Avionics in England, and Kaman in the USA. These systems are intended primarily for geophysical and safeguards applications. In addition, several geophysical corporations, such as Schlumberger, Haliburton, Dresser, and Gearhart manufacture such tubes, but they have not been described in the literature and are not for sale.

6. EXAMPLES OF OPERATING D-T GENERATORS

6.1. RTNS II

The most intense operating D-T sources are the RTNS II sources at

Livermore.¹²⁾ They use typically 125 mA of atomic deuterium ions at 370 keV to bombard a rotating target that contains tritium in Ti. The target is 50 cm in diameter and rotates at 5000 r.p.m. A fresh target contains about 5000 Ci of tritium and produces about 3×10^{13} neutrons/sec. The source strength gradually decreases at a rate that varies from target to target. For an average target the source strength drops to half its original value after bombardment by 15 A hr. Some targets have substantially better life times, some considerably worse. The reason for the variations is not known. Targets are usually replaced after they have produced more than 10^{19} neutrons. This means that 4000 tritium atoms are lost from the target for every neutron that is produced.

During 1985 RTNS II was operated around the clock five days per week. During the year it produced 2.9×10^{20} neutrons and the availability of the sources averaged 84%.

6.2 Oktavian

Oktavian¹³⁾ is an intense D-T source at Osaka University similar to RTNS I at Livermore. It uses 20 mA of analyzed D^+ at 300 keV on a rotating TiT target. Its output is 3×10^{12} /sec in steady operation. It can be operated in a pulsed mode with bursts 1.5 to 3 ns long and at a 1 kHz to 2 MHz repetition rate with 10^4 neutrons per pulse.

There is a program to build an upgraded facility in which the deuteron current will be increased to 200 mA and the energy to 400 keV. The expected output is 5×10^{13} neutrons/sec in steady operation. In the pulsed mode an increase by a factor of fifty in the number of neutrons per pulse is expected.

6.3 Dynagen

The facility⁹⁾ at Eppendorf Hospital in Hamburg, Germany, is used for radiation therapy. The accelerator built by Radiation Dynamics produces 12 mA of unanalyzed 500 keV deuterium ions. Originally it had a conventional rotating target, but, since an unanalyzed beam was used, the target life was very short. More recently the atomic and molecular beams were separated by about one cm by a small magnet, and the target now consists of a rotating cylinder. Both target spots serve as neutron sources. The total output is 3.5×10^{12} /sec. The active total target area is 300 cm^2 . Each target produces about 4×10^{17} neutrons before it is replaced.

6.4 University of Wisconsin Gas Target Source

The only high intensity source with a differentially pumped gas target is at the University of Wisconsin-Madison.¹⁴⁾ It is used for radiobiological studies. Typically 12 mA of 210 keV unanalyzed deuterium ions are accelerated; about half the beam actually gets into the tritium target. Typical output is 1.4×10^{12} /sec, but occasionally up to 4×10^{12} /sec have been produced. The tritium use per neutron produced is considerably higher than for a solid target. The large physical size of the gas target is a disadvantage for experiments that require a high neutron flux density.

6.5 Karin

About 12 years ago a closed high-intensity tube was developed at Karlsruhe by K.A. Schmidt.¹⁵⁾ Generators using these tubes were manufactured by Haefely in Basel, Switzerland. Inquiries to Haefely

about the status and availability of these generators have remained unanswered.

These tubes use 150 mA of mixed deuterium and tritium beams accelerated by 200 kV. The beam impinges on a scandium target. The tube contains 500 Ci of tritium and is rated to produce 6.5×10^{12} neutrons/sec. The life expectancy of the tube is several hundred hours.

Five such generators have been purchased, three for radiation therapy, one for activation analysis, and one for a fusion-fission test facility. The therapy units are isocentrically mounted to allow the source to be moved around the patient.

7. PULSED SOURCES

Neutron spectra are most readily measured by the time-of-flight method, and for this purpose sources that produce nanosecond bursts are needed. RTNS I is an early example of such a source. It uses bunched deuterons that produce neutron pulses of 2 ns width with repetition rates of the order of a MHz.¹⁶⁾

A more recent example is the PNG-300 pulsed neutron generator at Debrecen.¹⁷⁾ It produces pulses 1 ns long with repetition rates of several MHz. The average neutron output is 10^9 /sec with intensities as high as 4×10^{10} /sec in the pulses. This is achieved with an average deuteron beam current of 10-20 μ A.

8. PLANNED INTENSE SOURCES

Oktavian II mentioned earlier, with a deuteron beam current of

200 mA would be the most intense D-T source both for continuous and pulsed operation. Its output would be 5×10^{13} /sec continuous, and 5×10^5 /sec in a 2 ns pulse.

Other intense sources, which are similar to RTNS I, are under construction in various laboratories. They include INGE-1 at Dresden, Intense NG at Bratislava, and similar sources at Debrecen and at Lanzhou University in China. All these sources use rotating targets and are expected to produce $1-2 \times 10^{12}$ neutrons/sec.

9. RADIATION HAZARDS

The use of D-T sources exposes the operators to radiation produced by radioactivities induced by the neutrons, and to the tritium in the target.

The experience with RTNS II, which is the most intense operating source may be of interest. The original design included a plan to change targets and experiments remotely by using a cart that traveled on rails to the target position. When this system was first installed, it did not work satisfactorily, and it turned out to not be necessary. The activities are allowed to decay over a weekend before a target change. The operators who change targets get an annual exposure of about 3 mSv from induced radioactivity.

Tritium contamination turned out to be a more serious problem not so much because of high exposure to personnel, but because unexpected contamination was occasionally found outside the accelerator area in spite of regular surveys. The explanation appears to be that specks of Ti containing tritium come off used targets but are missed by the swipes which appear to show no contamination. These specks migrated

in uncontrolled ways and occasionally found their way into the office areas. Until these occurrences were explained and preventive measures were instituted two years ago, there were extended shut downs of the facility to track down tritium contamination. Last year the annual average exposure to tritium was 0.6 mSv for the operating personnel.

10. REFERENCES

1. H.H. Barschall, "14 MeV d,t Sources" in "Neutron Sources for Basic Physics and Applications", edited by S. Cierjacks, Pergamon Press, 1983.
2. Proceedings of the XIVth International Symposium on the Interaction Fast Neutrons with Nuclei, edited by D. Seeliger and U. Jahn. Report Zfk-562 (1985).
3. H.H. Barschall and R.F. Taschek, Phys. Rev. 75, 1819 (1949).
4. D.W. Kneff, B.M. Oliver, H. Farrar, and L.R. Greenwood, Nucl. Sci. and Eng. 92, 491 (1986).
5. R.C. Haight, S.M. Grimes, R.G. Johnson, and H.H. Barschall, Nucl. Sci. and Eng. 87, 41 (1984).
6. J. Csikai, T. Chimoye, T. Vilaithong, N. Chirapatpimol, and S. Singkarat, Nucl. Inst. Meth. A239, 641 (1985).
7. R. Booth, IEEE Transactions NS14, 938 (1967).
8. R. Booth and H.H. Barschall, Nucl. Inst. Meth. 99, 1 (1972).
9. A. Hess, R. Schmidt, and H.D. Franke, Proc. 5th Symp. on Neutron Dosimetry, Comm. Eur. Comm. EUR9762, p. 1019 (1984).
10. M. Catterall, I. Sutherland, and D.K. Bewley, Brit. Med. J. 2, 653 (1975).
11. A. Wambersie, J.J. Battermann, and N. Breteau, J. Eur. Radio-therapie 5, 120 (1984).
12. D.W. Heikkinen and C.M. Logan, Nucl. Inst. Meth. B10/11, 835 (1985).

13. K. Sumita, et al., Proc. 12th Symp. on Fusion Technology, Juelich 1982, p. 675.
14. G.M. Chenevert, P.M. DeLuca, C.A. Kelsey, and R.P. Torti, Nucl. Inst. Meth. 145, 149 (1977).
15. K.A. Schmidt and H. Dohrmann, Atomkernenergie 27, 159 (1976).
16. L.F. Hansen, et al., Nucl. Sci. Eng. 35, 227 (1969).
17. T. Sztaricskai, et al., Atomki Report E/5 (1985).

PROGRESS IN FAST NEUTRON DETECTION TECHNIQUES

Horst Klein

Physikalisch-Technische Bundesanstalt (PTB), Bundesallee 100,
3300 Braunschweig, Fed. Rep. of Germany

Progress in fast neutron detection techniques since 1979 is discussed, but restricted to the energies between 0.2 MeV and 20 (30) MeV.

Various organic scintillation detector systems such as the black detector or the dual thin scintillator are well suited for precise fluence measurements with neutron TOF spectrometer and have to be selected in dependence on the energy range to be investigated. He-3 based detectors may be an alternative in TOF monitoring even in the low (gas scintillator) or high (liquid scintillator) energy region.

The most versatile instrument proved to be the twin gridded ionization chamber. The angular distribution of the applied reaction is considered in 2π geometry. Multiparameter data acquisition and analysis enable online control of the efficiency.

1. INTRODUCTION

Fast neutron detectors applied for fluence measurements and spectroscopy in the energy region from 0.2 MeV up to 20 (30) MeV are generally based on only a few materials showing a smooth energy dependence of their neutron interaction cross sections. In the case of the reference standards¹⁾ $H(n,n)H$, $^{235}U(n,f)$ and $^{238}U(n,f)$ the reactions are unique or can be clearly identified. The cross sections are sufficiently large and well known (fig. 1 right), but in particular for the neutron induced fission of the uranium isotopes a considerably improved data base is to be expected from a recent evaluation²⁾. The fast neutron interaction with 3He ^{1,2)} also seems to be a candidate and besides the elastic scattering, the various reaction channels also exhibit the right behavior (fig. 1 left) but must be separated in the detector system.

In a 1979 comprehensive review of nuclear detectors and related

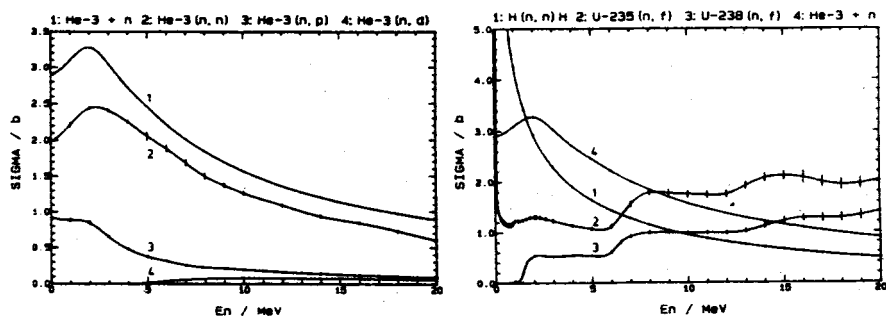


Fig. 1: Cross sections of fast neutron induced reactions (data and uncertainties from ref. 1)

techniques³⁾, all commonly used fast neutron detectors are discussed in great detail and, indeed, no revolution has taken place in recent times comparable with the introduction of Si and Ge detectors in charged particle and photon spectroscopy. In this paper therefore, although no spectacular new ideas can be reported, various improvements regarding the general set-up, the reliability of the various components including electronics, the theoretical description of the response and the realistic estimate of the uncertainties, particularly with respect to absolute neutron fluence measurements, are worth summarizing.

According to the conclusions recently stated in a review of detectors applied at white neutron sources⁴⁾, only hydrogen based detectors (see sect. 2) and fission chambers (sect. 4) should be discussed, but it will be shown in sect. 3 that particularly liquid ³He scintillation detectors are well suited for monitoring up to 30 MeV neutron energy. In most applications the detectors are part of neutron time-of-flight spectrometers, but spectroscopy by means of unfolding methods could also be improved.

2. HYDROGEN BASED DETECTOR SYSTEMS

Proton recoil spectrometers have been used from the very beginning of fast neutron measurements. Organic scintillation detectors such as anthracene or stilbene crystals and plastic or

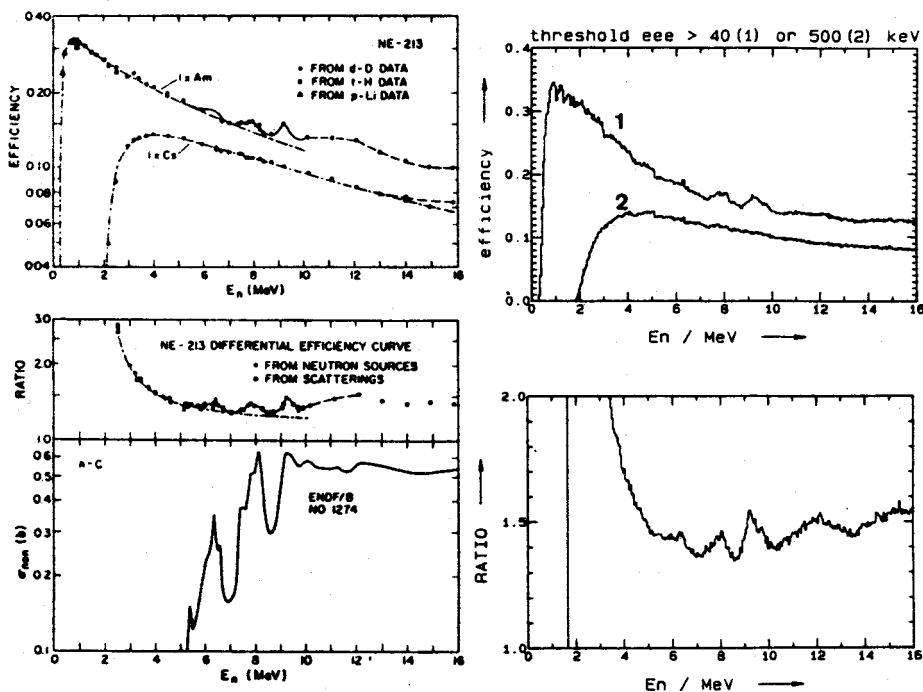


Fig. 2: Neutron detection efficiencies of NE 213 liquid scintillators for Am- and Cs-bias settings and their ratios demonstrating the influence of nonelastic interactions with carbon
 left: experimentally determined (fig. 1 and 2 of ref. 5)
 right: calculated with the MC code NEFF4 (ref. 6)

liquid scintillators are given preference for use in TOF spectrometry due to the excellent timing at reasonable efficiency, partially combined with a high selectivity for neutron induced secondary charged particles by means of pulse shape analysis. In practice any shape and size of detectors has been realized, depending on the particular application.

Indeed, a serious problem is introduced by the relatively high carbon content of the organic base material. Due to the high total cross section the neutron interaction with carbon can significantly influence the response and efficiency. A very careful experimental calibration of a liquid scintillator⁵⁾ has clearly demonstrated this influence, showing a pronounced structure in the neutron detection efficiency according to resonances in the inelastic n-C cross section

(fig. 2 left) just in an energy region where usually a smooth interpolation between scarce data points is commonly practiced. In this way errors of up to $\pm 5\%$ are introduced which can be avoided by considering realistic Monte Carlo simulations⁶⁾ which clearly confirm the suggested explanation and should be used at least for interpolation purposes (fig. 2 right).

2.1 Black Neutron Detector (BND)

The design of the black neutron detector⁷⁾ was the first successful attempt to overcome the carbon problem at reasonable detection efficiency. Assuming a well collimated neutron beam entering the detector within a reentrant hole and a detector volume sufficiently large for almost all neutrons to undergo multiple interactions in certain energy regions the extremely high efficiency ($\epsilon > 90\%$) can be predicted with uncertainties of less than 1 %, almost independent of uncertainties in the differential cross sections of the constituents. Recently, the NBS-BND⁸⁾ has been calibrated at $E_n = 2.43$ MeV by means of the time-correlated associated particle (TCAP) method⁹⁾ showing excellent agreement between the measured and the calculated efficiency within the estimated uncertainty of $\pm 1.2\%$, even if the efficiency was reduced to $\epsilon_{MC} = 0.76$ and the response (fig. 3 right) no longer shows the peak structure typical of lower energies (fig. 3 left).

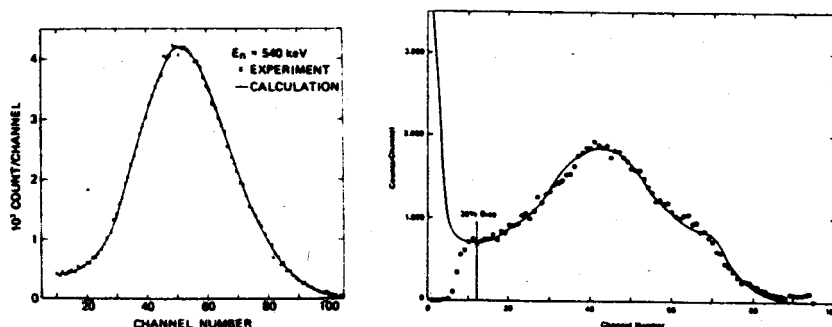


Fig. 3: Response of the NBS black neutron detector
 left: $E_n = 0.540$ MeV (fig. 7 of ref. 8)
 right: $E_n = 2.29$ MeV (fig. 4 of ref. 9)

However, the detector volume is limited due to the internal light attenuation, the background radiation and the number of phototubes necessarily used simultaneously. The thresholds in each channel and the coincidence requirements influence the efficiency and must be explicitly considered in the efficiency calculation. The regular use of a large BND for fluence measurements up to 30 MeV neutron energy finally failed due to these difficulties¹⁰⁾.

In addition, the energy dependent time response spectra⁷⁾ must be considered by means of unfolding procedures if continuous neutron energy distributions are investigated¹¹⁾. Nevertheless, the use of a BND is recommended in the energy range below 5 (10) MeV if a precise neutron fluence measurement is required.

2.2 Proton Recoil Spectrometer

Proton recoil telescopes (PRT) are the absolute reverse of a BND as regards efficiency. The maximum energy transfer to the proton by central collision should be exploited to achieve a narrowly peaked response for monoenergetic neutrons. In this way neutron energy distributions can be directly spectroscopied with reasonable resolution, but with remarkably reduced efficiency ($\epsilon \sim 10^{-4} \dots 10^{-5}$). Nevertheless, these devices are often used for precise fluence measurements and therefore most recent investigations have dealt with corrections and uncertainty estimates¹²⁻¹⁴⁾. Considering the influence of the structural materials of the neutron target and the telescope, the angular distribution of the neutron-producing reaction and the uncertainty of the differential n-p scattering cross section, uncertainties not lower than 1.5 - 2 % can be achieved in the energy range of $2 \text{ MeV} \leq E_n \leq 20 \text{ MeV}$ ¹³⁾.

An improvement is to be expected from the application of a gridded ionization chamber (see section 4).

2.3 Dual Thin Scintillator (DTS)

The limitations in the application of a PRT (efficiency) or a BND

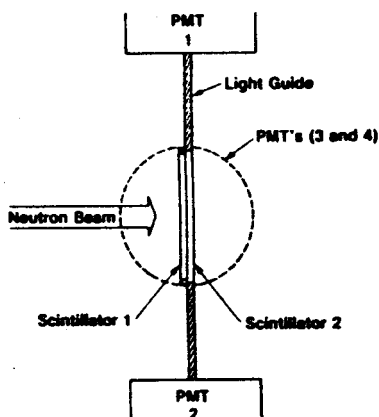


Fig. 4:
Schematic of the dual thin
scintillator (fig. 3 of
ref. 15)

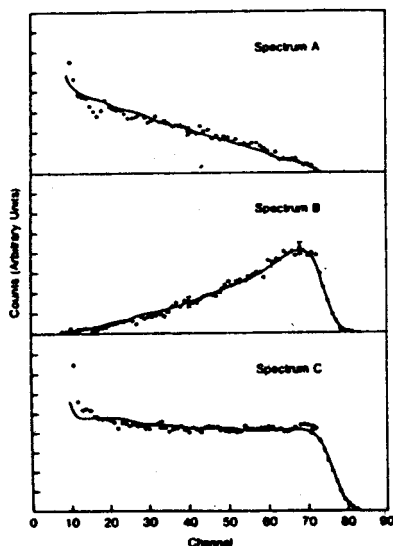


Fig. 5:
Response spectra of the DTS
for $E_n = 14$ MeV (fig. 8 of
ref. 15) as measured (dots)
and calculated (lines) for
the first (A), the second
(B) detector and the
coincident sum (C)

(energy range) for precise neutron fluence measurement have given rise to the design of the dual thin scintillator¹⁵⁾.

The thickness of the first plastic scintillator (or probably a stilbene crystal if n/γ discrimination is required) is chosen according to the maximum range of recoil protons to be investigated, i.e. about 2.5 mm for 15 MeV protons (fig. 4). The response spectrum for monoenergetic neutrons is far from the ideal proton recoil spectrum (fig. 5A), but the recoil protons not stopped in the first scintillator can be measured in coincidence in the second scintillator (fig. 5B). Thus, the summed spectrum (fig. 5C) shows the almost ideal shape only weakly influenced by multiple scattering. Uncertainties due to interaction with carbon can also be neglected as long as the threshold is set above the response of neutron induced reactions on

carbon. TCAP calibration measurements at 2.43 MeV and 14.0 MeV caused an energy-independent correction of the MC simulated efficiency of about 1.5 - 2 % which is still not understood. Even if the threshold of the first detector gating the summed signals is a sensitive parameter to be considered in the calculations, uncertainties in the order of 1 ... 2 % have been estimated for the energy dependence of efficiency in the entire energy region from 1 MeV up to 15 (20) MeV. The disadvantage of the low efficiency ($\epsilon \sim 1\%$) is therefore overcompensated by the fact that the DTS can be used for precise fluence measurements in a wide energy range not necessarily requiring a well collimated neutron beam (as for the BND).

2.4 "Normal" Sized Organic Scintillators

The restrictions for both the BND (collimator, time resolution) and the DTS (low efficiency) prevent the general use of one of these detectors in neutron TOF spectrometry. As the response of both systems is well described by MC simulations (CARLO BLACK code^{7,8}) this method should also be applicable for any other size of organic scintillators which has to be optimized with respect to the efficiency, the solid angle, the time resolution and an efficient n/γ discrimination depending on the actual problem investigated.

Indeed, the response of aluminum capsuled liquid scintillators (BA-1 type of NE 213) is satisfactorily described in a wide energy range (0.5 - 20 MeV) and for various sizes (3.8 cm x 3.8 cm \varnothing up to 5.08 cm x 25.4 cm \varnothing) by means of the PTB NRESP code⁶) which considers

- the light output and resolution functions which must be carefully determined for any particular detector system and
 - the evaluated differential cross sections for the constituents of the scintillator (H,C), the light guide (H,C) and the capsule (Al).
- As a typical example, a comparison of the calculated and the measured response is shown in fig. 6 for a medium energy where already improved angular distributions for the C(n, α) reaction were taken into account in the MC code¹⁶). Provided that the more problematic breakup

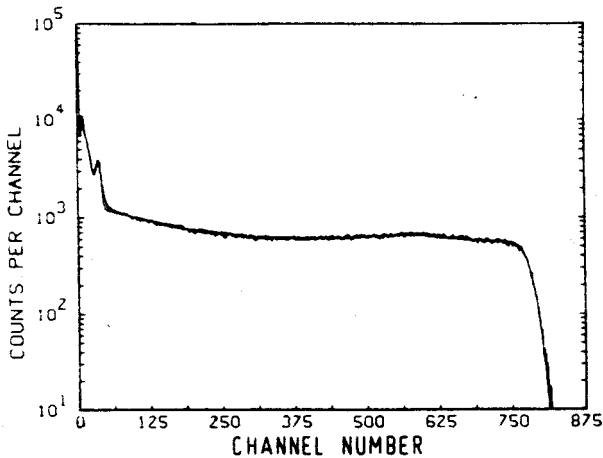


Fig. 6:
Response spectra of an
NE 213 scintillator,
5.08 cm x 5.08 cm
diam., for $E_n = 9.2$ MeV
as measured (histogram)
and calculated (line)

reactions on carbon can also be realistically simulated, the energy-dependent efficiency can be calculated for any threshold with reasonable accuracy ($\Delta\epsilon/\epsilon \sim 2\%$ for $E_n \geq 1.1 \times E_{thr}$). In the case of a medium sized detector (NE 213, 2.54 cm x 10.16 cm \emptyset), a detailed intercomparison of fluence measurements obtained with a PRT and this scintillator showed excellent agreement for neutron energies from 6 MeV up to 14 MeV within the estimated uncertainties of $\pm 2\%$. However, it should be pointed out that from the intercomparison of various detectors energy independent correction factors between 1.0 and 1.05 were derived.

Indirect neutron detection via photons from the inelastic scattering on the structural materials are not considered in the MC simulation, even if these events can amount to a few percent below 6 MeV (due to the Al capsule) up to 15 % of the total response in the vicinity of 11 MeV incident neutron energy. Because of the additional problems in handling these contributions we prefer to generally apply n/ γ discrimination.

A well defined response matrix finally enables even complex neutron spectra to be determined by means of a matrix inversion unfolding of scintillation spectra, as has been proved by comparing with the results derived from simultaneously measured neutron TOF spectra¹⁷⁾. More advanced unfolding procedures such as an iterative differentiation method¹⁸⁾ or a Monte Carlo technique¹⁹⁾ may even

improve the energy resolution achievable.

Summarizing it can be stated that the neutron response of any "normal" sized cylindrical detector fitted via a light guide to a single phototube can be satisfactorily described by Monte Carlo simulations if the influence of multiple scattering events is properly considered.

2.5 General Techniques

Reliable neutron spectroscopy with organic scintillators not only requires a sophisticated description of the neutron induced response but also a careful design of the detector set-up and selection of adequate electronics. Some of the recent investigations should be considered.

2.5.1 Light transmission and resolution. Quite a simple recipe was given to prevent the light transmission from the scintillator to the photocathode from being dependent on the locus of the primary interaction²⁰⁾. When the scintillator is coupled via a partially coated light guide to the sensitive area of the phototube, the resolution can be considerably improved at high proton recoil energies. On the other hand, the Monte Carlo simulation of the light transport also showed that the mean light output decreases if a light guide is introduced. The best resolution is therefore achieved at low proton recoil energies by direct coupling to a phototube selected for the best quantum efficiency of the cathode.

2.5.2 Gain stabilization. A common and serious problem which also besets modern phototubes - the gain instabilities due to changes of the count rate (fig. 7), temperature, magnetic fields etc. - seems to have finally been solved. Various attempts to stabilize the gain by means of LED reference pulses failed because the light pulser itself was unstable. A complex but successful solution to the problem is to stabilize in a loop the LED light output by means of a more stable photosensitive device^{21,22)}, while the stabilized LED can in turn be

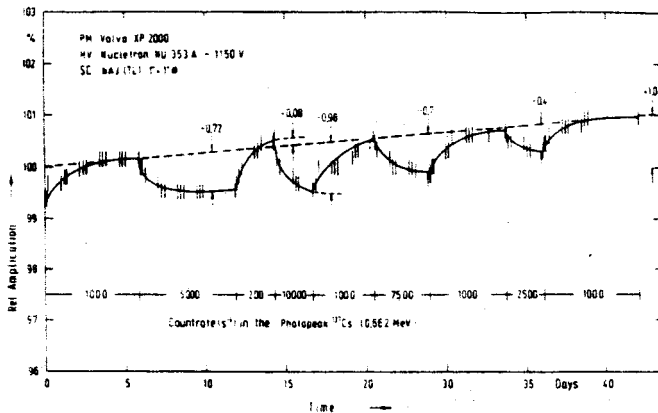


Fig. 7: Typical gain instabilities of phototubes due to count rate variations

used to control the PM gain in a second loop. Excellent results recently published²³⁾ were obtained with an electronic circuit, which is meanwhile commercially available. This method entails the use of a PIN diode as a reference device, but great care must be taken in the mechanical set-up of the PIN diode, LED and detector in order to guarantee a long-term stable ratio of the light fractions decoupled for the reference diode and the photocathode.

3. ^3He BASED SCINTILLATORS

^3He filled proportional counters are still used for neutron spectroscopy up to 1.2 MeV, but their application in TOF spectroscopy is chiefly hindered by the insufficient time resolution. Scintillation detectors on the basis of ^3He were therefore investigated.

3.1 Liquid ^3He Scintillator (L^3He)

Reasonable efficiency and excellent timing were achieved with a liquid ^3He scintillator first described in 1976²⁴⁾. Recently 290 cm³ and 60 cm³ L³He systems were carefully investigated^{25,26)} and applied in cross section measurements and in fast neutron fluence monitoring.

The complex cryogenic system with liquid nitrogen and liquid ^4He baths finally allows ^3He to be liquidized at about 2.2 K. The wave lengths of the scintillations are shifted and the light pulses are decoupled via a quartz window to a phototube. This scintillator shows an almost linear light output versus energy relation up to 30 MeV for the total energy of the reaction products ($p + t$ or $d + d$).

Fortunately, the light output for ^3He recoils is about 10 % lower and the resolution achieved is sufficient to quantitatively separate the various reactions. The partial cross sections extracted from spectra for neutrons up to 30 MeV are in fairly good agreement with the evaluated cross section of the inverse reactions, but the results are quite sensitive to corrections considering the losses of particles due to long ranges and edge effects²⁵⁾.

3.2 ^3He Gas Scintillation Counter

The much simpler but less efficient solution is the gas scintillation detector recently tested at the NBS²⁷⁾. The closed stainless steel tube filled with a mixture of ^3He and Xe gas functioned stably for about 2 years, but the energy resolution (which is about 50 % worse than for the liquid scintillator) is not sufficient to quantitatively separate $p + t$ events from ^3He recoils. Improvements are expected from the construction of a gas proportional scintillation counter, where the primary scintillations are also used for the fast timing while the internal amplification reduces the width to about 10 %.

4. IONIZATION CHAMBERS

The fission fragments (ff) originating from the neutron induced fission of ^{235}U or ^{238}U must clearly be separated from the underlying α -particle background. Parallel plate ionization chambers are very well suited for this purpose, but problems arise in specifying the layer of fissionable material and in the determination of the ff-detection efficiency.

4.1 Gridded Ionization Chamber

Both problems can be solved by means of a gridded ionization chamber²⁸⁾. The uranium layers are deposited on the cathode (fig. 8) and the charge signal induced by α 's or fission fragments on the anode, the cathode and the grid are simultaneously analysed with an electronic time constant just between the drift times of the electrons and the ions. While the cathode and grid signals depend on the direction and length of the ion track, the anode signal is only related to the total number of ion pairs produced between cathode and grid, provided that the distance between cathode and grid and the gas filling are adjusted with respect to the range of the particles investigated. The energy and the angle of emission can then be determined simultaneously. In the case of the α spectroscopy of extremely thin U layers the expected isotropic angular distribution is observed, while for thicker samples the losses due to self absorption become obvious but can be corrected by an extrapolation to 100 % efficiency. In the meantime this method is routinely applied to determine the sample thickness with a precision comparable with the "low geometry" α -counting²⁹⁾. The same chamber can then be adapted to the range of fission fragments to be used for neutron fluence measurements. The ff-detection efficiency is automatically under control as long as the energy of the incident neutrons is determined by TOF-spectroscopy and can be considered in the interpretation of the ff-angular distribution³⁰⁾.

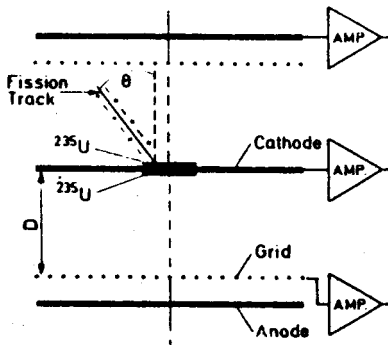


Fig. 8:
Twin gridded ionization chamber
(ref. 28-32) with induced charges at the

$$\text{anode: } q_a = q_0 \sim E$$

$$\text{cathode: } q_c = q_0 (1 - X \cos \theta/D)$$

$$\text{grid: } q_g = q_0 X \cos \theta/D$$

(X ~ half of the track length)

The extraordinary capabilities of this instrument have recently been demonstrated in the course of correlation measurements between the fission fragments and the neutrons from the spontaneous fission of $^{252}\text{Cf}^{31}$). A thin Cf source on an aluminum foil was mounted in a twin gridded chamber. Both fission fragments were analysed in coincidence delivering an angular resolution of $\Delta \cos / \cos \leq 5\%$. In the case of cold fragmentation the masses of both fragments could be clearly separated ($\Delta m \sim 0.5 \text{ AMU}$).

The twin chamber is also the one best suited to investigate neutron induced reactions, i.e. $^6\text{Li}(n,\alpha)\text{T}^{32}$), with respect to the fission yield.

Very recently, the proton recoil spectra were taken from tristearine layers of various thicknesses³³). Even if problems with the inhomogeneity of the evaporated layers still make the quantitative analysis more difficult, this proton recoil spectrometer has the advantage of a much higher efficiency (2π geometry) compared with a telescope and of not being so sensitive on the uncertainty of the differential n-p scattering cross section. However, the extreme range of high energy protons may prevent its being applied for neutron energies above 10 MeV.

4.2 Low Mass Ionization Chamber

The gridded ionization chamber can be optionally used in the compensation and double differentiation method²⁸⁾ in order to suppress high α -particle background (up to 10^8 α -particles/fission event) and to process high counting rates. In these cases, a ΔE chamber could be an alternative solution. Small spacing between the electrodes and methane gas filling yield fast ($t_r \leq 2 \text{ ns}$) and short ($t_{1/10} \sim 15 \text{ ns}$) current pulses proportional to the energy loss. High counting rates, i.e. of Cf sources, can be processed at high ff-detection efficiency and quantitative α -particle suppression³⁴⁾. In addition, the energy loss spectrum also provides information on the angle of emission which can be used to correct for ff-detection losses. The low mass of these devices considerably reduces the

corrections due to absorption, in-scattering or additional neutron production.

5. CONCLUSION

Progress in fast neutron techniques has chiefly concerned a better understanding and more reliable use of standard instruments.

For precise neutron fluence measurements various types of hydrogen based detectors can be used in TOF techniques. Depending on the energy range to be investigated and the source strength available the best suited detector can be selected from BND, DTS, PRT or gridded ionization chambers, but high precision and reliability can now also be achieved with "normal" sized liquid scintillators. The absolute scaling should be checked by completely independent methods, i.e. TCAP measurements, or by means of other reactions.

The liquid ^3He scintillator seems to be an adequate solution particularly at high energies (10 ... 30 MeV), but requires a complicated experimental technique.

The most versatile instrument is the gridded ionization chamber, as various standard reactions can be applied. In particular high quality assaying and the intrinsic ff efficiency control make this instrument a suitable candidate for a uranium fission monitor. However, an improved evaluation of these standard cross sections is required.

6. REFERENCES

1. Nuclear Data Standards for Nuclear Measurements, IAEA Technical Reports Series No. 227, Vienna 1983 and ENDF/B-V file, Brookhaven 1979
2. Carlson, A.D., Progress in Nuclear Energies 13, No. 2/3, 79 (1984)
3. Nucl. Instr. Meth. 162 (1979) Special issue, ed. D.A. Bromley
4. Gayther, D.B., Proc. Conference on Nuclear Reference Standard Data, IAEA TECDOC-335, 345 (1985)
5. Drosig, M.; Drake, D.M. and Lisowski, P., Nucl. Instr. Meth. 176, 477 (1980)
6. Dietze, G. and Klein, H., PTB-report ND-22, Braunschweig (1982)
7. Pönitz, W.P., Nucl. Instr. Meth. 109, 413 (1973)
8. Wasson, O.A.; Meier, M.M. and Duvall, K.C., Nucl. Sci. Eng. 81, 196 (1982)
9. Duvall, K.C.; Carlson, A.D. and Wasson, O.A., IAEA TECDOC-335, 332 (1985)
10. Schwarz, P.; Klages, H.O.; Doll, P.; Häsner, B.; Wilczynski, J. and Zeitnitz, B., Nucl. Phys. A398, 1 (1983), Schwarz, P., Ph. D. thesis, Universität Karlsruhe (1982) and Klages, H.O., private communication (1986)
11. Pönitz, W.P. and Tamura, T., Nuclear Data for Science and Technology, p. 465, ed. K.H. Böckhoff, Reidel Publ. Dordrecht (1983)
12. Thomas, D.J. and Lewis, K.E., Nucl. Instr. Meth. 179, 397 (1981)
13. Siebert, B.R.L.; Brede, H.J. and Lesiecki, H., Nucl. Instr. Meth. A235, 542 (1985)
14. Kobayashi, N.; Kinoshita, T. and Michikawa, T., Nucl. Instr. Meth. A242, 164 (1985)
15. Dias, M.S.; Johnson, R.G. and Wasson, O.A., Nucl. Instr. Meth. 224, 532 (1984)
16. Dietze, G.; Brede, H.J.; Klein, H. and Schölermann, H., Nuclear Data for Science and Technology, p. 930, ed. K.H. Böckhoff, Reidel Publ. Dordrecht (1983)

17. Antunes, L.; Börker, G.; Klein, H. and Bulski, G., Proc. of the Int. Conf. on 'Nucl. Data for Basic and Applied Science', Santa Fe 1985, to be published
18. Böttcher, J.; Feigel, A.; Finckh, E.; Forstner, Ch.; Jaumann, W.; Schall, G.; Scheuring, H.; Schneidereit, U.; Stauber, K.; Tröger, P. and Weipert, A., Nucl. Instr. Meth. 219, 369 (1984)
19. Matzke, M. and Weise, K., Nucl. Instr. Meth. A234, 324 (1985)
20. Schölermann, H. and Klein, H., Nucl. Instr. Meth. 169, 25 (1980)
21. Reiter, W.L. and Stengl, G., Nucl. Instr. Meth. 173, 275 (1980)
22. Hohn, L.; Fielding, H.W. and Nelson, G.L., Nucl. Instr. Meth. A234, 517 (1985)
23. Holler, Y.; Koch, J. and Naimi, A., Nucl. Instr. Meth. 204, 485 (1983)
24. van Staa, R.; Reher, J. and Zeitnitz, B., Nucl. Instr. Meth. 136, 241 (1976)
25. Häsner, B., Ph. D. thesis, Universität Karlsruhe (1982)
26. Jany, P., Ph. D. thesis, Universität Karlsruhe (1985)
27. Wasson, O.A., Proc. Int. Symp. on Nuclear Physics - Nuclear Fission, Nov. 1985 in Gaussig, to be published
28. Knitter, H.H. and Budtz-Jørgensen, C., NBS Special Publ. 594, 947 (1980)
29. Budtz-Jørgensen, C.; Knitter, H.H. and Bartels, G., Nucl. Instr. Meth. A236, 630 (1985)
30. Budtz-Jørgensen, C.; Knitter, H.H., Nucl. Sci. Eng. 86, 10 (1984)
31. Budtz-Jørgensen, C.; Knitter, H.H., Proc. Int. Symp. on Nuclear Physics - Nuclear Fission, Nov. 1985 in Gaussig, to be published
32. Knitter, H.H. and Budtz-Jørgensen, C.; Smith, D.L. and Marletta, D., Nucl. Sci. Eng. 83, 229 (1983)
33. Knitter, H.H. and Budtz-Jørgensen, C. and Bax, H., Proc. Conference on Nuclear Reference Standard Data, IAEA TECDOC-335, 470 (1985)
34. Böttger, R.; Klein, H. Chalupka, A. and Strohmaier, B., Nuclear Data for Science and Technology, p. 484, ed. K.H. Böckhoff, Reidel Publ. Dordrecht (1983)

A NEW NEUTRON TOF FACILITY AT OKTAVIAN

A. Takahashi, H. Sugimoto and E. Ichimura

Department of Nuclear Engineering, Osaka University

Yamadaoka 2-1, Suita, Osaka 565, Japan

A new TOF facility at OKTAVIAN is introduced. Design and characteristics of shield system and neutron detector are shown. Double differential cross sections at $E_n = 14$ MeV are being measured with this facility.

1. INTRODUCTION

Double differential neutron emission cross sections around 14 MeV have been measured at OKTAVIAN^{1),2)}, based on the ring-sample & TOF method, which has however a drawback of E_n variation according to the change of scattering angle. In order to fix incident energy to $E_n = 14.1$ MeV, a new TOF line was constructed at 85 deg against the pulsed beam line²⁾. Cylindrical samples are adopted for scatterers.

2. SHIELD SYSTEM

An overall view of the TOF and shield system is shown in Fig.1. A cylindrical sample with 3 cm diameter and 7 cm length is rotated around the ns pulsed D-T source²⁾ with 17 cm radius to change scattering angle. The 85 deg fixed flight path was selected to avoid the effect of target flange. The flight path length is 8.25 m with small variation by the sample rotation. Small variation of E_n , 14.1 ± 0.05 MeV, by the sample rotation from 0 to 180 deg scattering angle can be neglected within the overall energy resolution ± 0.2 MeV of the whole TOF system. Within the shadowed zone by a shadow-bar shield of special shape, a conical collimator with 12cmx18cm sectional hole is settled. In order to minimize scattered-in background-neutrons from the collimator, collimation is done near the mid-point of flight path. To eliminate room-returned background-neutrons almost completely, a 10" diam 10 cm thick NE213 neutron detector is heavily shielded with ordinary concrete and is set inside a 5 cm thick lead box with 10 cm inner

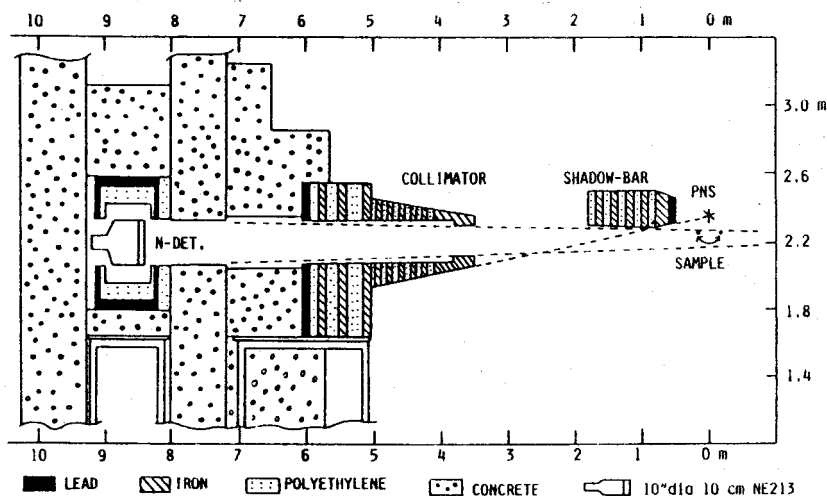


Fig.1 Schematic view of shield for TOF experiment

polyethylene layer for suppressing re-incidence of scattered neutrons by the NE213 detector. Evacuation of the target & sample zone of 1 m diam 1 m long volume is planned to eliminate air-scattered background-neutrons.

3. NEUTRON DETECTION

To realize conditions of good counting statistics and n- γ separability which are comparable with those of the ring-geometry experiment 1),2), a large (10" diam 10 cm thick) NE213 detector was designed and manufactured. The configuration is shown in Fig.2. Electronics diagram of the neutron-TOF-measuring system is the same as the previous one²⁾. For n- γ separation, parallel pulse shape discrimination circuits with "low" and "high" gain-set double delay line amplifier respectively are adopted. Examples of n- γ separability are shown in Figs.3-a & -b, for 14 MeV neutron incidence, where the "high discr" and the "low discr" cover 2-15 MeV and 0.3-3 MeV range of recoil proton, respectively. Sufficient separability is attained for a dynamic range of 0.3-14 MeV neutron energy.

Energy-dependent efficiency curve of the detector was determined

by two methods; i) 5.5 m TOF experiment using ^{252}Cf neutron source for the range 0.3-9 MeV, and ii) 8 m TOF experiment using a 1 cm diam 5 cm long cylindrical polyethylene sample as a scatterer of 14.1 MeV neutrons (see Fig.1), for the range 5-14 MeV.

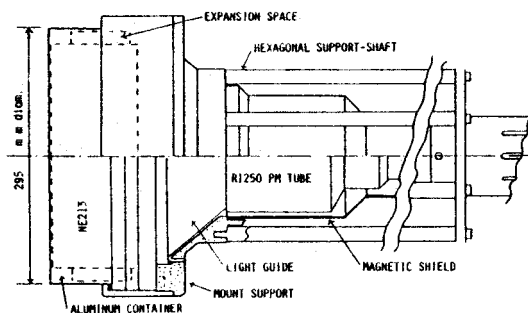
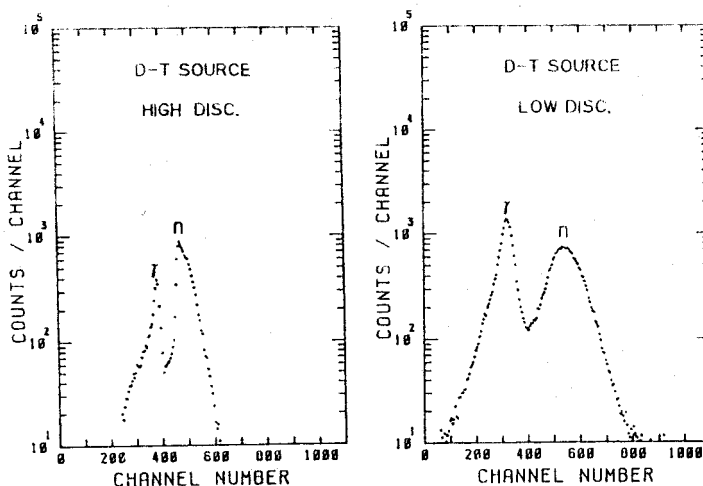


Fig.2 A 10" diam NE213 detector



Figs. 3-a & -b Pulse shape distribution of 10" diam NE213

The result is shown in Fig.4. The efficiency curve is well reproduced by the O5S calculation except the region near threshold.

4. DDX MEASUREMENT

An example of measured raw TOF spectra for carbon is shown in Fig.5, together with a background spectrum which was taken by removing a sample; Data accumulation time was an hour for each run. Foreground/background ratio is not good except 4 peaks corresponding to elastic

and three kinds of inelastic scattering. The 5th peak is due to background-neutrons by air-scattering of D-D neutrons in the vicinity of sample; Therefore, evacuation of air for the target & sample zone will be effective to further eliminate backgrounds. The present condition without the evacuation is good enough for

measuring emission spectra having broad peak by (n,2n) or continuum-inelastic scattering neutrons, i.e., for Pb, Fe and so on. To finally obtain double differential neutron emission cross section (DDX), some corrections are done for the angle-dependence of 14 MeV incident neutron yield (using measured distribution of $^{27}\text{Al}(n,\alpha)^{24}\text{Na}$ reaction), the effect of lower energy tail of source spectrum (using measured spectrum or Monte Carlo calculation) and the effect of multiple scattering.

DDX measurements have been done for C, Pb, Al, Cu, Si and Mg. For each sample, DDX data have been taken for 15-20 angle-points from 15 to 160 deg scattering angle. Examples for C and Pb are shown in Figs.

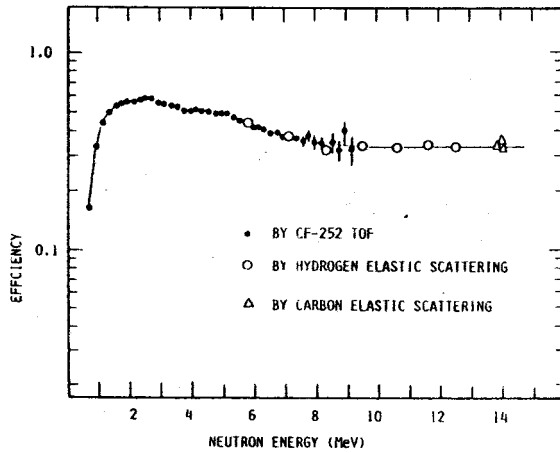


Fig.4 Efficiency of a 10" diam NE213

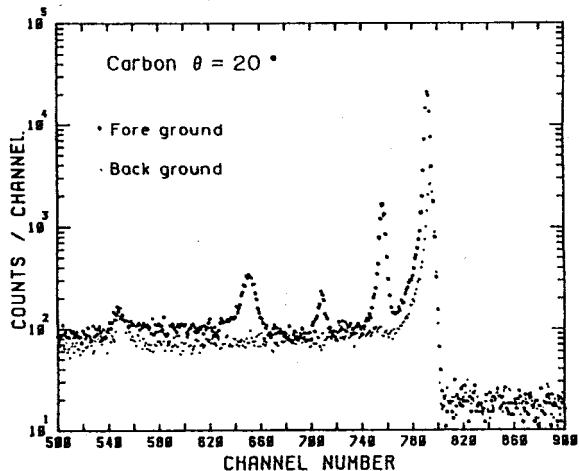


Fig.5 Raw TOF data for carbon sample

6 & 7 in comparison with evaluated data. These data are comparable with those by the ring-sample experiment¹⁾, from view-points of energy resolution and counting statistics. Partial differential cross sections for various reaction channels at 14.1 MeV, i.e., elastic, level-inelastic scattering, $(n,2n)$, $(n,n'\alpha)$ reaction, etc., have been obtained. Some of the results are given elsewhere³⁾.

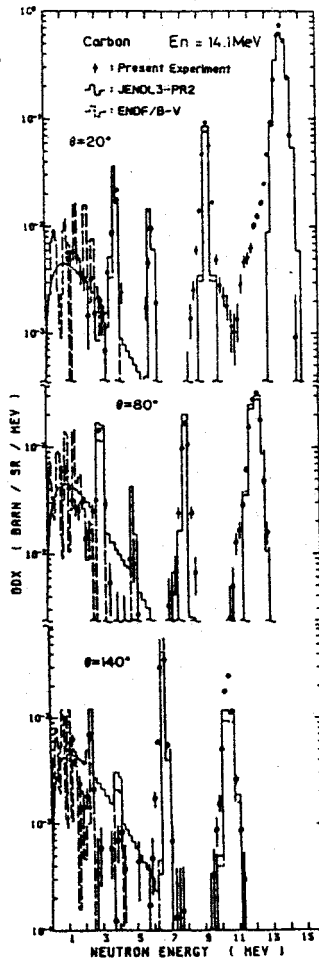


Fig.6 DDX for C

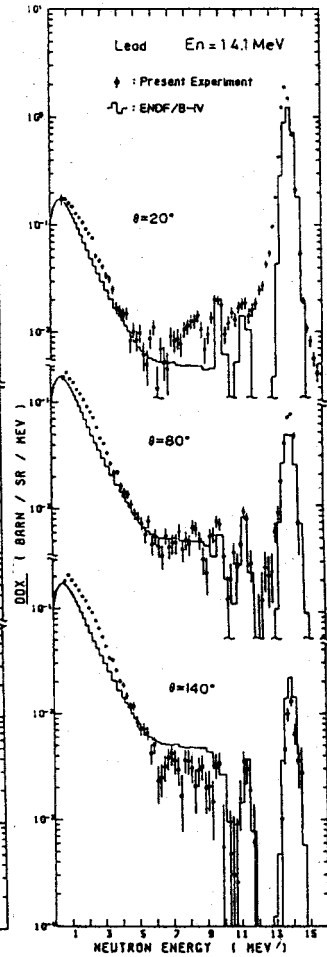


Fig.7 DDX for Pb

REFERENCES

- 1) Takahashi, A., et al., Proc. Conf. Nucl. Data Sci. Tech., 1982 at Antwerp, 360-367, D. Reidel Pub. (1983)
- 2) Takahashi, A., et al., J. Nucl. Sci. Tech., 21, 577-598 (1984)
- 3) Takahashi, A., Proc. JNDC 1985 Seminar Nucl. Data, 1985 at Tokai, Japan, to be published in JAERI-M

THE STUTTGART 'SCORPION' FACILITY FOR SCATTERING EXPERIMENTS WITH FAST POLARIZED NEUTRONS IN THE ENERGY RANGE OF 7 TO 8 MEV

J. W. Hammer, G. Bulski, W. Grum, K.-W. Hoffmann, G. Keilbach,
G. Schleußner and G. Schreder
(Institut für Strahlenphysik, Universität Stuttgart)

Neutron scattering experiments, although requiring complex experimental setups, play an important role in the exploration of nuclear structure. The new theoretical models of nucleon scattering, yet describing high energy data with great success, will demand for a broad data base in the low energy region. Together with the corresponding analysing power data differential cross section measurements produce much more constraints on nuclear model calculations. Especially the spin-dependence of all the effective nucleon-nucleus potentials becomes better

defined. In Stuttgart scattering data over a wide range of elements have been obtained at the incident energy of 7 to 8 MeV. The high currents of a Dynamitron accelerator together with the ${}^9\text{Be}(\alpha, n){}^{12}\text{C}$ reaction have provided a source of highly polarized neutrons. At the typical energy of 7.75 MeV the polarization amounts 60%. Fig. 1 shows the top view of the SCORPION facility. It consists of a neutron

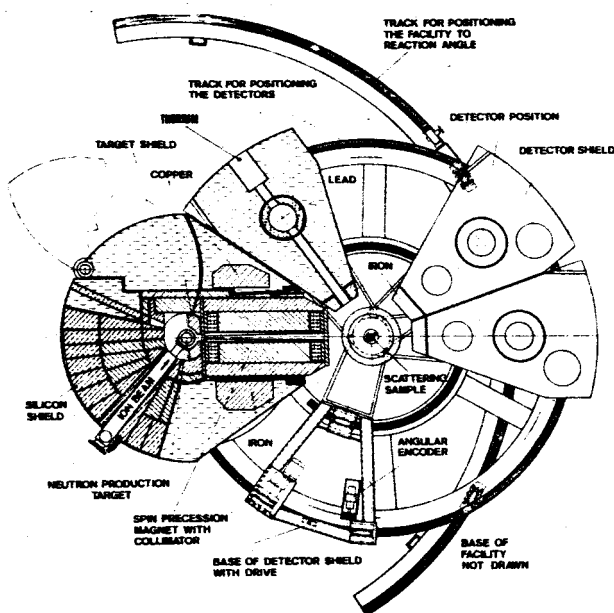


Fig. 1: Top view of the SCORPION facility

producing target, the spin-precession magnet, the scattering sample,

4 NE213 detectors and 4 additional monitor detectors. After unfolding the proton recoil spectra the angular distributions have been corrected for multiple scattering and finite geometry effects by Monte Carlo calculations. More details are given elsewhere ¹⁾.

The investigation of cryogenic samples has been made possible by a Dewar recently constructed. The results of the oxygen-measurements are shown in Figs. 2-3. Data evaluation of many other nuclides is in progress, as an example for a heavier nucleus Fig. 4 shows the results of tantalum. For appropriate nuclides, optical model calculations have been carried out with the code ECIS-79 by J. Raynal.

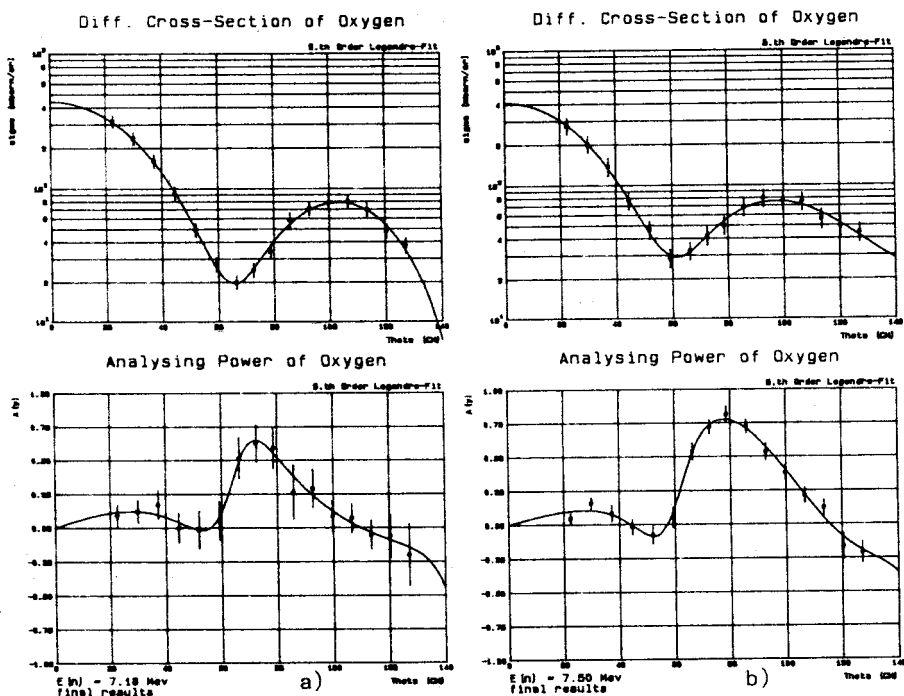


Fig. 2: Differential cross section and analysing power of oxygen at a) 7.18 MeV and b) 7.50 MeV neutron-energy. The full curves are Legendre fits to the data.

1. J.W. Hammer, G. Bulski, W. Grum, W. Kratschmer, H. Postner and G. Schluöner, Nucl. Instr. and Meth. 244, 455 (1986)

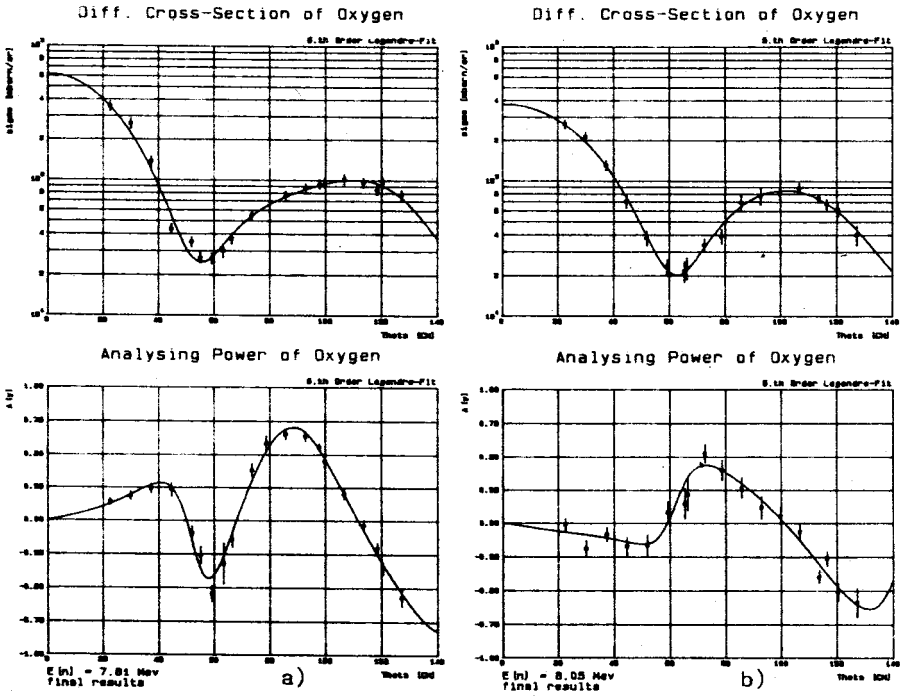


Fig. 3: Oxygen data at a) 7.81 MeV and b) 8.05 MeV. For explanations see Fig. 2.

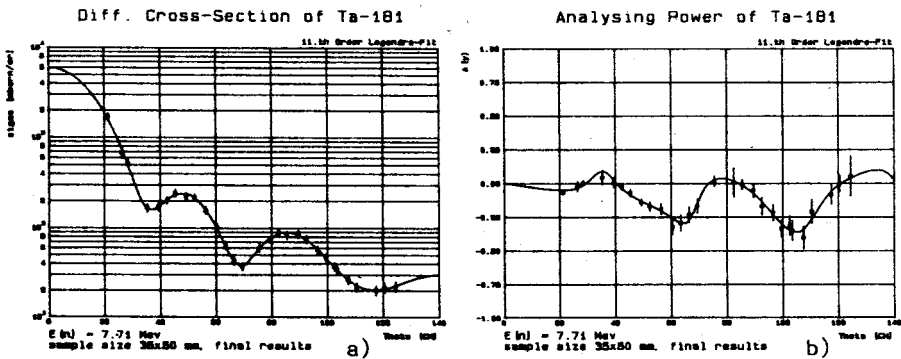


Fig. 4: a) Differential cross section and b) analysing power of tantalum for 7.71 MeV neutron-energy. The full curves are Legendre fits to the data.

A SPECTROMETER FOR DOUBLE-DIFFERENTIAL NEUTRON-EMISSION CROSS SECTION MEASUREMENTS

E. Dekempeneer, H. Liskien

Commission of the European Communities, Joint Research Centre,
Geel Establishment, Central Bureau for Nuclear Measurements,
2440 Geel, Belgium

L. Mewissen, F. Poortmans

S.C.K./C.E.N., 2400 Mol, Belgium

1. INTRODUCTION

Double-differential neutron-emission data are requested for the various constituent elements of the blanket of a fusion reactor and are important for a better understanding of the nuclear reaction mechanism, in particular for the pre-equilibrium neutron-emission process.

Up to now, such data were mostly obtained with pulsed monochromatic neutron sources so that the secondary neutron energy spectra could be measured by the time-of-flight method. We have set up a spectrometer at a pulsed white neutron source which allows the measurements of the angle-energy distributions of the secondary neutrons in one run for a broad range of primary neutron energies.

2. EXPERIMENTAL DETAILS

2.1 General description

The sample is mounted in an evacuated cylindrical vacuum tube at 60 meter from the pulsed neutron source at GELINA ¹⁾ and surrounded by eight NE 213 proton-recoil liquid scintillators ($\varnothing = 5$ cm, $h = 5$ cm) at a distance of 20 cm from the sample. The incident neutron energy is determined by time-of-flight and the energy of the secondary neutrons by unfolding the pulse-height spectra of the liquid scintillators.

2.2 Neutron detectors

Relative response functions for the NE 213 liquid scintillators were measured in the energy range 0.3 MeV-16 MeV in steps of 0.1 MeV using the pulsed white neutron source.

A relative efficiency curve was established experimentally in the range 0.4-7.5 MeV and 13-16 MeV using monoenergetic neutrons produced in the reaction $T(p,n)^3\text{He}$, $D(d,n)^3\text{He}$ and $T(d,n)^4\text{He}$ at the 7 MV Van de Graaff and by Monte-Carlo calculations using the code NEFF4 2) for the gap between 7.5 MeV and 13 MeV.

2.3 Electronics and Data-acquisition

The anode output of each photomultiplier tube is used as stop pulse for the time-digitizer and for pulse-shape discrimination. The output of the ninth dynode is used for pulse height analysis and detector identification. The information for each event is transmitted to a HP 1000F computer with central 2 Mbyte memory through a 128 word buffer of 32 bits. The information is stored in the memory as a three-dimensional array: detector (angle), time-of-flight (incident energy), pulse-height (secondary neutron energy).

2.4 Background sources

The major source of background is due to the scattering of the incoming neutron beam by the windows of the aluminium vacuum chamber in which the sample is mounted. This background is easy to measure.

The sample-dependent background can not be measured but the results of the $^7\text{Li}(n,xn)$ measurement show that this contribution is very small.

2.5 Data reduction

The code FORIST 3) is used for the unfolding of the pulse-height spectra. After the unfolding, the data are corrected for dead time, for multiple scattering in the sample and for attenuation of the emitted neutrons by the sample and by the wall of the vacuum tube.

The Monte-Carlo code written for the calculation of the multiple scattering corrections only takes into account the elastic scattering component which in many cases is the most important contribution to the total number of emitted neutrons. This approximation is permitted because very thin samples (transmission > 0.9) are used.

The normalization of the data is done by measuring the ^{12}C differential elastic yield below 2 MeV 4) and by measuring the relative neutron flux with an ^{235}U fission chamber which is mounted in the neutron beam at a 100 meter flight-path station.

3. EXAMPLE: THE $^7\text{Li}(n,xn)$ REACTION

Data-taking was performed during 600 hours for incident energies between 1.6 MeV and 16 MeV. However, above 10 MeV, the present data have not yet the required statistical precision for unfolding the pulse-height spectra. A new neutron producing target which will produce a harder neutron spectrum than the present uranium target is under construction.

As an example, we show on fig. 1 the differential neutron emission cross section for an incident energy window between 8.4 MeV and 8.7 MeV and for four angles. The sample was a metallic ^7Li plate, enriched to 99.97% with a thickness of 0.0325 at/b.

The sample-independent background varied from roughly 7% for backward angle detectors to 3% for forward angles. On fig. 1, we see the contribution from elastic scattering and inelastic scattering to the 478 keV state which are not separated, the inelastic peak from the 4.6 MeV state and a continuum part due to the $^7\text{Li}(n,n'\alpha)t$ reaction. The valley between the elastic peak and the continuum part gives us an idea how small the contribution of the sample-dependent background is.

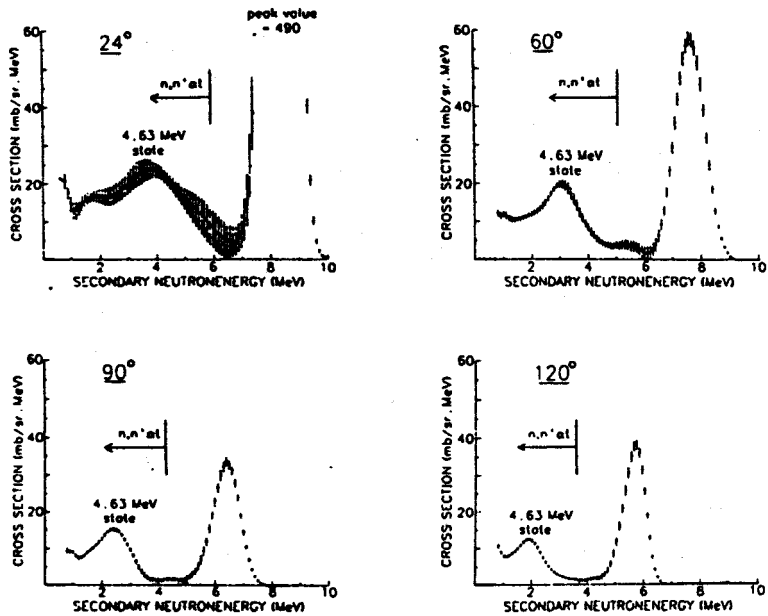
E = 8.55 MeV

Fig. 1 An example of double-differential neutron-emission cross sections for ${}^7\text{Li}$

5. REFERENCES

1. Salomé, J.M., Cools, R., Nucl. Instr. Meth. 179, 13 (1981)
2. Dietze, G., Klein, H., PTB Bericht, PTB-ND-22, Okt. 1982
3. "Forist Spectra Unfolding Code", Rad. Shield. Inf. Center, Computer Code Collection PSR-92, ORNL (1975)
4. Fu, C.Y. and Perey, F., Atomic Data and Nuclear Data Tables, 22, 249 (1978)

FIRST RESULTS AT THE A.P.T. - FAST NEUTRON FACILITY OF THE L.N.L.

R.CHERUBINI[◊], G. GALEAZZI^{◊+}, F.JIMENEZ^{◊(*)}, C.MANDUCHI^{◊+}, G.MOSCHINI^{◊◊},
R.NINO[◊], R.POLICRONIADES^{◊(*)}, M.T.RUSSO MANDUCHI^{◊+}, G.F.SEGATO^{◊+},
B.M.STIEVANO[◊] and A.VARELA^{◊(*)}.

◊ INFN - Laboratori Nazionali di Legnaro, 35020 LEGNARO (PADOVA), ITALY

◊ Dipartimento di Fisica, Università di Padova, 35100 PADOVA

+ INFN - Sezione di Padova, 35100 PADOVA, ITALY

The request for reliable neutron data (1,2), in particular for neutron energy from 5 to 14 MeV, and for calibrated neutron detectors are still open and has nowadays enhanced by the need of precise fast neutron data for fusion reactor development.

In order to respond to these needs, at the 7 MV Van de Graaff accelerator of the INFN - Laboratori Nazionali di Legnaro (L.N.L.) it was built-up a multipurpose scattering chamber (50 cm inner diameter, 24.2 cm long) adequate for fast neutron spectroscopy with Associated Particle Technique (A.P.T.) (2), used with thin Ti-T and home made deuterated polyethylene targets.

As well known (3), the A.P.T. with d-D and d-T reactions provides a simple method for producing collimated beam of neutron of accurately determined flux in a wide energy range.

Deuteron beams with energy from 2 to 7 MeV were able to produce monoenergetic neutron flux in the energy range 2 to 20 MeV. The obtained results are presented to demonstrate the performances of this system (2).

An explosive view of the A.P.T. chamber is shown in Figure 1. The basic components illustrated in the Fig. 1 are:

- 1) External cylindrical body with interchangeable 137° large thin window;
- 2) Rotating target assembly suitable for self-supporting deuterated polyethylene and thin Tritium-Titanium targets;
- 3) Turnable charged particle detector table;
- 4) Beam collimator system;
- 5) External scattering table with sliding neutron detector mounting;
- 6) Automatic vacuum system.

Figure 2 illustrates the n- γ pulse shape discrimination taken with a typical electronic arrangement and a stilbene detector (3.81 cm diameter, 1.27 cm thick), using D(d,n) ³He reaction for E_d=5.5 MeV, E_n=4.4 MeV and $\theta_n=80.2^\circ$ and T(d,n) ⁴He reaction for E_d=6.0 MeV, E_n=18.2 MeV and $\theta_n=72.47^\circ$. The figures of merit obtained were F₁=1.29 and F₂=1.17, respectively.

In Figure 3 a Time-of-Flight (ToF) spectrum is shown, which illustrates the time correlation between the neutron and the associated ³He, obtained for a D(d,n) ³He reaction with E_d=4.0 MeV, E_n=4.1 MeV and $\theta_n=76.5^\circ$. The FWHM was 2nsec.

(*) On leave: Instituto Nacional de Investigaciones Nucleares, Mexico and IAEA Fellows.

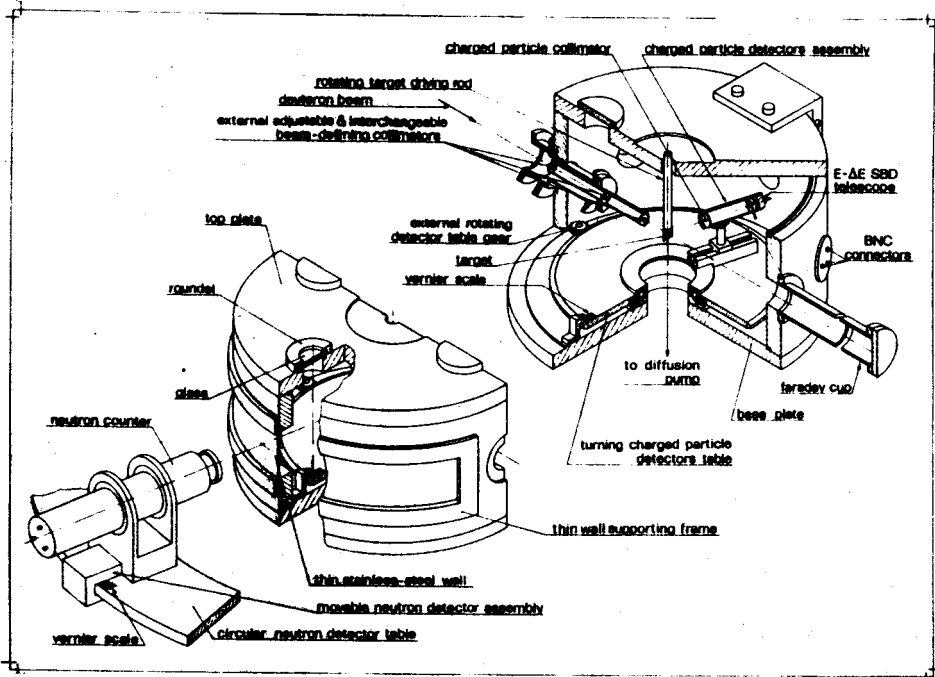


Fig. 1. Explosive view of the A.P.T. Chamber.

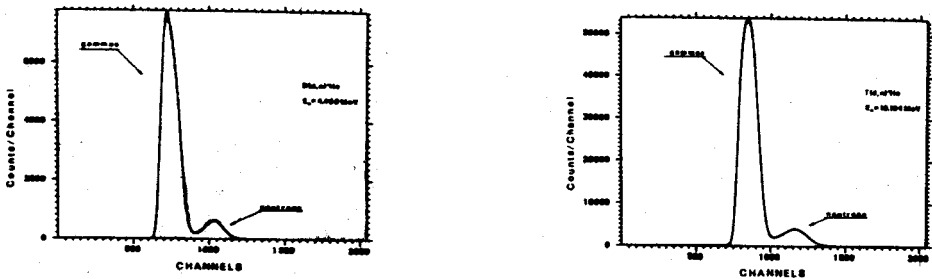


Fig. 2. n - γ pulse shape discrimination spectra.

Figure 4 shows a vertical and horizontal measurements of the neutron profile taken from a $D(d,n)^3\text{He}$ reaction for $E_n=2.4$ MeV ($E_d=2.0$ MeV). The profiles are taken at a distance of 30.6 cm from the target. The vertical scales give a relative measure of the ToF to ^3He counts.

Figure 5 shows typical ^3He yields obtained for 119 $\mu\text{g}/\text{cm}^2$

and $151 \mu\text{g}/\text{cm}^2$ deuterated polyethylene with carbon baking ($18 \mu\text{g}/\text{cm}^2$ and $19 \mu\text{g}/\text{cm}^2$) home marked targets.

The thickness of the 137° large thin stainless steel window used during the performances test was 2 mm.

The properties of the A.P.T. chamber described here are adequate for accurate measurements in neutron physics field.

REFERENCES

- 1) CINDA 83, IAEA, Vienna, 1983.
WREND 83/84, IAEA, Vienna, 1983.
- 2) R.CHERUBINI et al., Report INFN/TC - 85/23.
- 3) H.H.BARSCHALL et al., Rev.Mod.Phys., 24 (1952) 1.
J.L.LOWLER et al., Nucl.Instr. and Meth., 175 (1980) 449.

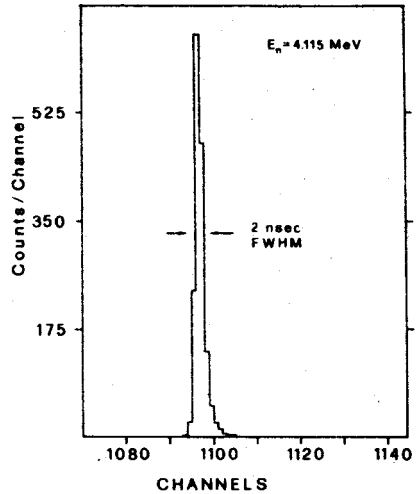


Fig. 3. ToF spectrum.

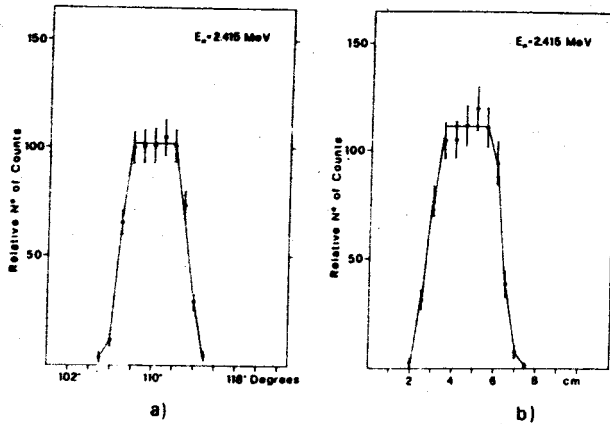


Fig. 4. Horizontal and vertical neutron profiles.

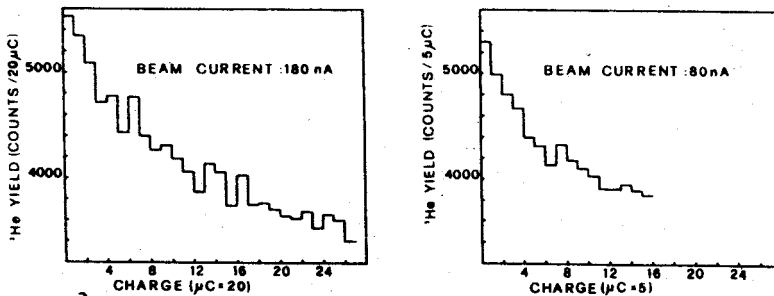


Fig. 5. ^3He yield as function of the total integratel beam current.

**A DEUTERIUM/TRITIUM GAS TARGET FOR PRODUCTION
OF FAST NEUTRON WITH THE d-D AND d-T REACTIONS AND WITH
THE ASSOCIATED PARTICLE TECHNIQUE**

C. CERNIGOI⁺, R. CHERUBINI^{*}, G. MOSCHINI^{*°} and C. TUNIZ⁺.

⁺ Dipartimento di Fisica, Università di Trieste, TRIESTE, Italy.

^{*} INFN - Laboratori Nazionali di Legnaro, LEGNARO (Padova), Italy.

[°] Dipartimento di Fisica, Università di Padova, PADOVA, Italy.

Monoenergetic neutron beams with energy in the region up to 50 MeV are in continuing demand for neutron cross section measurements, mainly for theoretical interpretations of reaction mechanisms or nuclear structure as well as for bio-medical applications or reactor design.

As known, for neutrons there exists the disadvantage that they have to be produced by nuclear reactions. The Associated Particle Technique (A.P.T.) provides an accurate method of producing collimated, monoenergetic neutron beams of known flux (1).

This technique is applicable in the case of those neutron producing reactions where a detectable light charged particle is produced together with the neutron with a two-body kinematics.

The $D(d,n)^3\text{He}$ and $T(d,n)^4\text{He}$ reactions are widely used as such neutron sources. Among the effects which influence the monochromaticity of the neutron beam those connected with the target features are very important. To this respect, gas targets offer several advantages over solid targets. The target density can be determined directly from pressure and temperature measurements. Also, the effective target thickness is accurately known and can be easily varied. The background contamination problems can be more carefully controlled and in many cases avoided.

In order to produce clean monoenergetic neutron fluxes with energy up to 50 MeV, we have designed and constructed a deuterium/tritium gas target, schematically shown in Figure 1.

The target cell, 340 mm long and 8.4 mm in diameter, consists of a solid piece of free-cutting stainless steel bar. A narrow cross-shaped tube is screwed to the body of the cell. One way is used to evacuate the cell, the second to fill the cell with deuterium or tritium gas and the third one is connected to a manometer. Two safety vacuum chambers (450 mm long), upstream and downstream the cell, are designed to separate the cell from the accelerator beam line vacuum system.

Thin windows (5 and 6 mm in diameter) soft-soldered to aluminium bodies are used for the safety chambers and the cell. The window material has to be chosen in order to minimize energy loss and energy straggling of the deuteron incident beam; to sustain a pressure differential of few atm; to withstand beam currents of at least 1 μA and, finally, to remain impermeable to the target gas used.

A thin mylar foil (5 μm thick and 1 mm in diameter) separates the cell from an evacuable extension housing the charged particle detection system. The unambiguous identification of the associated charged particle is performed with a time-of-flight telescope employing a

microchannel plate as start detector and a silicon surface barrier detector, SSBD (900 mm) giving both timing and energy signals. The flight path is 40 cm. The angular position of the extension is chosen according to neutron energy requirements.

The cell, the safety vacuum chamber and the charged particle system extension are connected with an independent high vacuum system.

The deuteron beam is defined with four insulated tantalum collimators (3 mm in diameter) connected with current digitizers.

The thickness of the cell wall is 2 mm.

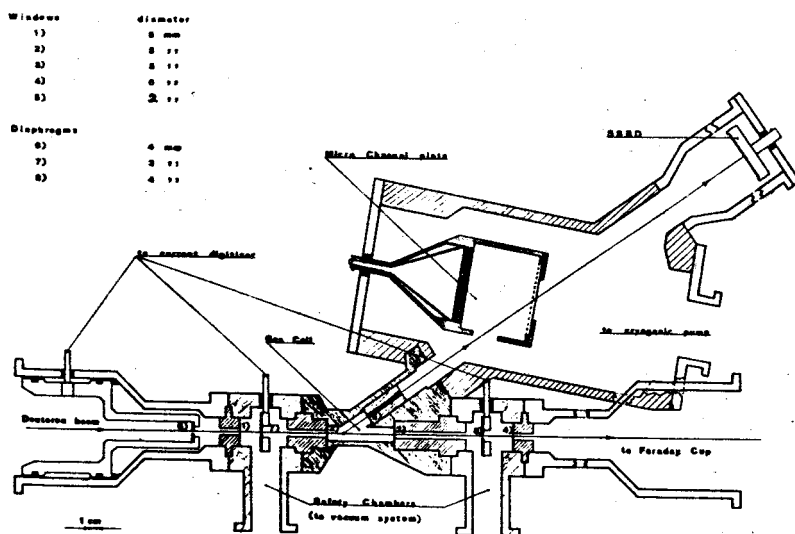


Fig. 1. Schematic horizontal section of the gas target.

Preliminary experiments have been performed at the 7.0 MV Van de Graaff accelerator of the INFN Laboratori Nazionali di Legnaro to test, with the d-D reaction, the performances of the target for different windows, gas pressure and deuteron beam intensities and energies.

In these first tests we have investigated for comparison the performances of aluminized mylar and Havar foils as windows. The Havar windows performed much better than the aluminized mylar ones. The associated charged particles were detected only by the SSBD at 35° degrees with respect to the deuteron beam. The results with 0.000062 inch Havar foils are shown in Figure 2. Beam intensities of 2 to 200 nA in the range 2+6 MeV produced about 3 neutrons/sec·nA·atm, according to the energy, with a good discrimination of the charged

particles detected only by the SSBD (see Fig. 2). A better identification of the associated charged particles (p, ^3H and ^3He) will be achieved with the Time-of-Flight measurements.

The Time-of-Flight telescope are presently being tested.

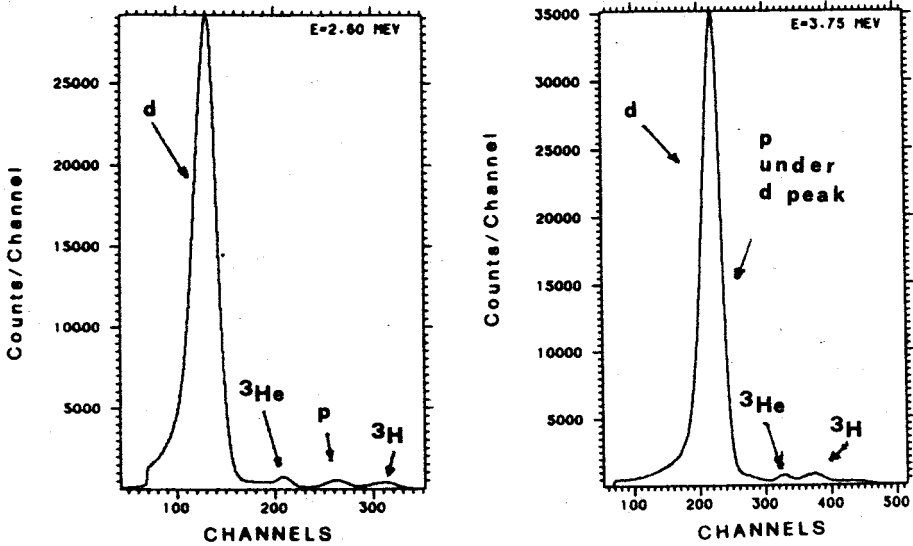


Fig. 2. Charged particles energy spectra for the d-D reactions at $E_d=2.60$ MeV and $E_d=3.75$ MeV, respectively.

REFERENCES

- (1) H.H. BARSCHALL et al., Rev. Mod. Phys., 24 (1952) 1.
 C.M. BARTLE et al., Nucl. Instr. and Meth., 95 (1971) 221.
 J.L. FOWLER et al., Nucl. Instr. and Meth., 175 (1980) 449.

ENERGY AND ANGULAR DISTRIBUTIONS OF NEUTRONS FROM THE ${}^2\text{H}(\text{d},\text{n}){}^3\text{He}$ AND ${}^3\text{H}(\text{d},\text{n}){}^4\text{He}$ REACTIONS

J. Csikai, Zs. Lantos and Cs. M. Buczkó

Institute of Experimental Physics, Kossuth University,
Debrecen, 4001, Pf. 105. Hungary

Simple analytical expressions are given for the calculation of the energy and angular distributions of neutrons emitted in D+D and D+T reactions for the $E_d=20-500$ keV energy range. The results obtained were compared with the measured and calculated thin and thick target energy and angular distributions of D+T neutrons.

1. INTRODUCTION

The accurate knowledge of the energy and angular distributions of neutrons emitted in the ${}^2\text{H}(\text{d},\text{n}){}^3\text{He}$ and ${}^3\text{H}(\text{d},\text{n}){}^4\text{He}$ reactions is needed for the cross section measurements especially around 14 MeV and for the design of thermonuclear devices. The aim of this work was to find simple analytical expressions for the description of the source yield and the energy of neutrons emitted in the D+D and D+T reactions below 500 keV bombarding deuteron energy as well as to check these expressions by experiments and calculations in the cases of thin and thick targets.

2. FITTING PROCEDURE

The thin-target data recommended¹⁾ for the energy and angular distributions of neutrons emitted in the D+D and D+T reactions in laboratory system were approximated by the following expressions:

$$Y_n(E_d, \theta) = Y_o(E_d) + \sum_{i=1}^n Y_i(E_d) \cos^i \theta \quad (1)$$

$$E_n(E_d, \theta) = E_o(E_d) + \sum_{i=1}^n E_i(E_d) \cos^i \theta \quad (2)$$

In eqs.(1) and (2) $n=5$ and 3 for D+D while $n=3$ and 2 for D+T reactions, respectively. It was found that the evaluated data²⁾ for the energy and angular distributions in the case of thick target can also be described by eqs.(1) and (2). The values of Y_0 , Y_1 , E_0 and E_1 coefficients obtained from a least-squares fit are tabulated for the $E_d=50-500$ keV energy range. The E_0 and E_1 values for the D+T reaction have been determined between 20 and 70 keV in 10 keV steps.³⁾

3. EXPERIMENTAL PROCEDURE

The effect of target thickness on the source yield and the energy of neutrons as a function of emission angle in D+T reaction was investigated in an improved experimental arrangement shown in Fig.1. This scattering-free irradiation facility rendered it possible to measure the source yield and the neutron energy in 2π interval. The details of the foil activation method used for the determination of the neutron energy around 14 MeV are described in Ref.⁴⁾. The neutron energy as a function of emission angle was determined from the measurements of the activity ratios of $^{89}\text{Zr}/^{92\text{m}}\text{Nb}$, $^{89}\text{Zr}/^{180\text{m}}\text{Ta}$ and $^{89}\text{Zr}/^{196}\text{Au}$ produced in (n,2n) reactions. The measured values together with those obtained by relativistic⁵⁾ and nonrelativistic⁶⁾ calculations are indicated in Fig.2.

4. RESULTS AND DISCUSSION

Figure 2 shows that good agreement exists between the measured and calculated neutron energies. An analysis of the data at different energies led to the conclusion that the deviation from the relativistic calculation does not exceed 30 keV for D+T and D+D neutron if $E_d \leq 500$ keV. The shapes of the source yield curves measured by Nb, Ta and Au foils deviate slightly from each other indicating that the (n,2n) excitation functions of the flux monitor reactions are not constant around 14 MeV. Accepting the cal-

culated angular distributions^{5,6)} for thick target we have deduced the shapes of the monitor reactions around 14 MeV. The relative change in the cross section curves for the ^{93}Nb , ^{181}Ta and $^{197}\text{Au}(n,2n)$ reactions between 13.5 and 14.8 MeV is + 0.35%, -2.4% and +1.6%, respectively.

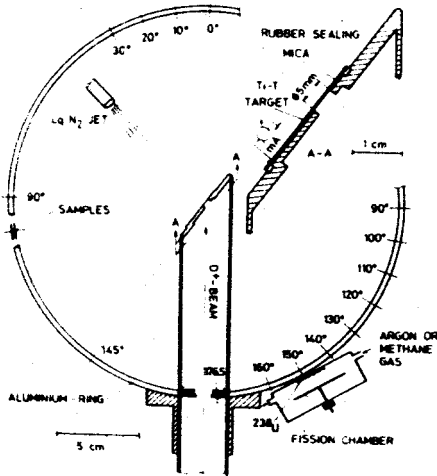


Figure 1.

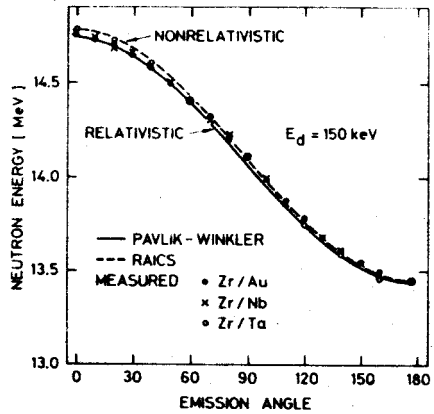


Figure 2.

REFERENCES

1. Liskien, H. and Paulsen, A., Nucl. Data Tables, 11(569)1973
2. Seagrave, J.D., Graves, E.R., Hipwood, S.J. and McDole, C.J., LAMS-2162, Los Alamos (1958)
3. Csikai, J., Handbook of Fast Neutron Generators, CRC Press Inc., USA, (in press)
4. Csikai, J., in Proc. of the Int. Conf. on Nuclear Data for Science and Technology, Antwerp (1982)p.414
5. Pavlik, A. and Winkler, G., private communication
6. Raics, P., private communication

THE FAST NEUTRON SPECTRUM MEASUREMENT WITH SCINTILLATION DETECTOR

D.Nikolić, M.Milošević, M.Pešić

"Boris Kidrič" Institute of Nuclear Sciences

Nuclear Engineering Laboratory, 11001 Belgrade, P.O.Box 522

YUGOSLAVIA

The fast neutron spectrum is measured in the mixed gamma and neutron radiation field, using zero-crossing technique of pulse shape discrimination. The measured pulse height distribution is treated with computer program which unfolds the neutron spectrum. Measured neutron spectrum from $^{241}\text{Am-Be}$ source is presented.

1. MEASURING DEVICE

The zero-crossing technique of pulse shape discrimination (PSD) method is used for suppressing gamma ray background in neutron detection system which utilise organic scintillators, especially stilbene crystals and the NE213 organic liquid. The main advantage of this method of PSD is its suitability for use over a large dynamic range of pulse amplitudes, with variations greater than 100:1¹⁾. This paper describes measurements with NE213 scintillation detector 50x50 mm. The block diagram of the PSD system used in measurement is shown in Fig.1. It is based on the fact

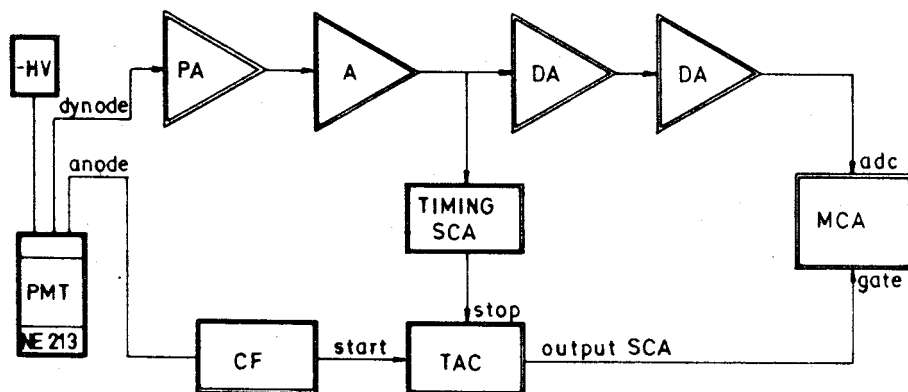


Fig.1. Block diagram of spectrometer pulse shape discrimination system

that the zero-crossing time of a doubly differentiated (bipolar) signal is dependent on the risetime, and is essentially independent of amplitude. Gamma-ray induced pulses have smaller risetimes than neutron induced pulses.

The signal derived from the leading edge of the detector anode signal starts time-to-amplitude converter (TAC). The dynode signal is fed through preamplifier and amplifier, and routed to the zero-crossing pickoff in the timing SCA. It provides a stop pulse for TAC, and establishes the proper time relations between the pulses. The output of the TAC is a signal whose amplitude is proportional to the time delay between leading edge and crossover and it is used to gate the multi-channel pulse (height analyzer (MCA)). A/D input of multichannel analyzer receives signal from delay amplifier. The low level discrimination on timing SCA is set to accept the amplitudes corresponding to neutrons, and a coincident pulse is generated and used to gate MCA such that only neutron pulses are analysed.

1.1. Calibration

Calibration of light output of the detector is carried out with gamma source ^{22}Na by means of the Compton edge position. For peak energies of 1,274 MeV and 0,511 MeV corresponding Compton edge are 1,06 and 0,34 MeV, respectively. Determination of the Compton edge position relative to the position of the maximum and half maximum of the distribution is determined from table ²⁾. Relation between measured pulse amplitude and channel number k is $h = a + bk$ ³⁾, where a and b are constants obtained in calibration. Proton induced pulse heights versus energy are determined by interpolating values obtained in absolute calibration with monoenergetic neutrons ⁴⁾.

2. UNFOLDING METHOD

Differential method is applied for unfolding neutron spectrum from measured pulse-height distribution induced by recoil protons in scintillation detector ⁵⁾. The effects of the double neutron scattering on hydrogen and the loss of recoil protons through the end of the detector are mostly removed with shape correction factor ⁶⁾. Computer code

PULNE ⁷⁾ is developed basing on previous algorithm and can be adapted for use on personal computer. The detector efficiency is calculated with the separate program in 100 energy points, with 0,1 MeV step and involved as a data library. The slope of the recoil-proton energy distribution is obtained by average over 6 energy intervals (0,6 MeV), omitting one interval on each side of neutron energy. Averaging the same data over a larger energy tended to smear out the resolution and decrease the statistical fluctuations.

3. RESULTS AND CONCLUSION

Neutron spectrum from ²⁴¹Am-Be source is estimated from measured pulse height distribution by program PULNE. Comparing with referent spectrum ⁸⁾ shows good agreement, Fig.2. Employed measuring technique and developed computer code enable further investigation in neutron spectrometry and dosimetry.

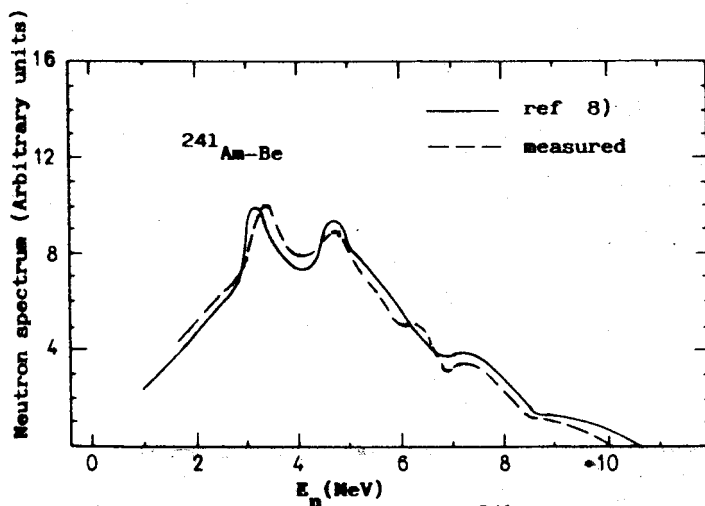


Fig.2. Neutron spectrum from ²⁴¹Am-Be source

4. REFERENCES

1. Winyard, R.A. at all, Nucl.Inst.and Meth.95, 141-153 (1971)
2. Dietze, G. and Klein, H., Nucl.Inst.and Meth. 193, 549-556 (1982)
3. Nikolić, D., Milošević, M., Pešić, M., Acta Physica Vol.59 107,110(1986)
4. Verbinski, V.V. at all, Nucl.Inst.and Meth.65, 8-25 (1968)
5. Holman, M. at all, ZJE Report 191, 1976
6. Toms, M.E., Nucl.Inst.and Meth. 92, 61-70 (1971)
7. Nikolić, D., Program PULNE for Unfolding Fast Neutron Spectrum from Measured Pulse Height Distribution, ETAN, to be published
8. Profio, A.E., "Experimental Reactor Physics", 172 (1976)

UNFOLDING OF SCINTILLATION SPECTRA USING APPROXIMATELY KNOWN RESPONSE FUNCTIONS

M. Zadro and M. Bogovac

Rudjer Bošković Institute, POB 1016, 41001 Zagreb, Yugoslavia

1. INTRODUCTION

The problem of reconstructing the neutron spectrum from the measured pulse height spectrum is related to the solution of the Fredholm integral equation. This problem is known to be ill-posed. The solution is highly sensitive to small random errors in the data, i.e. the errors in the scintillation spectrum and the errors in response functions. In this paper it is presented an iterative unfolding procedure, based on the Tikhonov regularization method, which takes into account both of these errors.

2. PROBLEM OF UNFOLDING

The response of the scintillation detector is related to the incident neutron spectrum $\Phi(E)$ by the following equation:

$$U(x_1) = \int_a^b \epsilon(x_1, E) \Phi(E) dE + \delta(x_1) \quad (1)$$

where $\epsilon(x_1, E)$ is the efficiency at an incident neutron energy E for a bias x_1 , i.e. the integral of the response function from x_1 to ∞ , $U(x_1)$ is the integral of the measured spectrum from x_1 to ∞ , and $\delta(x_1)$ is the random error associated with $U(x_1)$.

If ϵ is known only approximately, then eq. (1) can be written as

$$U(x_1) = \int_a^b \epsilon(x_1, E) \Phi(E) dE + \delta(x_1, \Phi) \quad (2)$$

where

$$\delta(x_1, \Phi) = \delta_\epsilon(x_1, \Phi) + \delta_u(x_1) \quad (3)$$

$$\delta_{\epsilon}(x_1, \Phi) = \int_a^b \delta_{\epsilon}(x_1, E) \Phi(E) dE \quad (4)$$

$\delta_{\epsilon}(x_1, E)$ and $\delta_u(x_1)$ are the errors in the determination of $\epsilon(x_1, E)$ and $U(x_1)$, respectively.

It is assumed that the errors δ are uncorrelated and that their means and variances are known, $\bar{\delta} = 0$, $\bar{\delta}^2 = \sigma^2$. Using eqs. (3) and (4), after discretization of $\Phi(E)$, one obtains

$$\sigma^2(x_1, \Phi) = \sigma_{\epsilon}^2(x_1, \Phi) + \sigma_u^2(x_1) \quad (5)$$

$$\sigma_{\epsilon}^2(x_1, \Phi) = \sum_j \sigma^2(x_1, E_j) \Phi^2(E_j) (\Delta E_j)^2 \quad (6)$$

3. REGULARIZATION

3.1 Tikhonov's Regularization Method, $\delta_{\epsilon} = 0$

In accordance with the method of Tikhonov¹⁾, the solution of the problem (1) minimizes the functional

$$F = \sum_1 \omega_1^2 \left[\int_a^b \epsilon(x_1, E) \Phi(E) dE - U(x_1) \right]^2 + \alpha \int_a^b \left[\frac{d\Phi(E)}{dE} \right]^2 dE \quad (7)$$

where ω_1^2 are the weights, $\omega_1^2 = 1/\sigma^2(x_1)$. An optimal regularization parameter α is determined by the residuals¹⁾

$$\sum_1 \omega_1^2 \left[\int_a^b \epsilon(x_1, E) \Phi_{\alpha \text{opt}}(E) dE - U(x_1) \right]^2 = R \quad (8)$$

$$R = \sum_1 \omega_1^2 \sigma^2(x_1) \quad (9)$$

3.2 Solution of Problem with $\delta \neq 0$

Since σ (eq. (5)) depends on the unknown function Φ an iterative procedure is used in this case. The initial approximation of the solution is calculated setting $\sigma_{\epsilon} = 0$ and applying the method of Tikhonov. If the minimum of the first term in eq. (7) is larger than R , then it has

to be added to R in eq. (8)². σ_ϵ^2 is then calculated from eq. (6). The new $\sigma^2 = \sigma_u^2 + \sigma_\epsilon^2$ is used to calculate a more accurate neutron spectrum Φ . This process continues until a converged spectrum is obtained.

4. CALCULATIONS

In test calculations the "experimental" data $U(x)$ are calculated from the efficiency $\epsilon(x, E) = 1 - x/E$, $x < E$, and neutron spectrum $\Phi(E)$ taken to be the sum of two or three Gaussian. The noise added to ϵ and U was given by Gaussian random number generator with a standard deviation $\sigma_u(x) = U(x)^{1/2}$ and $\sigma_\epsilon(x, E) = p \epsilon(x, E)^{1/2}$. The parameter p is varied in the range $10^{-4} - 5 \times 10^{-2}$. The error of $U(x)$ is controlled by the total number of detected neutrons, $N_d = U(0)$.

Fig. 1 shows typical results of test calculations. The unfolded spectrum is in good agreement with its original. The optimal amount of smoothing of the solution, and thus the energy resolution of the method, depends on the errors in the data.

5. CONCLUSION

An iterative unfolding procedure based on the Tikhonov method is proposed. It can be applied to the problem of unfolding of scintillation pulse height spectra. The errors in the data, both in the scintillation spectrum and in response functions are taken into account in the determination of the degree of smoothing.

6. REFERENCES

1. Tikhonov, A. and Arsenin, V.. Méthodes de résolution de problèmes mal posés, Éditions Mir, Moscow (1976).
2. Goncharski, A.V., Leonov, A.S. and Yagola, A.G.. Zh. Vychisl. Mat. i Mat. Fiz. 13, 294 (1973).

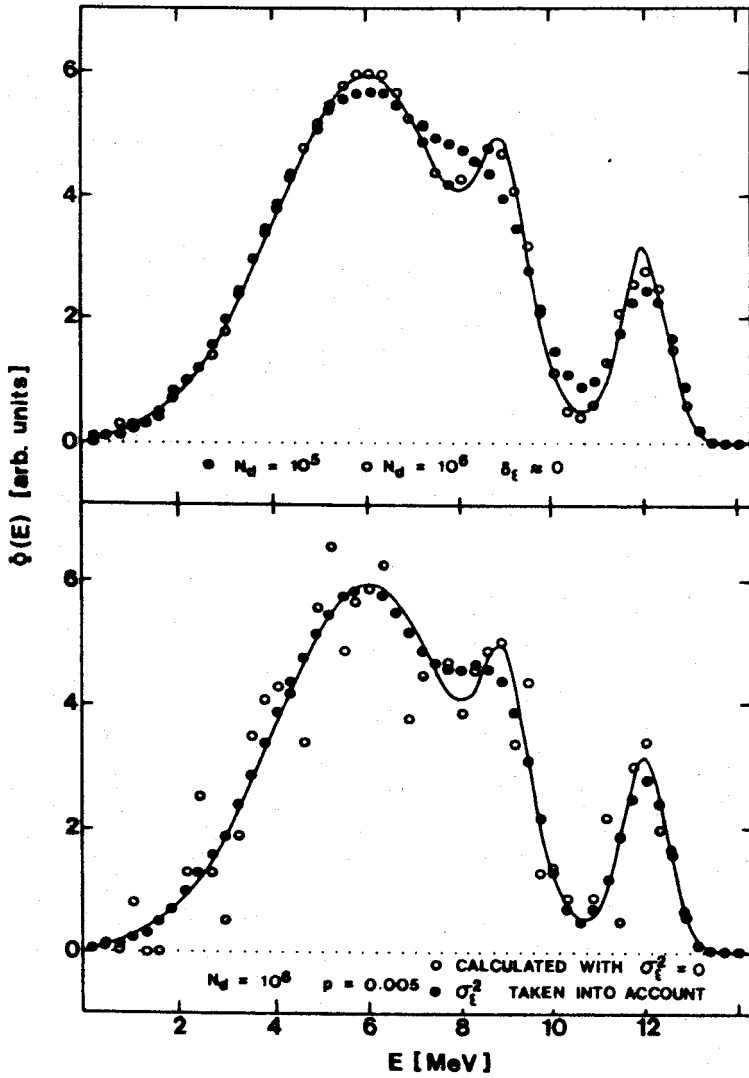


Fig. 1. The true (—) and unfolded (•,○) neutron spectra for different error levels.

A NEW APPLICATION OF Am-Be NEUTRON SOURCE--- PRODUCTION OF 5--10 MeV GAMMA RAYS FOR CALIBRATION

Ye Zongyuan, Li Jingwen, Yue Gang and Shi Detang

Institute of Atomic Energy
P.O. Box 275-60, Beijing, China

Discrete high energy γ -rays were produced utilizing the Am-Be neutrons through the radiation capture process and the (n, α) reaction. The device can be conveniently used for energy calibration of gamma detectors.

The energies of the γ -rays from radioisotope sources are usually lower than 3 MeV. For higher energies of γ -rays one has to use nuclear reactor or particle accelerator. Here we report a method which uses a 10^5 n/s Am-Be neutron source to generate monochromatic γ -rays in 5--10 MeV range. The device is very simple and can be conveniently used for the energy calibration of Ge(Li) and HpGe detectors, and may also be used as energy reference for NaI(Tl) and BGO detectors.

A sketch of the experimental arrangement is shown in Fig. 1. The neutron source with a strength of 1.8×10^5 n/s was surrounded by a 1 cm thick paraffin layer, a layer of radiator material and a 5 cm thick paraffin layer successively. The γ -spectrum was measured with a Ge(Li) detector under the

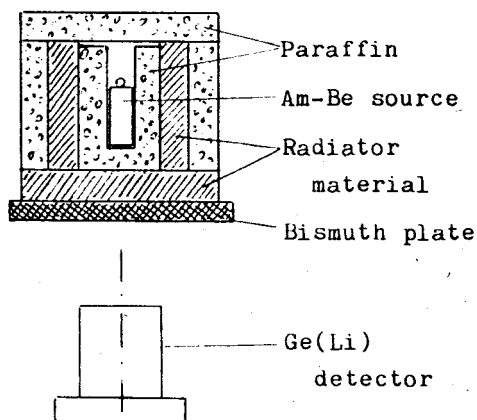


Fig. 1 Experimental arrangement

neutron source at a distance of 10 cm. Between the source and the detector we placed a 10 mm thick bismuth plate to reduce soft γ -rays. The γ -detector was shielded by a cap made of Pb and B_4C . The energy resolution of the germanium detector was 3.5 keV for ^{60}Co γ -lines.

The γ -energies were roughly calibrated by a ^{60}Co source and the 4430 keV γ -line from the neutron source itself. The accurate values were obtained from the level scheme of final nucleus of the reaction.

Fig.2 shows the γ -spectrum accumulated in 5 hrs. In the right part one can see the peaks of the 7638 keV γ -line. The peaks in the left part belong to 4430 keV γ -ray coming from the $^9\text{Be}(\alpha, n)$ $^{12}\text{C}^*$ reaction. A $\phi 100 \times 100$ mm NaI(Tl) scintillation counter, whose efficiency had been calculated by Monte-Carlo method, was

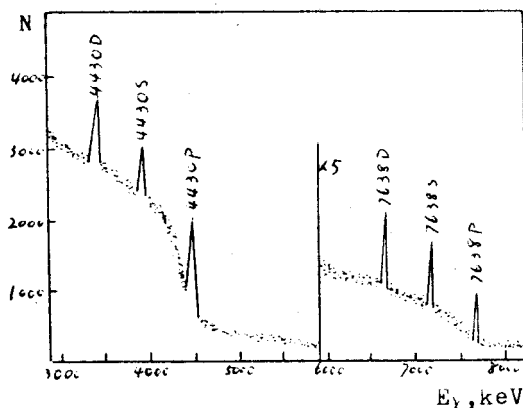


Fig.2 γ -spectrum from Fe radiator

used to measure the strength of the γ -lines. The intensity of 7638 keV line was about 500 /s, while the 4430 keV line is 20 times stronger. In addition, there also exists a 2230 keV line in the spectrum, which comes from the capture of neutrons by hydrogen.

A series of γ -lines can be generated by means of a Ni radiator. Among the high energy part of the γ -spectrum the intensity of 8998 keV line is the highest which amount to more than 40 % of the total.

Fig.3 shows the γ -ray spectrum for Cl capture (we used MgCl_2 as radiator) obtained from a three hour run. The energies (in keV) for these γ -lines are as follows: 8578.65, 7790.40, 7414.01, 6627.96, 6619.76, 6111.00 and 5715.40, re-

spectively¹⁾.

Through the $^{19}\text{F}(\text{n},\alpha)$ ^{16}N reaction a single line of 6128 keV can be obtained. In this case the experimental arrangement was similar to K.J.King²⁾.

It has been estimated for the above geometry that the fast neutron fluence rate at the γ -detector site was 40 n/s, which is small comparing to the damage threshold of the ordinary germanium detectors (10^{10} n/cm²).

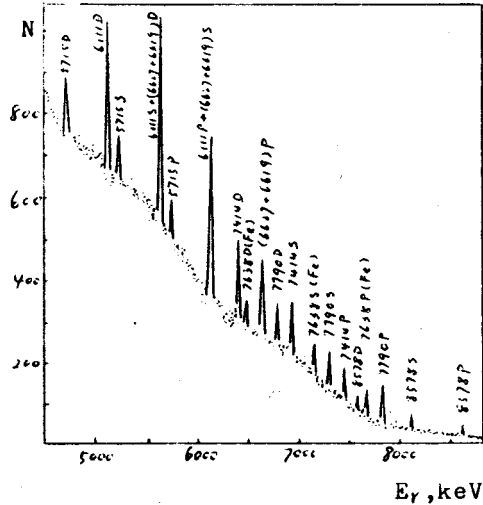


Fig. 3 γ -spectrum from Cl radiator

From above we may conclude that with Fe, Ni, Cl and F converters a moderate intensity Am-Be neutron source can be used as a convenient tool for the calibration of gamma detectors. Especially the γ -rays from the chlorine capture can provide very accurate energy scales for germanium detector calibration in the on line measurements.

We would like to thank Profs. Huang Shengnian and Gu Yifan for enlightening discussions.

1. Stels, M.L. and Chrien, R.E., Nucl. Instr. and Meth., 155, 253(1978)
2. King, K.J. et al., Nucl. Instr. and Meth., 227, 257(1984)

FAST NEUTRON SPECTRUM DETERMINATION WITH THRESHOLD DETECTORS AT THE RB REACTOR

M.Šokčić-Kostić, M.Pešić, D.Antić

The Boris Kidrič Institute of Nuclear Sciences
Nuclear Engineering Laboratory, 11001 Belgrade, P.O.B 522
YUGOSLAVIA

The fast neutron spectrum determination with threshold detectors at the RB reactor is described in this paper. The experimental results which are obtained on the coupled fast-thermal system CFTS-2 are given. At the end two different numerical methods for obtaining the fast neutron spectrum on the basis of experimental results are compared.

1. RB REACTOR

The RB is a zero power nuclear facility in the Boris Kidrič Institute of Nuclear Sciences¹⁾. It is possible to create the fast neutron fields by applying 80% enriched uranium fuel elements. The possibilities to obtain different neutron spectra are investigated using the converter and additional nonfissionable screens²⁾. The modified experimental fuel channel EFC³⁾ and convertors of neutrons inside the RB reactor CFTS-1 and CFTS-2 were created in continuing of this investigation⁴⁾. The devices give well defined neutron fields.

1.1. Coupled Fast-Thermal System No.2-CFTS-2

The fast core of CFTS-2 is formed of natural metal uranium fuel elements. The central area of the fast core is an air filled cylindrical experimental space with diameter of 150 cm and height up to 120 cm. The thermal RB core (driver) has a standard RB lattice pitch of 12 cm of 2% enriched metal uranium and 80% enriched UO_2 fuel elements in D_2O moderator.

2. NEUTRON FLUX DENSITY MEASUREMENTS IN CFTS-2

Neutron flux density is measured by activation technique^{5),6)}.

Thermal and epithermal flux density are measured by foil activation technique. Gamma activities of these foils are measured using scintillation technique. The experimental results are treated with ACT code that gives foil saturated activity and neutron flux density. It is based on analytical relations accounting for all necessary physical and geometrical corrections.

The absolute value of thermal neutron flux density in the centre of CFTS-2, for RB being 1W power is

$$F_{th} = (4.05 \pm 0.20) \times 10^5 \text{ n/cm}^2/\text{s}, \quad E \leq 0.625 \text{ eV}$$

Radial and axial distribution of fast neutron flux density is measured by means of threshold foil detectors. Gamma and beta activities of foils are measured using scintillation technique and $4\pi/\beta$ absolute counting method, respectively. The measurement results are also treated by ACT code. Some of results are given in Table 1.

Table 1. Axial distribution of fast neutron flux in CFTS-2

H(cm)	ϕ (n/cm ² /s/W)	H(cm)	ϕ (n/cm ² /s/W)
15	$(4.92 \pm 0.18) \times 10^5$	75	$(8.67 \pm 0.31) \times 10^5$
30	$(6.80 \pm 0.25) \times 10^5$	90	$(7.37 \pm 0.27) \times 10^5$
46	$(8.80 \pm 0.32) \times 10^5$	112	$(4.32 \pm 0.16) \times 10^5$
60	$(8.79 \pm 0.32) \times 10^5$	122	$(3.13 \pm 0.12) \times 10^5$

3. FAST NEUTRON SPECTRUM IN CFTS-2

Codes HEFEST⁷⁾ and PRAG are used for obtaining the fast neutron spectrum in CFTS-2 on the basis of results of ACT code. The codes are based on methods of maximal probability and adequate shape functions in fast region respectively. Code HEFEST returns fast neutron spectrum which is given in Table 2.

Table 2. Fast neutron spectrum in CFTS-2

E(MeV)	$\phi(n/cm^2/s/MeV)$	E(MeV)	$\phi(n/cm^2/s/MeV)$
1	1.26×10^6	6.5	1.16×10^4
2	2.71×10^5	7	6.59×10^3
3	1.06×10^5	8	2.81×10^3
4	6.11×10^4	9	1.45×10^3
5.5	4.36×10^4	10	9.69×10^2

Code PRAG gives the following shape of fast neutron spectrum

$$F(E) = E^{-0.77} E^{1/2}$$

which is very similar to previous result.

4. CONCLUSION

Developed fast neutron fields will be used for further investigation in the fields of spectrometry, dosimetry, irradiation studies, etc.

5. REFERENCES

1. Popović D., A Bare Critical Assembly of Natural Uranium and Heavy Water, Proceeding of the Second United Nations International Conference on the Peaceful Uses of Atomic Energy, Vol.12, 392, Geneva, 1958.
2. Strugar P., Šotić O., Ninković M., Pešić M., Altiparmakov D., Kernenergie 24, 101, 1981.
3. Pešić M., Marković H., Šokčić-Kostić M., Mirić I., Prokić M., Strugar P., Kernenergie 27, 461, 1984.
4. Pešić M., Coupled Fast-Thermal System at the RB Reactor, Master Thesis, University of Belgrade, 1984 (in Serbocroatian)
5. Kramer Ageev E.A., Troshin V.S., Tikhonov E.G., Aktivacioniye Metody Spektrometrii Neitronov, Moskva, Atomizdat, 1976.
6. Neutron Fluence Measurements, IAEA Technical Reports Series, No.107, Vienna 1970.
7. Cupać S., Šokčić-Kostić M., Pešić M., Program HEFEST for Calculation of Neutron Spectrum on the Basis of the Activity of Threshold Detectors, ETAN, Vol.9, 59, Belgrade, 1985. (in Serbocroatian)

FAST NEUTRON FIELDS AT THE RB NUCLEAR REACTOR

M. Pešić, P. Strugar (IAEA, Vienna), H. Marković,
D. Stefanović, "Boris Kidrič" Institute of Nuclear
Sciences, Nuclear Engineering Laboratory, Vinča, Yugoslavia

In Yugoslavia nuclear power technology has been introduced recently. That means that nuclear power plant Krško is in operation since a couple of years ago.

The RB nuclear reactor at the Nuclear Engineering Laboratory of the "Boris Kidrič" Institute of Nuclear Sciences (1) was the first, zero power, bare, heavy water critical facility in Yugoslavia. The natural metal uranium, the 2% enriched metal uranium and 80% enriched uranium dioxide fuel elements are available.

The investigations of fast Neutron fields at the RB reactor were initiated in 1976. These studies were performed on the NEUTRON CONVERTOR (NC) using 80% enriched fuel elements (2). The NC transforms the RB thermal leakage neutron flux into a fast fission neutron flux. The principal advantages of the NC are easy accessibility to the large experimental space and the possibility of down-shifting the fast neutron spectrum using screens of various materials.

The intensity of the fast neutron flux was up-graded in 1982. when an EXPERIMENTAL FUEL CHANNEL (EFC) was constructed (3). The EFC was formed of modified 80% enriched UO_2 fuel elements in a standard fuel element channel of the RB reactor.

Almost simultaneously, in 1981. a feasibility study on a COUPLED FAST-THERMAL SYSTEM (CFTS) began. It was based on the know-how acquired through the work on the NC and the EFC and the theoretical methods and numerical codes for fast neutron fields developed at the Nuclear Engineering Laboratory.

The goal was the realisation of the CFTS at the RB reactor using existing nuclear fuel with minimal reactor system modification. It was achieved at the end of 1984.

All the calculations for the CFTS on the RB reactor were performed using numerical codes developed at the Nuclear Engineering Laboratory.

The fast core of the CFTS-1 was formed of 80% enriched UO_2 fuel and the natural metal uranium fuel elements forming a blanket (4). The central area of the fast core is an air filled cylindrical experimental space with a diameter from 20 cm to 30 cm and a height of up to 120 cm. The thermal RB core (driver) has a standard RB lattice pitch of 12 cm of 2% enriched metal U fuel elements and 80% enriched UO_2 fuel elements in the D_2O moderator.

Very thorough safety analyses were performed for possible accidents during the operation of the RB reactor as an CFTS. It was shown that the operation of the RB reactor with the CFTS is safe. Neither the staff, nor the system components will be exposed to higher doses during serious accidents. The safety system of the RB reactor can quickly and safely shut-down the reactor during the most probable accidents.

The main characteristics of the obtained fast neutron fields at the RB reactor, NC, EFC and CFTS-1, are shown in Table 1.

The following various goals set for production and investigation of the fast neutron fields of the RB reactor are achieved: Production of the fast neutron fields by small modifications of a zero power research thermal reactor as a step leading to development of fast reactor technology in Yugoslavia, Significant contribution in developing new theoretical methods and numerical codes for fast neutron fields computations, experimental methods for fast neutron fields study, etc.

REFERENCES

1. D.Popović, S.Takač, H.Marković, N.Raišić, Z.Zdravković, B. Lolić, "Zero Energy Reactor RB" Bull. "B. Kidrič" Institute, Vol. 9, No.163 (1958).
2. P.Strugar, O.Šotić, M. Ninković, M.Pešić, D. Altiparmakov, "Conversion of the RB Reactor Neutrons by High-Enriched Uranium Fuel and Lithium Deuteride". Kernenergie, Bd.24, H.3, pp.101-104, Berlin, Marz (1981).
3. M.Pešić, H.Marković, M.Šokčić, I.Mirić, M.Prokić, P. Strugar, "Modified Fuel Channel for Sample Irradiation at the RB Reactor" Kernenergie, Bd. 27. 11/12, pp.461-464, Berlin (1984).
4. M.Pešić, "Coupled Fast-Thermal System at the RB Reactor", the M.Sc. Thesis, University of Belgrade, Faculty of Electrical Engineering, June 1984.

Table 1. Fast Neutron Fields Characteristics at the RB Reactor

Fast neutron Field	Neutron Converter (NC)	Exp. Fuel Channel (EFC)	Coupled Fast-Thermal System (CFTS-1)
Fast Neutron Flyx at 1 W RB Power	1.10^5 , E_n 0.1 MeV	$2.7 \cdot 10^6$, E_n 0.1 MeV	$1.4 \cdot 10^6$, 0.8 MeV
Max.Exp.Space	Air space: width 100 cm height 100 cm lenght 100 cm	Air hole: Diameter 2.5 cm Height 110 cm	Air hole: Diameter 20 or 30cm Height 120 cm
Max. Tot. \dot{D}_n (1 W)	8 mGy/h	410 mGy/h	290 mGy/h
Max. Tot. \dot{D}_t (1 W)	0.6 mGy/h	350 mGy/h	75 mGy/h

Chapter V

FAST NEUTRON REACTIONS (EXPERIMENTAL)

MEASUREMENTS FROM 5 to 10 MeV OF DOUBLE DIFFERENTIAL (n, α) CROSS SECTIONS
OF Ni AND Cu

Eric Wattecamps and Felix Arnotte

Commission of the European Communities,
Joint Research Centre - Geel,
Central Bureau for Nuclear Measurements,
BELGIUM

In the framework of CBNM's programme on fusion reactor neutron data, the alpha-particle angular- and energy- distributions of (n, α)-reactions on Ni and Cu were measured at the Van de Graaff laboratory from 5 to 10 MeV neutron energy in steps of 0.5 MeV. Our alpha-particle yield data are compared to all data available in literature and in particular to the recommended sets ENDF-B-5, JEF-1 and JENDL-2. This comparison illustrates the agreement between experimental data obtained by various techniques but also indicates significant differences from the ENDF-B-5 data.

1. EXPERIMENTAL CONDITIONS

A recent retrieval of (n, α) requests¹⁾ shows 105 requests for (n, α) and total α -production cross-section measurements. Many requests are made for structural materials of fusion reactors, such as Ni and Cu. The requested data are needed for dosimetry, activation and radiation damage studies. Measurements are scarce, and evaluations are quite diverse. Therefore, (n, α)-cross-sections were measured.

To measure prompt (n, α) rates a multitelescope composed of five telescopes, each of them with two ΔE and one E-detector, was designed and used by A. Paulsen et al.²⁾ To increase the efficiency and to reduce the background, the multitelescope (see Fig. 1,) was adapted by several means 3-4): sample closer to the target, but withdrawal of shield; multi-wire proportional counters with a cross-sectional area limited to the angle subtended by the surface barrier detector; inner surfaces of the detector housing and the frames sustaining the wires made of tantalum; implementation of an on-line dead time determination system.

A detailed description of the data acquisition system together with double differential cross-section data will be published elsewhere.

The measurements yield α -particle rates for five angle ranges and 64 alpha-particle energy groups at eleven neutron energies between 5 and 10 MeV. Integration over all alpha energies above 2 MeV is straight forward. Integration over 4π is done by weighted summation, with the weights proportional to the angular acceptance of each telescope. The rates are converted to absolute cross-sections by normalisation to $H(n,p)$ rates observed under identical conditions with the 14° telescope.

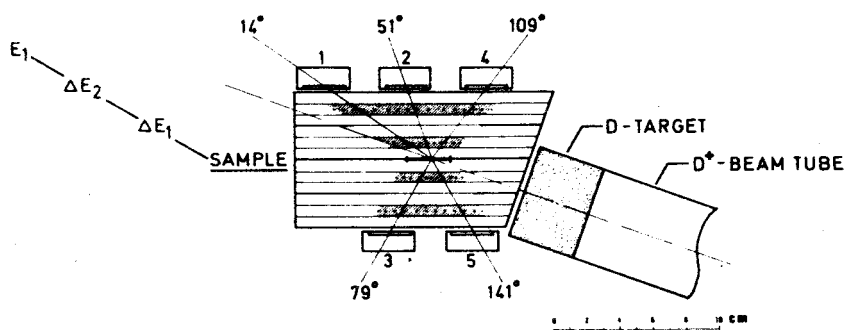


FIG.1 THE MULTI-TELESCOPE. MULTI WIRE PROPORTIONAL COUNTERS TO DETECT ΔE AND SURFACE BARRIER DETECTORS TO DETECT E .

2. RESULTS

Energy- and angle-integrated α -production cross-section data of Ni are shown in Fig. 2 together with earlier measurements (2,5,6). Data of ref. 5 are deduced from activation measurements, whereas data of ref. 6 rely on a combined technique of a two element telescope (ΔE , E) as well as E by time-of-flight. Our data are slightly and systematically lower than the data of ref. 2, are much lower than the data of ref. 5, but agree with data for elemental Ni deduced from recent measurements of $^{58}\text{Ni}(n,\alpha)$ and $^{60}\text{Ni}(n,\alpha)$ made by S.L. Graham et al. (6). The evaluation of ENDF/B-5 for gas production (7) recommends larger values than any measurement; the evaluations JENDL-2 and JEF-1 (9) are lower but still slightly higher than our data.

Energy- and angle-integrated (n,α) cross-section data of Cu are summarised in fig. 3. Three measuring campaigns are shown with consistent results. The $\text{Cu}(n,\alpha)$ cross-section deduced from $\text{Cu}(n,\alpha)$ to $\text{Ni}(n,\alpha)$ ratio measurements is obtained with the $\text{Ni}(n,\alpha)$ cross section previously determined (see Fig. 2). There are no measurements of prompt (n,α)

reactions of natural copper, but our measurements can be compared and agree well with (n,a) data obtained by combining activation measurements for ^{63}Cu ref. 10) with the small contribution of ^{65}Cu deduced from an evaluation ref. 11). (Fig.3). The comparison of measured data with the evaluations of the ENDF/B-5 gas production file, and JEF-1 as well, clearly shows two different slopes.

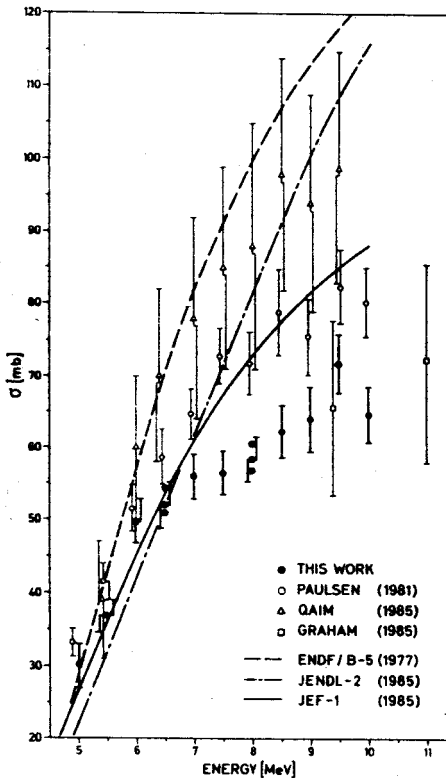


FIG. 2 MEASURED AND EVALUATED ALPHA PRODUCTION CROSS-SECTIONS OF Ni.

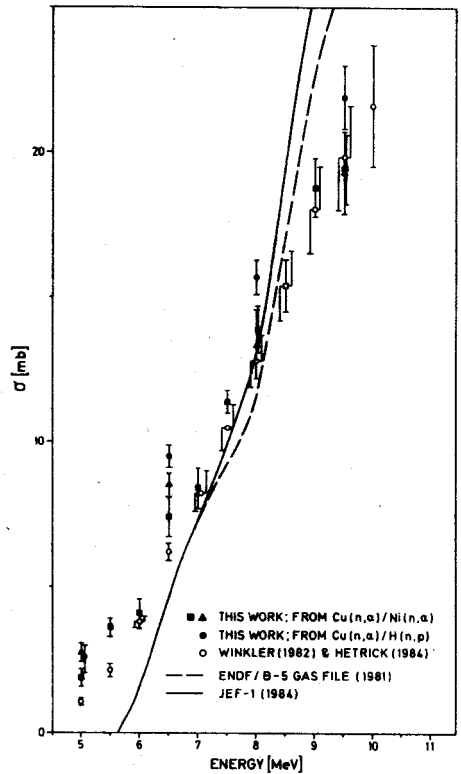


FIG. 3 MEASURED AND EVALUATED ALPHA PRODUCTION CROSS-SECTIONS OF Cu.

3. CONCLUSIONS

The multitelescope is a sensitive device for measuring double differential (n,a) cross-sections in reasonable measuring periods for cross-sections as small as $300 \mu\text{b sr}^{-1}$.

Measured Ni(n, α) cross-sections data as well as evaluations scatter by approximately 20 %. Our data are lowest and agree well with recent data obtained by a different technique.

Our measured Cu(n, α) cross-section data agree well with data from another laboratory obtained by another technique but are quite different in slope compared to evaluations.

It is questionable whether the large number of double-differential data now available is wanted and whether it is senseful to implement them in new files as long as a consensus on integral (n, α) data is not yet achieved.

Double differential (n, α) cross-section measurements of single nuclides of ^{58}Ni , ^{60}Ni and ^{63}Cu are planned, to compare more closely with activation measurements and to provide experimental data more suited for comparison with nuclear model calculations.

A (n, α) cross-section from a nucleus with a high coulomb barrier and with a large yield of α -particles of some MeV, such as $^{58}\text{Ni}(n,\alpha)$ if known well, could be a convenient reference cross-section for measuring other (n, α) cross-sections in identical conditions, thus avoiding any change in detector settings or accelerator conditions as required when H(n,p) is the reference reaction.

The authors are very thankful to Dr. H. Liskien for many helpful discussions and for his continuous support.

4. REFERENCES

1. Piksaikin, Y., Wrenda 23/24, INDC (SEC)-88/URSF (1983)
2. Paulsen, A., et al., Nucl. Sci. and Eng. 78, 377-385 (1981)
3. Wattecamps, E., et al., Proc. B2-meeting on Fusion Neutronics, EFF-Doc-8, p.41, Geel, (1985)
4. Wattecamps, E., et al., Proc. Int. Conf. Nuclear Data for Sci. and Tech., p.156, Antwerp (1982).
5. Qaim, S.M. et al., Proc. Int. Conf. Nuclear Data for Basic and Applied Science, Santa Fe, May 1985 (in press).
6. Graham, S.L., et al., Nucl. Sci. and Eng. to be publ. (1986).
7. ENDF/B-5 Library, gas production file.
BNL(NNDC) Evaluation, 1977
8. Kikuchi, Y., et al., NEANDC(J) 114/11, INDC(JPN)100L (1985)
9. NEA-DB JEF-1, JEF Report 1 and files (1985)
10. Winkler, E., Proc. Europhysics Conf. Neutron Induced Reactions, p. 417, Smolenice (1982).
11. Hetrick, D.M., et al., ORNL/TM-9083 and ENDF-337 (1984)

FAST NEUTRON CROSS SECTIONS ON ZIRCONIUM ISOTOPES

A. Marcinkowski, K. Stankiewicz⁺ and U. Garuska⁺⁺
 Institute for Nuclear Studies, 00-681 Warsaw, Poland
⁺Institute of Atomic Energy, Świerk
⁺⁺University of Łódź, Łódź

Cross sections for the (n,p) reaction on $^{90,91,92,94}\text{Zr}$ and for the (n, α) reaction on $^{90,94}\text{Zr}$ have been measured in the neutron energy range from 13 MeV to 16.6 MeV. Use was made of the activation technique in connection with high-resolution γ -ray spectroscopy.

1. INTRODUCTION

Besides interest from the viewpoint of validation of nuclear reaction models measurements of cross sections for neutron induced threshold reactions as a function of projectile energy are also of interest for applications. This is particularly true for reactions on isotopes of zirconium since it has been proposed as constituent of structural materials for fusion reactors. So far excitation curves have been measured on $^{90}\text{Zr}^{1,2}$). Measurements for reactions on heavier zirconium isotopes are very scanty and confined to neutrons with energies around 14 MeV only. These facts stimulated us to measure the (n,p) reaction cross sections on $^{90,91,92,94}\text{Zr}$ and the (n, α) reaction cross sections on $^{90,94}\text{Zr}$ in the neutron energy range from 13 MeV to 16.6 MeV.

2. EXPERIMENTAL PROCEDURE AND RESULTS

The irradiation with neutrons was conducted at the Van de Graaff accelerator, which provides about 40 μA of deu-

teron beam. Deuterons have been accelerated to 440 keV and 990 keV in order to obtain monoenergetic neutrons at high output from the $T(d,n)^4\text{He}$ reaction. The samples were metallic zirconium cylinders manufactured by Johnson Matthey and Co. They were held at 2.5 cm from the beam spot on a tritiated zirconium layer. The neutron flux was monitored by irradiation of iron samples in the same geometry but separate accelerator runs. The fluctuations of the flux during runs were detected by measuring protons recoiled from a thin polyethylene foil with help of a Cs(Tl) scintillator.

The activation products were determined by γ -ray spectroscopy with use of a $80\text{ cm}^3\text{ Ge(Li)}$ crystal, accompanied with standard ORTEC electronics and a ND-4420 analysing system. Both the characteristic γ -ray energy and half-life were considered in the determination of activation product.

The final results have been corrected for summing of pulses in the Ge(Li) crystal due to cascading γ -rays in the sample. The (n,p) cross sections contain minor contributions from the $(n,d + n,np + n,pn)$ reactions. The errors contain both statistical and systematic uncertainties. The latter ones consist mainly of the error of the reference reaction, estimated to about 5%, and of the uncertainty in tegration of the pulse height spectrum, which amounts to 10% for weak γ -ray lines.

3. STATISTICAL MODEL CALCULATIONS

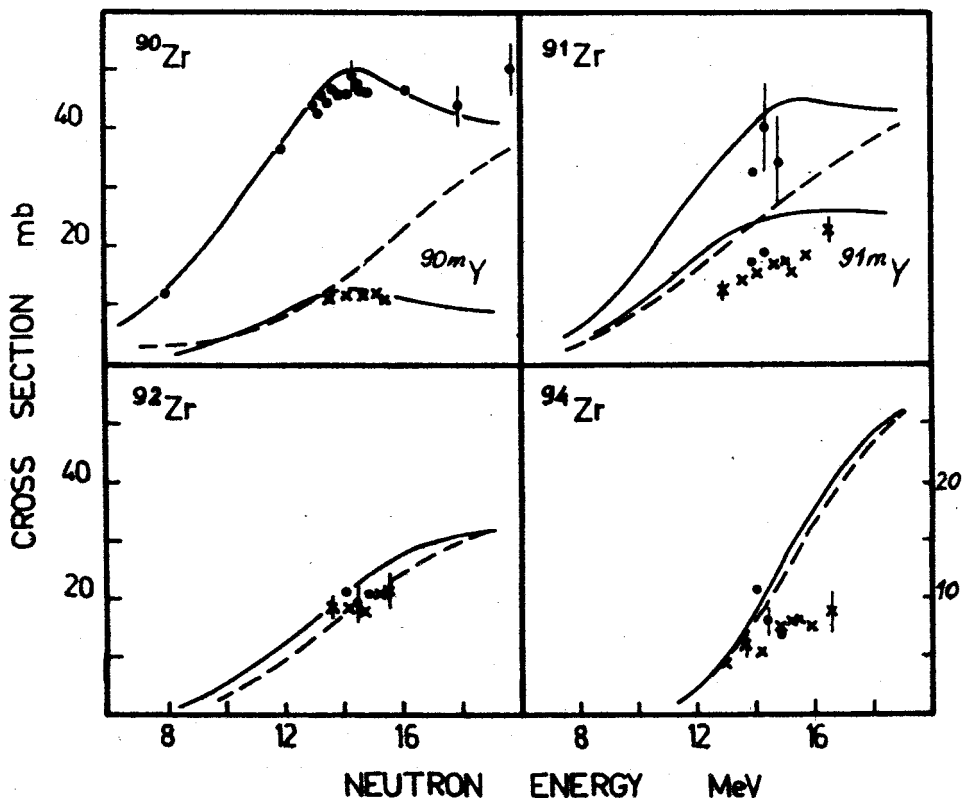
The measured cross sections were analysed in terms of the H-F and the geometry dependent hybrid models³⁾. The computer code **EMPIRE**³⁾ has been used for conducting the calculations. The parametrisation of the computations was based on the global optical potentials of Moldauer⁴⁾ for neutrons, of Björklund and Fernbach for protons and of McFadden and Satchler^{5,6)} for alphas. The level densities of Cameron and Gilbert⁷⁾ were used with parameters from

ref.⁸).

The theoretical calculations are compared with experimental results in figs. 1-4. The theory reproduces well the excitation curves for the $^{90}\text{Zr}(n,p)^{90}\text{g,mY}$ reactions. This is further confirmed by the good fit between the calculated and measured⁹) proton spectra. For the heavier target isotopes the agreement is less satisfactory, which seems to indicate that the global optical potentials fail to describe the local isotopic effects.

4. REFERENCES

1. Bayhurst, B.P. and Prestwood, R.J., J. Inorg. Nucl. Chem. 23, 173 (1961)
2. Abboud, A. et al., Nucl. Phys. A139, 42 (1969)
3. Herman M., Marcinkowski, A. and Stankiewicz, K., Comp. Phys. Comm. 33, 373 (1984)
4. Moldauer, P., Nucl. Phys. 47, 65 (1963)
5. Björklund, F. and Fernbach, S., Phys. Rev. 109, 1295 (1958)
6. McFadden, L. and Satchler, G.R., Nucl. Phys. 84, 177 (1966)
7. Cameron, A.G.W. and Gilbert, G., Can. J. Phys. 43, 1446 (1965)
8. Reffo, G., CNEN-Report RT/FI/78911, Bologna 1978
9. Haight, R. et al., Phys. Rev. 23, 700 (1981)
10. Bormann, M., Neuert, H. and Scobel, W., in Handbook on Nuclear Activation Cross Sections, IAEA Technical Report Series No 156, Vienna 1974, p. 87



Figs. 1 - 4. Comparison of the calculated and measured cross sections for the (n,p) reaction on ^{90}Zr , ^{91}Zr , ^{92}Zr and ^{94}Zr targets. Circles are from ref. 10) and crosses are present results. The dashed line shows the compound nucleus contribution. Solid line shows both the compound nucleus and pre-compound sum. Cross sections for population of isomeric states are indicated.

RECENT DEVELOPMENTS IN THE STUDY OF (n, α) REACTIONS ON HEAVY NUCLEI

L.Głowacka⁺, M.Jaskóła⁺, J.Turkiewicz⁺,
J.Dalmas⁺⁺, A.Chiadli^{++||}, E.Gadioli⁺⁺⁺,
E.Gadioli Erba⁺⁺⁺, L.Zemko⁺⁺⁺⁺

- + Institute for Nuclear Studies, Świerk, Poland
- ++ Centre d'Études Nucléaires de Bordeaux, France
- +++ Istituto di Fisica Nucleare and Dipartimento di Fisica dell'Università, Milano, Italia
- ++++ Heavy Ion Laboratory, Warsaw University, Poland

The energy and angular distributions of α -particles emitted in (n, α) reactions induced by 14.3 and 18.1 MeV neutrons on zirconium nuclei (one with a magic neutron shell and the other with one more neutron outside, the shell) have been measured and compared with each other.

In our earlier work it was shown that in (n, α) reactions induced by fast neutrons on nearly magic nucleus ^{143}Nd , the last 83rd slightly bound neutron acted as a spectator in the process¹⁾. These results prompted us to investigate the spectator role of the 51st neutron in ^{91}Zr .

The experimental arrangement was similar to that used in our earlier work²⁾. Fast neutrons were produced in the $^3\text{He}(d, n)^4\text{He}$ reaction with 2 MeV deuterons accelerated in a Van de Graaff accelerator. The neutron flux was monitored by counting the recoiled protons from a polyethylene foil in a thin CsI(Tl) scintillator counter.

The investigated targets were made of zirconium oxides (enriched to 91.1% in ^{91}Zr and 97.7% in ^{90}Zr) which

|| On leave of absence from Rabat University, Morocco

were deposited onto thick aluminum backings by sedimentation technique. The target thicknesses were between 1.5 - 4.0 mg/cm².

The energy of α -particles were measured by silicon surface barrier detectors. All α -particle spectra were measured at an average angle of 25.5° with the angular spread of $\pm 16^\circ$.

Comparison of the α spectra from the investigated reactions (fig.1) shows that ^{88}Sr levels below about 4 MeV

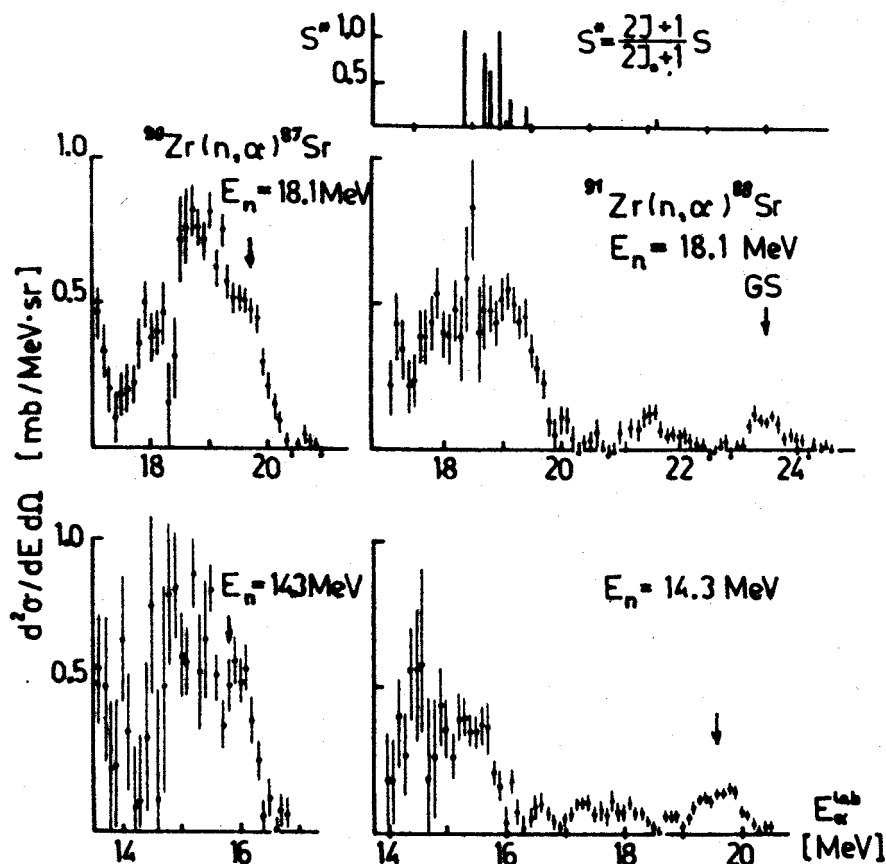


Fig.1. Energy distributions of α -particles from (n, α) reactions on ^{90}Zr and ^{91}Zr isotopes.

are very weakly excited. On the contrary low lying levels of ^{87}Sr are populated with high intensity. The main maxima in the two spectra are correlated and also the absolute yields of alphas in both reactions are comparable, suggesting that similar configurations must be involved in the excitation of those two residual nuclei. Assuming the spectator role played by the 51st neutron ($2d_{5/2}$) in ^{91}Zr we would expect to excite predominantly states corresponding to the coupling of this neutron to the neutron hole states in ^{87}Sr . The neutron particle-hole states in ^{88}Sr have been investigated through the reaction $^{87}\text{Sr}(d,p)^{88}\text{Sr}$ and the spectroscopic factors taken from ref.³⁾ are reported in the upper part of fig.1. One can see the correspondence of the spectroscopic factors distribution and α -particles yield.

The measured angular distributions show that α -particles are predominantly emitted in the forward direction.

Detailed theoretical calculations for the considered reactions using both pick-up and knock-on DWBA theories^{4,5)} are in progress.

REFERENCES

1. Gadioli, E., Gadioli Erba, E., Głowacka, L., Jaskóła, M., Turkiewicz, J. and Zemło, L., Phys. Rev. C24, 2331(1981)
2. Jaskóła, M., Turkiewicz, J., Zemło, L. and Osakiewicz, W., Acta Phys. Pol. B2, 521 (1971)
3. Cosman, E.R. and Slater, D.C., Phys. Rev. 172, (1126) 1968
4. Gadioli, E., Gadioli Erba, E., Głowacka, L., Jaskóła, M., Turkiewicz, J., Zemło, L., Dalmas, J. and Chiadli, A., to be published
5. Gadioli, E., Gadioli Erba, E., Guazzoni, P., Hodgson, P. E. and Zetta, L., Z.Phys. A, 318, 147 (1984)

ANOMALOUS BEHAVIOUR OF THE RATIO OF (n, α) AND (n, p) CROSS SECTIONS
ON ALUMINIUM MEASURED AROUND 14.7 MeV

M. Ibn Majah^{*}, A. Ait Haddou^{*}, M. Viennot^{*} and G. Paic^{**}

^{*}Laboratoire de Physique Nucléaire, Rabat, Morocco

^{**}Rudjer Bošković Institute, POB 1016, 41001 Zagreb, Yugoslavia

A very careful analysis of the energy behaviour of the activation cross sections for the $Al(n, p)$ and $Al(n, \alpha)$ reactions has been made in the energy range available with a 300 kV neutron generator. The results indicate that at energies around 14.7 MeV there is a departure from the trend of the ratio as predicted by the latest evaluations of $\sigma(n, \alpha)$ and $\sigma(n, p)$. The departure is of the order of 10% and is much larger than the uncertainty in measurements.

Comparison of the behaviour of the cross sections measured for other nuclei indicate that the observed anomaly should be attributed to an increase in the $Al(n, \alpha)$ cross section.

1. INTRODUCTION

The $Al(n, \alpha)$ and $Al(n, p)$ reactions are often used as monitor reactions. We have measured the ratio of the two reactions in function of the energy of the neutrons and compared it to the ratios obtained from evaluated data^{1,2)}.

2. EXPERIMENT

The measurements have been performed using the unanalyzed deuteron beam of the neutron generator of the Mohammed V University in Rabat. The accelerating voltage was 250 kV. The target used was a CEA target AD35, with a 1.1 mm Cu backing and a TiT layer $600 \mu\text{g}/\text{cm}^2$ thick. The target is covered with a plastic hood in which the cooling water circulates on the sides. The irradiated samples were placed at 5 cm from the center of the

target. The beam spot is about 1 cm diameter. The counting of the Al foils is done 1 cm from a GeLi detector with corrections for pile up, sum coincidences, and dead time accounted for.

3. RESULTS

The measurements were made at different angles with respect to the deuteron beam and the results of measurements and corresponding results from evaluations are presented in Table I.

Table I

Angle (E_n)	$\sigma_{n\alpha}/\sigma_{n,p}$	
	Experiment	Evaluation
0° (14.7 MeV)	1.77 ± 0.02	1.56
60° (14.4 MeV)	1.66 ± 0.02	1.57
90° (14.1 MeV)	1.58 ± 0.02	1.56
110° (13.9 MeV)	1.56 ± 0.02	1.57

The results indicate a disagreement around 14.7 MeV between the results predicted by the evaluations and the present measurements. The comparison of the cross sections for $^{56}\text{Fe}(n,p)$, $^{59}\text{Co}(n,\alpha)$, and $^{65}\text{Cu}(n,2n)$ obtained with both monitor reactions at 0° give results that are lower than literature values when the (n,α) reaction is used as monitor. This fact seems to indicate that there would be a rise in the (n,α) cross section around 14.7 MeV.

REFERENCES

1. Tagesen, S. and Vonach, H., Physik Daten Fachinformationszentrum Karlsruhe, ISSN0344-8401, 13-3 (1981)
2. Young, P.G., Forster, D.C., Pist, J.R., ENDF/B Material n^o 6313 (1979)

(n,t) REACTION ON ^9Be AT 14.6 MeV

M. Zadro, S. Blagus, Đ. Miljanić and D. Rendić

Rudjer Bošković Institute, POB 1016, 41001 Zagreb, Yugoslavia

The sum of the $^9\text{Be}(n,t_0)^7\text{Li}$ and $^9\text{Be}(n,t_1)^7\text{Li}$ reaction cross sections was measured at an incident neutron energy of 14.6 MeV using a counter telescope for triton detection. The angular distribution of these reactions was obtained for the c.m. angles up to 90° . It is nearly isotropic. Assuming a forward-backward symmetry of the angular distribution, the total cross section for the (n,t) reaction on ^9Be is found to be 24 ± 2 mb. This result (empty square on Figure 1) compares favourably with the data from the tritium beta counting experiments.

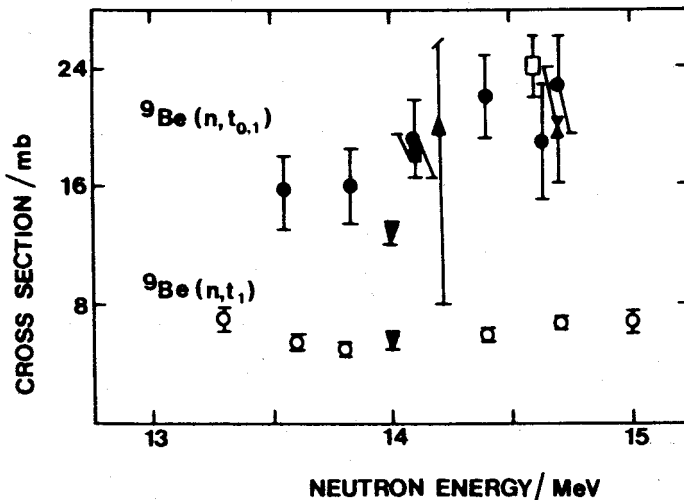


Fig. 1 Measured $^9\text{Be}(n,t)^7\text{Li}$ reaction cross sections

The complete version of this paper was submitted for publication in Nuclear Science and Engineering.

STUDY OF $^{56}\text{Fe}(n, n'\gamma)$ REACTION AT 14.1 MeV

A.A.Lychagin, S.P.Simakov, O.A.Salnikov, B.V.Dewkin,
A.B.Pashchenko

Institute for Physics and Power-Engineering
249020 Obninsk, USSR
and

T.Sztaricskai, G.Petö
Institute of Experimental Physics, Kossuth University,
H-4001 Debrecen, Hungary

Experimental and theoretical studies were carried out on $^{56}\text{Fe}(n, n'\gamma)$ reaction at 14.1 MeV. The neutron spectrum measured by a gamma correlated neutron spectrometer was compared with spectra from other experiments and also with the calculated one by STAPRE code. Contributions of secondary effects were taken into account.

1. EXPERIMENTAL TECHNIQUE

The geometry of the experiment is shown in Fig.1. A detailed description of the spectrometer is under publication 1.)

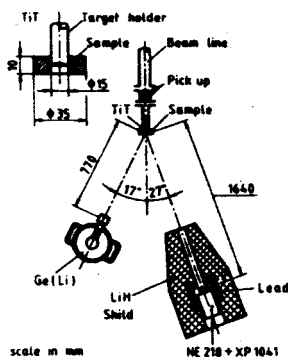


Fig.1. The experimental setup and geometry

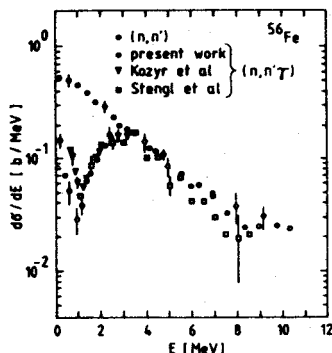


Fig.2. The emitted neutron spectra

2. EVALUATION OF THE MEASURED DATA

A comparison of the present experimental $(n, n'\gamma)$ spectrum with the data of other experiments 2-4.) is given in Fig.2. The deviations in the energy range of 1-3 MeV demonstrate the important contribution of energy resolution de-

terminated by the incident neutron energy spread, the time resolution of the spectrometer and the uncertainty of the flight path. The comparison of the total energy resolution of the four experiments is shown in Table 1.

Table 1.

Comparison of $(n, n'\gamma)$ experiments around 14 MeV on ^{56}Fe

Experiment	E_0 [MeV]	ΔE [MeV] around $E=2.5\text{MeV}$	$\langle \Gamma_\gamma \rangle$ [eV]	$\int \delta(E)/dE$ exp.	[mb] calc.
Present work	14.1	0.5	1-5	55 ± 29 ($0.1 < E < 0.9\text{MeV}$)	29
Stengl et al.2.)	14.4	1.0	-	-	-
Kozyr et al.3.)	14.6	0.6	20	30 ($0.5 < E < 1.1\text{MeV}$)	54
Betak et al.4.)	14.6	0.65	-	-	-

The experimental neutron spectrum below 1 MeV shows an intense rise to lower energies both in Ref.3) and the present experiment, too. This rise in the energy spectrum was interpreted in Ref.3.) by the contribution of $(n, \gamma n')$ process.

3. CALCULATIONS

To check the above statement we have calculated the neutron spectra by STAPRE code 5.) in the frame-work of Hauser-Feschbach-Moldauer formalism, taking into account the cascade emission of gammas and the preequilibrium secondary particle emission. The $(n, \gamma n')$ process was calculated as well, which should have a high contribution according to Kozyr et al.3.). Calculated emitted neutron spectrum in Fig. 3 shows good agreement with experimental data up to 9 MeV confirming the models and parameters chosen. The neutron spectrum from $(n, n'\gamma)$ reaction in Fig.3 shows a very strong fall below 2.9 MeV corresponding to the decreasing value of $\langle \Gamma_\gamma \rangle$ average radiation width. The high contribution of $(n, \gamma n')$ process has not been confirmed by the present calculations. The most probable explanation for this rise is

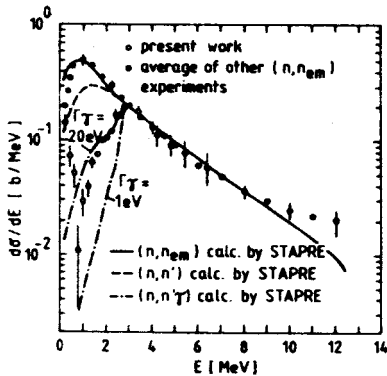


Fig.3. Comparison of the experiment with calculations

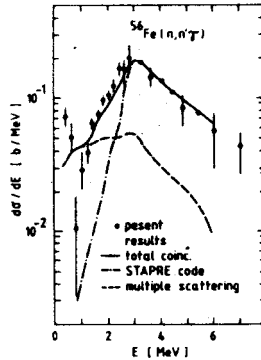


Fig.4. The correction for multiple scattering

the uncertainty of neutron detection in the low energy region.

The analysis of the gamma correlated experiments shows a high contribution of the multiple scattering of neutrons in the sample in the energy range of 1-3 MeV. This contribution was calculated by the BRAND code 6.) based on the Monte-Carlo method.

Fig.4 shows a comparison of the experimental data with the calculated spectrum. The calculations for the $(n,n'\gamma)$ spectra based on STAPRE code with $\langle\Gamma_\gamma\rangle=1$ eV were corrected by BRAND code for the actual conditions of the present experiment. The calculated spectrum shows a relatively good agreement with the measured data in the energy range of 1-3 MeV.

4. REFERENCES

1. Andriashin, A.V. et al, Scientific Instrumentation (in print)
2. Stengl, G. et al, Nucl. Phys. A290, 9 (1977)
3. Kozyr, Yu.E. et al, Yadernaja Physica 27, 616 (1978)
4. Betak, E. et al, Izv. AN USSR ser. physics 49, 1023 (1985)
5. Uhl, M. et al, IRK-76/01, Vienna (1976)
6. Simakov, S.P. et al, Yadernaja Physica 37, 801 (1983)

${}^7\text{Li}(n,n'){}^7\text{Li}$ * (478) NEUTRON ANGULAR DISTRIBUTION
DERIVED FROM DOPPLER-BROADENED γ -ENERGY
DISTRIBUTIONS

Horst Liskien and Shanglian Bao*
Commission of the European Communities,
Joint Research Centre - Geel,
Central Bureau for Nuclear Measurements,
BELGIUM

Doppler-broadened γ -energy distributions from the decay of the 1st excited state of ${}^7\text{Li}$ (478 keV, 73 fs, $\frac{1}{2}^-$) have been determined for primary neutron energies between 4 and 10 MeV in steps of 0.5 MeV and for γ -observation angles between 45° and 135° in steps of 22.5° . The observed width is about 10 times the resolution of the Ge-detector. Position and shape are determined by the energy- and angle-distribution of the excited ${}^7\text{Li}$ recoils. The short half-life ensures that energy loss of the recoils before γ -emission is small and can be treated as correction. The angular distributions of the reaction in terms of C.M.-Legendre coefficients are deduced by applying a combination of Monte-Carlo calculations and least-squares fitting.

* Guest from University of Beijing

1. INTRODUCTION

Tritium breeding ratio determinations for fusion blankets need double-differential neutron emission cross sections as input data for transport calculations. Angle-integrated inelastic scattering cross sections via the 1st excited state of ${}^7\text{Li}$ (478 keV, 73 fs, $\frac{1}{2}^-$) stem from observing the C.M. isotropic 478 keV γ -line. Angle-differential data exist only for lower primary neutron energies where the transition to the 1st excited state can still be separated from the ground state by time-of-flight techniques. In the absence of any experimental information the available files 1-3) assume simply C.M. isotropy. The present paper presents such missing data which were obtained applying a novel technique.

2. METHOD

Not the neutron angular distribution but the ${}^7\text{Li}^*$ recoil angular distribution has been determined and this via the Doppler shift of the 478 keV γ -quanta. This Doppler shift is given by:

$$\Delta E_\gamma = \frac{E_\gamma}{c} \cdot v_{\text{LAB}} [\cos \theta_{\text{LAB}} \cdot \cos \alpha + \sin \theta_{\text{LAB}} \cdot \sin \phi \cdot \sin \alpha] \quad (1)$$

where α is the γ -observation direction relative to the incoming primary neutron and ϕ the azimuthal angle of the reaction. The short half-life of ${}^7\text{Li}^*$ means that the γ -deexcitation of the excited recoil occurs very soon after the reaction such that the energy loss of the recoil in the sample material (metallic lithium) can be treated as small correction. Details of the method have been presented recently ⁴⁾. Use is made from the fact that for a given primary neutron energy both, the recoil velocity v_{LAB} and the recoil direction θ_{LAB} , are simple kinematic functions of the C.M. recoil angle θ_{CM} only.

3. EXPERIMENTAL

Doppler-broadened γ -energy distributions from the decay of the 1st excited state of ${}^7\text{Li}$ were determined for primary neutron energies between 4 and 10 MeV in steps of 0.5 MeV and for γ -observation angles α between 45° and 135° in steps of 22.5° . The pulsed monoenergetic neutrons were produced via the $\text{D(d,n)}{}^3\text{He}$ reaction in the same manner as described in ref. 4 for 8 MeV. The effect of X(d,n) -neutrons produced by the structural material of the gas target (foil, beam stop, etc.) was found negligible below 9 MeV neutron energy. Break-up neutrons from the $\text{D(d,np)}\text{D}$ reaction ⁵⁾ strongly influence the shape of the Doppler-broadened γ -line above 8.5 MeV. These data have therefore not been analysed.

The experimental set-up was that of ref. 4 and includes a fast timing channel. The obtained TOF-spectrum allows partly a distinction between γ 's produced in the sample and in the detector. By setting an appropriate window the flat background below the 478 keV γ -line could be reduced. It stems mostly from Compton-scattered γ 's which are produced in the Ge-detector itself by $\text{Ge(n,n'}\gamma)$ processes of neutrons which were before (elastically) scattered in the Li-sample.

Data were accumulated in list mode with a resolution of 125 eV/channel. The amplification gain (and the detector resolution) was controlled by a ^7Be -source. After shifting the spectra accordingly and background subtraction the data were condensed to 1 keV/channel. (Fig.1)

4. ANALYSIS

Assuming the C.M. angular distribution can be expressed as a sum of Legendre polynomials we have calculated for each observation angle and each Legendre term theoretical line shapes using equation (1). The programme averages over the azimuthal angle Φ and uses Monte Carlo techniques to include several corrections (energy/angle-distribution of primary neutrons, sample scattering, recoil energy loss, detector resolution). Having established these spectra the problem of finding the angular distribution is now reduced to a simple least-squares fitting procedure which does not use any free parameters other than the 4 relative Legendre coefficients A_1/A_0 to A_4/A_0 .

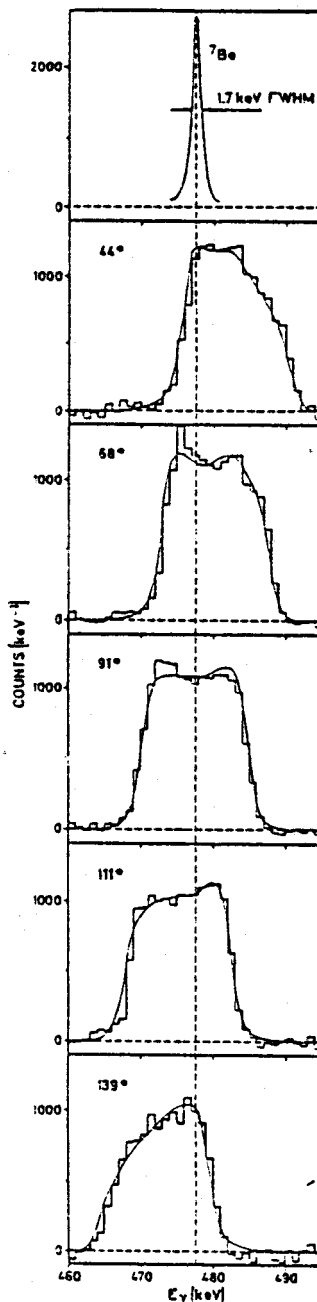


Fig. 1: Observed and fitted Doppler-broadened γ -lines at 8 MeV neutron energy.

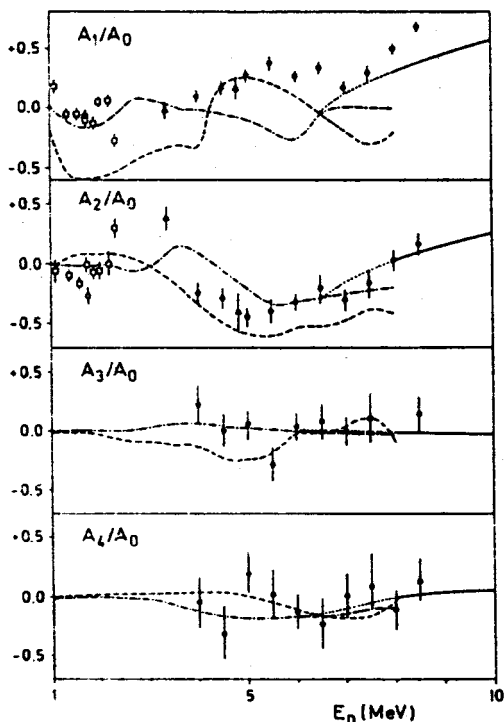


Fig. 2: Present knowledge of the neutron angular distribution of ${}^7\text{Li}(n,n'\gamma)$ $Q=-478$ keV.

5. RESULTS

Our results are presented in Fig. 2 together with other experimental information (6-8). There is excellent agreement in the 4-5 MeV range with TOF-results (7). Theoretical predictions are based on DWBA (full line, ref. 11) or on R-matrix calculations where the level scheme of ${}^8\text{Li}$ is based on a cluster model (dashed line, ref. 9) or on the shell model (dash-dotted line, ref. 10). Neither our experiment nor the calculations can say anything essential concerning A_3 and A_4 .

6. REFERENCES

1. Labauve, R.J. et al., ENDF/B-4 file MAT 1272 (1974)
2. Shibata, K., JENDL-3 file MAT 307 (1984)
3. NEA-DB, JEF-1 file MAT 4037 (1985)
4. Liskien, H., Proc. Intern. Conf. on Nucl. Data for Basic and Applied Science, St. Fe (1985) to be published
5. Smith, D.L., Meadows, J.W., Report ANL/NDM-9 (1974)
6. Batchelor, R., Towle, J.H., Nucl. Phys. **47**, 385 (1963)
7. Hopkins, J.C. et al., Report LA-3765 (1967)
8. Knitter, H.-H., Coppola, M., Report EUR 3903e (1968)
9. Knox, H.D., Lane, R.O., Nucl. Phys. **A359**, 131 (1981)
10. Knox, H.D., Proc. Intern. Conf. on Nucl. Data for Basic and Applied Science, St. Fe (1985) to be published
11. Young, P., LANL (1981) priv. communication

INELASTIC NEUTRON SCATTERING CROSS SECTIONS ON ACTINIDE NUCLEI [Th,U]*

E.Sheldon, L.E.Beghian, J.J.Egan, G.C.Goswami, G.H.R.Kegel and A.Mittler
 Department of Physics, University of Lowell, Lowell, MA 01854, U.S.A.

New experimental and theoretical cross-section data of the Lowell group are presented for ^{232}Th and ^{238}U $(n,n_1'_{2})$ scattering to the 2^+ and 4^+ rotational states in the form of level excitation functions from threshold to 2.4 or 3.1 MeV and of level angular distributions at $E_n = 0.185$ and 0.550 MeV. Cross sections measured with the direct (n,n') time-of-flight high-resolution technique are compared with ENDF/B-V evaluations and "standard" (CN+DI) or statistical S-matrix computations. Preliminary angular-distribution results for $^{235}\text{U}(n,n')$ scattering at 0.185 and 0.550 MeV to the experimentally-unresolvable adjacent rotational-level doublet ($9/2^-$ [48 keV], $5/2^+$ [52 keV]) are also shown.

Complementing the Lowell group's ongoing set of investigations into the dependence upon energy and angle of actinide (n,n') scattering cross sections for higher-lying vibrational states,¹⁻³⁾ and previous studies of the ^{238}U lowest rotational levels,^{4,5)} we have latterly employed the subnanosecond-resolution time-of-flight technique⁶⁾ for detailed measurements of $(n,n_1'_{2})$ cross sections to the first (2^+ [49 or 45 keV]) and second (4^+ [162 or 148 keV]) excited levels in the ground-state rotational band of the even-even (deformed, fertile) actinide nuclei ^{232}Th and ^{238}U , of importance to breeder-reactor design and operation. Level excitation functions were determined from threshold to 2.4 or 3.1 MeV, and compared with ENDF/B-V evaluations and a variety of theoretical computations, as were also the $(n,n_1'_{2})$ angular distributions at $E_n = 0.185$ and 0.550 MeV. The theoretical calculations were based upon the "standard" (CN+DI) formalism: angle-integrated and differential cross sections were derived from a combination of the Hauser-Feshbach-Moldauer CN programmes CINDY⁷⁾ or JACQUI (the Lowell version of NRLY⁸⁾) with the DWBA coupled-channels DI program KARJUP (the Karlsruhe⁹⁾ variant of JUPITOR¹⁰⁾) or, alternatively, from the HRTW¹¹⁾ statistical S-matrix programme NANCY.^{12,13)} Generally good fits ensued,¹⁴⁾ compatible with the findings¹⁵⁾ of the Bruyères-le-Châtel group. The data shown in Figs. 1-4 corroborate some previous results¹⁶⁾ and negate others from earlier studies by other groups.

KEY: \blacklozenge = this exp.; --- = CINDY+KARJUP; ... = JACQUI+KARJUP; - - - = NANCY; — = ENDF/B-V.

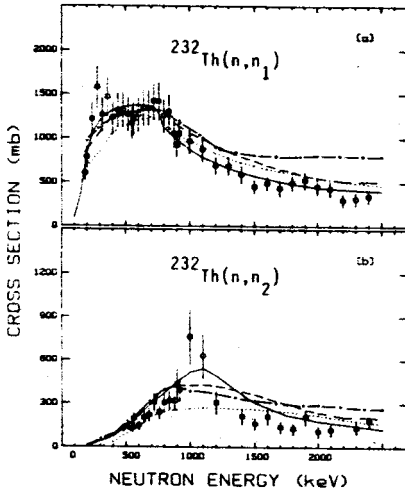


Fig. 1. $^{232}\text{Th}(n, n_{1,2})$ excitation functions to (a) 2^+ [48 keV] and (b) 4^+ [162 keV] states from threshold to $E_n = 2.5$ MeV.

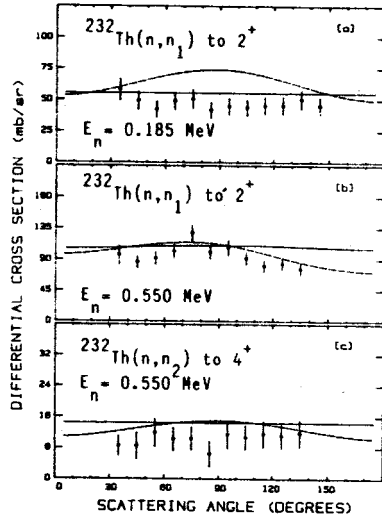


Fig. 2. $^{232}\text{Th}(n, n_{1,2})$ angular distributions to (a,b) 2^+ and (c) 4^+ states at energies (a) $E_n = 0.185$ MeV and (b,c) $E_n = 0.550$ MeV.

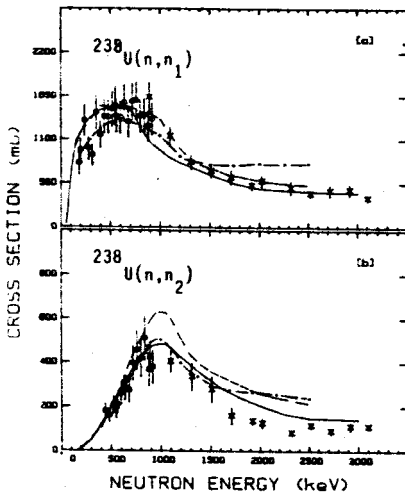


Fig. 3. $^{238}\text{U}(n, n_{1,2})$ excitation functions to (a) 2^+ [45 keV] and (b) 4^+ [148 keV] states to $E_n = 3.1$ MeV. (††† = Ref. 5).

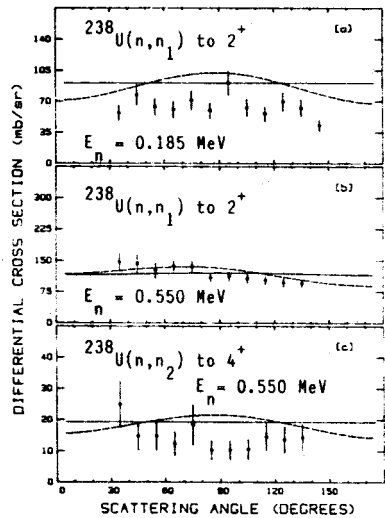


Fig. 4. $^{238}\text{U}(n, n_{1,2})$ angular distributions to (a,b) 2^+ and (c) 4^+ states at energies (a) $E_n = 0.185$ MeV and (b,c) $E_n = 0.550$ MeV.

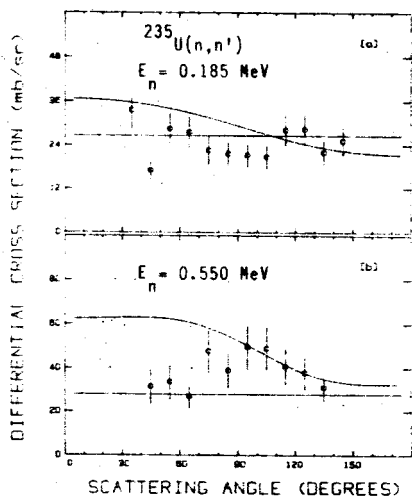


Fig.5. $^{235}\text{U}(n,n')$ "composite" angular distribution to combined $9/2^-$ & $5/2^+$ excited states at (a) 0.185, (b) 0.550 keV.

Tentative results are shown in Fig.5 for $^{235}\text{U}(n,n')$ "composite" differential cross sections for inelastic scattering at $E_n = 0.185$ and 0.550 MeV to the experimentally-unresolvable $(9/2^- [46.21 \text{ keV}], 5/2^+ [51.69 \text{ keV}])$ doublet of rotational states belonging to the $K = 7/2$ [743] (ground state) and $K = 1/2$ [631] (73 eV) band families. The findings are again compatible with the only other such data (at $E_n = 0.7$ and 3.4 MeV) currently available.¹⁵⁾

* Supported in part by the U.S. Department of Energy. Thanks are also due to Dr. Jacqueline Jary for the Bruyères CN computer program "NRLY".

- Sheldon, E., Beghian, L.E., Ciarcia, C.A., Couchell, G.P., Dave, J.H., Egan, J.J., Goswami, G., Kegel, G.H.R., Li, S.Q., Mittler, A., Pullen, D.J., Schier, W.A. and Shao, J.Q., *J. Phys. G: Nucl. Phys.* **12**, 237 (1986).
- Sheldon, E., Beghian, L.E., Chan, D.W.S., Chang, A., Couchell, G.P., Egan, J.J., Goswami, G., Kegel, G.H.R., Li, S.Q., Mittler, A., Pullen, D.J., Schier, W.A., Shao, J.Q. and Wang, A., *J. Phys. G: Nucl. Phys.* (in pub.).
- Sheldon, E. and Chan, D.W.S., *J. Phys. G: Nucl. Phys.* (to be published).
- Marcella, T.V., Ph.D. Thesis, University of Lowell, 1977 (unpubl.).
- Beghian, L.E., Kegel, G.H.R., Marcella, T.V., Barnes, B.K., Couchell, G.P., Egan, J.J., Mittler, A., Pullen, D.J. and Schier, W.A., *Nucl. Sci. Eng.* **69**, 191 (1979).
- Goswami, G.C., Ph.D. Thesis, University of Lowell, 1986 (unpublished).
- Sheldon, E. and Rogers, V.C., *Computer Phys. Commun.* **6**, 99 (1973).
- Jary, J., Bruyères Internal Report PNN-771/81 (30. September 1981).
- Rebel, H. and Schweimer, G.W., *Kernforschungszentrum Karlsruhe Report KFK-1333* (1971) (unpublished).
- Tamura T., *Rev. Mod. Phys.* **37**, 679 (1965); Oak Ridge National Lab. Report ORNL-4152 (1967) (unpublished).
- Hofmann, H.M., Richert, J., Tepel, J.W. and Weidenmüller, *Annals Phys.*, N.Y., **90**, 391, 403 (1975).
- Chan, D.W.S., Ph.D. Thesis, University of Lowell, 1981 (unpublished).
- Chan, D.W.S. and Sheldon, E., *Phys. Rev.* **C26**, 861 (1982).
- Sheldon, E., Egan, J.J., Goswami, G.C., Kegel, G.H.R. and Mittler, A., *Bull. Am. Phys. Soc.* (to be published).
- Haouat, G., Lachkar, J., Lagrange, Ch., Jary, J., Sigaud, J. and Patin, Y., *Nucl. Sci. Eng.* **81**, 491 (1982).
- Haouat, G., Nordborg, C., Nagel, P. and Nakagawa, T., (compilers), *Compilation of Actinide Fast Neutron Scattering Data, NEANDC-158 "U"*, (OECD/OCDE Paris, 1982) (1981 OECD Specialists' Meeting Proc. Suppl.).

NEUTRON EMISSION FROM LEAD BOMBARDED WITH 14 MEV NEUTRONS

T. Elfruth, D. Hermsdorf, H. Kalka, J. Pöthig, D. Seeliger
K. Seidel and S. Unholzer

Technische Universität Dresden, Sektion Physik,
Mommсенstr. 13, Dresden, DDR-8027, GDR.

Differential neutron emission cross sections were measured with a time-of-flight spectrometer which allows accurately to take angular distributions. The data are compared with calculations basing on direct, pre-equilibrium and equilibrium emission models.

1. INTRODUCTION

Lead is used as neutron multiplier material in conceptual designs of fusion reactors. Therefore, the differential neutron emission cross sections at 14 MeV neutron incidence energy have to be determined with relatively high accuracy. Direct and pre-equilibrium reaction components cause anisotropic, forward-peaked angular distributions, so that the emission spectra must be studied for a wide angular range, especially in their high-energy part.

2. EXPERIMENT

The time-of-flight spectrometer had ring geometry with flight path perpendicularly arranged to the deuteron beam direction, so that the incidence neutron energy was 14.1...14.2 MeV for all emission angles θ . The 14 MeV neutron generator was operated in a pulsed regime with deuteron pulses of 2 ns f.w.h.m. and 5 MHz repetition rate ¹⁾. The source strength was determined by counting the α -particles.

Measurements of TOF spectra were carried out for θ from 15° to 165° in steps of 15°. In one run, 5 or 6 of these θ were chosen symmetrically to $\theta = 90^\circ$ and the run was so subdivided in short-time data acquisition periods that the θ could be successively covered more than 10 times.

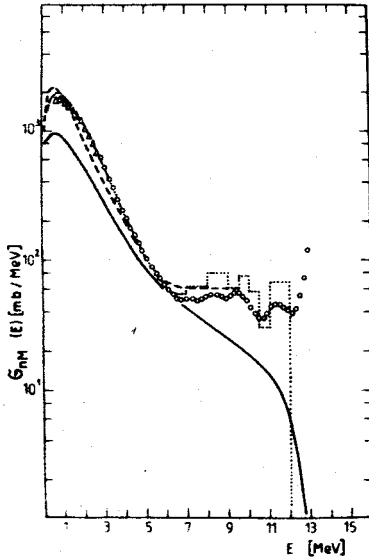


Fig. 1.

Measured neutron emission spectrum from Pb (o, present data; Δ , ²) compared with the ENDF/B-IV evaluation (---) and with a theoretical interpretation (...) as direct collective excitations, pre-equilibrium and equilibrium emission of primary neutrons (—) and secondary neutrons from (n, 2n).

3. RESULTS

Fig. 1 shows the angle-integrated emission spectrum. Angular distributions are presented in Fig. 2 for three different emission energies E . The experimental data are theoretically

interpreted as superposition of three components: direct excitations of vibrational modes calculated in DWBA approach ⁵⁾, pre-equilibrium and compound-nucleus neutron emission calculated with the Generalized Exciton Model code AMAPRE ⁶⁾ and secondarily emitted neutrons of (n, 2n) calculated with the statistical model code STAPRE ⁷⁾. The agreement of the calculated angle-integrated spectrum with the experimental is satisfactory in the low-energy part. In the high-energy part the neutron emission is overestimated. The direct component with the averaged deformation parameters used would alone explain the neutron emission for $E \gtrsim 8$ MeV. But, reducing adequately the pre-equilibrium emission, discrepancies appear in the middle part of the spectrum where only the pre-equilibrium component is able sufficiently to describe the experimental data. The theoretically obtained angular distributions describe the present experimental data at $E = 5.5$ MeV satisfactory. At $E = 3.5$ MeV they deviate for $\theta \gtrsim 30^\circ$ and at $E = 7.5$ MeV

the sum of the calculated direct collective excitations and of the pre-equilibrium emission overestimates the neutron emission as discussed for the angle-integrated spectrum.

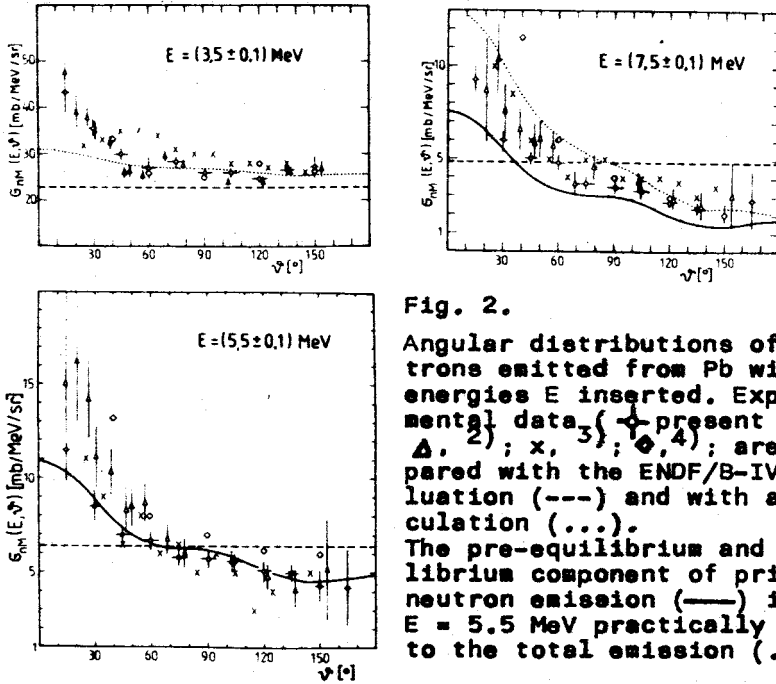


Fig. 2.

Angular distributions of neutrons emitted from Pb with the energies E inserted. Experimental data (∇ , 2; Δ , 3; \times , 4) are compared with the ENDF/B-IV evaluation (---) and with a calculation (...).

The pre-equilibrium and equilibrium component of primary neutron emission (—) is at $E = 5.5$ MeV practically equal to the total emission (...).

4. REFERENCES

1. Helfer, H., et al., INDC(GDR)-34, IAEA Vienna, 1985, 13
2. Takahashi, A., et al., Oktavian-Report A-83-01, 1983
3. Kammerdiener, J.L., Thesis Ph.D., UCRL-51232, 1972
4. Hermsdorf, D., et al., ZfK-277(0)(1975), INDC(GDR)-2/L
5. Ignatyuk, A.I. and Lunec, V.P., private comm. 1983
6. Kalke, H., Diploma work, TU Dresden, 1983
7. Uhl, M., Strohmaier, B., IRK-76, 1976

NEUTRON EMISSION CROSS SECTIONS OF Pb AND Cu AT 14.6 MeV NEUTRON ENERGY

K. Gul, M. Anwar, S.M. Saleem and M. Ahmad

Pakistan Institute of Nuclear Science and Technology
Nilore - Islamabad
PAKISTAN

Double differential neutron emission cross sections of Pb and Cu have been measured for 14.6 MeV incident neutron energy at several angles in the 3-14 MeV energy range. The energies of emitted neutrons have been measured using the time of flight technique based on the associated particle method. The values of nuclear temperature and level density parameter have been derived and compared with previous measurements.

1. INTRODUCTION

The present paper reports some results of the neutron emission cross sections of Cu and Pb for 14.6 MeV incident neutrons. The values of nuclear temperature and level density parameter have also been determined.

2. EXPERIMENTAL DETAILS

The measurements were carried out using the 14 MeV neutron generator facility at Pinstech¹⁾. The energies of neutrons were measured by the time-of-flight technique based on the associated particle method using a flight path of 2.3 m for scattering angles below 90 degree and was increased to 3.3 m for those above it. The incident neutron flux was normalized by carrying out neutron scattering measurements on the target of ¹²C of the same size and using the known values of cross sections based on the measurements reported by Haouat et al²⁾. The details of the data reduction have been published earlier^{3,4)}.

3. RESULTS AND DISCUSSION

The details of the neutron emission cross sections of Cu and Pb for the 6-11 MeV energy region are given in Table-I. The comparison of the present integrated neutron emission cross sections with previously reported values is given in Table-II. There are two values listed in the column of present measurements for both the elements. The present upper value in the Table-II was obtained by integrating the double differential cross sections in the 6-11 MeV energy region at each angle and then giving a Legendre Polynomial fit whereas the lower value is derived by adding the neutron emission cross sections listed in the Table-I. Values of the neutron emission cross sections given by Pearlstein⁵⁾ and Akkermans et al⁶⁾ are based on calculations while the values of

Hermesdorf et al⁷⁾ have been taken from these two theoretical papers.

TABLE-I The neutron emission cross sections of Cu and Pb in the 6-11 MeV region

Energy Interval (MeV)	Neutron emission cross sections (mb/MeV)	
	Cu	Pb
6-7	61 ± 3	71 ± 3
7-8	44 ± 2	52 ± 2
8-9	32 ± 2	54 ± 4
9-10	28 ± 2	52 ± 4
10-11	29 ± 2	47 ± 4

TABLE-II Comparison of the present measurements and previously reported values of neutron emission in the 6-11 MeV energy range. The cross sections are given in mb.

Element	Present measurements	Pearlstein ⁵⁾	Akkermans et al ⁶⁾	Hermesdorf et al ⁷⁾
Cu	198 ± 10 194 ± 11	186	192	131 ± 7
Pb	306 ± 16 272 ± 17	261	386	350 ± 21

The preliminary values of the level density parameter, a , have been obtained through the analysis of data taken at 90 degree using the standard slope method. These were obtained by making a least squares fit of the straight line given by

$$\ln \left(\frac{U^2}{E_n} \cdot \frac{2 d\sigma}{d\Omega dE} \right) = 2/a/U + \text{Const.} \quad (1)$$

whereas the values of the nuclear temperatures were obtained through the same method using the equation

$$\ln \left(\frac{1}{E_n} \cdot \frac{2 d\sigma}{d\Omega dE} \right) = \frac{1}{T} U + \text{Const.} \quad (2)$$

where U is the excitation energy. No pairing correction was applied. Thirty data points lying in the 3-6 MeV emitted neutron energy range were used for the fit. The values of the spin cut-off parameter, σ , were obtained using the equation given by Gilbert and Cameron⁸⁾. The present measurements are compared with previously reported values in Table-III. The present values of the level density parameter and spin cut-off parameters of Cu give level density of $1/2^+$ states at 8.8 MeV as 87 levels per MeV which compares well with the derived level density value of 83 from measurements of Browne et al¹¹⁾.

The present value of the level density parameter of Pb agrees with its previously reported value⁹⁾.

TABLE-III Comparison of the present values of level density parameter, nuclear temperature and spin cut-off parameters with previously reported results.

Reference	Cu			Pb		
	a (MeV ⁻¹)	T (MeV)	σ	a (MeV ⁻¹)	T (MeV)	σ
Present Work	6.2	1.69	3.33	10.2	1.2	5.62
Mathur et al ⁹⁾	6.7	1.26	-	10.7	1.04	-
Lu et al ¹⁰⁾	6.6-6.8	-	-	-	-	-

4. ACKNOWLEDGEMENT

The present work was partly done through the IAEA Contract No. 3310/RB for which the financial grant from the IAEA is gratefully acknowledged.

5. REFERENCES

1. Gul, K., Anwar, M., Ahmad, M., Saleem, S.M., Nucl. Instr. Meth. **B10/11**, 401 (1985).
2. Haouat, G., Lachkar, J., Sigaud, J., Patin, Y., and Cocu, Nucl. Sci. Eng. **65**, 331 (1978).
3. Gul, K., Anwar, M., Ahmad, M., Saleem, S.M., and Khan, N.A., Phys. Rev. **C24**, 2458 (1981).
4. Gul, K., Anwar M., Ahmad, M., Saleem, S.M., and Khan, N.A., Phys. Rev. **C31**, 74 (1985).
5. Pearlstein, S., Nucl. Sci. Eng. **68**, 55 (1978).
6. Akkermans, J.M., Gruppelaar, H., and Reffo, G., Phys. Rev. **C22**, 73 (1980).
7. Hermsdorf, D., Meister, A., Sassonoff, S., Seeliger, D., Seidel, K., and Shaheen, F., Zentral Institut Fur Kernforschung, Rossendorf, bei Dresden, Report ZFK-277, (1974).
8. Gilbert, A., and Cameron, A.G.W., Can. J. Phys. **43**, 1446 (1965).
9. Mathur, S.C., Buchanan, P.S., and Morgan, I.L., Phys. Rev. **186**, 1038 (1969).
10. Lu, C.C. Varz, L.C. and Huzinga, J.R., Nucl. Phys. **A196**, 229 (1972).
11. Browne, J.C., Newson, H.W., Bilbuch, E.G., and Mitchell, Nucl. Phys. **A153**, 481 (1970).

DISCRETE γ RAY PRODUCTION CROSS SECTIONS IN $^{52}\text{Cr}(n,x\gamma)$ AT 14.6 MeV

S. Hlaváč and P. Obložinský

Institute of Physics EPRC SAS, 842 28 Bratislava
CZECHOSLOVAKIA

Highly enriched sample of ^{52}Cr was irradiated by 14.6 MeV neutrons and γ ray production spectra were measured by the $\text{Ge}(\text{Li})$ spectrometer. Angular distributions and angle-integrated production cross sections were determined for 10 transitions in the $(n,n'\gamma)$ channel as well as for 2 transitions in the $(n,2n'\gamma)$ channel.

As a part of our research program we observed γ rays emitted in $^{52}\text{Cr}(n,x\gamma)$ reactions. Earlier we reported on the coincident data¹⁾, here we concentrate on discrete γ ray production cross sections.

Measurements were performed using the multidetector system described in detail elsewhere²⁾. The system employs the associated α particle method. Part of the system used in the present study is sketched in fig. 1. Neutrons of ener-

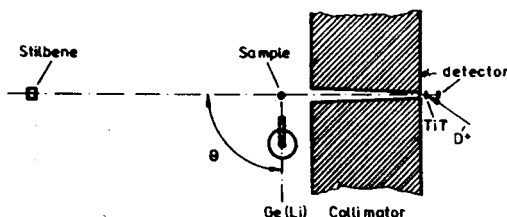


Fig. 1. Simplified drawing of the experimental arrangement.

gy 14.6(2) MeV are collimated electronically by the associated particle detector and pass through a mechanical collimator. We used 119.8 g of highly enriched (99.8 %) ^{52}Cr sample in metallic powder form delivered by TECHSNABEXPORT, Moscow. Its average thickness during the experiment was 0.071 at/barn.

We observed differential cross sections at 6 angles, ranging from 42° to 156° toward the neutron beam, by a 70 cm^3 $\text{Ge}(\text{Li})$ detector. Part of the γ ray spectrum observed with

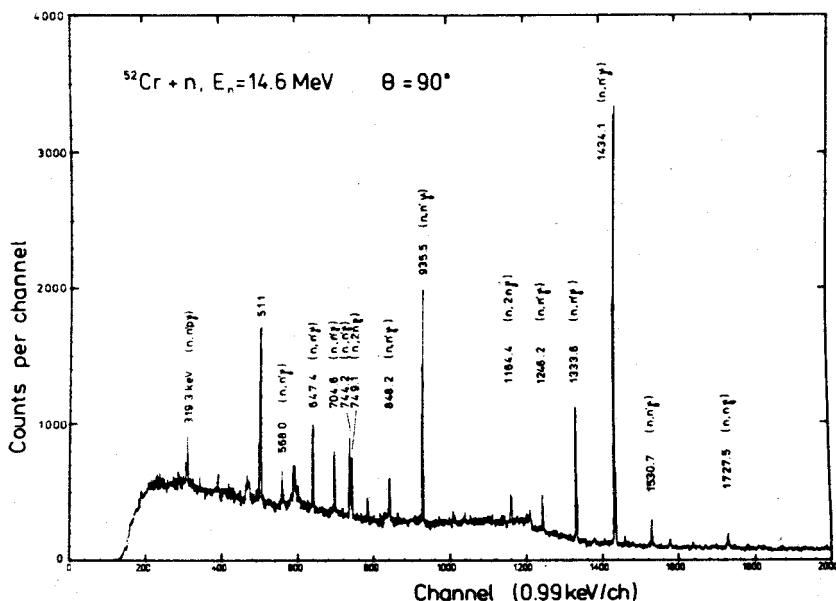


Fig. 2. γ ray spectrum from $^{52}\text{Cr}(n, x\gamma)$ reactions observed at 90° .

^{52}Cr sample at 90° is given in fig. 2.

Absolute neutron fluence was determined from the associated α particle counts corrected for coincident neutron fraction as measured by the stilbene monitor.

The γ ray spectra were analysed using the nonlinear least squares code GWENN³). Corrections for neutron and γ ray absorption as well as voluminous sample were applied.

Observed differential cross sections for 15 discrete transitions are given in fig. 3. Uncertainties were obtained assuming independent contribution from the Ge(Li) absolute efficiency, peak area and the neutron fluence.

γ ray angular distribution can be described by the expression

$$\frac{d\sigma}{d\omega} = \frac{\sigma_{\text{rx}}}{4\pi} (1 + a_2 P_2(\cos\vartheta) + a_4 P_4(\cos\vartheta)).$$

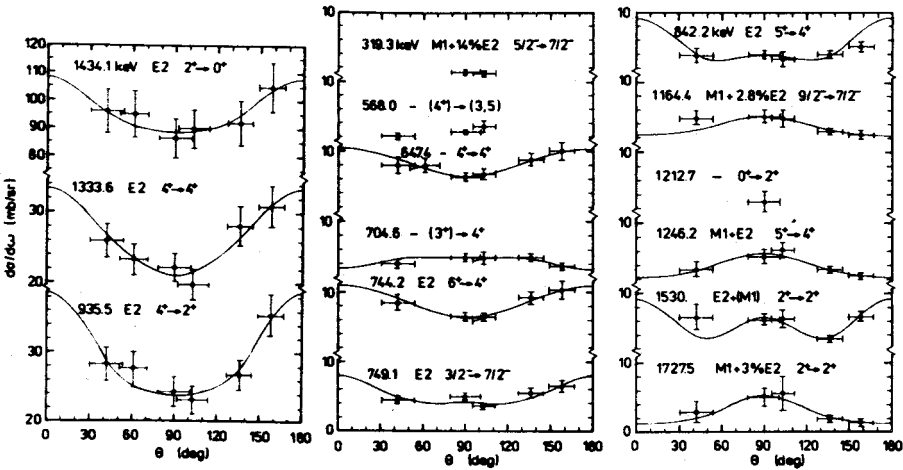


Fig. 3. Differential cross sections of observed transitions. Curves are fits to the experimental data.

The angle-integrated cross sections $\sigma_{4\pi}$ as well as the Legendre coefficients a_2, a_4 were extracted from the observed angular distributions using weighted linear least squares method. Uncertainties were obtained by normal matrix inversion. The angle-integrated cross sections and Legendre coefficients are given in Tab. 1.

Tab. 1. Discrete γ ray production cross sections at 90° , Legendre coefficients and angle-integrated production cross sections for $^{52}\text{Cr}(n, x\gamma)$ at 14.6 MeV. Given in brackets are the uncertainties.

E_γ (keV)	Reaction	$\frac{d\sigma}{d\omega}(90^\circ)$ (mb/sr)	a_2	a_4	$\sigma_{4\pi}$ (mb)
319.3	(n, np γ)	1.5(2)	-	-	-
568.0	(n, n' γ)	2.8(3)	-	-	-
647.4	(n, n' γ)	6.4(6)	0.33(14)	-0.02(17)	99(5)
704.6	(n, n' γ)	4.9(5)	-0.19(11)	-0.11(15)	59(4)
744.2	(n, n' γ)	6.6(6)	0.39(13)	-0.01(18)	101(5)
749.1	(n, 2n γ)	5.1(5)	0.42(13)	0.26(20)	59(3)
848.2	(n, n' γ)	4.0(6)	0.60(16)	0.60(20)	53(4)
935.5	(n, n' γ)	24.3(2.1)	0.31(09)	0.12(12)	339(12)
1164.4	(n, 2n γ)	5.2(9)	-0.52(19)	0.13(20)	50(5)
1212.7	(n, n' γ)	3.1(1.4)	-	-	-
1246.2	(n, n' γ)	5.3(1.0)	-0.59(17)	0.10(19)	55(5)
1333.6	(n, n' γ)	22.3(2.0)	0.31(09)	0.04(12)	310(12)
1434.1	(n, n' γ)	86.5(7.0)	0.12(08)	0.04(11)	1171(40)
1530.7	(n, n' γ)	6.3(8)	0.04(15)	0.74(18)	65(5)
1727.5	(n, n' γ)	5.1(1.3)	-0.90(30)	0.32(28)	42(7)

Only cross sections of the most prominent γ rays from $^{52}\text{Cr}(n, x \gamma)$ reactions were reported earlier. Using the associated α particle method, the NaI(Tl) spectrometer and a massive sample ($\varnothing 60 \text{ mm} \times 120 \text{ mm}$) of natural Cr, Abbondanno et al.⁴⁾ observed angular distribution of 1434.1, 1333.6 and 935.5 keV lines at 14.2 MeV. The shape of these distributions are in accord with ours, the angle-integrated cross sections 757(56), 239(36) and 221(31) mb, respectively, are by about 30 % higher than our values. However, they did not apply corrections for neutron absorption and multiple scattering, which seem to be necessary for their 2.4 kg sample.

Larson⁵⁾ reports cross sections of 1434.1 and 749.1 keV transitions in $(n, n' \gamma)$ and $(n, 2n \gamma)$ channels, respectively, observed at the ORELA white neutron source. He used the Ge(Li) detector placed at 125° toward the neutron beam and a natural sample. For 1434.1 and 749.1 keV transitions we extracted cross sections 810 and 50(12) mb, respectively, from his fig. 9. The neutron bin width around 14 MeV neutron energy was larger than 1 MeV. Again, Larson's cross sections for 1434.1 keV transition is lower than our value. However, his cross section of 749.1 keV transition is in accord with our figure.

The rest of our angular distributions and cross sections is reported for the first time. Our measurement is the only one performed so far with the enriched ^{52}Cr sample.

References

1. Obložinský P. and Hlaváč S., in Report INDC(CSR)-6/GI, (IAEA Vienna 1985) p. 17
2. Hlaváč S. and Obložinský P., Nucl. Instr. Meth. 206, 127 (1983)
3. Gmuca Š. and Ribanský I., Jad. Energie 29, 56 (1983)
4. Abbondanno U. et al., J. Nucl. Energy 27, 227 (1973)
5. Larson D. C., Proc. Int. Conf. on Nuclear Data for Basic and Applied Science, Santa Fe, May 13 - 17, 1985

CROSS SECTION OF $^{209}\text{Bi}(\gamma, n)$ REACTION INDUCED BY
Fe THERMAL NEUTRON CAPTURE GAMMA RAYS

Yue Gang, Ye Zongyuan, Li Jingwen,
Shi Detang and Huang Shengnian
Institute of Atomic Energy
P.O.Box 275-60, Beijing, China

The production cross section of two monochromatic groups of neutrons emitted from the $\text{Bi-209}(\gamma, n)$ reaction induced by 7645 keV γ -photons were determined by means of a He-3 spectrometer.

Thermal neutron capture provides intense gamma rays in 5--10 MeV energy range, which can be used in a variety of photo-nuclear experiment. In present work the photoneutrons from the bismuth were investigated using a ^3He spectrometer. The $^{209}\text{Bi}(\gamma, n)$ reaction occurs with a chance overlap between the Fe capture discrete γ -ray spectrum and the nuclear level of ^{209}Bi at 7645 keV. As a process of deexcitation after resonance absorption, neutron emission is possible for population on different energy states of ^{209}Bi nucleus. We have measured the production cross section of two monochromatic neutron groups with energies 130 keV and 193 keV, corresponding to the first excitation state and ground state of ^{208}Bi , respectively.

1. THE γ -RAY SOURCE

The γ -beam was obtained from the capture of thermal neutrons by iron radiator at the swimming pool reactor of IAE. The radiator was located in the berillium reflector of the reactor. The capture γ -beam was extracted through a horizontal experimental channel. In order to reduce the neutron and low-energy γ -ray backgrounds, a series of absorbers was placed in the collimator of the beam. The details of the γ -source facility have been published elsewhere¹⁾.

2. THE He-3 SPECTROMETER

The spectrometer consists of three proportional ^3He counters combined in parallel and the relevant electronic circuits. The energy response and the relative efficiency of the spectrometer were calibrated using 21 groups of monochromatic neutrons obtained from $\text{T}(p,n)$ and $^7\text{Li}(p,n)$ reactions at electrostatic accelerator. The resolution of the spectrometer is 4 % for thermal neutrons. The absolute efficiency of the counters was determined in situ through a Na-Be photo-neutron source whose neutron emission rate was calibrated by comparison with the standard Am-Be neutron source of IAE.

3. MEASUREMENT

The sample used in the experiment was bismuth plate $20 \times 10 \text{ cm}^2$ in area and 9.9 mm thick. The angle between the sample surface and the incident beam is 45° . Three ^3He counters were located separately at a distance of 9 cm from the centre of the Bi sample. The counters were covered with 0.5 mm Cd and 2 mm B_4C capsule to reduce the thermal neutron background.

In order to monitor the thermal neutron fluence of the reactor a BF_3 counter was placed at the exit of another horizontal channel and its counts were used for normalization.

The strength of the incident γ -rays at the sample site was determined by a $\text{NaI}(\text{Tl})$ scintillation counter whose efficiency had been calculated precisely by Monte-Carlo method.

4. RESULT

The data obtained have been corrected for the background, the attenuation of incident γ -beam in the sample, the attenuation and the anisotropy of emitted neutrons. The attenuation factors were obtained from Monte-Carlo calculation.

The production cross sections are as follows:

$$\sigma(130 \text{ keV}) = 8.5 \pm 0.7 \text{ mb},$$

$$\sigma(193 \text{ keV}) = 13.8 \pm 1.4 \text{ mb}.$$

In order to check our result we have measured the cross section of 86 keV neutron group from the $^{207}\text{Pb}(\gamma, n)$ reaction induced by 7631 keV γ -photons also coming from iron capture of thermal neutrons in the same way and compared it with other author's data. Our value is $\sigma(86 \text{ keV}) = 383 \pm 49 \text{ mb}$, which is in good agreement with Moreh's result $\sigma(86 \text{ keV}) = 370 \pm 50 \text{ mb}$.

1. Li Jingwen, Ye Zongyuan et al., Chin.Jour.Nucl.Phys., 6,15 (1984)
2. Moreh, R. et al., Nucl.Instr. and Meth., 155,429 (1978)

NEUTRON ACTIVATION CROSS SECTIONS OF SOME ISOTOPES OF MOLYBDENUM AT 14.6 MeV

M. Rahman, N.I. Molla, S. Khatun, A.K.M. Fazlul Hoque,
Rahezuddin Miah and Ayesha Akhtar Khan

Institute of Nuclear Science and Technology (INST),
Atomic Energy Research Establishment,
Savar, P.O. Box 3787, Dhaka,
Bangladesh

The neutron activation cross sections of some isotopes of Molybdenum have been measured for 14.6 MeV neutrons using high resolution γ -ray spectroscopy. Results are compared with the recent literature values, measured at 14.6-14.8 MeV.

1. INTRODUCTION

Molybdenum being one of the potential elements for use in reactor technology, neutron activation cross section measurements for the isotopes of this element have been measured previously by many authors¹⁻⁷⁾. But the reported values exhibit mutual disagreements. In this paper we present measurements of the neutron activation cross sections for some isotopes of Molybdenum at 14.6 MeV which is a continuation of our previous work for measuring precision nuclear data.

2. EXPERIMENTAL PROCEDURE

Cross sections were measured by the activation technique using HPGe detector and γ -ray spectroscopy. High purity Mo samples (>99.99% purity), sealed in polythene bags and sandwiched between two layers of flux monitoring materials, were irradiated with 14.6 ± 0.3 MeV neutrons. Irradiations were performed at zero degree with respect to the deuteron beam. The beam current and size were 350 μ A and 1 cm. dia respectively. The neutrons were produced via (D-T) reaction at the Neutron Generator of INST, AERE, Savar, Dhaka. Neutron energy and its spread were estimated following Ricci⁸⁾. The flux densities were $(0.8-4) \times 10^8$ n/cm²/sec. Cross section values were determined using known cross sections 115 ± 3 mb and 970 ± 80 mb respectively for $^{27}\text{Al}(n,\alpha)^{24}\text{Na}$ and $^{75}\text{As}(n,2n)^{74}\text{As}$ reactions.

Table 1: Details of (n,p) and (n, α) cross section measurements
at 14.6 ± 0.3 MeV

Reaction	$T_{1/2}$	E_{γ} (keV)	I_{γ}	σ_{exp} (mb)	Literature	
					values	Ref.
$^{92}\text{Mo}(n,p)^{92m}\text{Nb}$	10.15d	934	0.992	65.9 ± 5.8	56.5 ± 4.8	1)
					71.8 ± 5.7	2)
					60.5 ± 4.5	3)
$^{92}\text{Mo}(n,\alpha)^{89}\text{Zr}$	78.4h	909	0.99	27.3 ± 3.7	22.5 ± 2.1	1)
					25 ± 3	4)
					20.1 ± 1.6	5)
					36 ± 7	6)
					24 ± 6	7)
$^{95}\text{Mo}(n,p)^{95}\text{Nb}$	34.97d	766	0.998	$34.4 \pm 2.8^{a,b)}$	41.1 ± 3.6	1)
					31.0 ± 3.6	4)
					44.8 ± 3.5	2)
					37 ± 6	3)
					84 ± 10	6)
$^{96}\text{Mo}(n,p)^{96}\text{Nb}$	23.35h	569	0.556	14.0 ± 1.6	20.8 ± 2.1	1)
					19.2 ± 2.1	4)
					12.0 ± 2.0	7)
					18.1 ± 1.4	5)
					64 ± 8	6)
$^{97}\text{Mo}(n,p)^{97}\text{Nb}$	74m	658	0.982	$21.3 \pm 1.7^{b)}$	11.5 ± 2.4	1)
					11.7 ± 2.3	3)
					14.6 ± 1.2	4)
					19.2 ± 1.4	5)
$^{98}\text{Mo}(n,p)^{98}\text{Nb}$	51m	787	0.932	3.26 ± 0.3	5.2 ± 0.6	1)
					2.6 ± 0.7	3)
					3.6 ± 0.3	5)
					10.0 ± 1.2	7)

a) Contribution from $^{98}\text{Mo}(n,\alpha)^{95}\text{Zr}$ reaction (via β^- -decay ^{95}Zr not subtracted,

b) Includes small contribution of (n,n'p) reaction from the neighbouring heavier mass target nucleus.

The activity of the irradiated Mo samples were determined by HPGe detector (2.5 keV resolution at 1332 keV γ -ray). The count rates at the end of irradiation were subjected to usual corrections for the dead time loss, pile up loss, efficiency of the detector, gamma transition intensities (f_d) and internal conversion coefficients (α). The sources of systematic uncertainties taken into account were sample weight(0.5%), irradiation time(0.5%), irradiation geometry(3%), neutron absorption and scattering in the sample(3%), background neutrons(1%), neutron flux(5%), detector counts(1-5%), γ -ray absorption in the sample(1%), detector efficiency(3%) and decay data.

3. RESULTS

The cross sections measured in the present investigations are given in Table 1 together with the half lives ($T_{1/2}$), the γ -ray energies (E_γ), absolute γ -ray intensity (I_γ) and literature values¹⁻⁷). Each value is based on two to three measurements and the quoted error includes statistical and systematic errors. The uncertainties in the cross sections values have been obtained by combining all the statistical and systematic errors in quadrature.

REFERENCES

- 1) Anemiya, S., Ishibashi, K. and Kato, T., J. Nucl. Sc. & Tech. 19, 781(1982)
- 2) Fukuda, K., Matsuo, K., Shirahama, S. and Kumabe, I., NEANDC(J)-56/U(1978)
- 3) Qaim, S.M. and Stocklin, G., Proc. Int. Conf. organised by British Nuclear Energy Society, 20-22 Sept., P.121 (1971) at Univ. of Canterbury
- 4) Qaim, S.M. and Stocklin, G., EUR-5182e, 939(1974)
- 5) Fujino, Y., Hyakatake, M. and Kumabe, I., NEANDC(J)-51/U(1977)
- 6) Haight, R.C., Grimes, S.M. and Johnson, R.G., Phys. Rev. C23, 700 (1981)
- 7) Rao, C.V.S., and Rao, J.R., Proc. Int. Conf. Nuclear Cross Sections for Technology, Tenn, 22-26, Oct. 1979, Published as NBS Special Pub. 594(1980)
- 8) E. Ricci, J. Inorg. Nucl. Chem. 27, 41(1965)

Excitation function of $^{93}\text{Nb}(n, ^3\text{He})^{91}\text{Y}$ reaction near its threshold:

Comparison of ^3He - and ^3H -emission probabilities

S.M. Qaim and R. Wölfle

Institut für Chemie I (Nuklearchemie),
Kernforschungsanlage Jülich GmbH, D-5170 Jülich
Federal Republic of Germany

H. Liskien

Commission of the European Communities, Joint Research Centre
Central Bureau for Nuclear Measurements, B-2440 Geel, Belgium

Cross sections for the formation of ^{91}Y in the interactions of 17.0 to 19.2 MeV neutrons with niobium were measured radiochemically. The major contributing process is the $^{93}\text{Nb}(n, ^3\text{He})^{91}\text{Y}$ reaction. Hauser-Feshbach calculations on the first-chance emission of an ^3He -particle show that the contributions of statistical processes are small. The ratio ^3He - to ^3H -emission increases rapidly beyond 17.5 MeV. This behaviour is interpreted in terms of reaction energies, level structures of the isobars formed, and the intrinsic nature of the two processes involved.

The complete version of this paper is going to be published in Physical Review C.

YIELDS AND AVERAGE CROSS SECTIONS OF RECOIL CHARGED PARTICLES
INDUCED REACTIONS ON ^{11}B , ^{12}C , ^{13}C , ^{14}N , ^{16}O AND ^{18}O

A. Ait Haddou, M. Berrada

Nuclear Physics Laboratory, Faculty of Sciences,

Rabat, Morocco

G. Paić

Rudjer Bošković Institute, POB 1016, 41001 Zagreb, Yugoslavia

The yield and average cross section for the reactions $^{11}\text{B}(\text{p},\text{n})^{11}\text{C}$, $^{12}\text{C}(\text{p},\gamma)^{13}\text{N}$, $^{13}\text{C}(\text{p},\text{n})^{13}\text{N}$, $^{12}\text{C}(\text{d},\text{n})^{13}\text{N}$, $^{14}\text{N}(\text{p},\alpha)^{11}\text{C}$, $^{16}\text{O}(\text{p},\alpha)^{13}\text{N}$, $^{16}\text{O}(\text{d},\text{n})^{17}\text{F}$, $^{16}\text{O}(\text{t},\text{n})^{18}\text{F}$ and $^{18}\text{O}(\text{p},\text{n})^{18}\text{F}$ have been measured in different compounds. The charged particles were created in the samples themselves either by scattering of 14 MeV neutrons off hydrogen and deuterium or by the (n,t) reaction on ^6Li using thermal neutrons.

The yields of reaction $^{12}\text{C}(\text{d},\text{n})$; $^{16}\text{O}(\text{p},\alpha)$; $^{16}\text{O}(\text{t},\text{n})$ and $^{18}\text{O}(\text{p},\text{n})$ have been measured using proton, deuteron and triton spectra generated by 14 MeV neutrons in the reactions $\text{D}(\text{n},\text{p})2\text{n}$; $^6\text{Li}(\text{n},\text{d})$; $^7\text{Li}(\text{n},\text{d})$ and $^{10}\text{B}(\text{n},\text{d})$; $^7\text{Li}(\text{n},\text{t})$ and $^{10}\text{B}(\text{n},\text{t})$, respectively.

The complete version is to be published in the Journal of Radio-analytical Chemistry.

ACTIVATION CROSS-SECTIONS OF SOME (n,p), (n,n'p) AND
(n, α) REACTIONS INDUCED BY 14.8 MeV NEUTRONS ON
Cr and Ti ISOTOPES

Hoang Dac Luc, Phan Nhu Ngoc, Nguyen Van Do, Ly Ba Bach
Institute of Physics, Hanoi, Vietnam

14.8 MeV neutrons from a small neutron generator (120 kV, 10^{10} D+T n/s) were used to irradiate samples of Cr and Ti which were prepared from oxide powder (enriched isotopes) or high purity metal foils (natural isotopic abundances). High resolution gamma spectrometry chain was used for measurement of gamma spectra. Data processing was performed by means of the PDP-11/23 computer in connection with the ND-66B multichannel analyzer. Corrections were made where necessary, including coincidence summing effect and interference of (n,n'p) processing into (n,p) reaction cross-section values.

Full version not received.

(Paper received after deadline)

EFFECT OF DEUTERIUM ION BEAM COMPOSITION ON THE 14 MEV NEUTRON YIELD FROM Ti-T TARGETS

Hurani, S.Y.; Wanis, B.M.; Mustafa, H.T. und Nikiforov, S.A.
Tajura Nuclear Research Center, Tripoli/Libya

I INTRODUCTION

Deuterium ion beam, extracted from the ion source, is composed of a mixture of atomic and molecular ions. The percentage of the components depend on the ion source operating parameters ¹⁾. Hence, neutron yield from Ti-T target, bombarded by mixed deuterium ion beam, is a result of interaction between tritium and deuterons with energies E , $1/2 E$ and $1/3 E$. E being the full acceleration voltage.

Measured neutron yield and target half-life using mixed and atomic beams show: 1. target half-life using atomic beam exceeds that of mixed by an order of magnitude or more ^{2,3,4)}. 2. Neutron yield per μC of atomic beam is more by a factor of 2 than that of mixed beam ⁴⁾. 3. Neutron yield decrement per unit dose of atomic beam is very small ($9 \times 10^{-3} / \text{mAh}$) as compared to that of mixed beam. 4. Target half-lives measured by different workers using mixed beam show considerable differences. ⁵⁾.

In this work, therefore, we investigated the effect of molecular ions on the neutron yield and target half-life.

II MEASUREMENT

Description of the accelerator and target system can be found in details somewhere else ⁴⁾. Beams of atomic and molecular deuterium ions are obtained from 150 keV accelerated mixed beam by an analysing magnet. These beams are used to irradiate Thick Ti-T targets. Neutrons from D-T reaction are detected by a plastic scintillator, which is calibrated by ^{63}Cu ($n, 2n$) ^{62}Cu reaction.

Neutron yield produced by D_1^+ , D_2^+ and D_3^+ ions incident on a Ti-T target is measured at different ion energy up to 150 keV.

The effect of molecular ions on neutron yield by mixed beam is investigated in the following way. Yield produced by 150 keV D_1^+ is measured before and after irradiation doses of D_3^+ , D_2^+ and $D_3^+ + D_2^+$ at 150 keV for three separate targets. Percentage and fractional decrement per unit dose of the yield is calculated for each case. Simultaneously, the same calculation is performed for the yield by D_3^+ , D_2^+ ions.

For comparison, a target is irradiated by $D_3^+ + D_2^+ + D_1^+$ doses at energy of 50 keV/ D_1^+ . Yet another target is irradiated by 100 keV D_1^+ . The yield by D_1^+ is measured with doses of 4.7, 9.7 and 15.8 mA.h at energies 150, 125, 100, 75 and 50 keV for each dose.

III RESULTS AND DISCUSSIONS

Measured neutron yield produced by D_1^+ , D_2^+ and D_3^+ is shown in fig. (1).

It can be confirmed that the yield by mixed beam is, to great extent, produced by D_1^+ .

The effect of 150 keV D_3^+ and D_2^+ on the yield by 150 keV D_1^+ simulates their effect on the yield by mixed beam, since the decrease of the former is very small (observation (2)).

Table (1) shows the fractional and percentage decrement due molecular and atomic ion doses.

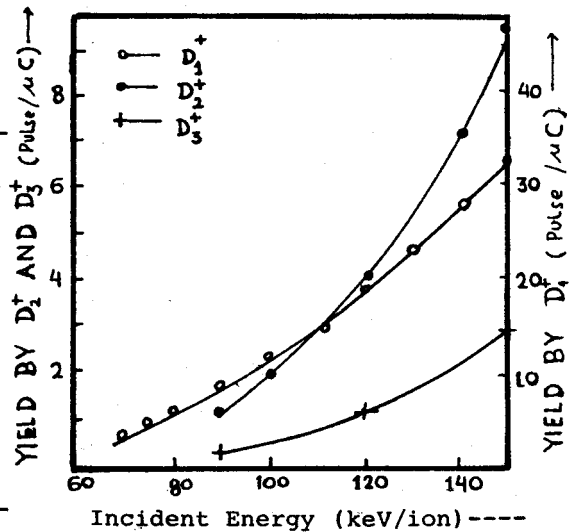


Fig 1: Neutron yield produced by atomic & molecular Deuterium ions

Table (1) shows the fractional and percentage decrement due molecular and atomic ion doses.

Table (1)

Fractional and percentage decrement of neutron yield by 150keV D_1^+ after irradiation doses of D_1^+ , D_2^+ and D_3^+

Dose type	Energy (keV)	Dose (mAh)	Decr. /mAh	Decr. %
D_3^+	150	1.27	0.39	49
D_2^+	150	1.54	0.23	36
		3.27	0.15	48
$D_3^+ + D_2^+$	150+150	0.9+0.58	0.30	44
$D_3^+ + D_2^+ + D_1^+$	150+100 + 50	563+1.11 +545	0.31	69
D_1^+	100	4.7	0.03	14

It is evident from table (2), that the yield decrease produced by molecular ions is large compared to that of atomic beam.

Table (2)

Fractional and percentage decrease of yield by molecular and atomic ions

D ions	E (Kev)	Dose /mAh	Decr. /mAh	Decr. %
D_3^+	150	1.27	0.11	14
D_2^+	150	3.27	0.13	42
D_1^+	150	3.0	0.006	2
D_1^+	100	9.7	0.03	29

Such behavior of yield by 150keV D_1^+ , and hence that of mixed beam, is interpreted on the basis of

deuteron range in Ti-T target. Deuterons of 150 keV D_2^+ and D_3^+ ions create a tritium depleted region in the target where they stop at the end of their ranges and replace tritium. The incident 150 keV D_1^+ arrives this depleted region with residual energy of about 75 and 100 keV which is responsible for high neutron yield. But replacement of tritium by deuterons causes the observed drop in the yield.

This behavior does not take place in case of irradiation dose of 150 keV D_1^+ because the tritium depleted region lies beyond its high yield producing region.

According to this interpretation, presence of heavy ions in the beam does not effect on the target half life due to its small percentage and short range.

The presence of tritium depleted region is proved also by the yield dependence on deuteron energy shown in fig. (2). It is clear that the yield tends to decrease with increasing energy. A similar, but more pronounced effect, was observed by Booth and Barschall²⁾.

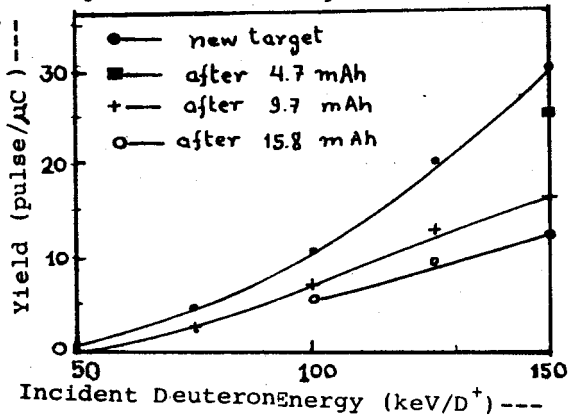


Fig.2: Energy dependence of yield versus dose of 100 keV.

REFERENCES

- 1) Hurani, S.Y.; Wanis, B.M.; Taha, H.M.; Morozov, A.V. Report TNRC-Tripoli 1984.
- 2) Booth, R. and Barschall, Nucl. Inst. and Methods 99,1(1972).
- 3) Stengle, G.; Vonach, H. and Fabian, H. Nucl. Inst. and Methods 126, 235 (1975).
- 4) Hurani, S.Y.; Morozov, A.V.; Wanis, B.M.; Taha, H.M. Proc. of Int. Seminar on the use of research reactors in fund. and Appl. Scien., Tripoli/Libya 1984.
- 5) References 1-4 quoted in ref. 3.

(Paper received after deadline)

NEUTRON FLUX AND ENERGY VARIATIONS FOR A LARGE BEAM DIAMETER AND A THICK ROTATING TARGET IN CLOSE PROXIMITY

B.M. Bahal, Ibrahim Juan, Shafiq ~~Hurani~~,
and Abdul Razac Mohabis

Tajura Nuclear Research Center, Tripoli/Libya

I INTRODUCTION:

At Tajura Nuclear Research Centre a 14MeV neutron generator NG-150 has been in operation for five years. Mixed ions of D_1^+ , D_2^+ and D_3^+ produced in a duoplasmatron ion source are accelerated to a voltage of 150 kV. The analyzed D_1^+ ions hit a rotating and thick water cooled tritium target of 40 mm diameter ¹⁾. The neutron producing area of the target is controlled by the beam diameter and can be changed by focussing electrode and collimators. The closest approach of a sample to the target is about 4 mm. For a new target and beam current of 1.5 mA, yield is 2×10^{11} n/s and a target half life of 40 hours. The activation facility is equipped with high purity germanium Y-spectroscopy and a pneumatic rabbit system. The cylindrical samples are transported to irradiation site where they rotate about their axis perpendicular to target axis.

For reactions having high threshold values, cross-section change in the energy interval between 14 to 15 MeV may be very large. Therefore NAA or cross-section measurement, an accurate knowledge of the flux and energy is essential. Moreover, a large flux gradient or change in neutron energy introduces errors which may be minimized by optimizing irradiation conditions.

II CALCULATIONS

Neutron energy E_n and flux ϕ of D-T neutrons depend on instantaneous kinetics energy of D_1^+ nucleus (E), angle of neutron emission (α), energy loss in the target

(dE/dX) , number of D_1^+ ions/s (K), number of tritium nuclei per cm^3 at the reaction site (T_n) and the cross section for D-T reaction (σ).

The differential neutron yield in 4 from D_1^+ alone will be given by ²⁾:

$$f(E) = K \sigma(E) T_n (dE/dX)^{-1} \quad (1)$$

and the neutron spectrum with energy E_n will be given by

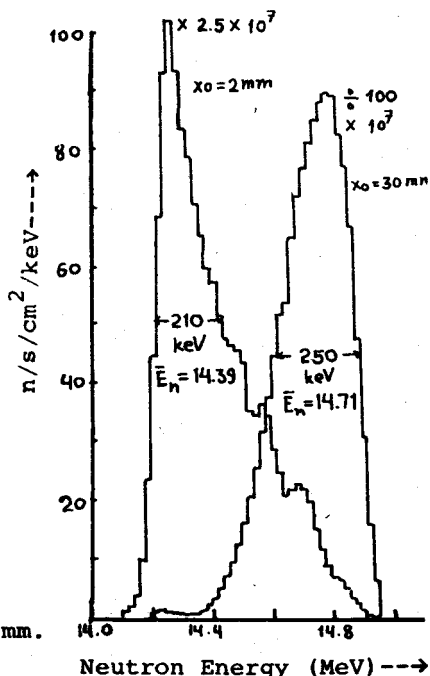
$$N(E_n) = f(E) \times (dE/dE_n) \quad (2)$$

where E_n and dE/dE_n are obtained from relativistic kinematic equation of D-T reaction. The neutron yield is obtained by integrating over all values of E_n .

A tritium distribution of the target is obtained by fitting neutron yield measured experimentally for deuteron energy range of 50-150 keV and these are used as input parameters for further calculations. The values of dE/dX for titanium, and hydrogen and are taken from ref. 3,4.

For the purpose of Flux and energy computation the target effective area is divided into small elements dA and each element used as point source for computation and a solid angle $d\Omega$ subtended by the element dA at a point p in space is considered for flux and energy contributions.

Fig. 1: Neutron spectrum for a 10 mm dia. target at axial positions of 2mm and 30 mm.



III RESULTS AND DISCUSSIONS

In fig (1) neutron energy spectrum for two axial positions are shown. An average neutron energy (\bar{E}_n) and half width can be calculated. It may be observed that peak neutron energy E_p is not necessarily same as \bar{E}_n . Variation of \bar{E}_n along the target axis for different diameter targets is shown in fig. 2.

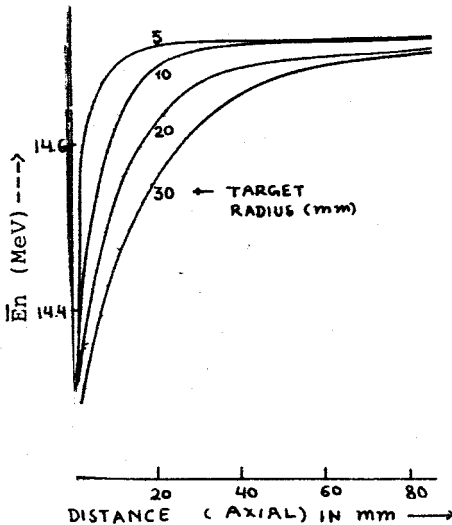


Fig.2: Neutron Energy Variat along target axis for differ size targets.

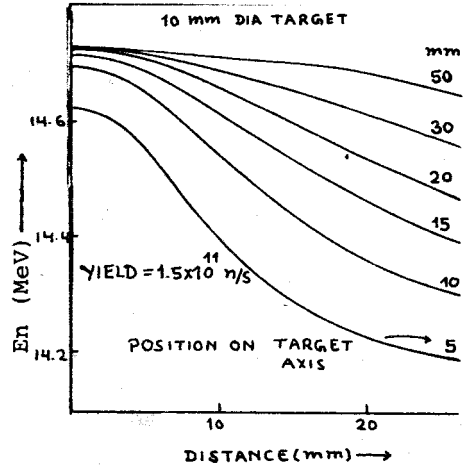


Fig.3: Variation of \bar{E}_n perpendicular to target axis.

The variation of \bar{E}_n perpendicular to the target axis for a 10 mm dia. target is shown in fig (3)

It is seen that the flux variation is large for small targets in close proximity. Increasing the target diameter also reduces the flux considerably (1 mm dia. target : 10^{11} n/s.cm², whereas for 30 mm it is : 1.8×10^9 n/s.cm² at 2 mm distance from the target). The average neutron energy \bar{E}_n variation is between 14.18 to 14.72 MeV, whereas the half width of a typical neutron spectrum is only 250 keV (Fig. 1).

It can be seen that position of the sample, its size and target radius will decide the average energy \bar{E}_n as seen by the sample, and hence accuracy of activation analysis or cross-section measurement. For example it may be seen that for ^{58}Ni (n, 2n) ^{57}Ni cross-section changes by 140% and ^{54}Fe (n, 2n) ^{53}Fe by 166% for a neutron energy change from 14.2 to 14.7 MeV^{5,6}.

The other factors effecting flux or neutron spectrum are scattering and attenuation of neutrons by surrounding materials as well as the sample itself. Work is in progress to include the scattering and attenuation also.

REFERENCES

1. Hurani, S.Y.; Morozov, A.V.; Wanis, B.M.; Taha, H.M. Proc. of Int. Seminar on the use of research Reactors in Fund. & Appl. Scien., Tripoli, Libya 1984.
2. Bahal, B.M. and Fanger, H.U. Nucl. Inst. & Methods, 211, 469 (1983).
3. Anderson, H.H. and Ziegler, J.F. Hydrogen stopping powers and ranges in all elements pergamon, New York, Vol. 3, P.1, 1977
4. Liskien, H. and Paulsen A. Nucl. Data Tables, 11, 601 (1973)
5. Winkler, G.; Pavlik, A. and Vonach, H. Proc. of Int. conf., Antwerp, 400 (1982)
6. Bormann, M.; Feddersen, H.K.; Hoscher, H.H.; Scobel, W. and Wagner, H. Z. Physik, A 277, 203 (1970)

LIST OF PARTICIPANTS

Austria

H. Vonach
 Institut für Radiumforschung
 Boltzmangasse 3
 A 1090 WIEN

Argentina

A.A. Ferri
 Comision Nacional de Energia
 Atomica
 Av. Libertador 8250
 1429 BUENOS AIRES

Bangladesh

M.M. Rahman
 Institute of Nuclear Science
 and Technology
 Atomic Energy Research
 Establishment
 Ganakbari, Savar
 P.O. Box 3787
 DHAKA

Belgium

P. Leleux
 Université de Louvain
 2, Chemin du cyclotron
 B 1348 LOUVAIN-LA-NEUVE

F. Poortmans
 S.C.K./C.E.N.
 Boeretang 200
 B 2400 MOL

I. Liskien
 Central Bureau for Nuclear
 Measurements
 Steenweg naar Retie
 B 2440 GEEL

E. Wattecamps
 Commission of the European
 Communities
 Joint Research Centre, CBNM
 Steenweg naar Retie
 B 2440 GEEL

China

Ye Zongyuan
 Institute of Atomic Energy
 P.O. Box 275-60
 BEIJING

Cuba

R. Lopez Mendez
 National Institute for Nuclear
 Research
 P.O. Box 6122
 HAVANA

Czechoslovakia

P. Obložinský
 Institute of Physics
 Physical Research Centre of the
 Slovak Academy of Sciences
 Dubravska cesta 9
 84228 BRATISLAVA

Germany, DR

K. Seidel
 Technische Universität Dresden
 Sektion Physik
 Mommsenstrasse 13
 DDR 8027 DRESDEN

Germany, FR

G. Dietze
Physikalisch-Technische Bundes-
anstalt (PTB)
Bundesallee 100
D 3300 BRAUNSCHWEIG

K. Geissdörfer
Physikalisches Institut
Erwin-Rommel-Str. 1
D 8520 ERLANGEN

W. Glöckle
Institut für theoretische
Physik II
Ruhruniversität Bochum
4630 BOCHUM

H. Klein
Physikalisch-Technische Bundes-
anstalt (PTB)
Bundesallee 100
D 3300 BRAUNSCHWEIG

H.G. Menzel
FR Biophysik, Universität des
Saarlandes
D 6650 HOMBURG (Saar)

S.M. Qaim
Institut für Chemie 1
Kernforschungsanlage Jülich
D 5170 JÜLICH

G. Schreder
Institut für Strahlenphysik
Universität Stuttgart
Allmandring 3
D 7000 STUTTGART

W. von Witsch
Universität Bonn
Institut für Strahlen-und
Kernphysik
Nussallee 14-16
D 5300 BONN

Hungary

J. Csikai
Institute of Experimental Physics
Kossuth University
Bem tér 18/A
Pf. 105
H 4001 DEBRECEN

T. Sztaricskai
Institute of Experimental Physics
Kossuth University
P.O. Box 105
H 4001 DEBRECEN

India and IAEA

M.K. Mehta
Bhabha Atomic Research Centre
Van de Graaff Laboratory
B.A.R.C.
BOMBAY - 400.085

Italy

R. Bonetti
Istituto di Fisica Generale
Applicata dell'Università di
Milano
Via Celoria 16
20133 MILANO

R. Cherubini
Laboratori Nazionali di Legnaro
I.N.F.N.
Via Romea, 4
I 35020 LEGNARO (Padova)

L. Chendi
 Laboratori Nazionali di Legnaro
 I.N.F.N.
 Via Romea, 4
 I 35020 LEGNARO (Padova)

Japan

A. Takahashi
 Department of Nuclear Engineering
 Faculty of Engineering
 Osaka University
 Yamadaoka 2-1, Suita
 OSAKA-565

Lybia

W. Bahlul
 Tajura Nuclear Research Center
 P.O. Box 78639
 TRIPOLI

S.Y. Hurani
 Tajura Nuclear Research Center
 P.O. Box 78639
 TRIPOLI

Malaysia

A.M. Ghose
 School of Physics
 Universiti Sains Malaysia
 MINDEN, PENANG

Morocco

A. Ait Haddou
 Laboratoire de Physique Nucléaire
 Faculté des Sciences
 B.P. 1014
 RABAT

M. Berrada
 Laboratoire de Physique Nucléaire
 Faculté des Sciences
 B.P. 1014
 RABAT

Netherlands

Shi Xiangjun
 Netherlands Energy Research
 Foundation ECN
 P.O. Box 1
 1755 ZG PETTEN

Pakistan

K. Gul
 Pakistan Institute of Nuclear
 Science and Technology
 P.O. Nilore
 ISLAMABAD

Poland

L. Duda-Głowacka
 Institute for Nuclear Studies
 Hoza 69
 00-681 WARSAW

A. Marcinkowski
 Institute for Nuclear Studies
 Hoza 69
 00-681 WARSAW

Sweden

N. Olsson
 The Studsvik Science Research
 Laboratory
 S 611 82 NYKÖPING

Thailand

T. Vilaithong
 Department of Physics
 Faculty of Science
 Chiang Mai University
 CHIANG MAI

United States of America

L.E. Beghian
 University of Lowell
 LOWELL, Massachusetts 01854

H.H. Barschall
 University of Wisconsin
 MADISON, Wisconsin 53706

R.S. Caswell
 Ionizing Radiation Division
 National Bureau of Standards
 GAITHERSBURG, Maryland 20899

R.W. Finlay
 Ohio University
 ATHENS, Ohio 45701

and
 Kernforschungszentrum Karlsruhe
 Postfach 3640
 D 7500 KARLSRUHE, FR Germany

R.C. Haight
 Los Alamos National Laboratory
 MS-D406
 LOS ALAMOS, NM 87545

L.F. Hansen
 Lawrence Livermore National
 Laboratory
 P.O. Box 808
 LIVERMORE, CA 94550

E. Sheldon
 Department of Physics
 University of Lowell
 1 University Avenue
 LOWELL, MA 01854

Viet Nam

Hoang Dac Luc
 Institute of Physics
 National Centre of Scientific
 Research
 Nghia do, Tu liem
 HANOI

Yugoslavia

B. Antolković
 Rudjer Bošković Institute
 P.O. Box 1016
 41001 ZAGREB

P. Beličev
 Vojno tehnički institut
 11000 BEOGRAD

S. Blagus
 Rudjer Bošković Institute
 P.O. Box 1016
 41001 ZAGREB

M. Bogovac
 Rudjer Bošković Institute
 P.O. Box 1016
 41001 ZAGREB

R. Čaplar
 Rudjer Bošković Institute
 P.O. Box 1016
 41001 ZAGREB

B. Eman
 Rudjer Bošković Institute
 P.O. Box 1016
 41001 ZAGREB

H. Marković
 "Boris Kidrič" Institute of
 Nuclear Sciences - Vinča
 P.O. Box 522
 11001 BEOGRAD

D. Miljanić
 Rudjer Bošković Institute
 P.O. Box 1016
 41001 ZAGREB

D. Nikolić
 "Boris Kidrič" Institute of
 Nuclear Sciences - Vinča
 P.O. Box 522
 11001 BEOGRAD

G. Paić
 Rudjer Bošković Institute
 P.O. Box 1016
 41001 ZAGREB

M. Potokar
 Institut "Jožef Stefan"
 E. Kardelj University
 Jamova 39
 61111 LJUBLJANA

F. Rašuo
 Vojno tehnički institut
 11000 BEOGRAD

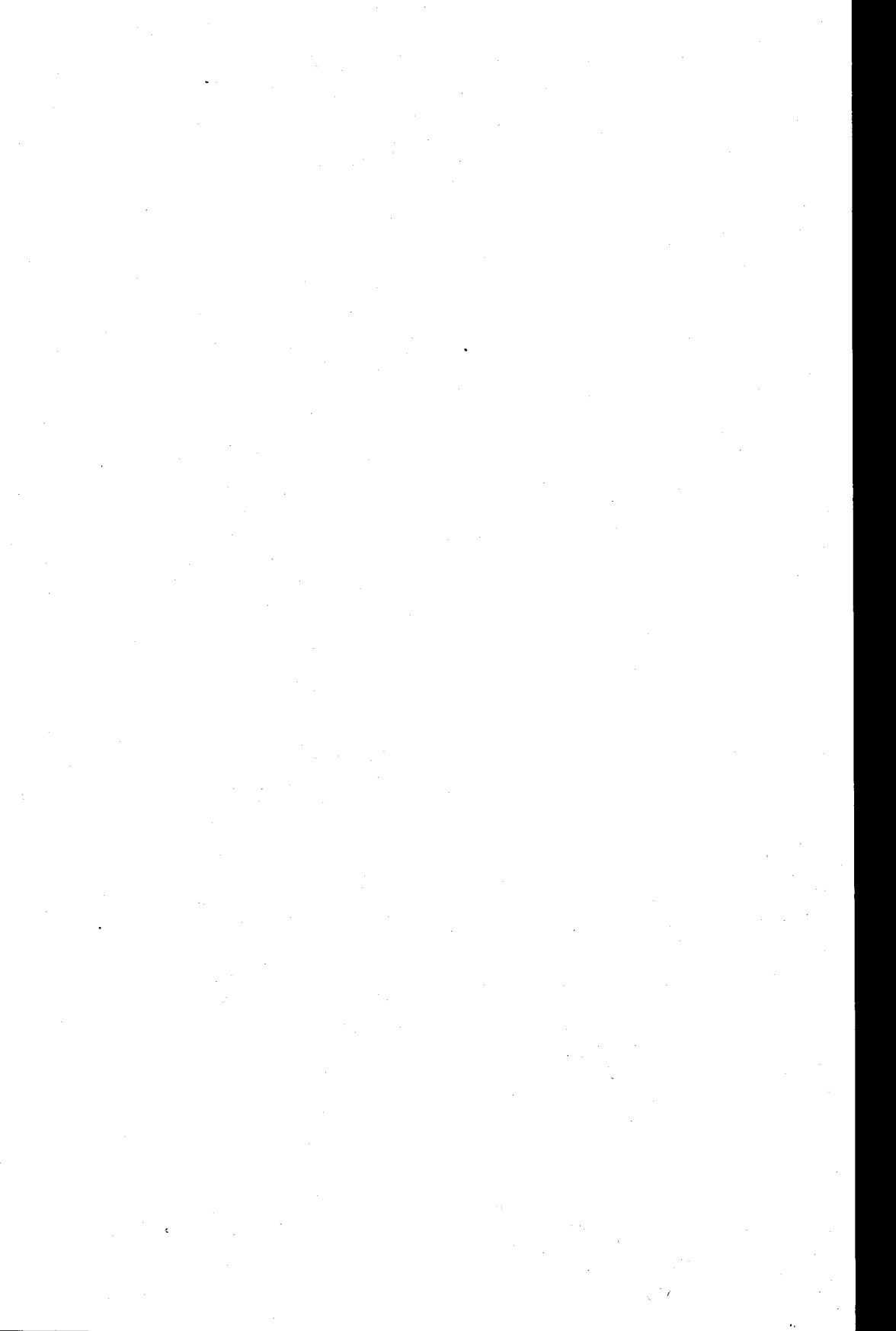
D. Rendić
 Rudjer Bošković Institute
 P.O. Box 1016
 41001 ZAGREB

M. Šokčić-Kostić
 "Boris Kidrič" Institute of
 Nuclear Sciences - Vinča
 P.O. Box 522
 11001 BEOGRAD

M. Zadro
 Rudjer Bošković Institute
 P.O. Box 1016
 41001 ZAGREB

Conference Secretary:

Zdenka Kuzmić
 Rudjer Bošković Institute
 P.O. Box 1016
 41001 ZAGREB



Printed by

**Viša tehnička škola za sigurnost pri radu i zaštitu od požara
Zagreb, Proleterskih brigada 68**